

Development of Aerogel Based Optofluidic Microreactors

by

Yaprak Özbakır

**A Thesis Submitted to the
Graduate School of Engineering
in Partial Fulfillment of the Requirements for
the Degree of**

Doctor of Philosophy

**In
Chemical and Biological Engineering**

Koç University

September 2018

Koç University

Graduate School of Sciences and Engineering

This is to certify that I have examined this copy of a PhD thesis by

Yaprak Özbakır

and have found that it is complete and satisfactory in all respects,

and that any and all revisions required by the final

examining committee have been made.

Committee Members:



Can Erkey, Ph. D. (Advisor, Koç University)



Alper Kiraz, Ph. D. (Co-Advisor, Koç University)



Yaman Arkun, Ph. D. (Koç University)



Ahmet Kerim Avcı, Ph. D. (Boğaziçi University)



Zeynep Ülker Demir, Ph. D. (Altınbaş University)



Erdal Uzunlar, Ph. D. (İzmir Institute of Technology)

Date:

14.09.2018

*dedicated to my family
for all the support, love and encouragement...*

ABSTRACT

Efficient light distribution in reaction medium in optofluidic microphotoreactors is highly desirable to fully harness their potential in light-driven chemical processes. The interaction of reactants, photocatalysts and light in microphotoreactors can be dramatically improved by enabling light propagation directly within the reactor using light guiding. In this study, liquid core optofluidic waveguides are utilized in microphotoreactors for guiding of light. In this approach, a suitable material confines the core liquid within internal channels and, simultaneously, behaves like waveguide cladding. For the propagation of non-lossy optical modes guided in the liquid by total internal reflection (TIR) of light from the channel walls, the cladding material should have a low absorption coefficient at working light wavelength and a lower refractive index than that of the core liquid ($n_{\text{core}} > n_{\text{cladding}}$). In applications with aqueous solutions, a material with a refractive index lower than the refractive index of water, 1.33, is required and only a narrow choice of solid host materials are available. An aerogel is a highly porous nanostructured material consisting of an interconnected open network of loosely packed, bonded particles separated by air gaps, and they feature extremely low refractive index of ~ 1 which makes them remarkable as solid cladding of liquid-core optofluidic waveguides without any additional coating.

A new, straightforward technique that uses direct manual drilling to manufacture TIR-based liquid-core optofluidic waveguides was first developed for aerogel monoliths. Fabrication of channels in aerogel blocks by manual drilling preserving nanoporous and monolithic structure of aerogels was demonstrated for the first time. Silica aerogels with densities ranging from 0.15 g/cm^3 to 0.39 g/cm^3 were produced by aging of alcogels in tetraethylorthosilicate solution for various time periods, followed by supercritical extraction of the solvent from the alcogel network. Subsequently, the resulting hydrophilic aerogel samples were made hydrophobic by hexamethyldisilazane (HMDS) vapor treatment. This method of fabrication is capable of producing channels with lengths significantly larger than those reported previously in the literature and it also provides relative flexibility in the channel shaping. Long channels (up to $\sim 7.5 \text{ cm}$) with varying geometries such as straight and inclined L-shaped channels could be fabricated. Multimode optofluidic waveguides prepared by filling the drilled channels in aerogel monoliths with water yielded high numerical aperture values (~ 0.8). Efficient guiding of light by TIR in the water-filled channels in aerogels was visually revealed

and characterized by monitoring the channel output. The resulting aerogel-based optofluidic waveguides exhibited efficient light guiding features, as verified by direct imaging of guided light modes and measuring the transmittance of the waveguides. The synthesized samples retained their low refractive index (below ~ 1.09) and, hence, they could serve as suitable optical cladding materials for aqueous waveguide cores (refractive index $n_{\text{core}} = 1.33$). Hydrophobic silica aerogel samples produced by the above technique also had low absorption coefficients in the visible part of the spectrum.

Next, a new type of aerogel-based microphotoreactor with integrated optofluidic waveguide was developed. This optofluidic microphotoreactor consists of a single liquid-filled channel fabricated inside a monolithic silica aerogel within which photochemical reactions are carried out. Due to the contrast of refractive indices between the aerogel and the liquid, optofluidic waveguides based on TIR are naturally formed to deliver the light to the liquid reaction medium inside the channel. This configuration is demonstrated to provide an excellent overlap between guided light and fluids in the channel for efficient photochemical activation. The microphotoreactor was shown to be well suited for photochemical degradation of a model organic compound – methylene blue (MB) dye – and the efficiency of the dye photoconversion as a function of the incident light power was characterized.

Finally, the field of optofluidics and highly porous, membrane-like properties of aerogels combined with a fully tunable three-dimensional structure were both exploited to construct photocatalytic microphotoreactors for controlled distribution of light through the reaction medium maintaining good interaction of light, fluid and the solid photocatalyst particles. Anatase TiO_2 nanoparticles were used as photocatalysts and they were successfully introduced into the mesoporous network of silica aerogels during sol-gel step of aerogel synthesis obtaining monolithic composite aerogels with varying titania content from 1 wt % to 50 wt % for the first time. The presence of TiO_2 and its desired crystalline structure in aerogel matrix was confirmed by XRD patterns and FE-SEM images. The silica-titania composite aerogels retained their interconnected mesoporous network with high porosity and pore volume as well as high surface area. Surface modification by HMDS was devised to alter the wetting conditions of the reactor walls for construction of liquid-core optofluidic waveguides in the channel. Cylindrical straight channels were then fabricated in the synthesized monolithic composites. Light was confined in the liquid in the channel and was guided in a controlled manner by TIR from the channel walls. Low and favorable propagation

losses ranged from 2.6 dB/cm to 3.9 dB/cm with increasing amount of the TiO_2 in the structure from 1 wt % to 50 % wt. The band gap of the SiO_2 - TiO_2 composites was estimated from Tauc plot calculated by Kubelka-Munk function from diffuse reflectance spectra of samples obtained using UV-visible reflectance spectroscopy. Using this technique, the anatase TiO_2 band gap was observed to be near expected value of ≈ 3.2 eV. The photocatalytic degradation of phenol over the immobilized photocatalysts in the channel walls by the light delivered through the constructed waveguide was used as model reaction to test the reactor and demonstrating very promising performance. The effect of incident light power, flow rate of the reactant and mass fraction of the photocatalyst in aerogel composites and additional oxygen supply on the performance of the reactor were investigated. Along with experimental studies, a simple model for immobilized photocatalytic microphotoreactors with integrated waveguide following a first order reaction rate with light dependency was developed and compared with experimental data for various conditions investigated. The reaction rate parameters were regressed from an exponential model. The model results and experimental data were found to be in good agreement. Lastly, carbon nanotubes (CNTs) were incorporated into the silica-titania matrix during sol-gel method resulting in monolithic composites and to their function on the photocatalytic degradation was investigated. As compared to the silica-titania composite aerogels, simply mixing of CNTs with TiO_2 presumably exhibited lower photocatalytic efficiency.

ÖZET

Optofluidik mikrofotoreaktörlerde ışık reaksiyonlarının verimli olarak gerçekleşebilmesi için ışığın reaksiyon ortamına dağıtımı kritik bir öneme sahiptir. Bu reaktörlerde ışığın reaktant ve fotokatalizör ile etkileşimi ışığın dalgakılavuzları yardımı ile reaksiyon ortamına doğrudan dağılımı ile önemli ölçüde geliştirilebilir. Bu önermede, sıvı çekirdekli dalgakılavuzları sıvı ile doldurulmuş bir kanal ile bu kanalı çevreleyen kaplama (cladding) işlevi gören katı bir malzemeden oluşur ve ışık kanal duvarlarından toplam iç yansıma (TİY) yaparak kanal boyunca ilerler. Kullanılan malzemenin ışığı akışkanın bulunduğu hacme hapsebedilmesi ve ışığın bu hacimde tam iç yansıma (TİY) ile kılavuzlanması gerekir. Bu amaç doğrultusunda kullanılabilecek uygun malzemenin, optofluidik dalgakılavuzlarında çekirdekteki sıvının kırınım katsayısından daha küçük kırınım katsayısına sahip olması ($n_{\text{çekirdek}} > n_{\text{kaplama}}$) gereklidir. Benzer, katı çekirdekli TİY temelli dalgakılavuzları için $n_{\text{çekirdek}} > n_{\text{kaplama}}$ koşulunu sağlayacak kaplama malzemeleri kolayca bulunsa da sıvı çekirdekli optofluidik dalgakılavuzlarında bu koşulu sağlayacak malzemelerin bulunması kolay değildir. Optofluidik dalgakılavuzunun çekirdeğindeki sıvının su olduğu düşünüldüğünde (görünür dalgaboylarında $n_{\text{su}} = 1.33$) 1.33 değerinden küçük kırınım katsayısına sahip kaplama malzemelerinin bulunması gerekmektedir. Bu noktada, sahip oldukları düşük kırınım katsayılarıyla (görünür dalgaboylarında $n \sim 1$), birbirlerine bağlı nanoparçacıkların oluşturduğu ve hava boşlukları ile ayrılmış açık bir ağdan oluşan oldukça gözenekli nanoyapılı özel bir malzeme olan aerojeller, TİY-temelli sıvı çekirdekli dalgakılavuzları için ideal kaplama malzemeleri olarak öne çıkarlar.

Çalışmanın ilk aşamasında, aerjel içinde monolitik ve nano gözenekli yapısını koruyarak TİY-temelli sıvı çekirdekli dalgakılavuzların üretimini sağlayan yeni bir teknik geliştirilmiştir. Özkütleleri 0.15 g/cm^3 ' den 0.39 g/cm^3 ' e kadar değişen silika aerojeller, alkojellerin Tetraetil Ortosilikat içinde farklı sürelerde yaşlandırılması ve superkritik ekstraksiyon işlemleri ile üretilmiştir. Hidrofilik yüzey özelliklerine sahip silika aerojeller, HMDS buharı altında hidrofobik olarak dönüştürülmüştür. Sentezlenmiş aerojellerin düşük kırınım katsayılarını korudukları ve optik kaplama için uygun oldukları gösterilmiştir. Geliştirilen kanal açma yönteminin literatürdeki diğer yöntemlere nazaran daha uzun kanalların oluşturulmasında elverişli olduğu gösterilmiştir. Düz ve L şeklindeki uzun kanallar ($\sim 7.5 \text{ cm}$) monolitik aerojeller içinde,

TİY-temelli sıvı çekirdekli verimli dalgakılavuzları oluşturulmuş ve öngörülen ışığın toplam iç yansıma kuramı deneysel olarak gösterilmiştir.

Monolitik aerogel içine entegre edilmiş olan TİY-temelli sıvı çekirdekli dalgakılavuzlarının sıvı reaktantlar ile iyi bir örtüşme sağlayarak fotokimyasal reaksiyonların gerçekleştiği ve aerogellerin optofluidik mikro-fotoreaktör olarak çalıştığı ilk kez gösterilmiştir.

Çalışmanın son kısmında, aerogellerin yüksek gözeneklilik ve yüzey alanına sahip üç boyutlu yapısı, fotokatalizör ilavesi için uygun bir ortam sağlamış ve monolitik yapılarına zarar vermeden yüksek oranda fotokatalizör nanoparçacıklarının yapı içerisine entegre edilebilmesini mümkün kılmıştır. Anataz titanyum dioksit (TiO_2) nanoparçacıkları fotokatalizör olarak kullanılmış ve silika aerogellerinin mezo gözenekli ağına aerogel sentezinin sol-jel aşaması sırasında başarıyla dahil edilmiş, ağırlıkça % 1 ile % 50 arasında değişen titanyum dioksit içerikli monolitik $\text{SiO}_2\text{-TiO}_2$ kompozit aerogeller elde edilmiştir. Elde edilen $\text{SiO}_2\text{-TiO}_2$ kompozit aerogellerin, ışığın reaktantlar ve kanal duvaralarında gömülü olan fotokatalizör ile iyi bir etkileşim sağlayabildiği ve fotokatalitik mikrofotoreaktörler olarak çalıştığı gösterilmiştir. Fenol'ün kanal duvarlarında immobilize edilmiş fotokatalizörler üzerinde, optofluidik dalgakılavuzları ile kanal boyunca yönlendirilen ışık altında fotokatalitik bozunması model reaksiyon olarak kullanılmıştır. Gelen ışık gücünün, reaktant akış hızının, fotokatalizör ve oksijen miktarının reaktörün performansı üzerindeki etkisi araştırılmıştır. Deneysel çalışmalara ilaveten, fotokatalitik mikrofotoreaktörlerde ışığın ve reaktantların akış hızının organik bileşiklerin degradasyonuna olan etkisini tanımlayan bir model geliştirilmiş ve deneysel veriler ile karşılaştırılmıştır. Model sonuçları ve deneysel verilerin uyumlu olduğu bulunmuştur. Son olarak, sol-jel metodu ile $\text{SiO}_2\text{-TiO}_2$ matrisine karbon nanotüpler dahil edilerek monolitik kompozitler elde edilmiş ve bunların fotokatalitik bozunma üzerindeki fonksiyonları araştırılmıştır. $\text{SiO}_2\text{-TiO}_2$ kompozit aerogellere kıyasla, karbon nanotüplerin SiO_2 ve TiO_2 ile karıştırılması, daha düşük fotokatalitik performans ile sonuçlanmıştır.

ACKNOWLEDGEMENTS

First and foremost, I would like to express my special thanks to my academic advisor, Prof. Dr. Can Erkey, for the guidance, positive attitude, motivation and support throughout my research. He is a great source of inspiration and patience with brilliant mind. His scientific intuition and comprehension have always been very helpful. I would like to extend my deepest gratitude to him for invaluable knowledge and professional experience that I have gained over these years which I will use all along in my academic life.

I would like to express my deepest appreciation to my co-advisor, Prof. Dr. Alper Kiraz, for opening up a new and very interesting field of study to me and providing insights into different areas. I am extremely grateful to him his guidance, motivation and suggestions during my Ph.D. study and for the opportunity to conduct my experimental studies in his laboratory.

My special thanks are extended to Dr. Alexandr Jonáš for his invaluable guidance, motivation and comments which extended this study and leading to success. I appreciate the feedback offered by him and I am truly thankful for his help and encouragement during this study. It was a unique and instructive experience to collaborate with him.

I would also like to express my deepest appreciation and gratitude to my thesis monitoring committee members, Prof. Dr. Yaman Arkun and Prof. Dr. Ahmet Kerim Avcı, for their inputs, comments and the time they spent during evaluating my progress and thesis. I would like to extend my sincere gratitude to thesis committee members Asst. Prof. Dr. Zeynep Ülker Demir and Asst. Prof. Dr. Erdal Uzunlar for their reading and comments on my thesis. I also thank Assoc. Prof. Dr. Seda Kızılel for her tolerance for use of Nanodrop spectrophotometer.

Many thanks to former and current members of Nano-Optics Research Laboratory for their help and creating a friendly working environment.

My sincere thanks to my colleagues in Energy Technologies and Supercritical Fluids Research Group, Dr. Selmi Erim Bozbağ, İbrahim Şahin, Shadi Khan Baloch, Işık Sena Acar, Gözde Tekeli, Bengisu Barım, Zeynep İnönü and Hande Güneş for their help and support in the laboratory throughout my graduate study. It has been a great joy to know you and to work with you.

I express my warmest thanks to Volkan Balci for his unconditional friendship and being always supportive along the way of this study and as it was in the past. I am

also immensely grateful to my friends, Seyhan Uçar, Fatih Rahim, Ehsan Sarayloo, Ayşenur Eser and Çiğdem Altıntaş for their warm friendship and support during these years.

Last, but not least, I would like to express my wholehearted thanks to my dear family for their endless love, encouragement and faith in me throughout my life. Their support and encouragement was worth more than I can express.

TABLE OF CONTENTS

Chapter 1	1
INTRODUCTION	1
Chapter 2	7
LITERATURE REVIEW	7
2.1 Optofluidic Microphotoreactors	7
2.2 Liquid-core Optofluidic Waveguides	10
2.3 Aerogels	12
2.4 Why Use Aerogels for Optical Applications?	14
2.5 Optical Properties of Aerogels.....	17
2.5.1 Haze of Aerogels	19
2.5.2 Refractive Index of Aerogels	20
2.6 Aerogel-Based Optofluidic Waveguides	22
2.7 Preparation of Aerogel Waveguides	25
2.7.1 Synthesis of Aerogels	25
2.7.2 Surface Modification of Aerogels.....	27
2.8 Techniques for Fabrication of Optofluidic Channels in Aerogel Monoliths	28
2.8.1 Preform Removal	29
2.8.2 Laser Ablation.....	31
2.9 Construction of Liquid-Core Optofluidic Waveguides in Aerogels	33
2.10 Characterization of Light Propagation in Aerogel-Based Optofluidic Waveguides.....	35
2.11 Applications of Aerogel-Based Optofluidic Waveguides	40
Chapter 3	43
CHARACTERIZATION TECHNIQUES	43
3.1 Bulk Density and Porosity	43
3.2 Pore Structure Characteristics with N ₂ Adsorption/Desorption	43
3.3 Optical Properties of Aerogels by UV-VIS Spectrophotometer.....	44
3.4 Hydrophobicity	49
3.5 Photochemical Reactions	49
Chapter 4	51
TOTAL INTERNAL REFLECTION-BASED OPTOFLUIDIC WAVEGUIDES FABRICATED IN AEROGELS	51
4.1 Introduction.....	51
4.2 Materials and Methods.....	52

4.2.1	Preparation of Silica Aerogel Monoliths	52
4.2.2	Surface Modification with HMDS.....	53
4.2.3	Channel Formation in Aerogel Monoliths	54
4.2.4	Refractive Index of Aerogels	55
4.2.5	Characterization of Optofluidic Waveguides	57
4.3	Results And Discussion	58
4.3.1	Properties of Synthesized Aerogel Samples	58
4.3.2	Channel Formation in Aerogel Blocks	66
4.3.3	Light-guiding in liquid-core optofluidic waveguides in aerogels.....	67
4.4	Conclusions.....	71
Chapter 5.....		72
A NEW TYPE OF MICROPHOTOREACTOR WITH INTEGRATED OPTOFLUIDIC WAVEGUIDE BASED ON SOLID-AIR NANOPOROUS AEROGELS.....		72
5.1	Introduction.....	72
5.2	Materials and Methods.....	73
5.2.1	Materials	73
5.2.2	Synthesis of Silica Aerogels	73
5.2.3	Characterization of Silica Aerogels	74
5.2.4	Fabrication of Channels in Aerogel Monoliths.....	75
5.2.5	Experimental Setup for Carrying Out Photochemical Reactions	76
5.3	Results and Discussion	78
5.3.1	Properties of Synthesized Aerogel Samples	78
5.3.2	Light-guiding in Aerogel-based Microphotoreactors	80
5.3.3	Photodegradation of Organic Compounds.....	82
5.4	Conclusions.....	90
Chapter 6.....		91
PHOTOCATALYTIC TRANSFORMATION IN SILICA-TITANIA COMPOSITE AEROGEL-BASED OPTOFLUIDIC MICROREACTORS		91
6.1	Introduction.....	91
6.1.1	Design of aerogel-based microphotoreactor	94
6.2	Materials and Methods.....	95
6.2.1	Materials	95
6.2.2	Synthesis of SiO ₂ -TiO ₂ Composite Aerogels.....	95
6.2.3	Surface Modification with HMDS.....	97
6.2.4	Experimental Set-up for Photocatalytic Chemical Reactions	98
6.3	Results and Discussion	100

6.3.1	Properties of SiO ₂ -TiO ₂ Aerogel-based Microphotoreactor	100
6.3.2	Optical Properties of SiO ₂ -TiO ₂ Aerogel-based Microphotoreactor	108
6.3.3	Photocatalytic Reactions in Silica-Titania Aerogel-based Microphotoreactor	113
6.3.4	Effect of Flow Rate on Photocatalytic Degradation of Phenol.....	116
6.3.5	Effect of photocatalyst amount on photocatalytic degradation of phenol	117
6.3.6	Effect Of Dissolved Oxygen on Photocatalytic Degradation of Phenol	118
6.3.7	Effect of light power on photocatalytic degradation of phenol	119
6.3.8	Photocatalytic Transformation of Phenol In Carbon Nanotube Silica and Titania Composite Aerogel-Based Optofluidic Microphotoreactors.....	121
6.3.9	Model Study In Fabricated Microphotoreactors	128
6.4	Conclusions.....	133
Chapter 7	135
CONCLUSION	135
BIBLIOGRAPHY	138
APPENDIX	13850

LIST OF TABLES

Table 2.1. Empirical correlations between the density ρ and refractive index n / dielectric permittivity ε of aerogels proposed in the literature.	21
Table 2.2. Index of Refraction (n) of Various Cladding Materials	23
Table 4.1. Properties of HMDS-treated aerogel samples of various densities.....	59
Table 4.2. Pore characteristics of HMDS-treated aerogel samples of various density ..	60
Table 4.3. Hunt parameters for the silica aerogels.....	66
Table 6.1. Titania fraction measured by XRF.....	101
Table 6.2. Densities and pore characteristics of synthesized silica-titania composite aerogels.	101
Table 6.3. Densities and pore characteristics of synthesized silica-titania composite aerogels.	123

LIST OF FIGURES

Figure 2.1. Components of a typical optofluidic microphotoreactor.....	7
Figure 2.2. (a) Micro-capillary reactor with the inner wall coated with self-assembled SiO ₂ /TiO ₂ for methylene blue degradation ⁴⁴ . (b) Single straight microchannel reactor with immobilized TiO ₂ -coated silica beads ⁴⁵ . (c) Branched microchannel reactor ⁴⁶ . (d) Planar microreactor using immobilized nanoporous TiO ₂ film for methylene blue decomposition (on the left) ¹⁵ . Cross-section of the planar microreactor (on the right) ¹⁵ . (e) Scheme and photograph of thin TiO ₂ film coated planar microreactor ⁴¹ . (f) Scheme of nanofibrous TiO ₂ microreactor ²²	9
Figure 2.3. Total internal reflection in a stream of water flowing through a hole drilled at the bottom of a glass bottle. Light from a laser source is coupled into the water stream ⁵⁶	11
Figure 2.4. Transmission spectra of TEOS-based silica aerogel [56]. “Reproduced with permission from Tamon et al., Preparation of silica aerogel from TEOS; published by J. Colloid Interface Sci., 1998.”	19
Figure 2.5. Refractive index as a function of silica aerogel density. The solid line assumes an amorphous structure (proportionality constant 0.21), while the dashed line assumes a crystalline structure [72]. “Reproduced with permission from Henning et al., Production of silica aerogel; published by Physica Scripta, 1981.”	21
Figure 2.6. (a) Liquid-core optofluidic waveguide created in a microchannel within a silica aerogel monolith; (b) Nanometer-scale particles and pores in a monolithic aerogel ³⁶ ; (c) Longitudinal cross section of a liquid-core optofluidic waveguide. Red arrows indicate light rays confined within the waveguide core by TIR. ϕ is the angle of incidence on the core-cladding interface. “Reproduced with permission from Özbakır et al., Aerogels for Optofluidic Waveguides; published by Micromachines, 2017.”	25
Figure 2.7. Preparation of monolithic aerogels by the sol-gel method. (a) Reactants and solvents are mixed in the reaction vessel; (b) upon addition of a catalyst, colloidal suspension (sol) is formed; (c) condensation of the sol leads to the formation of alcogel containing impurities; (d) aging process reinforces the gel skeleton structure; (e) supercritical drying yields the final solid dry aerogel.....	27
Figure 2.8. Formation of optofluidic waveguides in aerogel monoliths using fiber-based channel preforms ³⁹ . (a) The precursor solution is poured over an optical fiber mounted inside a box, allowed to gel, and subsequently processed into a monolithic aerogel; (b) the fiber is pulled out of the aerogel block, leaving behind an open	

microchannel; (c) water is pumped into the microchannel through a capillary; (d) light is coupled into the water column via a reinserted optical fiber. “Reproduced with permission from Xiao et al., Optofluidic microchannels in aerogel; published by Opt. Lett., 2011”. Preparation of silica aerogel monoliths with an embedded U-shaped channel ¹⁰⁷. (e) Precursors are mixed in the reaction vessel; (f) acid and (g) base catalyst addition lead to the formation of sol into which the channel preform made of POSS is inserted; (h) aging in ethanol-water mixture and (i) solvent exchange with pure ethanol yield reinforced alcogel; (j) extraction with scCO₂ removes the POSS channel preform, leaving the final monolithic aerogel with an empty channel inside. “Reproduced with permission from Eris et al., Three-dimensional optofluidic waveguides in hydrophobic silica aerogels via supercritical fluid processing; published by J. Supercrit. Fluids, 2013.” 30

Figure 2.9. (a) A schematic representation of laser ablation process using a focused pulsed laser beam. (b) Experimental setup used for aerogel micromachining by fs-laser ablation ³⁸. “Reproduced with permission from Yalızay et al., Versatile liquid-core optofluidic waveguides fabricated in hydrophobic silica aerogels by femtosecond-laser ablation; published by Opt. Mater., 2015.” 33

Figure 2.10. Channels fabricated using fiber-based preforms. SEM images of cleaved cross-sections of microchannels with diameters (a) 100 μm, (b) 35 μm, and (c) 23 μm, (d) Optical micrograph of the cleaved cross-section of a microchannel with a diameter of 4 μm. (e) SEM image of the aerogel surface; the scale bar is 0.5 μm. ³⁹. “Reproduced with permission from Xiao et al., Optofluidic microchannels in aerogel; published by Opt. Lett., 2011.” 34

Figure 2.11. Channels fabricated using femtosecond laser ablation. (a) SEM image of the input face of a microchannel ablated in the aerogel. The depth of the channel is about 300 μm and the diameter is about 500 μm. (b) Axial cross-section view of the channel ablated in the aerogel. During machining, ablated silica particles accumulated inside the channel (see the right part of the channel) (c) Axial cross-section view of the channel ablated with simultaneous purging of the sample with high-pressure nitrogen gas. All the dust accumulated in the channel during the machining was removed. For recording the cross-sectional images shown in (b) and (c), the samples were cleaved along the axis of the channel ³⁸. “Reproduced with permission from Yalızay et al., Versatile liquid-core optofluidic waveguides fabricated in hydrophobic silica aerogels by femtosecond-laser ablation; published by Opt. Mater., 2015.” 34

Figure 2.12. Light propagation in aerogel-based optofluidic waveguides. (a) – (b) Waveguides fabricated using fiber preforms. (a) Guiding of 635 nm laser light in a 125 μm diameter aerogel microchannel filled with water. The light enters into the channel from the left through a fiber, and emerges from the end of the channel toward the right. The fiber ends at the bright scatter point about 2 mm inside the 10 mm long aerogel block; (b) (left to right) images taken at 40 s intervals at the end of the channel, as the water evaporates ³⁹. “Reproduced with permission from Xiao et al., Optofluidic microchannels in aerogel; published by Opt. Lett., 2011.” (c) Waveguides fabricated using supercritical extraction of POSS preforms. (c) Light guiding in a water-filled U-shaped channel inside a hydrophobic silica aerogel; the light was focused on the left end of the channel and exited from the right end of the channel ¹⁰⁷. “Reproduced with permission from Eris et al., Three-dimensional optofluidic waveguides in hydrophobic silica aerogels via supercritical fluid processing; published by J. Supercrit. Fluids, 2013.” (d) – (e) Waveguides fabricated using femtosecond laser ablation. (d) Photograph of an aerogel monolith with a liquid-filled channel in the center. (e) Green fluorescence emitted from the channel filled with fluorescein-doped ethylene glycol solution upon illumination with blue light. ³⁸. “Reproduced with permission from Yalızay et al., Versatile liquid-core optofluidic waveguides fabricated in hydrophobic silica aerogels by femtosecond-laser ablation; published by Opt. Mater., 2015.” (f) - (g) Waveguides fabricated using manual drilling. (f). Total internal reflection of guided light in the water-filled channel fabricated by drilling in a monolithic aerogel ($\rho = 0.15 \text{ g/cm}^3$). (g) Light propagation in a liquid-filled L-shaped channel within the aerogel monolith (side view) ³⁷. “Reproduced with permission from Özbakır et al., Total Internal Reflection-Based Optofluidic Waveguides Fabricated In Aerogels; published by J. Sol-Gel Sci. & Tech., 2017.” 36

Figure 2.13. Schematics of experimental setup used in the characterization of the light-guiding performance of liquid core optofluidic waveguides ^{38, 107}. “Reproduced with permission from Yalızay et al., Versatile liquid-core optofluidic waveguides fabricated in hydrophobic silica aerogels by femtosecond-laser ablation; published by Opt. Mater., 2015.” 39

Figure 2.14 (a) Grayscale CCD camera image of guided light in the liquid-core waveguide inside the aerogel. The red dashed curve indicates the channel contour, and the light outside the region delimited by the curve results from scattering losses. (b) Normalized power of light transmitted through the waveguide versus the propagation

distance along the waveguide axis, shown in semi-log scale. Blue dots: experimental data points; red line: exponential fit of the experimental data ³⁸ . “Reproduced with permission from Yalızay et al., Versatile liquid-core optofluidic waveguides fabricated in hydrophobic silica aerogels by femtosecond-laser ablation; published by Opt. Mater., 2015.”	40
Figure 2.15. Possible applications of aerogel-based optofluidic waveguides. (a) Aerogel-based photobioreactors. (b) Aerogel-based photoreactors. (c) Aerogel-based photocatalytic reactors. (d) Detection and diagnostic devices based on optofluidic waveguides ³⁶ . “Reproduced with permission from Özbakır et al., Aerogels for Optofluidic Waveguides; published by Micromachines, 2017.”	42
Figure 3.1. Micromeritics ASAP 2020 N ₂ adsorption-desorption analysis system; (A) degas ports; (B) heating jacket; (C) degas dewar; (D) analysis port; (E) sample port; (F) analysis dewar.....	44
Figure 3.2. (1) A photograph of Shimadzu UV-3600 with an auxiliary integrating sphere (2) BaSO ₄ powder (3) Integrating sphere system (4) Components of integrating sphere apparatus.....	45
Figure 3.3. Schematics of light transmission phenomena in aerogels.	46
Figure 3.4. (a) Schematic of total transmittance measurement. (b) Schematic of diffuse transmittance measurement.....	46
Figure 3.5. Schematics of diffuse reflectance measurement in the integrating sphere..	47
Figure 3.6. Two fluxes in Kubelka-Munk theory	48
Figure 4.1. Preparation of monolithic silica aerogels by aging silica alcogels in TEOS solution.....	53
Figure 4.2. Silanization of silica aerogel surface by vapor-phase deposition of HMDS	54
Figure 4.3. (a). Straight-channel formation in aerogel by manual drilling (b). L-shaped channel formation in aerogel by manual drilling (c). Side-view of inclined L-shaped channel in monolithic aerogel.....	55
Figure 4.4. Top view of experimental set-up for the measurement of the refractive index of silica aerogels ³⁷ . “Reproduced with permission from Özbakır et al., Total Internal Reflection-Based Optofluidic Waveguides Fabricated In Aerogels; published by J. Sol-Gel Sci. & Tech., 2017.”	56
Figure 4.5. Schematics of the experimental setup used in the characterization of light guiding in liquid-core optofluidic waveguides.	57

Figure 4.6. (a) Water droplet resting on the surface of hydrophobic silica aerogel, $\rho = 0.15 \text{ g/cm}^3$ (b) Water droplet resting on the surface of hydrophobic silica aerogel, $\rho = 0.22 \text{ g/cm}^3$	59
Figure 4.7. Refractive index of silica aerogels as a function of aerogel density. The proportionality constant between the refractive index and density is $k = (0.27 \pm 0.016) \text{ cm}^3/\text{g}^{37}$	61
Figure 4.8. Absorption spectra of synthesized aerogel samples of various densities. ...	62
Figure 4.9. Total transmittance spectrum (solid lines) and diffuse transmittance spectrum (dashed lines) of synthesized aerogel samples of various densities in the spectral range between 350 nm-1800 nm.	63
Figure 4.10. Haze (%) measurement of aerogel samples.....	64
Figure 4.11. Transmittance spectra of silica aerogels in the spectral range between 220 nm-1220 nm. (a) Transmittance spectra of the silica aerogel with a density of 0.15 g/cm^3 . (b) Transmittance spectra of the silica aerogel with a density of 0.22 g/cm^3 . (c) Transmittance spectra of the silica aerogel with a density of 0.39 g/cm^3	66
Figure 4.12 a. Side view of a hydrophobic silica aerogel rod with a channel parallel to the rod axis (channel length $L = 7.5 \text{ cm}$, channel diameter $D = 2.1 \text{ mm}$) b. Top-view of the aerogel rod shown in (a) with a channel parallel to the rod axis c. Silica aerogel sample with multiple channels d. Side view of a L-shaped channel with one horizontal and one inclined channel (channel lengths $L_1 = 1.2 \text{ cm}$ and $L_2 = 3.8 \text{ cm}$, respectively; channel diameters $D_1 = D_2 = 2.1 \text{ mm}$).....	67
Figure 4.13. Total internal reflection in the water-filled channel in a monolithic aerogel ($\rho = 0.15 \text{ g/cm}^3$)	68
Figure 4.14. (a). Light propagation through an optical fiber inserted into a water-filled channel in aerogel. A ray with the maximum acceptance half-angle of the fiber in air (Φ) is coupled into the fiber and subsequently propagates along the fiber and emerges with angle (α) into water. (b) Total internal reflection in the microchannel. d is the diameter of the fiber core (0.3 mm), D is the diameter of the microchannel (2.1 mm).....	69
Figure 4.15. (a) Light coupling into an empty channel in the aerogel (b) Light propagation in liquid-filled channel within the aerogel monolith (side view).	70
Figure 5.1. (a) Aerogel-based microphotoreactor with an integrated optofluidic waveguide (b) Cross-sectional view of the microphotoreactor/waveguide system illustrating light guiding in the liquid by TIR.....	73

Figure 5.2. A side-view of an aerogel monolith with the fabricated inclined L-shaped channel	75
Figure 5.3. Schematics of experimental set-up used in the characterization of light guiding and photochemical reactions in aerogel-based optofluidic microphotoreactors.	77
Figure 5.4. Calibration curve of aqueous MB solutions used for quantification of sample concentration in 2-140 μ M range.	77
Figure 5.5. Water droplet resting on the surface of HMDS-treated silica aerogel monolith.	79
Figure 5.6. FTIR-ATR spectra of (a) an untreated hydrophilic silica aerogel, (b) the surface of the channel fabricated in a HMDS-treated hydrophobic silica aerogel.	80
Figure 5.7. (a) Light propagation in a channel fabricated in an aerogel monolith and filled with aqueous MB solution under ambient light illumination (side view). (b) Light propagation in the same channel as shown in part a without ambient light illumination (side view). The guided light fills the whole volume of the channel.	82
Figure 5.8. Time variation of the concentration of aqueous MB solution contained in an aerogel channel kept in the dark. The initial concentration of MB was 37.2 μ M.	83
Figure 5.9. FTIR-ATR spectra of internal surfaces of channels fabricated in silica aerogel monoliths acquired before and after MB photolysis took place in the channel.	84
Figure 5.10. Time variation of the concentration of aqueous MB solution contained in an aerogel channel under illumination at 388 nm with varying power of the incident light. The initial concentration of MB was 36 μ M. The incident power values were measured before coupling the light into the input optical fiber.	86
Figure 5.11. Variation of photoconversion of aqueous MB solution illuminated by incident light at 388 nm with increasing power. The initial MB concentration was 36 μ M.	86
Figure 5.12. Light propagation in the plastic tubing filled with aqueous MB solution under ambient light illumination (side view).	88
Figure 5.13. Time variation of the percentage conversion of aqueous MB solution contained in the tubing and its photoconversion at an incident light of 70 mW. The initial concentration of MB was 30 μ M.	88
Figure 6.1. Schematic of the SiO ₂ -TiO ₂ composite aerogel-based microphotoreactor. .	95
Figure 6.2. Schematics of silica-titania composite aerogel synthesis through sol-gel method.	96

Figure 6.3. A photograph of the synthesized monolithic silica-titania aerogel composite with 50 wt% of titania.....	97
Figure 6.4. (a) Schematics of experimental set-up used in the characterization of light guiding and photocatalytic reactions in aerogel-based optofluidic microphotoreactors. (b) Schematics of the reactor system.	100
Figure 6.5. Pore size distribution and N ₂ adsorption–desorption isotherms of the silica aerogel and silica–titania composite aerogels.	102
Figure 6.6. N ₂ adsorption/desorption isotherms for the silica aerogel and silica–titania composite aerogels.....	103
Figure 6.7. FESEM images of native silica aerogel and silica-titania aerogel composites. (a) FESEM images of the native silica aerogel (scale bar=200 nm). (b-c) FESEM images of anatase titania particles (scale bar=200 nm). (d-h) FESEM images of the silica-titania aerogel composites with increasing wt% of titania (scale bar=200 nm): 1, 14, 24, 32, 50 wt%, respectively. (i-j) FESEM images of silica-titania aerogel composites 24 and 50 wt % of titania, respectively (scale bar=1 μm). (k) A typical EDX spectrum of the synthesized silica-titania composite.....	106
Figure 6.8. XRD patterns of native silica aerogel, silica-titania composites with increasing titania content from 1 to 50 wt % and anatase titania powder.	107
Figure 6.9. (a) DRS of the SiO ₂ -TiO ₂ aerogel composites. The inset represents the diffuse reflectance spectra of the native silica aerogel. (b) Tauc plot of transformed Kubelka Munk function versus the energy of the light absorbed for the SiO ₂ -TiO ₂ aerogel composites. The inset (top) represents Kubelka Munk function vs. the energy of light absorbed of the native silica aerogel and the inset (bottom) is Kubelka Munk function vs. the energy of light absorbed for the SiO ₂ -TiO ₂ aerogel composite with 32 wt% of titania.....	109
Figure 6.10. (a-e) Urbach energy plots for the silica-titania aerogel composites with increasing titania content from 1 to 50 wt%, respectively.....	111
Figure 6.11. Light propagation loss in the water-filled channel in the silica-titania aerogel composites with titania content varying in the range from 1 wt% to 50 wt%.	112
Figure 6.12. (a) Concentration of phenol in the exit stream of the silica-titania aerogel-based microphotoreactor (50 wt% titania) as a function of time in dark. (b) Concentration of phenol in the exit stream in the silica aerogel-based microphotoreactor as a function of time under illumination at 366 nm.	114

Figure 6.13. (a) Concentration of phenol in the exit stream of the silica-titania aerogel-based microphotoreactor (50 wt% titania) in dark. (b) Concentration of phenol in the exit stream in the silica aerogel-based microphotoreactor under illumination at 366 nm. (c) Concentration of phenol in the exit stream in the silica aerogel-based microphotoreactor in the dark after illumination.	115
Figure 6.14. (a) Time variation of the concentration of phenol in the exit stream in the silica aerogel-based microphotoreactor with varying reactant flow rate under illumination at 366 nm and incident power of 41 mW. (b) The corresponding percent degradation of phenol with varying flow rates. (c) The variation of phenol conversion with varying reactant flow rates.	117
Figure 6.15. (a) Time variation of the concentration of phenol in the exit stream in the silica aerogel-based microphotoreactor with varying reactant flow rate under illumination at 366 nm and incident power of 41 mW. (b) The corresponding percent degradation of phenol in varying amount of titania.	118
Figure 6.16. (a) Time variation of the phenol concentration with varying oxygen concentration. (b) The corresponding percent degradation of phenol in varying oxygen concentration.	119
Figure 6.17. (a) Time variation of the phenol concentration with varying incident light power. (b) Corresponding percent degradation of phenol with varying incident light power with time variation. (c) Corresponding conversion of phenol with varying incident light power.	120
Figure 6.18. A photograph of a monolithic silica-titania composite aerogel with embedded SWCNTs in 1 wt%.	122
Figure 6.19. N ₂ adsorption/desorption isotherms for the silica aerogel and silica–titania composite aerogels.	123
Figure 6.20. FESEM images of silica-titania aerogel composites with embedded CNTs with increasing weight percent. (a-b) FESEM images of the aerogel composites with 1 wt% of SWCNTs (scale bar=200 nm) (c) FESEM images of the silica-titania aerogel composites with 1 wt% of SWCNTs (scale bar=1 μm). (d) EDX spectrum of silica-titania composite with 1 wt% of SWCNTs. (e-f) FESEM images of silica-titania aerogel composites 5 wt% of MWCNTs (scale bars=100nm and 1 μm, respectively).	125
Figure 6.21. XRD patterns of native silica aerogel, silica-titania composites with increasing CNT content from 1 to 5 wt %.	126

Figure 6.22. Tauc plot of transformed Kubelka Munk function versus the energy of the light absorbed for the SiO ₂ -TiO ₂ -CNTs aerogel composites.....	127
Figure 6.23. Phenol degradation in silica-titania composite aerogel (wi=0.5:0.5 SiO ₂ :TiO ₂) and silica-titania-CNTs composite aerogel (wi=0.495:0.495:0.01 SiO ₂ :TiO ₂ :CNTs).....	128
Figure 6.24. Schematic representation of 1D model in the aerogel-based microphotoreactor with photocatalyst deposited channel.....	128
Figure 6.25. The comparison of model and experimental data of phenol conversion at varying absorbed light intensity by titania.....	131
Figure 6. 26. The variation of phenol concentration along the length of the channel in the microphotoreactor. (C ₀ =368 μM, Q = 14.3 μLmin ⁻¹ and P ₀ = 41 mW).....	132
Figure 6. 27. The variation of phenol conversion along the length of the channel in the microphotoreactor. (C ₀ =368 μM, Q = 14.3 μLmin ⁻¹ and P ₀ = 41 mW).....	132

Chapter 1

INTRODUCTION

Optofluidics is an emerging research field which combines optics and photonics with microfluidics in the same platform and exploits the synergy between the unique features of both disciplines for a wide range of applications including biological sensing¹⁻², chemical analysis², imaging³⁻⁵, detection⁶⁻⁹ and energy conversion¹⁰⁻¹⁵. Optofluidics allows for simultaneous delivery and control of light and fluids with microscopic precision. Since the light and the fluid share the same space within an optofluidic system, photons can be efficiently transferred to the fluid. Conversely, adjustment of optical properties of the fluid directly affects the photon propagation path.

Optofluidic microphotoreactors, in which light-activated photochemical reactions are carried out in solutions confined within microfluidic channels, have been recognized in the recent years to be versatile tools for light-driven photochemical and photocatalytic reactions as a new emergence field of optofluidics¹⁶⁻¹⁷. The capability of such microphotoreactors to integrate optics and photonics with fluidic channels at small volumes in the same platform provides simultaneous delivery and control of light and fluids with microscopic precision. Such a combination with maximized overlap between light and solutions residing in small reaction volumes therefore improves light-matter interactions in the channels, resulting in high-efficient photochemical and photocatalytic reactions¹⁸⁻²² at incident optical powers smaller than those used in conventional systems, with improved spatial homogeneity of irradiation and better light penetration through the reaction volume compared to the conventional large-scale photoreactors.

A variety of optofluidic microphotoreactors have been described in the literature, which generally consist of microchannels fabricated in a solid substrate covered by a transparent plate sealing the channels from the top. Microchannels have been directly fabricated in glass, polymer and ceramic substrates using various methods such as photolithography, dry/wet etching and micro/nano imprinting²³⁻²⁵. The solid photocatalyst particles are generally immobilized on inner walls of reactors in the form of a film coating. The reactant can flow through the channels through inlet and outlet of the reactors while externally irradiated resulting in and out by inlet and outlet while

using external light source to irradiate the reaction chamber. The excited electron (e^-) and hole (h^+) will react with the organics in the polluting water and decompose them. However, smooth surfaces of reactor walls might limit photocatalyst adhesion to the reactor walls as a stable and robust coating to survive extended periods at conditions during reactions. The above described microphotoreactors are designed to function exclusively with external irradiation delivered through the transparent top wall of the channel. Therefore, the thicknesses of the transparent plate, the depth of the channel walls and the geometry of the microphotoreactor have to be carefully adjusted to minimize the absorption and reflection losses. Despite optimizing the geometry, light access to confined spots in the reaction chamber may still be problematic²⁶⁻²⁸.

Implementation of optical waveguides into microphotoreactors has been recently gaining great deal of attention to tackle the limitations of the conventional optofluidic microphotoreactors so that the interaction of photocatalysts and light can be improved. Based on this concept, the photoreactor was typically constructed as bundles of photocatalyst-coated fibers in a glass where most of the light intensity propagates along the fiber by TIR, a small evanescent fraction refracts, penetrates through the cladding and excites the photocatalyst layer at the outer surface of the fiber, thus creating e^-h^+ pairs for photocatalytic reactions²⁹⁻³³. Photonic crystal fibers with a hollow core (HC-PCF) surrounded by a cladding structure with deposited photocatalyst films consisting of a periodic array of sub-micrometer-sized air-filled openings running along the entire length of the fiber³⁴ were also employed for the photocatalytic reactions¹⁶. Despite their successful applications, HC-PCF-based microphotoreactors exhibit several drawbacks and limitations. Due to the small sizes of fiber hollow cores, only a low volume of reactants can be treated in HC-PCF photoreactors. Since the glass structure of the fiber is impermeable for gases, gaseous reactants and products of photochemical reactions cannot be readily exchanged between the reactor and its surroundings. Similarly, air bubbles formed in the liquid solutions confined within the fiber core cannot be easily removed, which results in high optical loss from scattering and eventually causes failure of the waveguide.

Regarding the above review, it is obvious that two major issues need to be addressed for the microphotoreactors. The first is to attain high photon transfer to the reactants and solid photocatalyst particles through the same path with the reactants eliminating air-bubbles disturbing light propagation through the reaction volume. The second is stable photocatalyst immobilization in the reactor walls. Construction of a

microphotoreactor with channels made out of an interconnected open porous network which acts as a membrane for separation of the air bubbles from the liquid and concurrently manipulates the path of light in the channel might be a possible key to overcome the problems. The channels thus behave as an optical waveguide which simultaneously confines and overlap light and reactants. Aerogels appear as one of the most promising nanostructured materials to be implemented as optical waveguiding in liquids ³⁵⁻³⁸. They are highly porous nanostructured solids consisting of an interconnected open network of loosely packed, bonded particles separated by air gaps, and they feature very low refractive index and high specific surface area ³⁵⁻³⁸. These properties, particularly the low refractive index of ~ 1.05 for which the aerogels are often referred to as “solid air”, make aerogels a remarkable solid-cladding material for optofluidic waveguides that can be used without any additional modification, since almost all liquids have refractive indices exceeding that of aerogels. Optofluidic waveguides can be constructed by opening channels inside monolithic aerogel blocks. These channels are surrounded by a wall made up of interconnected particles that are around 40 to 80 nm in size, with pockets of air in between them that constitute pores with sizes less than 100 nm. The air in the aerogel pockets is responsible for guiding light by TIR in a liquid-filled channel. Following appropriate chemical treatment that makes the channel surface compatible either with polar or with non-polar liquids, the channels can be filled with a suitable reactant solution that also serves as the waveguide core liquid. In such an approach, the channel fabricated within the aerogel simultaneously confines the reaction medium and also serve as the waveguide cladding whereas the reaction volume resides within the liquid core of the waveguide ^{36, 39}. The propagation of non-lossy optical modes guided in the liquid by TIR from the channel walls requires the cladding material to have a low absorption coefficient at the working light wavelength and a lower refractive index than that of the core liquid ($n_{\text{core}} > n_{\text{cladding}}$) ^{36, 39}. These conditions can be easily met over the whole visible and near UV spectral regions, for example, by silica aerogels. In addition, the surface of aerogels can be chemically modified; therefore, there is no restriction on the type of liquid or aerogel that can be used, as long as the liquid can be confined inside the aerogel block without penetrating its porous network ^{36, 40}. Therefore, it should be possible to utilize such aerogel-based waveguides in microphotoreactors.

In this study, a new type of microphotoreactor we called “Aerogel-based Optofluidic Microphotoreactor with Integrated Optofluidic Waveguide” were developed

for photochemical and photocatalytic reactions. The field of optofluidics was successfully combined with monolithic hydrophobic aerogels by fabricating cylindrical channels within the monolithic aerogel blocks. Unlike conventional microphotoreactors, light was directly implemented into the channel by constructing liquid-core optofluidic waveguides within the same path of the reactant stream, which resulted in low and favorable propagation losses of light. As the first and crucial step to manufacture TIR-based liquid-core optofluidic waveguides in monolithic aerogel-based microphotoreactors preserving their intact and monolithic structure, a new, straightforward technique that uses direct manual drilling as a possible alternative among available techniques, was first developed. For this purpose, the mechanical strength and stiffness of silica aerogels was improved by synthesizing the aerogels with higher densities. Optical properties of resulting aerogels including light transmittance and scattering characteristics as well as refractive index were investigated. Efficient guiding of light by TIR in the liquid-filled channel in aerogels was visually revealed and characterized by monitoring the power at the channel output. The characterization of waveguide transmission indicated that the propagation losses demonstrated that the liquid-core waveguides with drilled aerogel cladding represent an attractive alternative in optofluidic applications targeting controlled routing of light along arbitrary three-dimensional paths. The fabricated microphotoreactors were shown to be well suited for photochemical degradation of a model organic compound – methylene blue (MB) dye – and the efficiency of the dye photoconversion as a function of the incident light power were investigated. Moreover, photocatalyst particles could be immobilized within the channel walls to perform photocatalytic reactions. Silica aerogel was chosen as a template to immobilize photocatalysts for its appealing attributes of interconnected nanoporous framework with high surface area-to-volume ratio to deposit high amount of photocatalyst and its desirable properties that complement photocatalytic processes acting as charge transfer catalyst. TiO_2 was used as photocatalyst and it was successfully introduced into the mesoporous network of silica aerogels by addition of anatase TiO_2 powder during sol-gel step of the aerogel synthesis. The resulting materials were characterized using ZEISS Ultra-Plus Field Emission Scanning Electron Microscope (FE-SEM), combined with energy dispersive X-ray spectrum (EDX), X-ray diffraction (XRD) and X-ray fluorescence spectroscopy (XRF). Diffuse Reflectance UV-VIS (DR-UV-VIS) spectra were used to obtain electronic band-gap of the SiO_2 - TiO_2 composites. These spectra were recorded with a Shimadzu UV-3600 UV-Vis-NIR

spectrophotometer using ISR-3100 integrating sphere attachment in the specular reflection (8°) mode. The band gap of the composites was estimated from Tauc method calculating Kubelka-Munk function, from the diffuse reflectance spectra of the samples,

A general overview of the physical and chemical properties of aerogels that are essential for controlled light guiding and their preparation methods are presented in Chapter 2. Possible techniques for fabricating channels in aerogel monoliths are described in detail. Subsequently, an extensive review of the studies in the literature on the characterization of light propagation in liquid-filled channels within aerogel monoliths as well as on the quantification of light-guiding characteristics of aerogel-based waveguides are provided. Finally, current and possible future applications of aerogel-based optofluidic waveguides are described in Chapter 2.

Experimental methods are provided in Chapter 3. This includes the synthesis of silica aerogels and silica-titania aerogel composites. The route for the surface modification of the aerogels is also described. The analytical techniques that were employed to characterize physicochemical properties of the derived materials are presented.

In Chapter 4, the development of total internal reflection-based optofluidic waveguides fabricated in aerogels by modified sol-gel process is described. The optical properties of resulting aerogels including light transmittance and scattering characteristics as well as refractive index measurement are defined. The light guiding properties of the fabricated channels are also provided.

Development of a new type of microphotoreactor with integrated optofluidic waveguide based on solid-air nanoporous aerogels for photochemical degradation of a model organic compound – methylene blue (MB) dye – and the efficiency of the dye photoconversion as a function of the incident light power is described in Chapter 5. Furthermore, a control experiment carried out in a plastic tubing filled with MB solution is provided to demonstrate that light guiding is superior in the MB filled channel in the aerogel. The characteristic of light propagation in the tubing is also demonstrated.

In Chapter 6, the development of aerogel-based photocatalytic microphotoreactor with an integrated optofluidic waveguide is described. Fabrication of monolithic and hydrophobic silica-titania aerogel composites and their characterization results are provided. The effects of incorporation of titania nanoparticles into the silicon dioxide network on its porous nature and morphology are described. Significant parameters, from the point of view of photocatalytic activity, are described and their

band gap energies are provided. The effect of addition of CNTs in the silica-titania network on the photocatalytic activity of the composites is provided along with their physical and optical properties and the results are compared with the silica-titania composite aerogels. Finally, a simple model for immobilized photocatalytic microphotoreactors with integrated waveguide following a first order reaction rate with light dependency was developed and compared with experimental data for various conditions investigated. The reaction rate parameters were estimated from an exponential regression model.

Finally, in Chapter 7, summary and conclusions of the overall study with further insights and future of the project are given.

Chapter 2

LITERATURE REVIEW

2.1 Optofluidic Microphotoreactors

Optofluidic microphotoreactors are promising platform for use as photochemical and photocatalytic reactors for several applications from waste water treatment to water splitting ^{19, 22, 41}. A typical optofluidic microphotoreactor, demonstrated in Figure 2.1, consists of microfluidic channels, fluidic connections and an external light source. The fabricated microchannels in the solid substrates are covered by a transparent plate sealing the channels from the top to function exclusively with external irradiation ²⁶⁻²⁸.

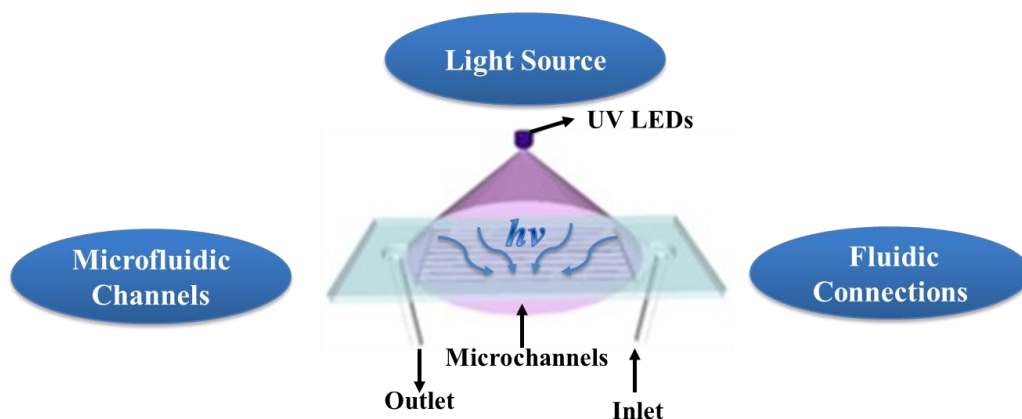


Figure 2.1. Components of a typical optofluidic microphotoreactor.

The fabricated channels were adopted for photocatalytic reactions with the same configuration for the reactor irradiation. The photocatalysts in the form of dispersed nanoparticles is considered to be impractical due to a nonuniform distribution of light as a result of absorption and scattering by the suspended particles and the need for costly separation of the photocatalysts at downstream after reaction ^{18-19, 21, 42}. Packed-bed microphotoreactors also lead to problems associated with the non-uniformity of light since the photons will be exclusively absorbed in the outer region or scattered to the neighbouring areas of the irradiated volume while the inner particles are shielded ⁴²⁻⁴³. This may be tackled by using packings which are transparent to the incident light with

specular reflectivity⁴³. Unlike suspended and packed photocatalyst, the immobilization of the catalyst on reactor walls in the form of a film coating is a more practical method of choice for photocatalytic reactions. The photocatalyst film is coated on the inner surfaces of the fabricated microchannel. The reactant can flow through in and out by inlet and outlet of the channel while it is irradiated by a light source mounted on the top of the cover. The incident light from the light source with energy equal or greater than the band gap of catalyst is absorbed by the immobilized catalyst in the walls which results in excitation of e^- to the conduction band, leaving h^+ in the valence band. The e^- and h^+ pair either recombines or diffuses to the catalyst surface to lead to oxidation-reduction reactions with reactants absorbed on the surface. Li *et al.*⁴⁴ constructed an optofluidic microreactor by using a capillary with an internal diameter of 200 μm whose inner wall was coated with a photocatalytic silicon dioxide/ titanium dioxide ($\text{SiO}_2/\text{TiO}_2$) film self-assembled from individual $\text{SiO}_2/\text{TiO}_2$ core-shell nanoparticles (Figure 2.2.a.). They investigated degradation of aqueous methylene blue solution which was passed through the capillary while the microreactor was irradiated with an external light source. However, the external irradiation used in these experiments was not ideal for utilization of light since a significant fraction of light was absorbed by the outer part of the photocatalyst layer, thus reducing the overall efficiency of the photocatalytic degradation¹³. Matsushita *et al.*⁴⁵ designed a single straight microchannel the bottom of which was covered with a sol-gel prepared TiO_2 thin film loaded with Pt particles (Figure 2.2.b.). Gorges *et al.*⁴⁶ used a microreactor with 19 branched parallel microchannels (Figure 2.2.c.). A nanoporous TiO_2 film was immobilized by anodic spark deposition and a UV-LED array was fixed above the area of the branched channels. Lei *et al.*¹⁵ designed a planar microreactor by using two nanoporous TiO_2 -coated glasses as the cover and substrate and a 100 μm -thick epoxy layer as the spacer and sealant (Figure 2.2.d.). Similarly, Ahsan *et al.*⁴¹ utilized a planar microfluidic platform to study the kinetics of photocatalytic water-splitting. They used glass slides which were coated with sol-gel prepared Pt- TiO_2 photocatalyst (Figure 2.2.e.). Furthermore, Meng *et al.*²² developed a new approach for the fabrication of planar photocatalytic microreactors by using electrospun TiO_2 nanofibres sealed between a polydimethylsiloxane (PDMS) substrate and a glass slide. They found a much higher

photocatalytic activity than that achieved previously by a TiO_2 film microreactor (Figure 2.2.f). However, conventional photocatalytic microphotoreactors have some other limitations than that of microphotoreactors. The coated layer should be stable and robust enough to survive extended periods at conditions during reactions take place; yet, the photocatalyst adhesion to the reactor walls with a smooth surface is relatively poor. Furthermore, the coated photocatalyst surface should be irradiated sufficiently to achieve excitation of the photocatalyst. Due to losses of incident light through the cover and catalyst layer, the conventional microphotoreactors were designed with a single film on one-side inner wall of either top or bottom wall of the microphotoreactor.

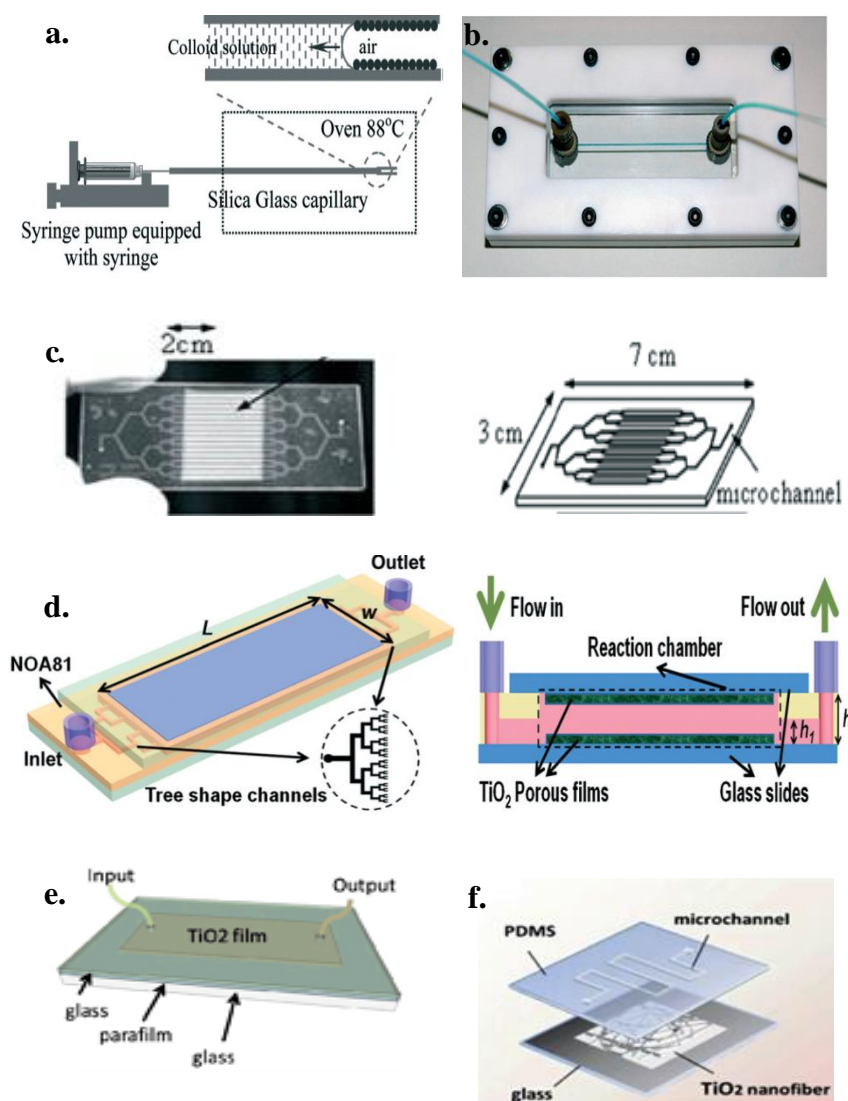


Figure 2.2. (a) Micro-capillary reactor with the inner wall coated with self-assembled $\text{SiO}_2/\text{TiO}_2$ for methylene blue degradation ⁴⁴. (b) Single straight microchannel reactor

with immobilized TiO₂-coated silica beads ⁴⁵. (c) Branched microchannel reactor ⁴⁶. (d) Planar microreactor using immobilized nanoporous TiO₂ film for methylene blue decomposition (on the left) ¹⁵. Cross-section of the planar microreactor (on the right) ¹⁵. (e) Scheme and photograph of thin TiO₂ film coated planar microreactor ⁴¹. (f) Scheme of nanofibrous TiO₂ microreactor ²².

2.2 Liquid-core Optofluidic Waveguides

Being based on the integration of microfluidics with optics, optofluidics allows for controlling the interaction of fluids with light at small spatial scales and developing new optical devices for detection, imaging, and chemical and biological analysis ^{10-12, 47}. Optofluidic waveguides that enable the controlled routing of light in integrated optofluidic systems are an important component of many of these devices. Light guiding can be achieved by using either TIR or interference ⁴⁸. Interference-based light guides require the waveguide core region to be covered with multiple reflective layers so as to achieve near-perfect light confinement due to constructive or destructive interference. Bragg waveguides ⁴⁹, Bragg fibers ⁵⁰, photonic crystal fibers ³⁴, and anti-resonant reflecting optical waveguides (ARROWs) ⁵¹⁻⁵² are primary examples of such interference-based waveguides. They require relatively complicated fabrication and coating techniques. In contrast, TIR-based waveguides can be simply obtained by a waveguide core material having a refractive index sufficiently higher than the refractive index of the surrounding cladding medium ⁵³⁻⁵⁴. This principle applies to both planar waveguides and optical fibers ⁵⁵. If TIR occurs inside a waveguide, the light losses due to light leakage out of the waveguide are extremely low.

TIR-based liquid-core optofluidic waveguides can be easily obtained provided a low refractive index cladding medium can be found. For example, since the refractive index of water is much higher than the refractive index of the surrounding air, light can be guided in a water stream pouring out of a water-filled bottle by TIR when the incident angle of light on the surface of the water filament is greater than the critical angle (see Figure 2.3) ⁵⁶. However, in manufacturing optofluidic devices, a solid cladding material is typically required. In TIR-based liquid-core waveguides, the core liquid is confined within channels fabricated in a suitable solid material that simultaneously acts as the waveguide cladding ⁵⁷⁻⁵⁸. In order to guide light by total internal reflection with low

attenuation, the cladding material should be non-absorbent and have a much lower refractive index than the core material ($n_{\text{core}} > n_{\text{cladding}}$), and a smooth interface should be present between the core and cladding material. When these requirements are met, the light remains confined in the waveguide liquid core, maintaining high intensities over long propagation distances. Devices based on TIR-based liquid core optofluidic waveguides have been attracting an increasing attention. For instance, Cai *et al.*⁵⁹ demonstrated direct detection and quantification of Ebola virus in an integrated optofluidic device including solid-core and liquid-core waveguides. Sample preparation and target pre-concentration were performed in a polydimethylsiloxane (PDMS)-based microfluidic chip, followed by single nucleic acid fluorescence detection in liquid-core optical waveguides on a silicon chip. Jung *et al.*⁶⁰ used a TIR-based liquid core optofluidic waveguide for efficient light delivery in PDMS-based photobioreactor (PBR) for cyanobacteria growth. TIR-based waveguides were built by coating a thin layer of amorphous fluoropolymer (Teflon AF) on the inner walls of PDMS channels; thus, total internal reflection occurred at the interface between the Teflon AF layer and the culture medium. They performed experiments with both regular and Teflon AF-coated PBRs for a comparison of cell growth. They demonstrated that photosynthetic cell growth improved by up to 9% in the optofluidic waveguide-based PBR compared to the regular PBR.



Figure 2.3. Total internal reflection in a stream of water flowing through a hole drilled at the bottom of a glass bottle. Light from a laser source is coupled into the water stream

In applications involving aqueous solutions, the refractive index of the core liquid is around 1.33 (refractive index of water). However, a limited choice of solid host materials with an index of refraction below that of water is available; thus it is a challenge to find a cladding material with a refractive index much lower than 1.33 to maintain a reasonable numerical aperture (NA)^{38, 54}. Most of the polymers, including those that are utilized in lab-on-a-chip devices such as PDMS, have higher refractive indices than water; thus, light cannot be confined and delivered by TIR in channels fabricated from these polymers. Among fluoropolymers, Teflon AF has a refractive index of 1.29–1.31 that is slightly lower than the refractive index of water. Therefore, Teflon AF or a layer of Teflon AF can be used to clad a liquid-core optical waveguide. Thin coatings of amorphous Teflon AF deposited on substrates such as glass, silicone, and PDMS have been commonly employed for this purpose⁶¹⁻⁶³. However, Teflon AF has poor adhesion to the common solid substrates used for manufacturing of microfluidic chips. Chemical functionalization of the surface of Teflon AF may improve adhesion, but it is very difficult to functionalize Teflon AF. Furthermore, low refractive index contrast of ~ 0.04 between the core liquid and Teflon AF prevents efficient propagation of light within the aqueous core⁶¹⁻⁶².

2.3 Aerogels

Aerogels are nanostructured materials with an internal solid structure consisting of crosslinked polymers with a large number of air-filled pores between the solid polymeric chains⁵⁰. The network of aerogels is characterized by well accessible and branched mesopores. Among other mesoporous materials including fumed silica, Vycor glass, carbon soot, or mesoporous silica, aerogels are unique owing to their extremely high porosity and high specific surface area, pore sizes ranging in mesopore range, electrical conductivity (carbon aerogels) and the possibility of synthesizing as both monoliths and beads⁴²⁵⁰.

These versatile nanoporous materials can be synthesized from a wide range of molecular precursors using sol-gel chemistry, followed by removal of the solvent from the gel network using drying⁶⁴⁻⁶⁶. The unusual flexibility of the sol-gel processing enables remarkable control over the aerogel properties. Their surface properties, porosities, thicknesses, and refractive indices can be tailored to desired values by

modifying the method of preparation and the composition of the reactant solution ⁶⁷⁻⁷⁰. Thus, aerogels are attractive for a wide range of applications in areas such as aerospace, thermal insulation, and acoustic device development ^{65, 71}.

Aerogels can be generally classified into three categories: inorganic, organic, and inorganic–organic hybrids. Inorganic aerogels are synthesized using metal alkoxides as precursors and include various aerogels such as silica (SiO_2), alumina (Al_2O_3), titania (TiO_2), or zirconia (ZrO_2) ^{64, 67, 69, 72}. Silica aerogels—the most extensively studied aerogels amorphous materials having a disordered molecular structure with tortuous paths through their solid network—have pores typically ranging from 5 to 100 nm, an average pore diameter between 20 and 40 nm, porosities up to 99.8%, and bulk densities ranging from 0.003 g/cm^3 to 0.5 g/cm^3 , which results in an extremely low refractive index in the range of 1.003–1.1 ^{67, 71, 73-75}. Because of their low refractive indices, they are often used in Cherenkov radiation detectors ⁷⁵⁻⁷⁹.

Resorcinol–formaldehyde and melamine–formaldehyde aerogels are the most commonly studied organic aerogels; they are formed from either connected colloidal particles or polymeric chains of about 10 nm in diameter. They have pores with small diameters ($\leq 50 \text{ nm}$) and high specific surface areas ($400\text{--}1000 \text{ m}^2/\text{g}$) ⁸⁰⁻⁸¹. Carbon aerogels, which are obtained by pyrolysis of organic aerogels, are attractive, especially in energy-related applications, due to their high electrical conductivity ⁸¹.

Hybrid aerogels are synthesized by incorporation of organic polymers such as polyacrylate, polyimide, or polyurea within an inorganic aerogel matrix such as silica aerogel. Hybrid aerogels may display enhanced mechanical properties as compared with either pure organic aerogels or pure inorganic aerogels while maintaining high porosity and high surface area ^{68, 82-86}.

Even though aerogels were first synthesized by Samuel Kistler as early as in 1932, they remained a laboratory curiosity for a long time and were not produced on a commercial scale until 2002, primarily due to their high production costs. In 2002, Aspen Aerogels developed an aerogel-based blanket for thermal insulation by impregnating a fibrous structure with an aerogel-forming precursor solution. Subsequently, other companies such as Nano Hi-Tech also started producing aerogel blankets. Cabot Corporation (Boston, MA, USA) developed silica aerogel granules

under the trade name of Nanogel[®] with excellent insulation, water-repelling, and light transmittance properties. Nanogel[®] is used in glazing systems such as glass, polycarbonate, acrylic, or structural composite panels due to its desirable characteristics resulting in an environmentally friendly, energy-efficient daylighting system ⁸⁷⁻⁸⁸. Recently, BASF (Ludwigshafen, Germany) also started producing organic aerogel insulation panels under the trade name Slentite. These are mechanically strong, high-performance insulating materials with low thermal conductivity (17 mW/(m·K)) compared to other insulation materials such as mineral wool, expanded polystyrene, extruded polystyrene, and polyurethane, with thermal conductivities typically in the range of 25 to 50 mW/(m·K) ⁸⁹. The panel offers space-saving, efficient insulation, allowing the insulating layer to be 25% to 50% slimmer than conventional materials for the same insulation performance ^{65, 87-89}. The above examples indicate that a wide variety of aerogels with different properties for optofluidics-related applications may be produced on a commercial scale in the future.

2.4 Why Use Aerogels for Optical Applications?

Unique optical characteristics of aerogels render them well suited for the development of novel optical devices such as sensors, radiation detectors, optical fibers, optofluidic waveguides, nonlinear optical components, or lightweight reflectors ^{67, 90-93}. The most appealing optical property of aerogels – the low index of refraction whose value lies well below that of common solids and liquids – results from the internal solid nanostructure of aerogels consisting of cross-linked polymeric nanoparticles with a large fraction of air-filled pores. Because of their very high porosity, aerogels are sometimes termed “solid air” and have refractive indices close to that of air (typically in the range of 1.003–1.1) ^{39, 69, 94-96}. Another remarkable property of some types of aerogels that makes them attractive for optical applications is their good optical transparency in the UV/visible region of the electromagnetic spectrum that is only limited by light scattering from the sub-wavelength internal structures of the aerogels. Since aerogels can be produced in arbitrary shapes using appropriate molds during the fabrication process, they can be readily formed into an optimal shape required by the particular application ^{64, 69, 97}. The combination of the above mentioned favorable material and processing characteristics has moved aerogels into the spotlight in the development of novel optical

and photonic components and systems, as evident from the steadily increasing number of scientific publications related to the subject in recent years.

The oldest optical applications of aerogels date back to the 1970s when silica aerogels were first successfully used as a source of Cherenkov radiation for charged-particle detection in high-energy and nuclear physics experiments ⁹⁸⁻¹⁰⁰. In charged-particle detectors based on registering Cherenkov radiation emitted upon the passage of a charged particle through a transparent (dielectric) medium, the refractive index of the medium is a crucial parameter that determines the threshold velocity of particles that can be detected. In particular, this threshold velocity is inversely proportional to the refractive index and its careful selection is critical for meeting the requirements of the specific experiment ⁹⁸. Since aerogels have refractive indices intermediate between those of common or cryogenic liquids and compressed gasses, they can successfully fill the gap between the particle detectors based on conventional fluid materials. Moreover, refractive index of aerogels is largely tunable by modifying the conditions of their synthesis and their compact, solid form makes their handling significantly easier in comparison with compressed gasses or cryogenic liquids.

The “solid air” property of aerogels has also made them attractive for fiber optics applications ⁹⁵. Since both optical fibers and silica aerogels are made from the same material (silica glass), they are fully chemically compatible. Thus, silica aerogels can serve to protect delicate fiber-optical components such as fused couplers and tapers from harsh environmental conditions and contamination without a negative influence on the performance of the embedded components ^{95, 101}. Aerogels can also serve as low-index claddings of optical fibers, providing higher numerical aperture and improved light propagation efficiency over conventional fibers ¹⁰¹. Moreover, aerogel-coated fibers were successfully used for gas sensing applications ^{39, 102}. These gas sensors took advantage of the open porous network of aerogels through which the gases could readily diffuse into the evanescent field region at the fiber core surface and modulate the properties of guided light by modifying the effective refractive index of the fiber cladding. Gas sensing and nonlinear optics applications of aerogel-clad optical fibers can be further enhanced by embedding suitable dopants in the aerogel structure that exhibit a strong chemical or optical response ^{95, 103-106}.

Recently, alternative optical waveguides using aerogels as their main structural element have been introduced. Conventional optical fibers consist of a solid core and cladding with a refractive index contrast. In particular, the refractive index of the core has to be higher than that of the cladding, which then allows transmission of light entering the core along the fiber by TIR. As the refractive index of the cladding decreases, the fraction of light that can propagate through the fiber increases. Recent studies have demonstrated that aerogels are ideal solid cladding materials for optofluidic waveguides with liquid cores that are able to guide light by TIR over a wide range of wavelengths without any additional optical coatings^{17, 38-39, 67, 95, 101, 107-108}. Due to the extremely low refractive index of aerogels, high numerical apertures can be obtained in aerogel-based optofluidic waveguides in applications based on aqueous liquid cores. This gives them a significant advantage over conventional polymer-based cladding materials^{17, 36-38, 107}. In order to construct the waveguides, uniform, extended channels can be created inside monolithic aerogel blocks using a wide variety of processes such as preform removal¹⁰⁷, drilling³⁷ or femtosecond laser ablation³⁸. Aerogel-based optofluidic waveguides can pave the way for development of innovative applications including photochemical reactors as well as light-driven detection, identification, and quantification of various compounds. Studies reported so far in the literature on aerogel-based optofluidic waveguides have utilized silica aerogels. However, other types of aerogels with desirable mechanical properties such as high tensile strength or flexibility can also be used. In addition, the aerogel market in the world is growing and many additional aerogel production plants are expected to be constructed in the coming years to meet this demand. Therefore, manufacturing of aerogels on a commercial scale for use in optofluidics-related applications seems very plausible in the near future.

Aerogels are characterized by the very low linear index of refraction; at the same time, their nonlinear intensity-dependent refractive index component can be very high. The optical nonlinearity of silica aerogels has a negative sign, which indicates that the refractive index is depressed at high irradiation intensities¹⁰⁹. This property of aerogels paves the way for implementation of high-power nonlinear optical devices such as optical limiters and switches, as well as for generation of spectral supercontinuum^{39, 104-105, 110-112}.

The number of studies exploring the potential of aerogels for optical and photonic applications is expected to increase in the coming years, as the relationship between the nanostructure of aerogels and their optical properties is better understood. New fabrication techniques are being developed for aerogel-based optical devices including lenses, waveguides, optical fibers, filters, dye lasers, and nonlinear optical devices. In the near future, one can expect many more new, hybrid optical components to join the family of already existing successful optical solutions based on aerogels.

2.5 Optical Properties of Aerogels

Optical properties of aerogels directly determine potential applications of aerogel-based optical devices. In this context, light transmittance and scattering characteristics as well as refractive index of aerogels are primarily significant. High optical transparency of aerogels is crucial for many optics-related applications such as fabrication of solar windows and Cherenkov radiators, fiber optics as well as optical waveguides, whereas translucent aerogels are generally good candidates for solar covers and collectors¹¹³⁻¹¹⁵. In general, both scattering and absorption of light reduce the amount of light transmitted through monolithic aerogels¹¹⁶. The nanostructure of aerogels determined by the nature of their pores and their solid network affects their optical properties in a complex manner¹¹⁷⁻¹¹⁸. Optical scattering in aerogels is characterized by contributions from the bulk and exterior surface scattering. The first scattering component is the Rayleigh-type light scattering from the structure-forming units of aerogels that are much smaller than the wavelength of the incident light. This type of scattering is strongly wavelength-dependent and it has been described for silica aerogels by Rayleigh-Gans theory that characterizes the overall attenuation of incident light by extinction coefficient, α , which is given by Equation 2.1¹¹⁸⁻¹²¹:

$$\alpha = 32\pi^4 \frac{\rho_{ap}}{\rho_{SiO_2}} \frac{d^3}{\lambda^4} \left(\frac{n^2-1}{n^2+2} \right)^2 \quad \text{Equation 2.1}$$

Here, ρ_{ap} is the apparent - or bulk - density of the silica aerogel, ρ_{SiO_2} is the density of amorphous silica (2.2 g/cm³), d is the particle (scattering center) radius, λ is the wavelength of light, and n is the relative refractive index of silica particles with respect to that of the external medium, i.e. air in most cases. Inspection of Equation 2.1 shows that the level of bulk scattering can be adjusted by the particle size and apparent

density of the aerogel. These parameters can be largely tuned at various stages of aerogel monolith synthesis to decrease the scattering and, therefore, increase aerogel transparency. Besides bulk scattering, transparency of aerogel monoliths is also limited by scattering from micrometer-size imperfections of their external surface. These surface inhomogeneities depend on the physical characteristics of the molds used to synthesize aerogel monoliths, possible contamination of the interior surface of the molds by dust particles, or mechanical vibrations during the synthesis, and they affect the transparency independently of the incident light wavelength ¹²⁰. Relative importance of the two scattering components then depends on the geometry of the aerogel monolith, in particular, on its surface-to-volume ratio.

Such a spectrum, recorded between 200 and 2500 nm for a silica aerogel sample obtained by hydrolysis tetraethylorthosilicate (TEOS) and drying by supercritical CO₂ (scCO₂), is given in Figure 2.4. The material is translucent in the visible spectral region. Since silica has no absorption band in the visible part of the spectrum, the decrease in the transmittance is predominantly due to the light scattering ¹²². In general, aerogel network contains a thin layer of adsorbed water molecules. Since the absorption of water is stronger in the near-infrared spectral region, the aerogel is less transparent in that region. In particular, the spectral absorption peaks between 900–1150 nm, 1300–1800 nm, and 1800–2000 nm can all be attributed to light absorption by adsorbed water in the aerogel network. The broad absorption band at 2200 nm then represents light absorption by the silanol group of aerogels ^{65, 121-122}. The relative contributions of scattering and absorption to the overall attenuation of incident light by aerogel monoliths can be determined by measuring both total transmittance and reflectance spectra of the sample and solving the inverse problem of the 1-D radiative transfer equation ¹¹⁶. Using this method, it is possible to obtain intrinsic scattering and absorption coefficients of the material that are independent of the sample geometry.

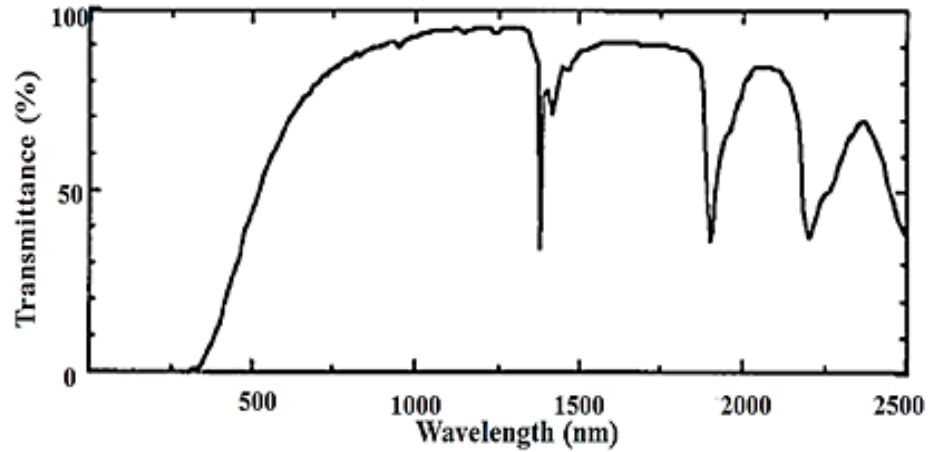


Figure 2.4. Transmission spectra of TEOS-based silica aerogel [56]. “Reproduced with permission from Tamon *et al.*, Preparation of silica aerogel from TEOS; published by J. Colloid Interface Sci., 1998.”

The transmittance of the aerogel, T , is generally parameterized by Hunt formula which represents the attenuation of incident light by a wavelength dependent optical scattering from the aerogel structure:

$$T(\lambda) = Ae^{-Ct/\lambda^4} \quad \text{Equation 2.2}$$

where A is the surface scattering coefficient, t is the aerogel thickness, λ is the wavelength of the light beam and C is the clarity coefficient and it is used to identify the optical quality of a sample together with A . A and C are called Hunt parameters. The aerogels with high optical quality have values for A and C close to 1 and 0, respectively. The clarity coefficient C , usually measured in $\mu m^4/cm$ is proportional to the radiation which is scattered/unit of sample length.

2.5.1 Haze of Aerogels

Haze (H_T) is described by the ratio of diffuse transmittance ($T_{diffuse}$) to total transmittance (T_{total}) where diffuse transmittance is defined as transmitted light varying by greater than or equal to a 5° separation from the direction of incident light. It is calculated by Equation 2.3. Haze of aerogels reveals what portion of the transmitted light is scattered from the aerogel surface. A high quantity of percent haze value indicate

that larger portion of the transmitted light is scattered, lowering the transmission and causing the sample to be translucent and milky¹²³⁻¹²⁴.

$$H_T(\%) = \frac{\text{Diffuse Transmittance}}{\text{Total Transmittance}} \times 100 \quad \text{Equation 2.3}$$

2.5.2 Refractive Index of Aerogels

Precise knowledge of the refractive index of aerogels is essential for any optical application. Therefore, this aerogel property has been extensively studied, especially for silica aerogels used in designing Cherenkov radiators^{98, 100}. The most commonly used technique to measure the refractive index of aerogels is angle of deflection measurement of an incident laser beam^{74, 121, 125-126}. Alternatively, refractive index of an aerogel monolith can be determined by imaging a grid through the monolith^{74, 127}. This method of measuring the refractive index uses images of the grid illuminated by a laser source, recorded with a CCD-camera. A reference image of the grid is acquired and, subsequently, the aerogel is tilted, which results in a shift of the grid image on the CCD imaging element. The refractive index can be then calculated using the measured image shift, thickness, and tilt of the aerogel sample.

According to the correlation described by Equation 2.4 and proposed by Henning *et al.*¹²⁸, which was also experimentally verified for aerogel samples with a density up to 0.3 g/cm³ (Figure 2.5.), the refractive index (n) of aerogels increases linearly with their density, (ρ , g/cm³)^{78, 98, 128-129}:

$$n = 1 + 0.21\rho \quad \text{Equation 2.4}$$

According to Equation 2.4, n is very close to 1 even for aerogels with higher densities. Thus, it is practical to use higher-density aerogels in optofluidics applications, as they provide increased mechanical stability without a significant deterioration of their optical characteristics. Some of the alternative empirical correlations between the density and refractive index of aerogels proposed in the literature are summarized in Table 2.1.⁷⁸.

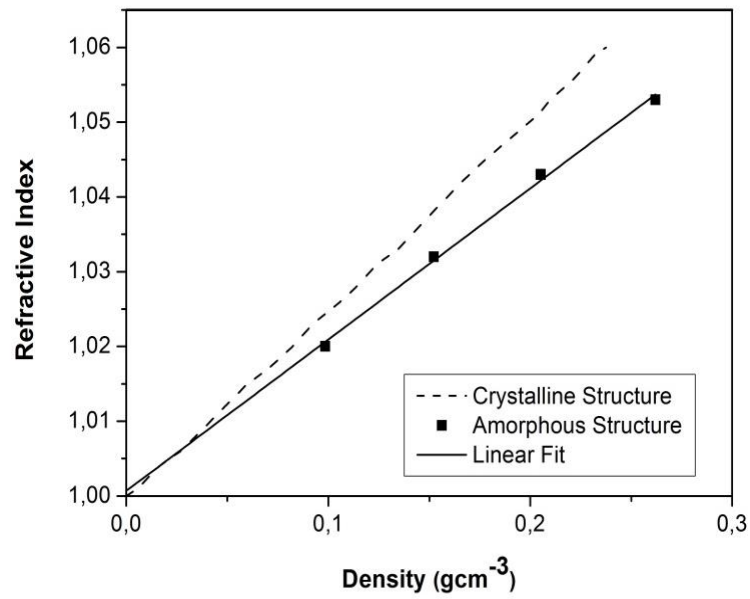


Figure 2.5. Refractive index as a function of silica aerogel density. The solid line assumes an amorphous structure (proportionality constant 0.21), while the dashed line assumes a crystalline structure [72]. “Reproduced with permission from Henning *et al.*, Production of silica aerogel; published by *Physica Scripta*, 1981.”

Table 2.1. Empirical correlations between the density ρ and refractive index n / dielectric permittivity ϵ of aerogels proposed in the literature.

Reference	Refractive index correlation
	$\epsilon=n^2=1+\beta\rho, n=1+k\rho$
Danilyuk <i>et al.</i> ¹³⁰	where ϵ is dielectric permittivity of materials. $\beta= 0.424 \pm 0.001, k= 0.206 \pm 0.001 \text{ cm}^3/\text{g}$
Wang <i>et al.</i> ¹²¹	$n=1+k\rho, k= 0.221 \pm 0.002 \text{ cm}^3/\text{g}$ before heat treatment $k= 0.193 \pm 0.002 \text{ cm}^3/\text{g}$ after heat treatment at 500 °C
Poezl <i>et al.</i> ¹³¹	$n=1+k\rho, k= 0.210 \pm 0.002 \text{ cm}^3/\text{g}$

Cantin <i>et al.</i> ⁷⁸	$n=1+k\rho$, $k=0.25 \text{ cm}^3/\text{g}$
Henning <i>et al.</i> ¹²⁸	$n=1+k\rho$, $k=0.21 \text{ cm}^3/\text{g}$
Özbakır <i>et al.</i> ³⁷	$n=1+k\rho$, $k = 0.27 \pm 0.016 \text{ cm}^3/\text{g}$

2.6 Aerogel-Based Optofluidic Waveguides

Optofluidic waveguides that enable controlled routing of light in integrated optofluidic systems are an important component of many optical devices used for detection, imaging, and chemical and biological analysis ¹³². Light guiding in such structures can be achieved by using the TIR phenomenon. TIR-based optical waveguides can be simply obtained by combining a waveguide core material with a surrounding cladding medium having a refractive index that is sufficiently lower than the refractive index of the core ($n_{\text{core}} > n_{\text{cladding}}$). In TIR-based liquid-core optofluidic waveguides, the core liquid is confined within channels fabricated in a suitable solid material that simultaneously acts as the waveguide cladding ⁵⁷⁻⁵⁸. In order to guide light by TIR with low attenuation, in addition to the necessary contrast of refractive indices, the cladding material should also be non-absorbing at the guided light wavelength and a smooth interface should be present between the core and the cladding to reduce light scattering from surface inhomogeneities. When the angle of incidence of the light propagating within the core on the core-cladding interface is greater than the critical angle, θ_c defined by Equation 2.5:

$$\theta_c = \sin^{-1}(n_{\text{cladding}}/n_{\text{core}}) \quad \text{Equation 2.5}$$

the light is totally internally reflected within the core medium (Figure 2.6). When these requirements are met for each successive incidence of the light on the core-cladding interface, the light remains confined in the waveguide liquid core, maintaining high intensities over long propagation distances.

In applications involving aqueous solutions, the refractive index of the core liquid is close to 1.33 which is the refractive index of pure water. However, there are only a few solid host materials with an index of refraction below that of water. The index of refraction of some commonly used cladding materials are provided in Table 2.2. Therefore, it is a challenge to find a cladding material with a refractive index sufficiently lower than 1.33 in order to obtain a reasonable numerical aperture (NA) ^{38, 54}. Most of the common polymers, including those that are utilized in lab-on-a-chip devices such as poly(dimethylsiloxane) (PDMS) have refractive indices which are higher than water and therefore, light cannot be confined and delivered by TIR in channels fabricated surrounded by these polymers. Among fluoropolymers, Teflon AF has a refractive index which ranges from 1.29 to 1.31 which is slightly smaller than the refractive index of water. Therefore, thin coatings of amorphous Teflon AF deposited on substrates such as glass, silicone, and PDMS have been commonly employed to clad a liquid-core optical waveguide ⁶¹⁻⁶³. However, Teflon AF has poor adhesion to common solid substrates which are generally employed in manufacturing of microfluidic chips. It has been suggested that functionalization of the surface of Teflon AF may help improve adhesion; however, it is quite difficult to functionalize Teflon AF due to its inertness ⁶¹⁻⁶².

Table 2.2. Index of Refraction (n) of Various Cladding Materials

Material	Refractive Indices
Polystyrene	1.59 ¹³³
Polydimethylsiloxane (PDMS)	1.41 ¹³⁴
Fused quartz	1.46 ¹³⁵
Fused silica	1.46 ¹³⁵
Silicone	1.46 ¹³⁶

Poly(methyl methacrylate) (PMMA)	1.4893 - 1.4899 ¹³⁷
Polytetrafluoroethylene (Teflon)	1.35-1.38 ¹³⁸
Teflon amorphous fluoropolymers (Teflon AF)	1.29-1.31 ¹³⁹

Aerogels - with their unusually low refractive index - are remarkable solid-cladding materials for optofluidic waveguides that can be used without any additional modification. Aerogel-based optofluidic waveguides are constructed by forming microchannels inside aerogel blocks which are filled with a suitable liquid that serves as the core liquid for the waveguide. There are no restrictions on the nature of liquid and the kind of aerogel that can be used, as long as the liquid can be confined inside the microchannels without penetrating the aerogel network. The refractive index of any piece aerogel will always be less than the refractive index of any liquid. As shown in Figure 2.6a and Figure 2.6b, a microchannel in a silica aerogel block is surrounded by a wall that is made up of interconnected particles made out of silica that are around 40 - 80 nm in size. There are pockets of air in between these particles that constitute pores with sizes less than 100 nm. The particles are made out of primary particles that are 2 to 10 nm in size (Figure 2.6c). The pockets of air are responsible for guiding light by total internal reflection in the liquid-filled microchannel ^{36-37, 39, 101}.

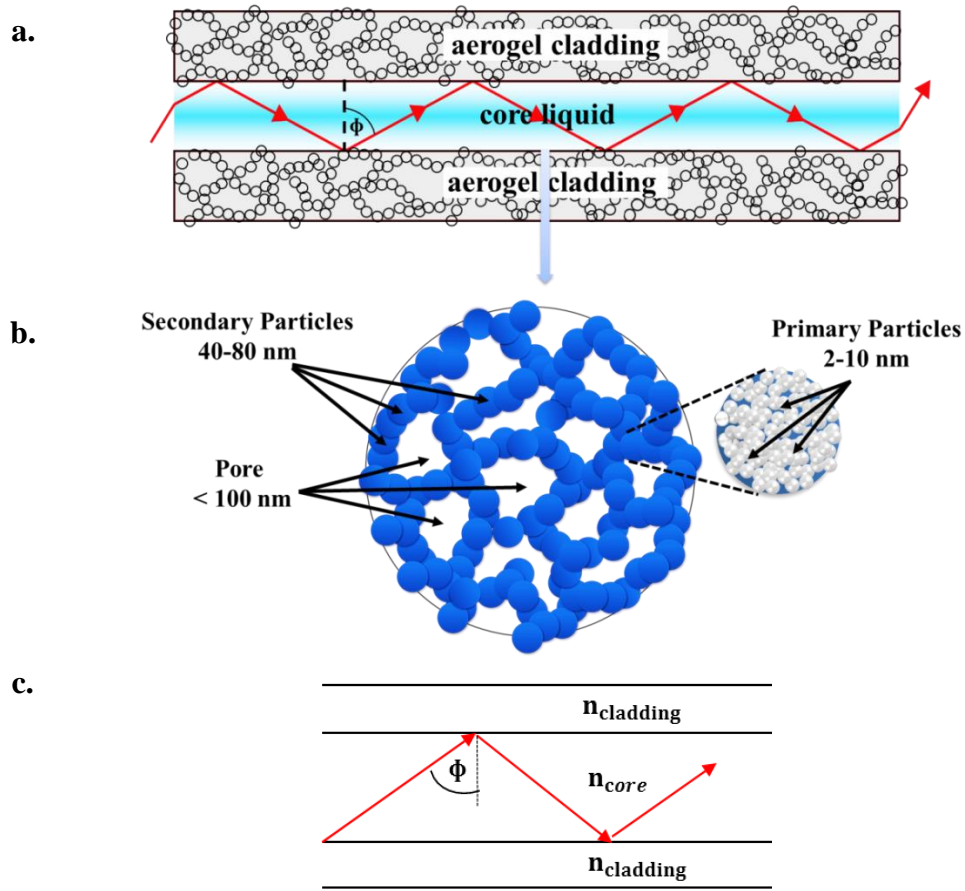


Figure 2.6. (a) Liquid-core optofluidic waveguide created in a microchannel within a silica aerogel monolith; (b) Nanometer-scale particles and pores in a monolithic aerogel³⁶; (c) Longitudinal cross section of a liquid-core optofluidic waveguide. Red arrows indicate light rays confined within the waveguide core by TIR. ϕ is the angle of incidence on the core-cladding interface. “Reproduced with permission from Özbakır *et al.*, *Aerogels for Optofluidic Waveguides*; published by *Micromachines*, 2017.”

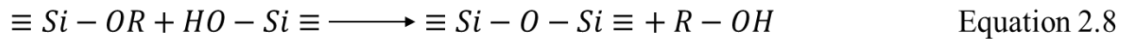
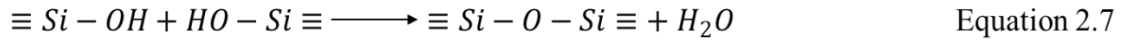
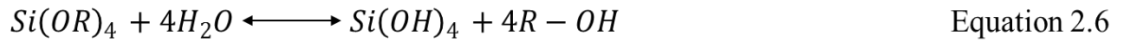
2.7 Preparation of Aerogel Waveguides

2.7.1 Synthesis of Aerogels

Aerogels are synthesized using a conventional sol-gel process, which generally consists of the formation of a sol, the gelation of the sol solution, the aging of the gel, and the extraction of the solvent from the alcogel network, or drying of the alcogel. Typical steps used in the synthesis of aerogels are summarized in Figure 2.7^{67, 72, 140-141}.

(i) Sol-gel: Metal oxides such as tetraethylorthosilicate (TEOS) or tetramethylorthosilicate (TMOS) are generally used precursors for silica aerogel

synthesis. The precursors are initially hydrolyzed in a mixture of water and alcohol with the presence of an acid or a base catalyst where the alkoxide groups of the precursor are replaced with hydroxyl groups as shown in which results in formation of colloidal particles (Figure 2.7a and Figure 2.7b). This colloidal suspension is known as sol (Figure 2.7b). These nanoscale sol particles are crosslinked and hierarchically assembled into an interconnected, porous network filled with liquid phase (Figure 2.7c) as a result of a set of chemical reactions given in Equations 2.7-2.9 and where $\text{Si}(\text{OH})_4$ molecules go through water (Equation 2.6) and alcohol (Equation 2.7) condensation reactions forming a silica network (Equation 2.8). The resulting three-dimensional open grid structure is called the gel. Some gels such as polymeric gels can directly be formed from linear polymers instead of a precursor solution without the intermediate occurrence of individual particles.



(ii) Aging: The subsequent step is the aging of the tenuous solid skeleton of the alcogel generated during the sol-gel process. This process increases the connectivity of the alcogel network and its fractal dimension which reinforces the alcogel skeleton (Figure 2.7.d).

(iii) Drying: The last step in the aerogel synthesis is the removal of the liquid solvent from the gel. Drying methods include ambient pressure drying (evaporation), freeze-drying, and supercritical drying. During drying at ambient pressure, the formation of a liquid-vapor phase boundary inside the pores results in a very high capillary pressure, which can cause the collapse of the pores and cracking of the gels. Cabot Corporation produces silica aerogels by ambient pressure drying; however, these aerogels are not monolithic but consist of irregularly shaped particles. Therefore, they would not be suitable for wave-guiding applications. In freeze-drying, the solvent temperature is reduced below its crystallization temperature and it is subsequently

removed by sublimation at a reduced pressure. This technique is also problematic for the production of monoliths as the solvent crystallization may cause volume expansion and stress, which results in the breakage of the gels. Currently, freeze-drying is not used on a commercial scale to produce aerogels. Differential strain arising from capillary pressure can be eliminated by using the supercritical drying process. Supercritical drying of the alcogel is extraction of the solvent in its pores with supercritical fluids, commonly scCO_2 . During supercritical drying, the formation of two phases (a liquid and a vapor) in the pores is prevented, and, therefore, the collapse of the porous gel network can be avoided and a highly porous aerogel structure can be obtained ¹⁴⁰⁻¹⁴¹ (Figure 2.7.e).

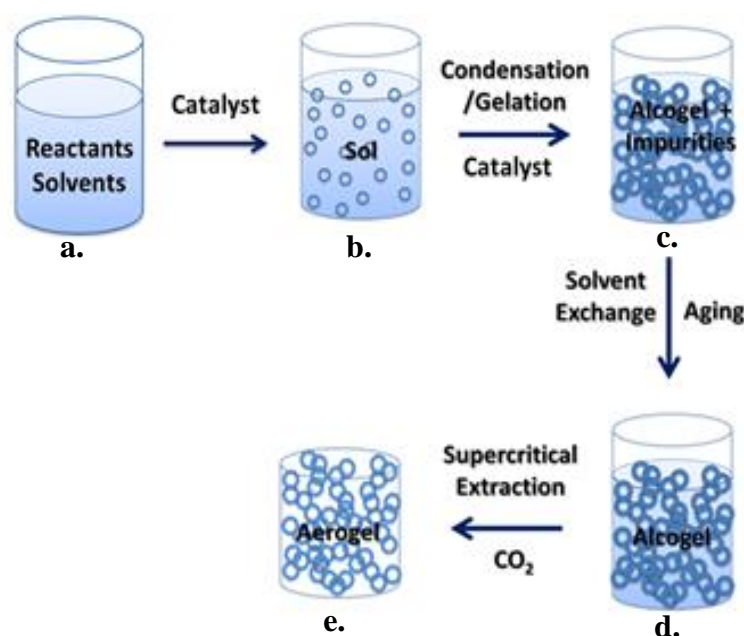


Figure 2.7. Preparation of monolithic aerogels by the sol-gel method. (a) Reactants and solvents are mixed in the reaction vessel; (b) upon addition of a catalyst, colloidal suspension (sol) is formed; (c) condensation of the sol leads to the formation of alcogel containing impurities; (d) aging process reinforces the gel skeleton structure; (e) supercritical drying yields the final solid dry aerogel.

2.7.2 Surface Modification of Aerogels

Some types of aerogels are hydrophilic due to the presence of polar hydroxyl groups within their porous framework. These hydroxyl groups can take part in strong hydrogen bonding with water, which can result in a structural collapse in a humid environment. However, the presence of non-polar hydrophobic groups on the aerogel

surfaces renders them hydrophobic. Therefore, for optofluidic applications requiring aqueous cores, hydrophilic surface groups of aerogel monoliths need to be replaced by hydrophobic groups so that they can meet the stability requirements for long-term use^{65, 142}. For silica aerogels, this replacement of the surface groups can be achieved by three primary techniques. One approach is to utilize organosilanes other than TEOS that contain hydrophobic groups and intermediary chains; these hydrophobic organosilanes can be incorporated into the aerogel network as additional silica precursors in the synthesis. Examples of possible hydrophobic co-precursors include methyltrimethoxysilane (MTMS), methyltriethoxysilane (MTES), dimethylchlorosilane (DMCS), trimethylethoxysilane (TMES), ethyltriethoxysilane (ETES), and phenyltriethoxysilane (PTES). The silyl groups of the co-precursors react with the silica network during the condensation reactions, resulting in aerogels with different degrees of hydrophobicity^{66, 143}. Surface modification of aerogels can also be performed either during the aging step or after the drying step by vapor-phase deposition and supercritical-phase deposition techniques. For example, hydrophilic nanocellulose aerogel surfaces were transformed into hydrophobic ones by using hydrophobic molecules such as triethoxyl(octyl)silane and MTMS by either vapor phase deposition or liquid phase deposition techniques¹⁴⁴⁻¹⁴⁶. Similarly, the hydrophilic surface of a silica aerogel could be modified via a reaction with gaseous methanol for 10 h¹⁴⁷. The treatment led to extremely hydrophobic aerogels that could even float on water for several hours without getting wet¹⁴⁸. HMDS can also be used as a surface modification agent either in pure vapor form or as a solution in scCO₂^{66, 149}. Aerogels with contact angles as high as 130° could be obtained using HMDS dissolved in scCO₂^{66, 150}. The surface of the silica aerogels can also be modified by amine groups that can be incorporated from either the gas phase or the liquid phase¹⁴³. To functionalize from the liquid phase, the alcogel can either be prepared with 3-(aminopropyl)-trimethoxysilane (APTMS) as the catalyst or it can be aged in APTMS containing an aging solution^{66, 143}.

2.8 Techniques for Fabrication of Optofluidic Channels in Aerogel Monoliths

As mentioned above, aerogel-based optofluidic waveguides are typically formed by fabricating channels inside monolithic aerogel blocks and filling these channels with the desired working liquid. There exist a number of possible strategies for fabricating

channels in aerogel blocks. Using processes such as preform removal, femtosecond laser ablation, and drilling, uniform and extended channels could be created in aerogel monoliths^{38-39, 107, 151}. This section reviews the possible techniques for fabricating channels in monolithic aerogels and summarizes their respective benefits and limitations.

2.8.1 Preform Removal

In their seminal work, Xiao and Birks demonstrated for the first time that water-filled microchannels fabricated in hydrophobic silica aerogel blocks can be used as optofluidic waveguides³⁹. In order to form the channels, they used a piece of a standard optical fiber as a channel preform with the desired cross section. The preform was inserted and fixed inside a mold, covered with the liquid precursor sol, and – after completing the aerogel synthesis – removed by careful pulling from the supercritically dried aerogel monolith. In addition to a single straight microchannel, two parallel microchannels merging together in a Y-junction could be created in the aerogel blocks using a twisted pair of fibers. Figure 2.8a-d illustrates the steps for the formation of optofluidic waveguides in the aerogel using fiber-based preforms. First, a solution of TMOS, water and methanol was poured into the mold containing the fiber (Figure 2.8a). After gelation of the solution, the resulting alcogel with the fiber inside was aged in methanol for at least two days. The alcogel with the embedded fiber was then soaked in 20 wt % HMDS solution in methanol for one day to replace most of the surface hydroxyl groups (–OH) with trimethylsilyl (–Si(CH₃)₃) groups, which rendered the alcogel surface hydrophobic. The alcogel was then immersed in pure methanol to remove unreacted HMDS from its structure. Finally, methanol within the alcogel was removed by supercritical extraction by scCO₂, resulting in a dry, monolithic aerogel block. As shown in Figure 2.8b, the fiber was carefully pulled out of the aerogel block, leaving a fiber-sized microchannel within the block that was subsequently filled with water (Figure 2.8c) and used as an optical waveguide (Figure 2.8d). Formation of optofluidic waveguides in aerogel monoliths using fiber-based channel preforms³⁹. (a) The precursor solution is poured over an optical fiber mounted inside a box, allowed to gel, and subsequently processed into a monolithic aerogel; (b) the fiber is pulled out of the aerogel block, leaving behind an open microchannel; (c) water is pumped into the

microchannel through a capillary; **(d)** light is coupled into the water column via a reinserted optical fiber. “Reproduced with permission from Xiao *et al.*, Optofluidic microchannels in aerogel; published by *Opt. Lett.*, 2011”. Preparation of silica aerogel monoliths with an embedded U-shaped channel ¹⁰⁷. **(e)** Precursors are mixed in the reaction vessel; **(f)** acid and **(g)** base catalyst addition lead to the formation of sol into which the channel preform made of POSS is inserted; **(h)** aging in ethanol-water mixture and **(i)** solvent exchange with pure ethanol yield reinforced alcogel; **(j)** extraction with scCO₂ removes the POSS channel preform, leaving the final monolithic aerogel with an empty channel inside. “Reproduced with permission from Eris *et al.*, Three-dimensional optofluidic waveguides in hydrophobic silica aerogels via supercritical fluid processing; published by *J. Supercrit. Fluids*, 2013.”). While this channel fabrication technique is rather simple to implement, withdrawal of the fibers embedded in the aerogel frequently leads to breakage due to the adhesion of the fiber to the silica aerogel network. Furthermore, this technique has only limited channel shaping and sizing capabilities.

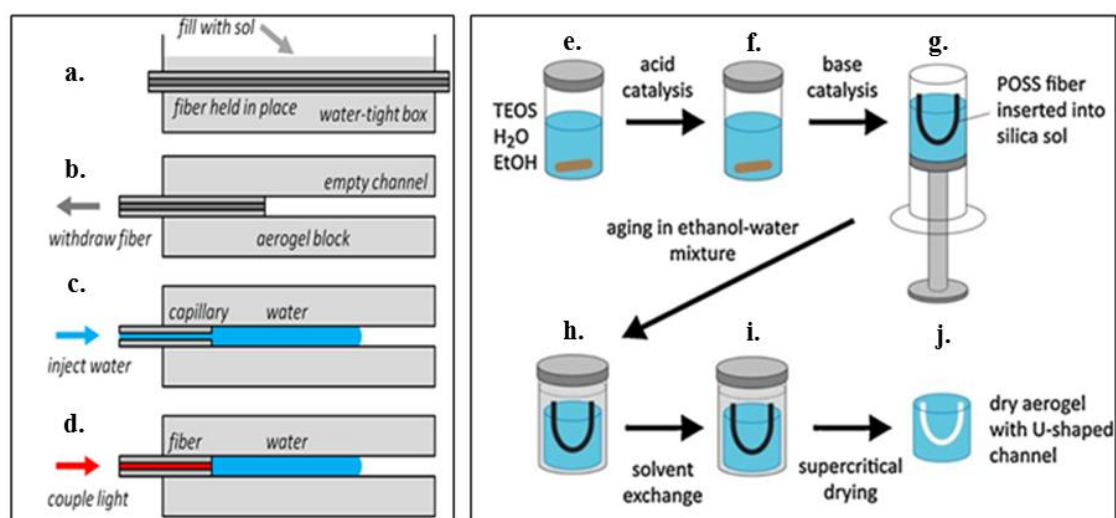


Figure 2.8. Formation of optofluidic waveguides in aerogel monoliths using fiber-based channel preforms ³⁹. **(a)** The precursor solution is poured over an optical fiber mounted inside a box, allowed to gel, and subsequently processed into a monolithic aerogel; **(b)** the fiber is pulled out of the aerogel block, leaving behind an open microchannel; **(c)** water is pumped into the microchannel through a capillary; **(d)** light is coupled into the water column via a reinserted optical fiber. “Reproduced with permission from Xiao *et al.*, Optofluidic microchannels in aerogel; published by *Opt. Lett.*, 2011”. Preparation of

silica aerogel monoliths with an embedded U-shaped channel ¹⁰⁷. (e) Precursors are mixed in the reaction vessel; (f) acid and (g) base catalyst addition lead to the formation of sol into which the channel preform made of POSS is inserted; (h) aging in ethanol-water mixture and (i) solvent exchange with pure ethanol yield reinforced alcogel; (j) extraction with scCO₂ removes the POSS channel preform, leaving the final monolithic aerogel with an empty channel inside. “Reproduced with permission from Eris *et al.*, Three-dimensional optofluidic waveguides in hydrophobic silica aerogels via supercritical fluid processing; published by *J. Supercrit. Fluids*, 2013.”

In order to circumvent the above limitations, Eris *et al.* developed a novel solution that eliminates the problems occurring during the withdrawal of embedded fiber ¹⁰⁷. They formed channels in aerogels by using channel preforms made of trifluoropropyl polyhedral oligomeric silsesquioxane (POSS). This particular POSS was found to be highly soluble in scCO₂ due to its trifluoropropyl groups and insoluble in the ethanol-water mixture used in the solvent exchange step in synthesis of aerogels. In order to prepare the channel preform, trifluoropropyl POSS was initially melted and then shaped into a U-shaped fiber during its solidification. A mixture of TEOS, water, ethanol, and acid catalyst was prepared and a base catalyst was added to the mixture, as shown in Figures. 2.8e and 2.8f. The U-shaped trifluoropropyl POSS fiber was then placed in the solution as demonstrated in Figure 2.8g. Subsequently, the solution gelled with the U-shaped fiber inside it. Afterwards, the alcogel with embedded POSS fiber was aged in ethanol (Figure 2.8h and Figure 2.8i). Subsequently, the POSS fiber was extracted together with ethanol from the alcogel using scCO₂ at 313.2 K and 9 MPa. The extraction led to the formation of a U-shaped empty channel inside the aerogel monolith as displayed in Figure 2.8j. The silica aerogel monolith with the U-shaped channel was subsequently treated with HMDS to make it hydrophobic. The monolith was immersed in a solution of HMDS in scCO₂ in a high-pressure vessel at 333.2 K and 10.34 MPa for 2 h. Subsequently, unreacted HMDS as well as the reaction products of HMDS with surface hydroxyl groups were extracted by flowing scCO₂ through the vessel. Finally, a monolithic, hydrophobic silica aerogel with an empty channel inside was obtained. The hydrophobicity of the samples was determined by measuring water contact angle of the aerogel surface and it was found to be 140 °. Using this technique, breaking of the

aerogel during preform removal could be prevented. Moreover, it should also be possible to form complex channel architectures in aerogel blocks by appropriate shaping of trifluoropropyl POSS or other scCO_2 soluble polymers.

2.8.2 Laser Ablation

A number of studies demonstrated that aerogels can be precisely ablated by femtosecond lasers (Figure 2.9) ¹⁵¹⁻¹⁵². Sun *et al.* ¹⁵¹ demonstrated that silica aerogels can be machined through ultrafast laser processing for the first time. An amplified femtosecond Ti:sapphire laser system was used to machine the silica aerogels. The laser beam at the wavelength of 790 nm, emerging from the femtosecond laser focused on the aerogel surface, which results in formation of holes in almost cylindrical shape. The depth of the generated holes changed with the applied number of pulses at constant fluence during the ultrafast laser machining. The depth of the channels in the silica aerogels increased with the increasing number of pulses of the laser. It increased from 250 μm by a single shot at a fluence of 7.3 J/cm^2 with 180 fs pulse duration to 1600 μm by applying 16 shots. Subsequently, Bian *et al.* ¹⁵² was able to slice cylindrical polyurea aerogel samples with diameters ranging from 10 to 15 mm into 1–3 mm disks using ablation by femtosecond laser pulses. They focused the laser beam operating at the wavelength of 800 nm at the center of the sample, which was placed on a micro-positioning stage so that the sample could be rotated or translated in 3D for cutting along a desired path. Then, Yalızay *et al.* ³⁸ was able to create channels in a hydrophobic monolithic silica aerogel with a density of 0.2 g/cm^3 and a refractive index of 1.037 using femtosecond laser ablation. The setup used for micromachining channels with the desired length and diameter in aerogel blocks by laser ablation is shown in Figure 2.9b. The power of the laser was adjusted using a combination of a polarizer and a half-wave plate. The direction of the laser beam was controlled by a dual-axis scanning galvo system. The beam was focused on the aerogel surface by a scan lens and the femtosecond laser pulses essentially vaporized the silica. Microchannels with desired dimensions could be machined by sending sinusoidal driving signals of different frequencies to both x - and y -axis of the galvo scanner so that the beam focused along a Lissajous pattern. A cylindrical channel was created inside the silica aerogel block by moving the aerogel along the z -axis of the system during the ablation process. In order to

prevent the accumulation of ablated silica particles inside the channel during the process, the ablated section of the sample was purged with nitrogen during the fabrication. Cylindrical microchannels which were formed inside the silica aerogel were approximately 5 mm long and had diameters around 500 μm . With the use of ultrafast laser pulses (duration ~ 100 fs), thermal effects common with long (nanosecond-scale) pulses can be largely eliminated, resulting in a highly localized and clean material ablation.

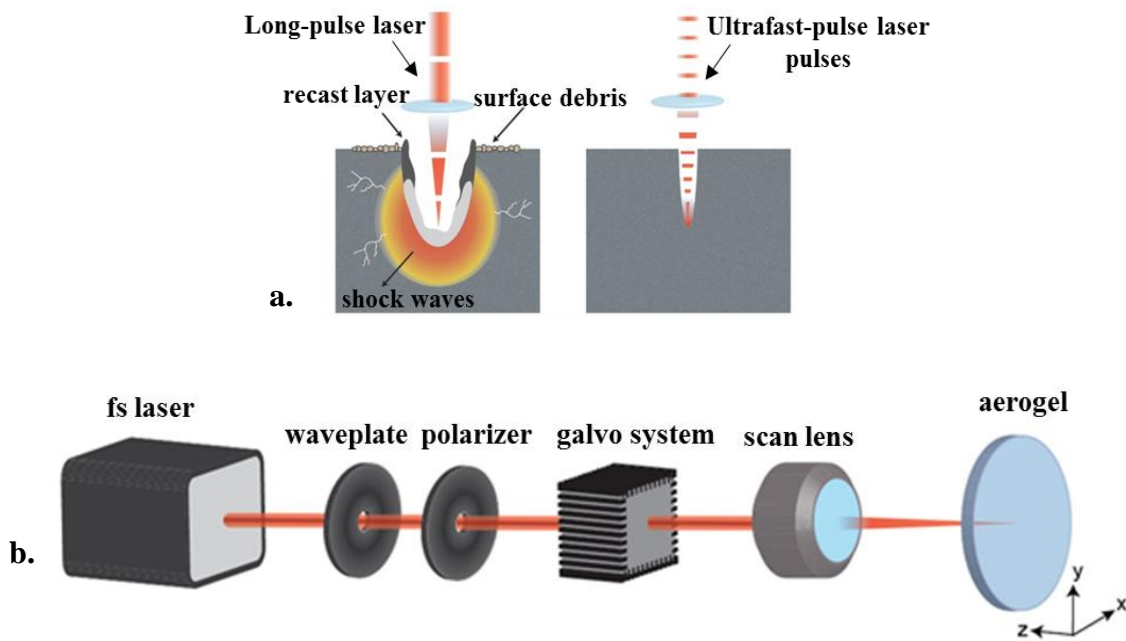


Figure 2.9. (a) A schematic representation of laser ablation process using a focused pulsed laser beam. (b) Experimental setup used for aerogel micromachining by fs-laser ablation ³⁸. “Reproduced with permission from Yalızay *et al.*, Versatile liquid-core optofluidic waveguides fabricated in hydrophobic silica aerogels by femtosecond-laser ablation; published by *Opt. Mater.*, 2015.”

2.9 Construction of Liquid-Core Optofluidic Waveguides in Aerogels

After creating channels in aerogel monoliths (see Figure 2.10 and Figure 2.11) for an overview of channels fabricated using the various methods described in Section 2.8), liquid-core optofluidic waveguides can be constructed by filling the channels with the working liquid with a high refractive index that serves as the waveguide core liquid.

Xiao and Birks used water as the core liquid with a refractive index of 1.33³⁹. Since the aerogels used in their experiments were hydrophobic, the microchannels could not be filled with water by simple immersion in water and action of capillary forces. Thus, the channels had to be filled by a syringe connected to a fiber-sized capillary that was carefully inserted into one end of the channel. Air bubbles formed during the filling of the channel were removed by simply pushing the water column towards the other end of the channel; the air in between could quickly escape sideways through the aerogel pores, leaving a continuous liquid path without any bubbles. Similarly, Eris *et al.* filled the fabricated U-shaped channels in hydrophobic silica aerogel blocks with water by a fast injection from a syringe, applying a sufficiently high pressure to overcome the resistance of hydrophobic channel surface to flow¹⁰⁷. Yalızay *et al.*³⁸ selected to work with ethylene glycol as the core liquid instead of water to eliminate evaporation of the core liquid during the course of the experiment. In their work, they demonstrated that ethylene glycol could remain confined within the hydrophobic channels without collapsing the solid aerogel network.

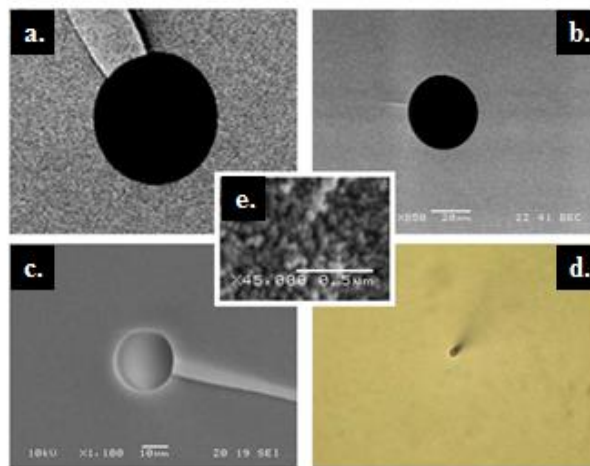


Figure 2.10. Channels fabricated using fiber-based preforms. SEM images of cleaved cross-sections of microchannels with diameters (a) 100 μm, (b) 35 μm, and (c) 23 μm, (d) Optical micrograph of the cleaved cross-section of a microchannel with a diameter of 4 μm. (e) SEM image of the aerogel surface; the scale bar is 0.5 μm.³⁹. “Reproduced with permission from Xiao *et al.*, Optofluidic microchannels in aerogel; published by *Opt. Lett.*, 2011.”

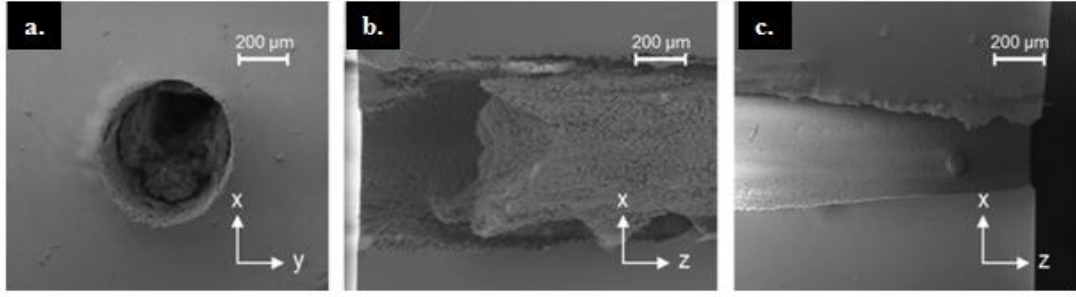


Figure 2.11. Channels fabricated using femtosecond laser ablation. (a) SEM image of the input face of a microchannel ablated in the aerogel. The depth of the channel is about 300 μm and the diameter is about 500 μm . (b) Axial cross-section view of the channel ablated in the aerogel. During machining, ablated silica particles accumulated inside the channel (see the right part of the channel) (c) Axial cross-section view of the channel ablated with simultaneous purging of the sample with high-pressure nitrogen gas. All the dust accumulated in the channel during the machining was removed. For recording the cross-sectional images shown in (b) and (c), the samples were cleaved along the axis of the channel ³⁸. “Reproduced with permission from Yalızay *et al.*, Versatile liquid-core optofluidic waveguides fabricated in hydrophobic silica aerogels by femtosecond-laser ablation; published by *Opt. Mater.*, 2015.”

2.10 Characterization of Light Propagation in Aerogel-Based Optofluidic Waveguides

During propagation through an optical waveguide, the power of the guided light is gradually attenuated due to absorption, scattering, leakage out of the waveguide at the waveguide bends, and other effects. The overall optical throughput of optical waveguides can be quantified by Equation 2.9 in terms of the input optical power, P_o , and the output power, $P(z)$, observed after the light has propagated a distance z along the waveguide axis:

$$P(z) = P_o e^{-\alpha_{total} z} \quad \text{Equation 2.9}$$

where α_{total} is the total attenuation coefficient (involving all contributions to attenuation). Usually, the propagation loss of the waveguide, η , is expressed in decibels per unit waveguide length from the fractional power transmission as given by Equation 2.10:

$$\eta = -\frac{10\alpha_{total}}{\ln 10} \quad \text{Equation 2.10}$$

Xiao and Birks³⁹ characterized the wave-guiding properties of water-filled channels with a diameter of 125 μm created within aerogel monoliths by coupling light into the channel via an optical fiber and measuring optical attenuation in the channel (see Figure 2.8. Formation of optofluidic waveguides in aerogel monoliths using fiber-based channel preforms³⁹. (a) The precursor solution is poured over an optical fiber mounted inside a box, allowed to gel, and subsequently processed into a monolithic aerogel; (b) the fiber is pulled out of the aerogel block, leaving behind an open microchannel; (c) water is pumped into the microchannel through a capillary; (d) light is coupled into the water column via a reinserted optical fiber. “Reproduced with permission from Xiao *et al.*, Optofluidic microchannels in aerogel; published by *Opt. Lett.*, 2011”. Preparation of silica aerogel monoliths with an embedded U-shaped channel¹⁰⁷. (e) Precursors are mixed in the reaction vessel; (f) acid and (g) base catalyst addition lead to the formation of sol into which the channel preform made of POSS is inserted; (h) aging in ethanol-water mixture and (i) solvent exchange with pure ethanol yield reinforced alcogel; (j) extraction with scCO_2 removes the POSS channel preform, leaving the final monolithic aerogel with an empty channel inside. “Reproduced with permission from Eris *et al.*, Three-dimensional optofluidic waveguides in hydrophobic silica aerogels via supercritical fluid processing; published by *J. Supercrit. Fluids*, 2013.” for illustration of their experimental geometry). Laser light with a wavelength of 635 nm was coupled into the free end of the fiber used in the characterization. Figure 2.12a and Figure 2.12b show water-filled channels inside aerogels, with light coupled into their left end. In both cases, diverging light beams emerge from the right end of the channels, since the light-guiding requirements are no longer met after leaving the aqueous waveguide core. Thus, upon emerging from the core, the propagating light has the form of a diverging cone of light formed due to scattering from aerogel particles. Due to evaporation through the aerogel pores and the open channel end, the water inside the channel receded from right to left in a short span of time, resulting in the channel partially filled with air (see a time sequence of channel images in Figure 2.12b,). As shown in Figure 2.12a and Figure 2.12b, laser light could be guided through the straight

water-filled channel. The total waveguide loss including input and output coupling losses in the 16 mm long water-filled channel was measured as 2.4 dB. This loss corresponds to a waveguide attenuation coefficient of $\eta = -1.5$ dB/cm. As the authors pointed out, improved quality of microchannel surface with lower channel wall roughness might eliminate the losses due to Rayleigh scattering. In such a straight waveguide, the dominant loss mechanism should mostly be the wavelength-dependent light absorption of the structure itself.

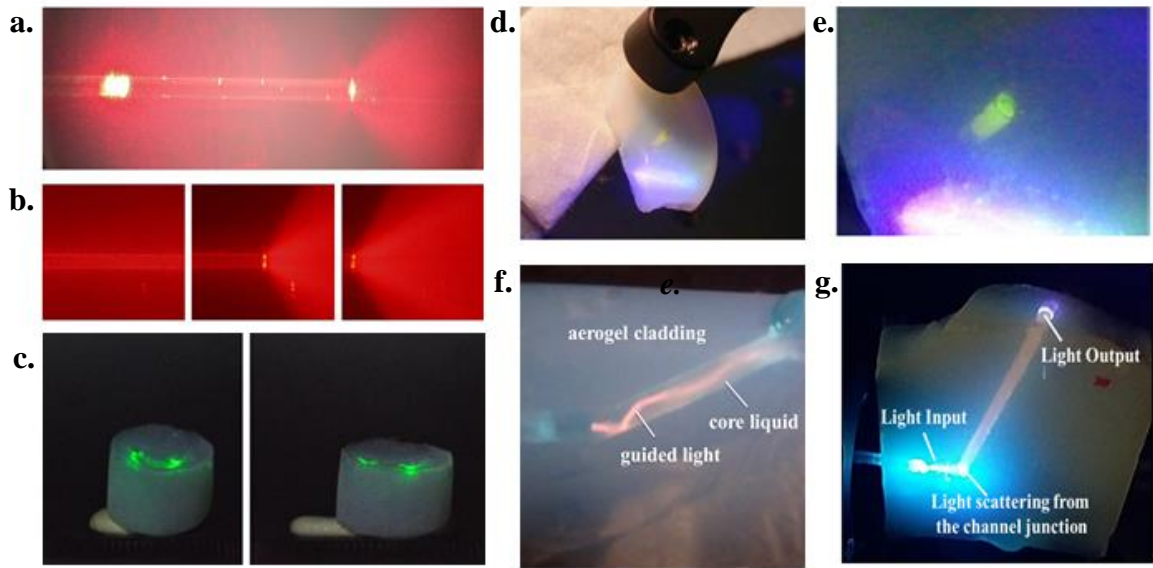


Figure 2.12. Light propagation in aerogel-based optofluidic waveguides. (a) – (b) Waveguides fabricated using fiber preforms. (a) Guiding of 635 nm laser light in a 125 μm diameter aerogel microchannel filled with water. The light enters into the channel from the left through a fiber, and emerges from the end of the channel toward the right. The fiber ends at the bright scatter point about 2 mm inside the 10 mm long aerogel block; (b) (left to right) images taken at 40 s intervals at the end of the channel, as the water evaporates³⁹. “Reproduced with permission from Xiao *et al.*, Optofluidic microchannels in aerogel; published by *Opt. Lett.*, 2011.” (c) Waveguides fabricated using supercritical extraction of POSS preforms. (c) Light guiding in a water-filled U-shaped channel inside a hydrophobic silica aerogel; the light was focused on the left end of the channel and exited from the right end of the channel¹⁰⁷. “Reproduced with permission from Eris *et al.*, Three-dimensional optofluidic waveguides in hydrophobic

silica aerogels via supercritical fluid processing; published by *J. Supercrit. Fluids*, 2013.” (d) – (e) Waveguides fabricated using femtosecond laser ablation. (d) Photograph of an aerogel monolith with a liquid-filled channel in the center. (e) Green fluorescence emitted from the channel filled with fluorescein-doped ethylene glycol solution upon illumination with blue light. ³⁸. “Reproduced with permission from Yalızay *et al.*, Versatile liquid-core optofluidic waveguides fabricated in hydrophobic silica aerogels by femtosecond-laser ablation; published by *Opt. Mater.*, 2015.” (f) - (g) Waveguides fabricated using manual drilling. (f). Total internal reflection of guided light in the water-filled channel fabricated by drilling in a monolithic aerogel ($\rho = 0.15 \text{ g/cm}^3$). (g) Light propagation in a liquid-filled L-shaped channel within the aerogel monolith (side view) ³⁷. “Reproduced with permission from Özbakır *et al.*, Total Internal Reflection-Based Optofluidic Waveguides Fabricated In Aerogels; published by *J. Sol-Gel Sci. & Tech.*, 2017.”

Eris *et al.* ¹⁰⁷ evaluated qualitatively the efficiency of their U-shaped optofluidic waveguides. In this study, a laser beam with a wavelength of 532 nm and 35 mW maximal output power was focused through a lens with a focal length of 150 mm at one end of the channel in the aerogel which was placed on a two-dimensional translation stage. The position of the beam focus was adjusted using the translation stage for maximal light transmission to the other end of the channel which was determined by monitoring the intensity of light visually. The green laser beam was initially directed into the right end of an air filled channel. In this case, the laser light was transmitted straight through the aerogel without any deflection indicating that there is no waveguiding as expected. The channel was then filled with water and the light was again directed to its right end. The laser light coupled into the liquid core could be guided along the liquid-core before exiting from the other end of the channel as shown in Figure 2.12c showing the presence of an optofluidic waveguide. Due to the U-shaped geometry of the liquid channel as well as the high divergence angle of the light transmitted through the channel, the loss of power could not be directly measured at the open end of the channel. For such U-shaped waveguides, most of the loss is expected to be due to the bends in the waveguide, in which a fair amount of the energy of the guided mode is located closer to the outer rim of the waveguide. Therefore, there is a possibility that the

light can partially leak into the surrounding cladding. However, for aerogel-based waveguides, the high refractive index contrast between the core liquid and the aerogel cladding enhances the confinement of light in the waveguide, leading to significantly smaller bending losses.

For straight waveguides, Yalızay *et al.*³⁸ used the experimental setup shown in Figure 2.13 for the characterization of light-guiding properties of the waveguides by measurement of their propagation losses. An auxiliary laser operating at 632.8 nm was coupled into the liquid core of the waveguide through a tapered optical fiber which was approximately 5 μm in diameter. The face at the exit of the liquid-filled channel was imaged on a charge-coupled device camera through a projection lens in order to quantify the amount of light transmitted through the waveguide. Subsequently, the tapered input fiber was moved along the channel axis and the total power of the light exiting the channel was simultaneously measured as a function of the distance between the fiber tip and the channel output. This was accomplished by adding the grayscale values of all pixels in the recorded image of the waveguide at the exit face. The images were recorded for each 100 μm increment of the position of the input fiber along the channel axis. A typical recorded image of the guided laser light is shown in Figure 2.14a. The light distribution covering the entire cross-section of the channel contained within the red dashed curve shows that the coupled light was indeed confined and guided inside the channel. Moreover, the speckle pattern of the output light distribution could be attributed to the multimode behavior of the large-core waveguide and interference of individual guided modes dependent on the relative differences of their optical path lengths. The total transmitted power determined by integrating over the cross section of the channel was then plotted as a function of the propagation distance along the waveguide. As shown in Figure 2.14b, the output power of the waveguide exhibited regular oscillations superimposed on an exponentially decreasing background. These oscillations were attributed to the path-dependent interference of multiple guided modes. The measured power of the transmitted light was fitted using Equation 2.9. From the particular measurement shown in Figure 2.14b, α_{total} was found as 2.278 cm^{-1} . Using Equation 2.10, the propagation loss of the waveguide (η) was then calculated as -9.9 dB/cm . This propagation loss is nearly 7 times higher than that was obtained by Xiao *et al.*³⁹ which

perhaps can be attributed to the increased roughness of the channel surfaces produced by laser micromachining, leading to higher scattering losses in the waveguides. Further experiments need to be performed with aerogels with surfaces of different roughnesses to confirm this hypothesis.

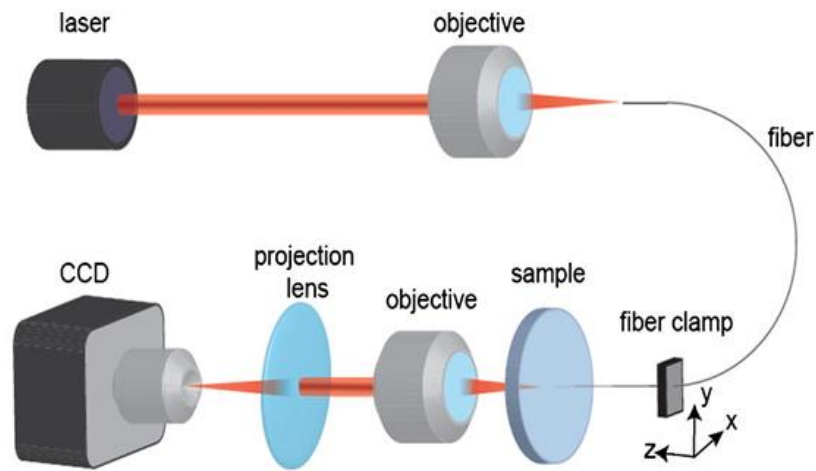


Figure 2.13. Schematics of experimental setup used in the characterization of the light-guiding performance of liquid core optofluidic waveguides ^{38, 107}. “Reproduced with permission from Yalçay *et al.*, Versatile liquid-core optofluidic waveguides fabricated in hydrophobic silica aerogels by femtosecond-laser ablation; published by Opt. Mater., 2015.”

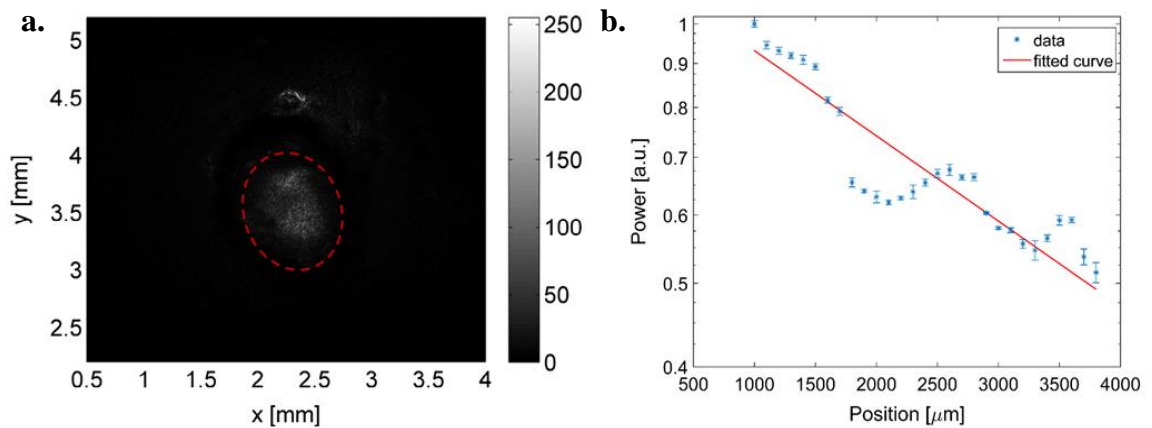


Figure 2.14 (a) Grayscale CCD camera image of guided light in the liquid-core waveguide inside the aerogel. The red dashed curve indicates the channel contour, and

the light outside the region delimited by the curve results from scattering losses. (b) Normalized power of light transmitted through the waveguide versus the propagation distance along the waveguide axis, shown in semi-log scale. Blue dots: experimental data points; red line: exponential fit of the experimental data ³⁸. “Reproduced with permission from Yalızay *et al.*, Versatile liquid-core optofluidic waveguides fabricated in hydrophobic silica aerogels by femtosecond-laser ablation; published by *Opt. Mater.*, 2015.”

2.11 Applications of Aerogel-Based Optofluidic Waveguides

The future potential of novel aerogel-based optofluidic waveguides can be extended to develop devices for several lines of applications. Photochemical reactions which utilize light energy are used in synthesis of chemicals, in detection, identification and quantification of a wide variety of chemicals or organisms, in modification of surfaces and in treatment of various diseases. Aerogel based optofluidic waveguides may therefore be utilized in all these areas. Furthermore, aerogel-based optofluidic waveguides can potentially improve the efficiency of conventional photobioreactors, providing increased light intensity delivery to photosynthetic organisms like algae located farther away from the illumination source and in confined places as shown in Figure 2.15a. Since aerogels are permeable to gases due to their porous nature and interconnected pores, they may readily allow gases to be transferred between the microchannel and the surroundings ¹⁵³⁻¹⁵⁴. For applications involving microorganisms, CO₂ required for biomass growth can diffuse into the channel from the pores and the product of photosynthesis, O₂, can diffuse out through the aerogel pores as shown in Figure 2.15b and Figure 2.15c.

Aerogel-based photoreactors are also promising for carrying out photochemistry. Light-initiated synthesis of novel molecular species, various types of polymerization reactions, as well as treatment of wastewater, including destruction of highly complex organic compounds such as dyes, surfactants, and pesticides can be carried out in such reactors in variety of scales as shown in Figure 2.15b. Aerogel-based optofluidic waveguides can also be used for photocatalytic reactions. As has been previously mentioned and shown in Figure 2.15c, microchannel walls in an aerogel monolith are mesoporous and particles with photocatalytic properties such as semiconductors can be

immobilized within these pores with good adhesion to the solid network. The light propagating through the waveguide can be then partially absorbed by the surface of the photocatalyst particles. The reactants can thus be converted into the desired products on the photocatalyst surface. Efficient light-guiding properties of the aerogel clad-TIR waveguides may enable development of devices for diagnostic monitoring of glucose and alcohol concentrations in the blood based on quantitative optical absorption measurements. This can perhaps be performed by the injection of a blood sample to the waveguide, or by using the aerogel-based optofluidic chips as implantable light-delivery lab-on-a-chip devices, particularly for photomedicine (Figure 2.15d). Additionally, various pathogens such as bacteria, viruses, and pesticides can be detected in various media based on optical absorption measurements. Finally, aerogel-based liquid-core waveguides might provide a straightforward way for guiding and controlled routing of light within tissues in light-based medical treatments such as photodynamic therapy (PDT) that is used to treat tumors using photosensitizing drugs and light in the presence of oxygen to initiate photochemical reactions ¹⁵⁵⁻¹⁵⁶ For the illumination in PDT, both lasers with perfect directionality and high intensity of output light and light-emitting diodes have been designed. However, light diffusely scattered or mis-located away from the target area accidentally irradiates large areas of healthy tissue, which - due to the huge power density - can result in collateral damage to the body ¹⁵⁶. Since aerogels can serve to construct robust biocompatible waveguides, aerogel-based optofluidic waveguides can be implemented directly into the tissue to deliver light to a point located deep within the body. Moreover, this ability of aerogel-based waveguides to carry the visible light to a small area deep within the body opens up new opportunities for exploring the applications of aerogels in biomedical imaging and therapy.

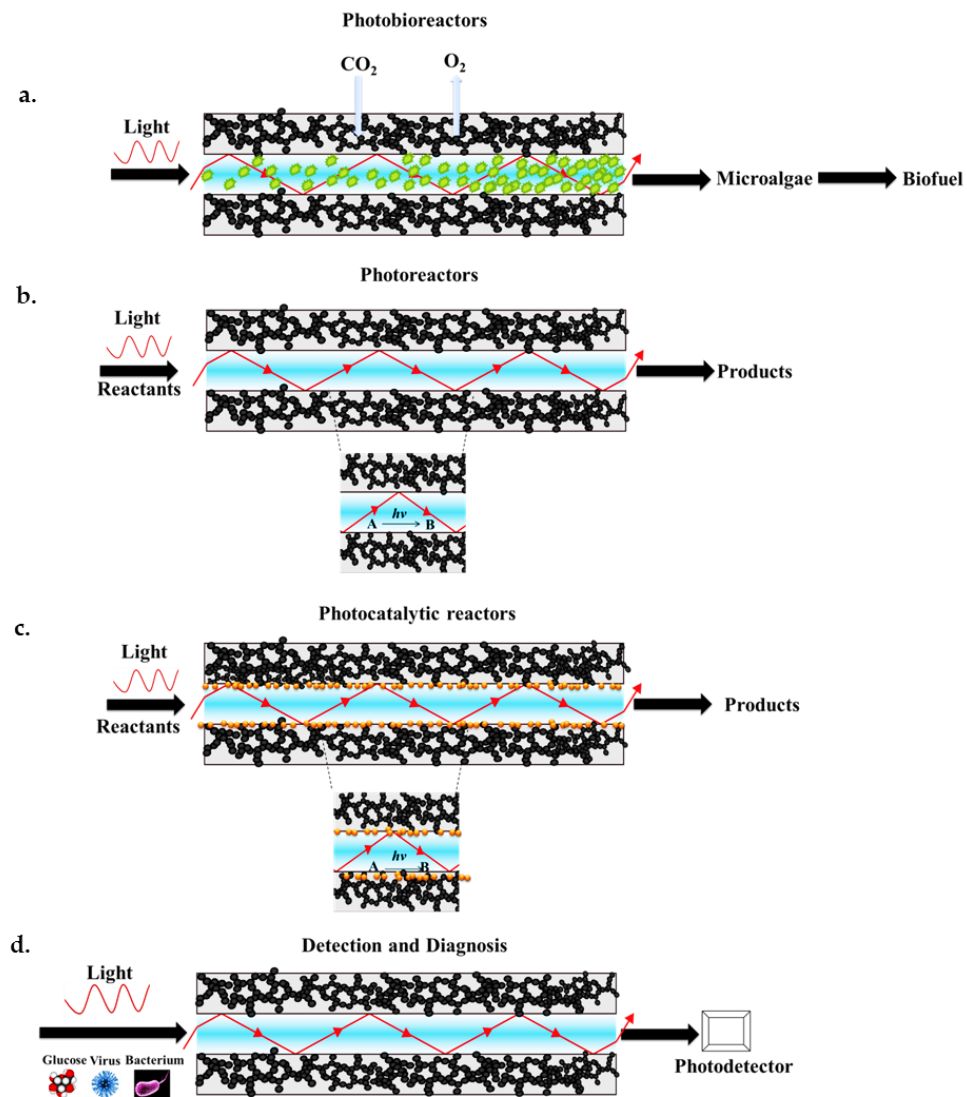


Figure 2.15. Possible applications of aerogel-based optofluidic waveguides. **(a)** Aerogel-based photobioreactors. **(b)** Aerogel-based photoreactors. **(c)** Aerogel-based photocatalytic reactors. **(d)** Detection and diagnostic devices based on optofluidic waveguides ³⁶. “Reproduced with permission from Özbakır *et al.*, Aerogels for Optofluidic Waveguides; published by *Micromachines*, 2017.”

Chapter 3

CHARACTERIZATION TECHNIQUES

3.1 Bulk Density and Porosity

The bulk densities of monolithic silica aerogels and silica-titania aerogel composites were calculated by dividing their mass of the aerogel by their final volume. The physical dimensions of the samples in the alcogel or aerogel conditions are measured with the help of a caliper for most accurate results.

$$\rho_{aerogel} = \frac{m_{aerogel}}{V_{aerogel}} \quad \text{Equation 3.1}$$

The porosity of the aerogels was calculated based on the following equation where ρ_{SiO_2} was the density of pure silica (2.19 g/cm³) and $\rho_{aerogel}$ was the bulk density of the aerogel.

$$Porosity (\%) = \frac{\rho_{SiO_2} - \rho_{aerogel}}{\rho_{SiO_2}} \quad \text{Equation 3.2}$$

3.2 Pore Structure Characteristics with N₂ Adsorption/Desorption

Pore properties of the aerogel samples including average pore size, pore size distribution, pore volume and surface area were determined by N₂ adsorption–desorption measurements by using Micromeritics ASAP 2020 instrument which is shown in Figure 3.1. Prior to the analysis, the samples were degassed at 300 °C (for silica aerogels) or 80 °C (for silica-titania composite aerogels) under vacuum for 1 day to remove remaining impurities from the surface. After exact weight of the degassed sample was determined, pore analysis was conducted using N₂ adsorption/desorption isotherms with a relative pressure (P/P₀) ranging from 10^{−7} to 0.999. The pore volume and pore size distributions were determined by Barrett–Joyner–Halenda (BJH) analysis. The surface area of the samples was determined by Brunauer–Emmett–Teller (BET) method which is an extended form of Langmuir’s kinetic theory to multilayer adsorption. Total pore volume of the sample was determined by converting the

adsorbed N₂ volume at STP to liquid N₂ volume at 77 K. The surface morphology of the composite samples was investigated using a ZEISS Ultra-Plus Field Emission Scanning Electron Microscope (FE-SEM), combined with energy dispersive X-ray spectrum (EDX). EDX was used for the elemental composition analysis on the above FE-SEM.

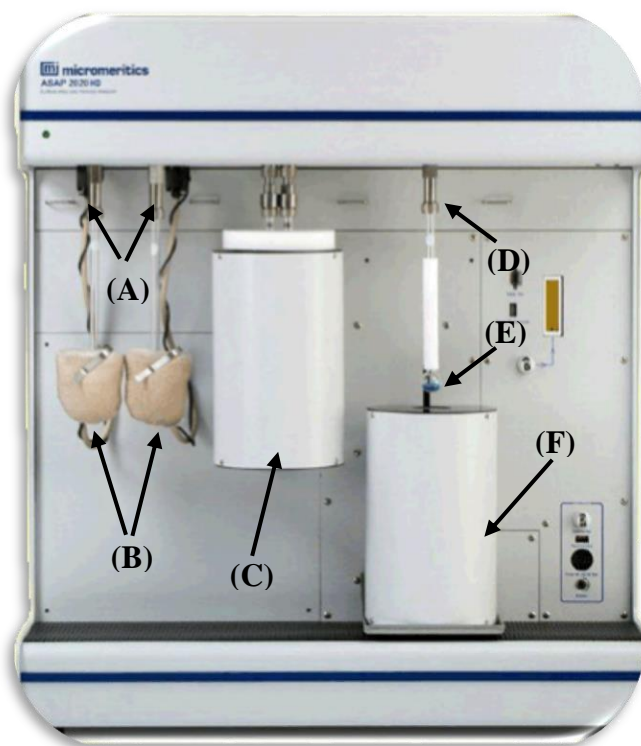


Figure 3.1. Micromeritics ASAP 2020 N₂ adsorption-desorption analysis system; (A) degas ports; (B) heating jacket; (C) degas dewar; (D) analysis port; (E) sample port; (F) analysis dewar.

3.3 Optical Properties of Aerogels by UV-VIS Spectrophotometer

A UV-VIS spectrophotometer (Shimadzu UV-3600) with a halogen lamp and deuterium lamp as irradiation sources was used to measure the absorbance of samples in the wavelength range of 350-1800 nm. Total luminous transmittance and diffuse transmittance were also measured using an ISR-3100 integrating sphere attached to the UV-VIS spectrophotometer, which is shown in Figure 3.2. The Integrating sphere system is composed of UV-VIS-NIR light source, sample holder, detector at the center of the system, two BaSO₄ powder to fully reflect the incoming light and reference beam. Scan speed was arranged as medium. Sampling interval (nm) was set as 1.0 and

auto mode is selected for sampling mode. Measuring mode was always transmittance and slit width was selected as 20 nm. External 2 detector (Not direct) was selected for detector unit. For both measurements, the characterized aerogel was placed in front of the input port of the integrating sphere through which the light beam enters. When measuring the total transmittance which is total of the scattered light from the solid and porous network of the aerogel and linear transmitted light, the sphere collected all the light passing through the aerogel sample (see Figure 3.3). For diffuse transmittance measurements, the same arrangement as in the total luminous transmittance measurements was used, but the light passing without deflection straight through the aerogel was not collected due to the presence of an opening in the wall of the integrating sphere exactly opposite to the input port.

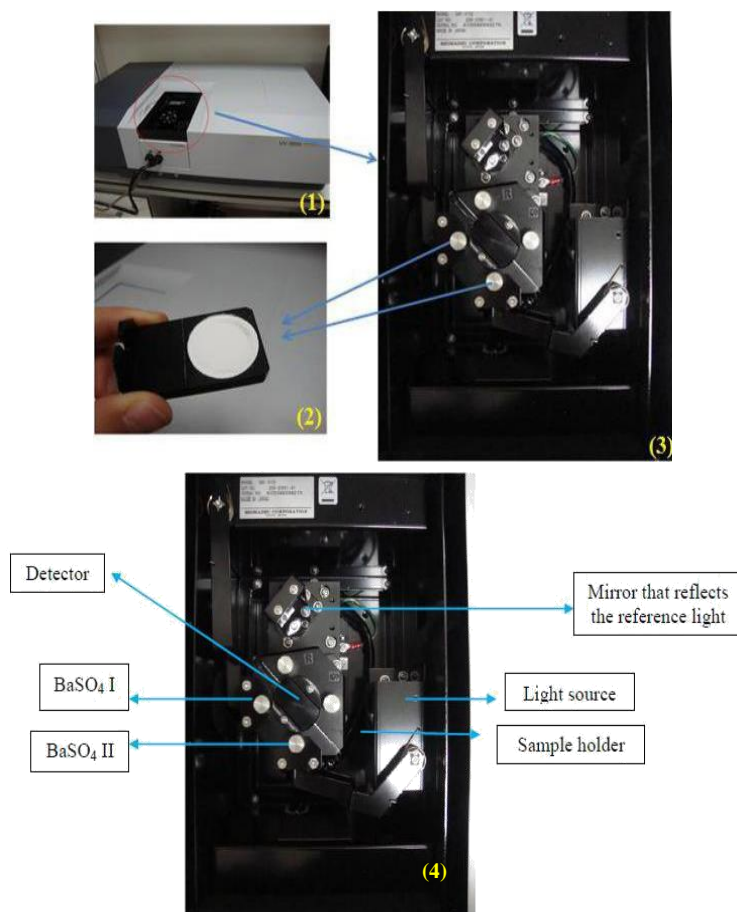
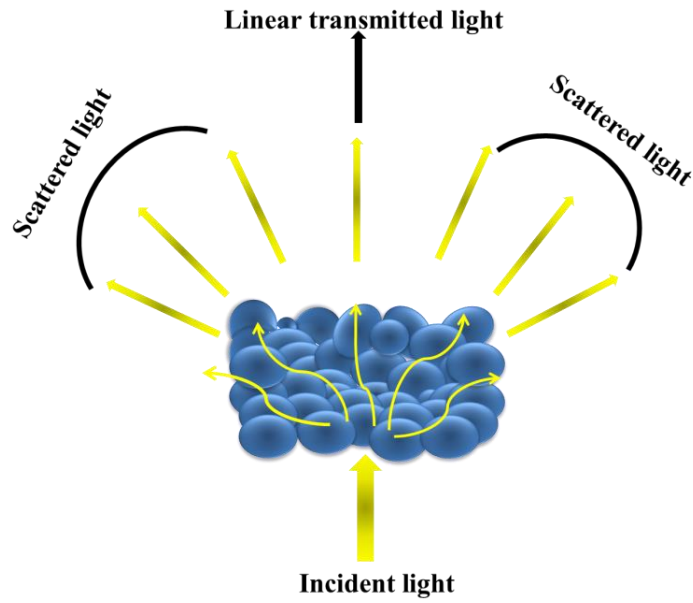


Figure 3.2. (1) A photograph of Shimadzu UV-3600 with an auxiliary integrating sphere (2) BaSO₄ powder (3) Integrating sphere system (4) Components of integrating sphere apparatus.



$$\text{Total Luminous Transmittance} = \text{Linear Transmittance} + \text{Diffuse Transmittance}$$

Figure 3.3. Schematics of light transmission phenomena in aerogels.

In order to determine haze value or transparency ratio of a sample, both total and diffuse transmittances should be analyzed by following three consecutive steps. First measurement was performed without sample for baseline correction. After baseline correction, sample was placed inside the integrating sphere shown in Figure 3.2(3) and Figure 3.2(4) and total transmittance was measured, as shown in Figure 3.4a. For diffuse transmittance, BaSO₄ I (Figure 3.2(2)) was removed from the integrating sphere and only forward scattered light was measured, as demonstrated in Figure 3.4b. The ratio of diffuse to total transmittance gives haze value for the measured aerogel samples (see Equation 2.3).

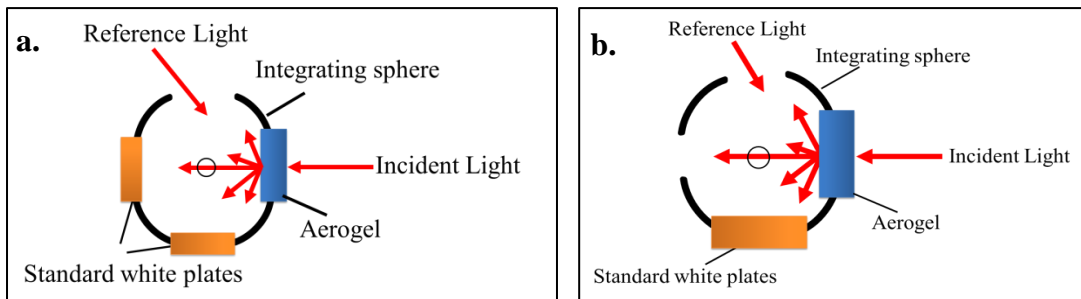


Figure 3.4. (a) Schematic of total transmittance measurement. (b) Schematic of diffuse transmittance measurement.

Diffuse Reflectance UV-VIS (DR-UV-VIS) spectra were used to obtain electronic band-gap of the SiO₂-TiO₂ composites. These spectra were recorded with the Shimadzu UV-3600 UV-Vis-NIR spectrophotometer using ISR-3100 integrating sphere attachment in the specular reflection (8°) mode as shown in Figure 3.5. The band gap of the composites was estimated from Tauc method calculating Kubelka-Munk function $F(R)$, which is given in Equation 3.5, from the diffuse reflectance spectra of the samples

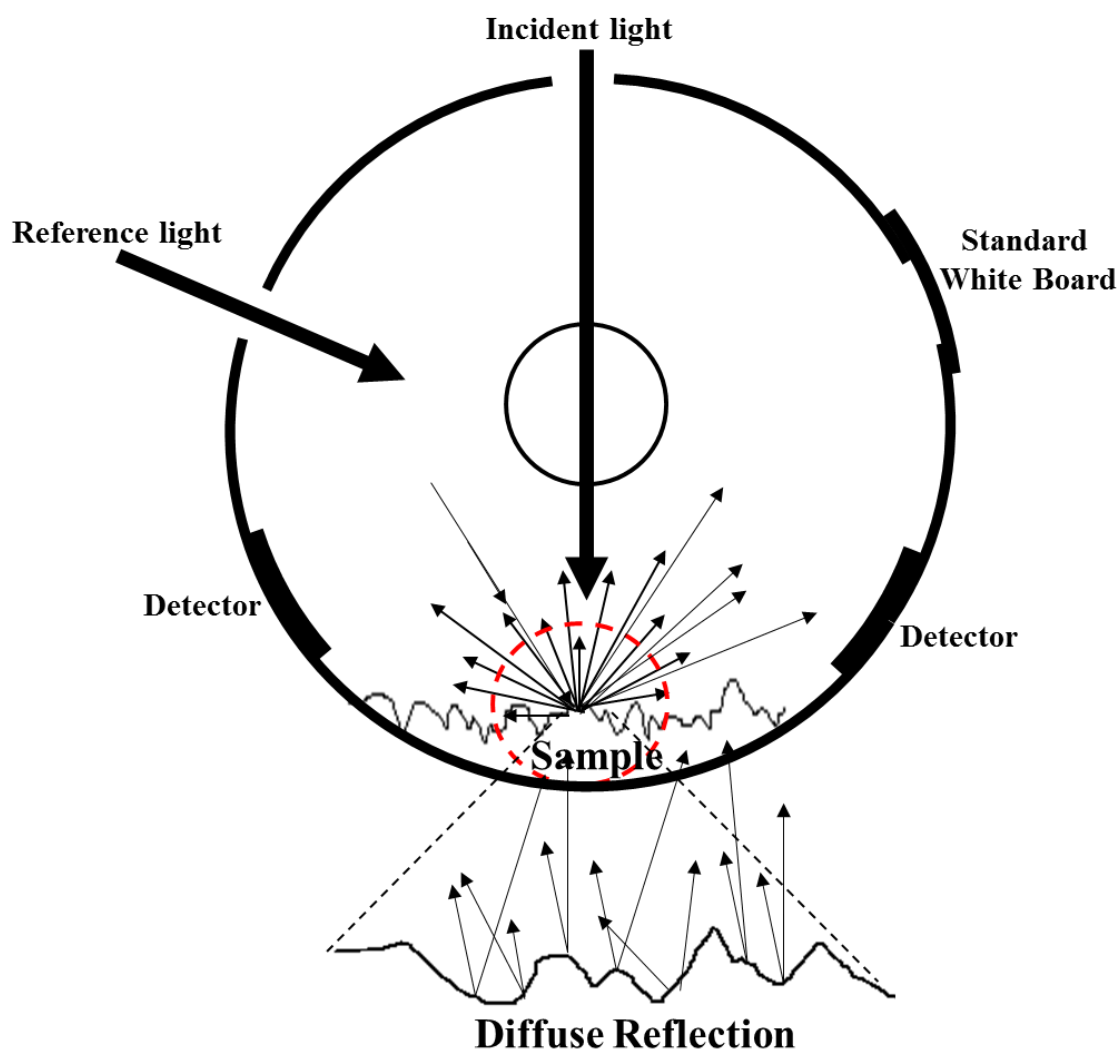


Figure 3.5. Schematics of diffuse reflectance measurement in the integrating sphere.

Kubelka Munk function considers a layer of light-absorbing and scattering particles. The radiant flux in the positive direction is denoted J and in the negative direction is denoted I (see Figure 3.6). Two differential equations for the changes in the flux in an infinitesimal thickness of dx in the material are defined by Equation 3.3 and Equation 3.4, which result in $F(R)$ ¹⁵⁹.

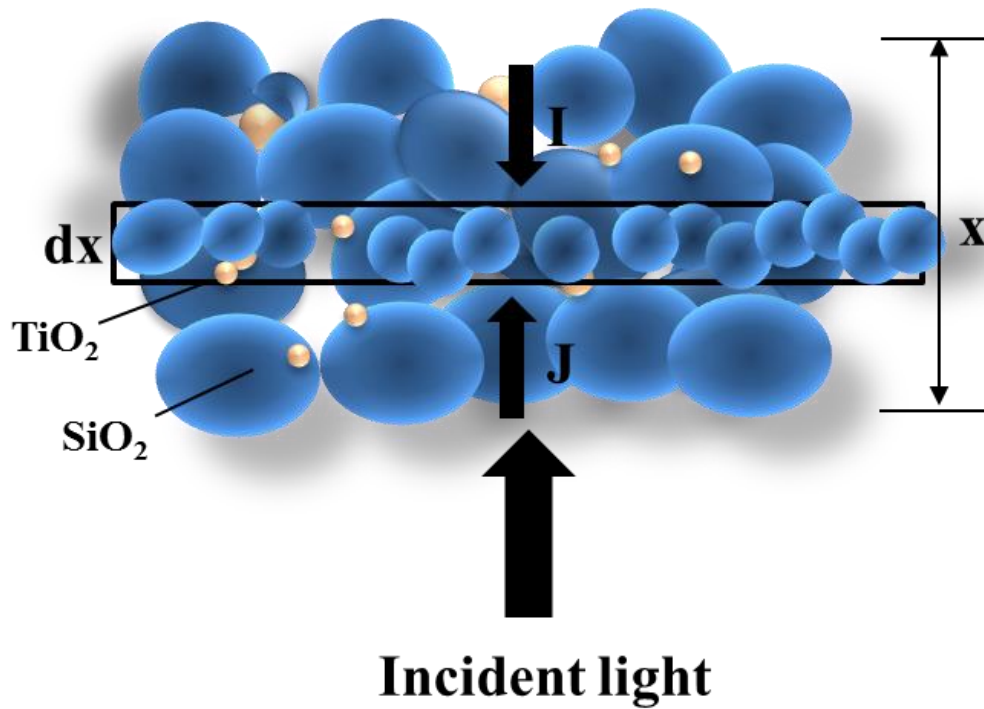


Figure 3.6. Two fluxes in Kubelka-Munk theory

$$\frac{dJ}{dx} = -(K + S)J + SI \quad \text{Equation 3.3}$$

$$\frac{-dI}{dx} = -(K + S)I + SJ \quad \text{Equation 3.4}$$

$$F(R) = \frac{(1 - R_{\infty}(h\nu))^2}{2R(h\nu)_{\infty}} \quad \text{Equation 3.5}$$

where R is diffuse reflectance of the samples obtained directly by from the spectrophotometer, h is planck constant and ν is frequency of the light.

Assuming an indirect band gap for titania, the band gap energy, E_g , is obtained from the plots of $[F(R) * h\nu]^{0.5}$ vs. energy of photon, $h\nu$ by extrapolation of the linear part of the plot and the intersection of the straight line at the photon energy axis where $[F(R) * h\nu]^{0.5} = 0$ provides the value of E_g for all the samples.

The crystal structure and crystallinity of the composites were analyzed by Bruker D8 Discover X-Ray Diffraction System (XRD) with a $\text{Cu K}\alpha_1$ radiation source. The set power rating of the X-ray generator was 40 kV and 40 mA. The 2θ range of the patterns varied between 5° and 90° with a step size of 0.01263° . The composition of the elements was determined by a Bruker S8 Tiger XRF spectrometer in standardless mode under helium atmosphere (a 4 kW, Rh anode X-ray tube was used to generate X-rays.). The powder samples were placed into an XRF sample cup (Mylar film with $2.5\ \mu\text{m}$ thickness, Chemplex Industries, Inc., Cat. No:106). The common impurities of this film are reported as Ca, P, Sb, Fe and Zn at ppm levels. The “Loose powder” method was preferred and performed with the “Best analysis” and “Oxides” options. To interpret the data, SpectraPlus Eval2 V2.2.454 was used.

3.4 Hydrophobicity

Hydrophobicity of the HMDS-treated aerogels was quantified by contact angle measurements based on direct imaging of water droplets deposited on the surface of the samples. Static contact angle measurements were performed on a Krüss G-10 goniometer, fitted with a high resolution digital camera (Spot Insight Color; Diagnostic Instruments, Inc.) at room temperature ($23 \pm 1\ ^\circ\text{C}$). For contact angle measurements, $10\ \mu\text{L}$ of deionized, triple distilled water was used. The images of water droplets on the aerogels were recorded and the contact angles were determined from those images by using MB-Ruler software. Wetting properties of the channel walls were also characterized by cutting the aerogel sample along the channel axis and dropping a water droplet directly on the channel surface.

3.5 Photochemical Reactions

The progress of light driven photochemical reactions in native silica aerogel-based microphotoreactors and photocatalytic reactions over titania was monitored

through absorbance-based quantification of concentration of the organic compounds using Nanodrop ND-2000C Spectrophotometer. Samples with a volume of 5 μL were collected at various times from the end of the channel by a micropipette and subsequently analyzed by Nanodrop ND-1000 Spectrophotometer for the concentration. The conversion of the compounds was calculated by Equation 3.6 and it was converted into a percent degradation by multiplying 100 which is given Equation 3.7.

$$\text{Conversion } (x) = \frac{C_{A_0} - C_A(t)}{C_{A_0}} \quad \text{Equation 3.6}$$

Here, C_{A_0} is the initial concentration of the compound and $C_A(t)$ is the concentration of the compound at time t .

$$\text{Degradation } (\%) = \frac{C_{A_0} - C_A(t)}{C_{A_0}} \times 100 \quad \text{Equation 3.7}$$

Chapter 4

TOTAL INTERNAL REFLECTION-BASED OPTOFLUIDIC WAVEGUIDES FABRICATED IN AEROGELS

4.1 Introduction

In this part of the study, liquid-core optofluidic waveguides based on total internal reflection of light were built in water-filled cylindrical microchannels fabricated in hydrophobic silica aerogels. Conditions for aerogel synthesis could be optimized to produce mechanically strong aerogel monoliths with the refractive index that is still sufficiently low for applications in optofluidic light guiding³⁷. Silica aerogels with densities ranging from 0.15 g/cm³ to 0.39 g/cm³ were produced by aging of alcogels in TEOS-based solution for various time periods, followed by supercritical extraction of the solvent from the alcogel network. Subsequently, the resulting hydrophilic aerogel samples were made hydrophobic by hexamethyldisilazane vapor treatment. The synthesized samples retained their low refractive index (below ~1.09) and, hence, they could serve as suitable optical cladding materials for aqueous waveguide cores (refractive index $n_{\text{core}} = 1.33$). Hydrophobic silica aerogel samples produced by the above technique also had low absorption coefficients in the visible part of the spectrum. Fabrication of microchannels in aerogel blocks by manual drilling preserving nanoporous and monolithic structure of aerogels was demonstrated for the first time. Long channels (up to ~7.5 cm) with varying geometries such as straight and inclined L-shaped channels could be fabricated. Multimode optofluidic waveguides prepared by filling the channels in the drilled aerogel monoliths with water yielded high numerical aperture values (~ 0.8). Efficient guiding of light by total internal reflection in the water-filled channels in aerogels was visually revealed and characterized by monitoring the channel output. The presented technique is expected to open up further possibilities for creating three-dimensional networks of liquid channels in aerogels for optofluidic applications.

4.2 Materials and Methods

4.2.1 Preparation of Silica Aerogel Monoliths

Silica aerogels were synthesized using a conventional two step sol–gel process and aged in TEOS-containing aging solutions as shown in Figure 4.1. TEOS (98% purity; AlfaAesar) was used as the silica precursor, hydrochloric acid (HCl) (37% purity; Riedel-de Haen) as the acid catalyst, and ammonium hydroxide (NH₄OH) (2.0 M in ethanol; Aldrich) as the base catalyst. TEOS, ethanol (99.9% purity; Merck), and water with a mass ratio of 1:0.89:0.26 were mixed together. After the addition of the acid catalyst, the solution was continuously stirred at room temperature for 60 min and transformed to a sol. Subsequently, the base catalyst was added to the sol to increase the rate of silanol condensation leading to gel formation. Before gelation, the solution was transferred into a polymethylmethacrylate (plexiglass) rectangular mold (height = 7 cm, length = 5 cm, width = 1.3 cm) or a cylindrical plastic mold with varying dimensions (diameter = 2.45 cm, height = 5 cm or diameter = 1.2 cm, height = 10 cm) tightly sealed to prevent evaporation of the solvent. After the gelation, the resulting alcogels were soaked in an aging solution (40 v/v % TEOS, 10 v/v % water, 50 v/v % ethanol) at 50 °C in an oven for 24 h. The samples were further kept in TEOS aging solution at room temperature for varying times ranging from one day to seven days to obtain aerogels with different densities. The alcogels were then washed in fresh ethanol for 3 days to remove any impurities and water remaining in the pores of the alcogels. Finally, the alcogels were dried at 40 °C and 100 bar with supercritical CO₂ (scCO₂) in Applied Separations Speed SFE unit for 6 h.

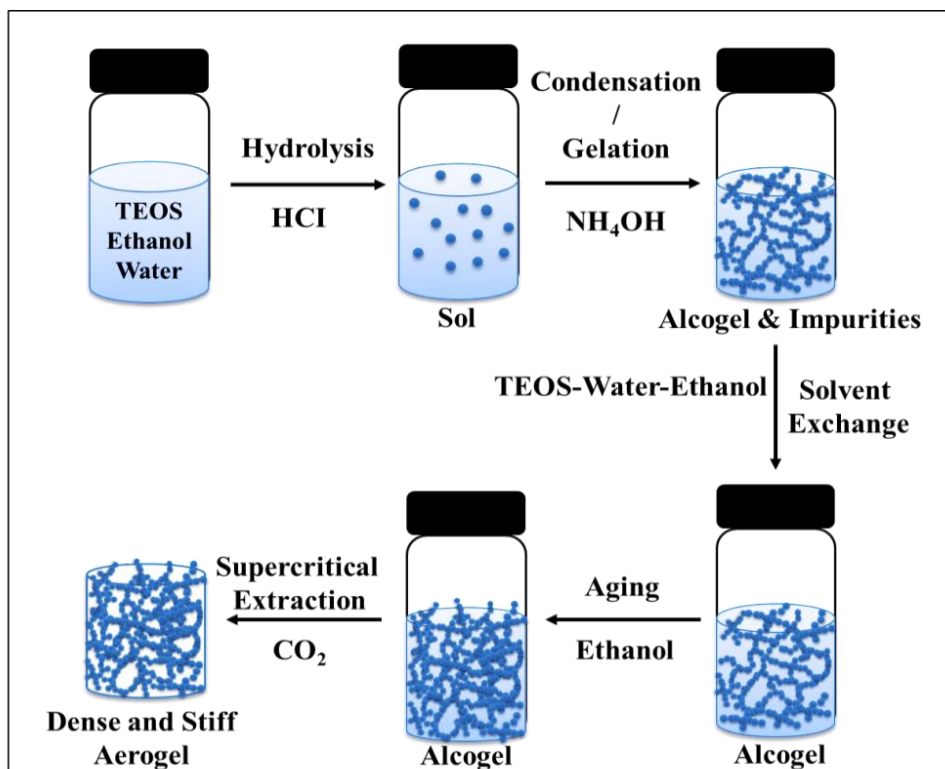


Figure 4.1. Preparation of monolithic silica aerogels by aging silica alcohols in TEOS solution

4.2.2 Surface Modification with HMDS

In order to render the aerogel surface hydrophobic, synthesized silica aerogel monoliths were treated with HMDS vapor in a tightly sealed beaker with a volume of 200 ml (Figure 4.2). A stainless-steel screen was put in the middle of the beaker where liquid HMDS was placed to prevent contact between the aerogel and liquid HMDS. 6 mL of HMDS was placed at the bottom of the vessel while the aerogel was placed on top of the screen. The beaker was then sealed and heated to 110 °C at ambient pressure. The aerogels were exposed to HMDS vapor for around 3 h. After the treatment, unreacted HMDS and reaction products of HMDS with surface hydroxyl groups were removed by evaporation by keeping the samples in the oven at 120 °C for 1 h. At the end of the process, monolithic, crack-free hydrophobic silica aerogels were obtained.

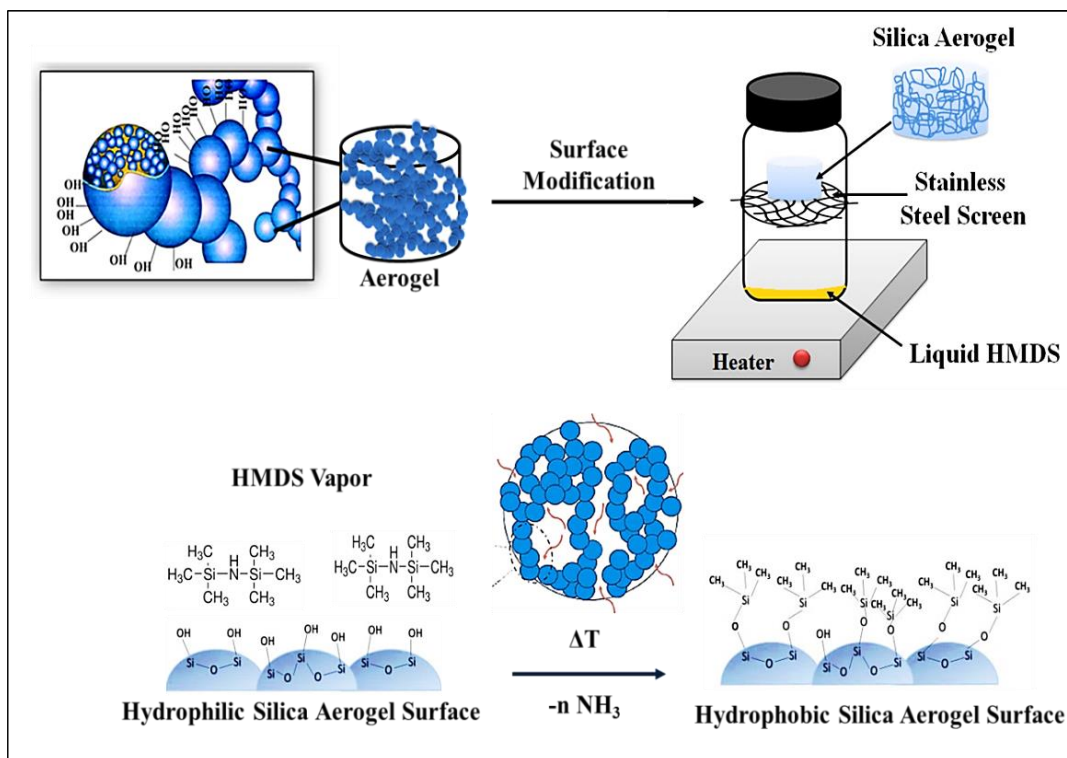


Figure 4.2. Silanization of silica aerogel surface by vapor-phase deposition of HMDS

4.2.3 Channel Formation in Aerogel Monoliths

Cylindrical microchannels were created in hydrophobic aerogel monoliths by manual drilling using a drill bit (diameter = 2.1 mm, length = 4 cm). Figure 4.3a. demonstrates how a straight channel was created within the aerogel block without cracking it and while preserving its monolithic structure. First, the sample was properly fixed. The hand-driven drill bit was then put perpendicularly to the aerogel surface and – while rotating continuously – moved slowly into the sample to prevent stress buildup. A straight channel with a diameter of ~2.1 mm was opened. An inclined L-shaped channel consisting of one horizontal channel intersecting with an inclined channel was also created as shown in Figure 4.3b. First, a straight horizontal channel was drilled parallel to the sample axis in the x direction, creating a hole in the lateral face of the monolith. Subsequently, another channel was delicately drilled starting from the top face of the monolith and proceeding at an angle with respect to the normal direction of the top aerogel face up to the end of the initially created straight horizontal channel. The side view of the resulting inclined L-shaped channel is depicted in Figure 4.3c.

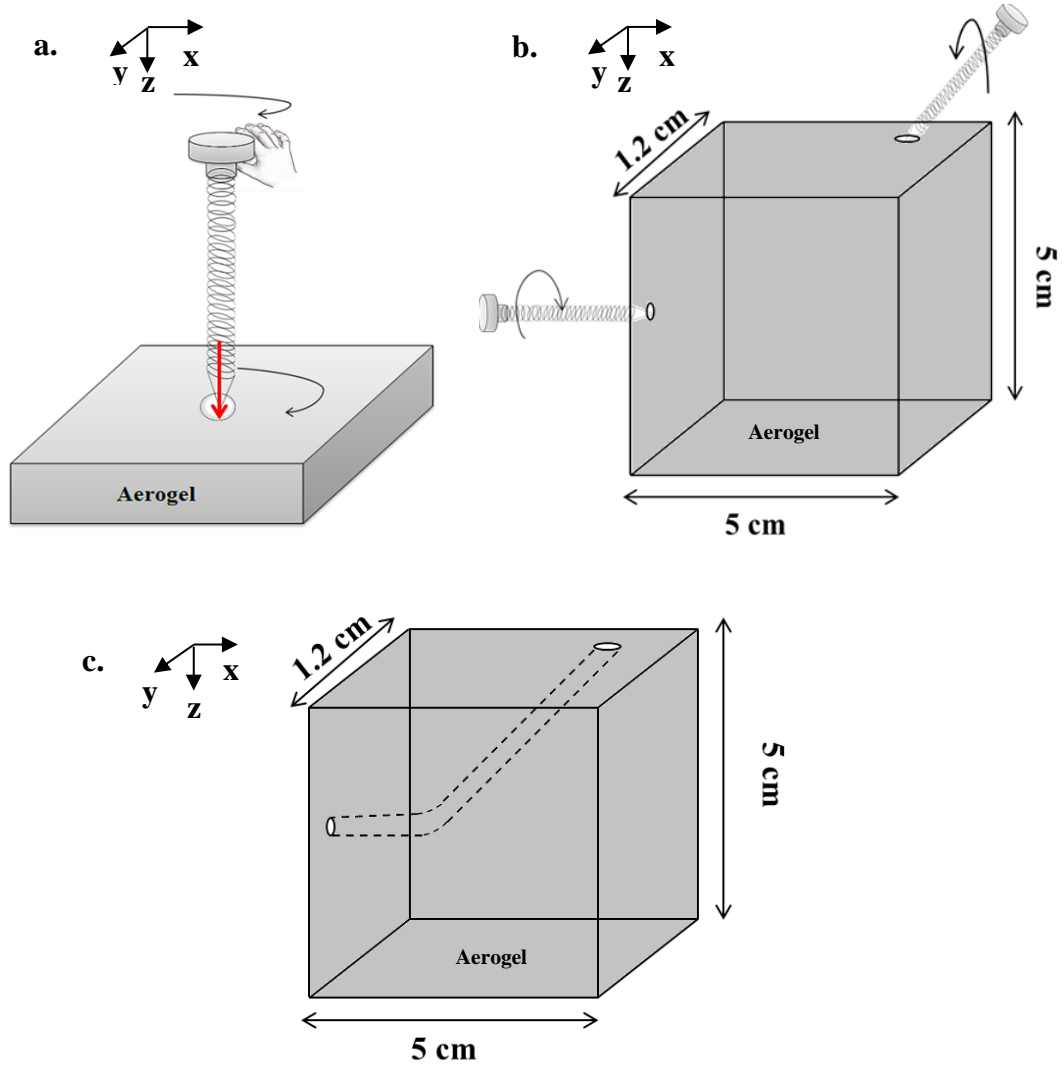


Figure 4.3. (a). Straight-channel formation in aerogel by manual drilling (b). L-shaped channel formation in aerogel by manual drilling (c). Side-view of inclined L-shaped channel in monolithic aerogel.

4.2.4 Refractive Index of Aerogels

The top-view of the experimental set-up used to measure of refractive index of aerogels using laser beam deflection is shown in Figure 4.4. A laser beam from a He-Ne laser source (wavelength 632.8 nm) was coupled to the lateral face of the aerogel sample. The laser source was placed at a fixed position and the sample stage was slowly rotated to change the angle of incidence, α , of the laser beam on the front surface of the aerogel monolith. The light beam incident from air was refracted at the interface and propagated into the aerogel at an angle θ (the angle of refraction) with respect to the surface normal. Since the front and rear surfaces of the aerogel monolith were parallel, θ was also equal to the angle of incidence on the rear surface of the aerogel. For θ values

smaller than the critical angle, θ_c , light was mostly refracted back into air at the rear surface of the aerogel block as shown in Figure 4.4a. As the sample was rotated counterclockwise, the angle of incidence on the rear surface of the aerogel block increased and eventually became equal to θ_c where the refracted ray emerges at 90° with respect to the rear surface normal as shown in Figure 4.4b. The refractive index of the aerogel (n) was then calculated for this configuration by using Equation 4.1 and the measured critical angle θ_c , assuming $n_{air} = 1$:

$$n = \frac{n_{air}}{\sin \theta_c} \quad \text{Equation 4.1}$$

When the sample was rotated slightly more in the counter-clockwise direction, the ray incident on the rear surface of the monolith was totally internally reflected back into the aerogel as shown in Figure 4.4c.

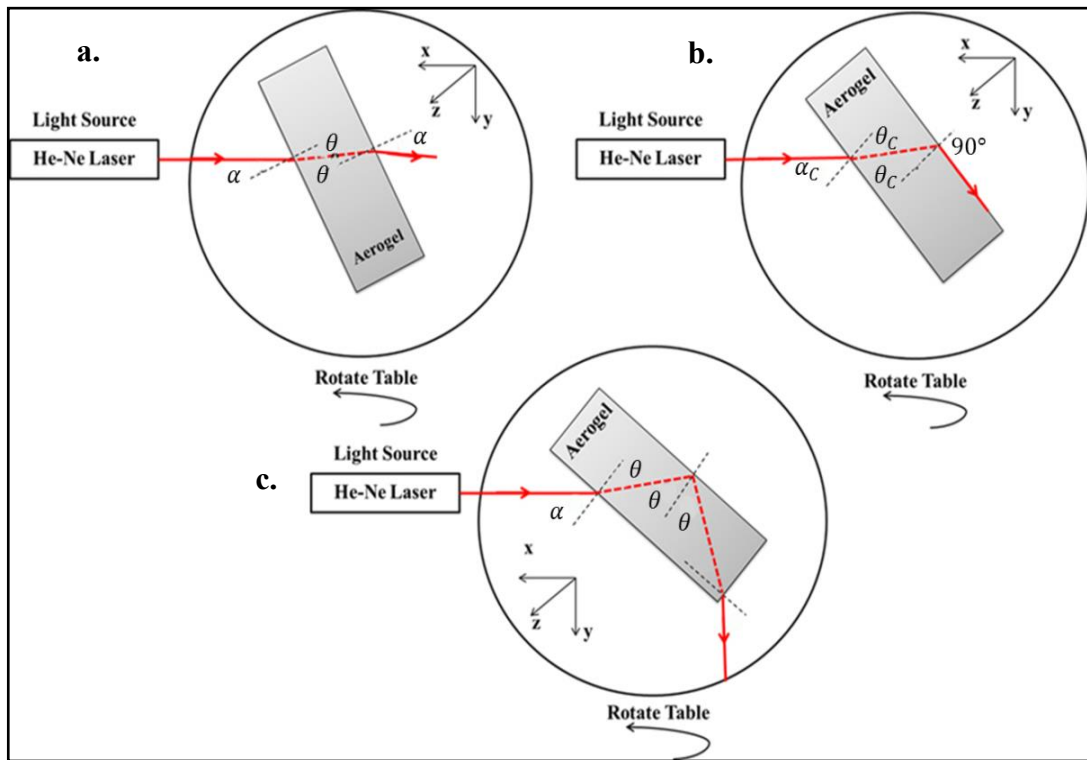


Figure 4.4. Top view of experimental set-up for the measurement of the refractive index of silica aerogels ³⁷. “Reproduced with permission from Özbakır *et al.*, Total Internal Reflection-Based Optofluidic Waveguides Fabricated In Aerogels; published by *J. Sol-Gel Sci. & Tech.*, 2017.”

4.2.5 Characterization of Optofluidic Waveguides

A schematic diagram of the experimental setup used for the characterization of liquid-core optofluidic waveguides fabricated in monolithic aerogels is given in Figure 4.5. A small piece of plastic tubing was glued to the input end of the channel drilled in the aerogel block by epoxy and the other end of the tubing was connected to a Union Tee adapter. Central port of the Union Tee was then connected to a syringe and the remaining end of the Union Tee was used to insert a solarization-resistant multimode optical fiber with a large core that served for coupling light into the channel. For the experiments, the aerogel was mounted in an adjustable metal holder. The channels formed in hydrophobic aerogels were filled with water by injection from the syringe. The microchannel was then illuminated by coupling a laser beam into the multimode optical fiber that subsequently delivered the light to the channel. The light at the operating wavelength of 488 nm from a frequency-doubled femtosecond-pulsed Ti:Sa solid-state laser source (Coherent Chameleon, maximum output power of 4 W at 800 nm) was coupled into the optical fiber with the aid of an objective lens. For the experiments, typical input power coupled into the optofluidic waveguide was 10 mW. The intensity of light transmitted through the waveguide was visually monitored and measured at the output end of the channel by a calibrated optical power meter.

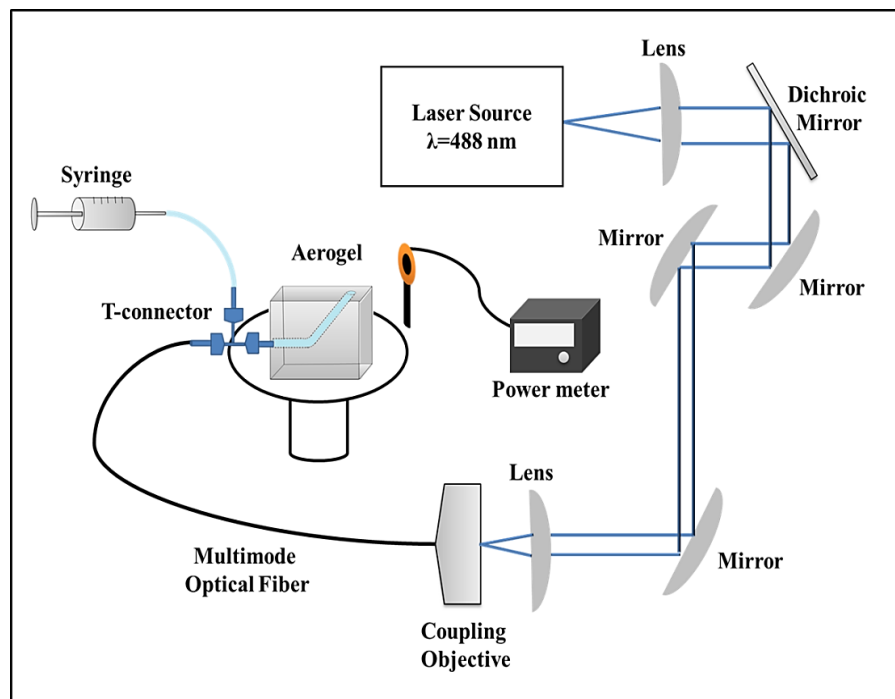


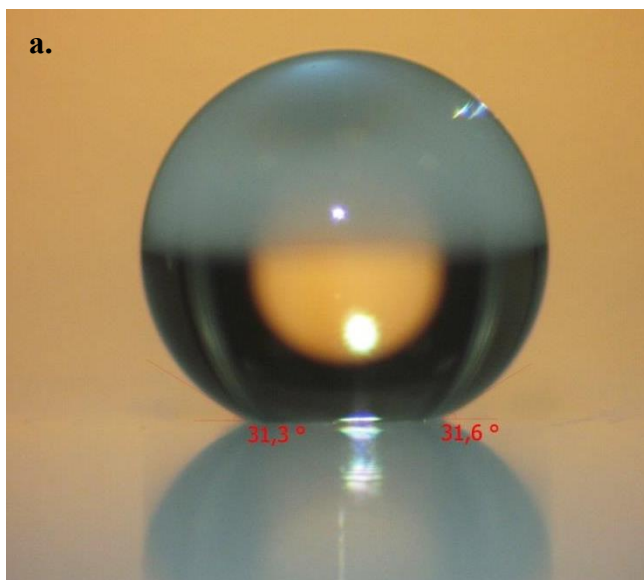
Figure 4.5. Schematics of the experimental setup used in the characterization of light guiding in liquid-core optofluidic waveguides.

4.3 Results And Discussion

4.3.1 Properties of Synthesized Aerogel Samples

The samples aged in TEOS-based solution for varying periods resulted in aerogels with different densities as shown in Table 4.1. The sample aged for one day had the lowest density of 0.15 g/cm^3 , the sample aged for two days had a density of 0.22 g/cm^3 and the density of the sample aged for seven days was 0.39 g/cm^3 . As the aging time increased, further condensation reactions took place and additional silica monomers from the aging solution were introduced to the already formed silica network and increased solid content in the network. These additional condensation reactions enhanced the mechanical strength and stiffness of the resulting aerogel.

After performing the silanization of surface silanol groups with HMDS vapor, hydrophobicity of the samples was determined by measuring water contact angle on the silanized aerogel surfaces. As shown in Figure 4.6a and Figure 4.6b, average contact angles on the aerogel surface were $148.0^\circ \pm 3.6^\circ$ (for aerogel density 0.15 g/cm^3) and $147.0^\circ \pm 1.8^\circ$ (for aerogel density 0.22 g/cm^3), indicating that the samples were quite hydrophobic. Furthermore, their hydrophobic nature was preserved during the experiments over several weeks as water did not penetrate into the aerogel pores and did not crack the samples in the course of time.



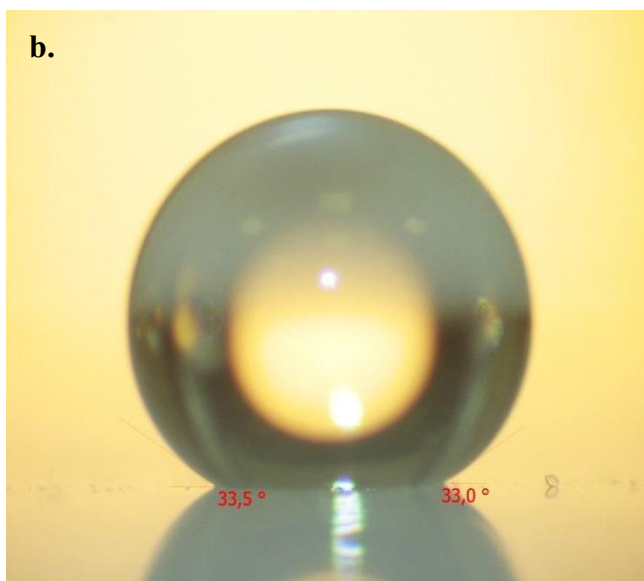


Figure 4.6. (a) Water droplet resting on the surface of hydrophobic silica aerogel, $\rho = 0.15 \text{ g/cm}^3$ (b) Water droplet resting on the surface of hydrophobic silica aerogel, $\rho = 0.22 \text{ g/cm}^3$.

Table 4.1. Properties of HMDS-treated aerogel samples of various densities

<i>Sample</i>	<i>Density (g/cm³)</i>	<i>Porosity (%)</i>	<i>Measured Refractive Index</i>	<i>Critical Angle (°)</i>	<i>Absorption Coefficient (cm⁻¹) at 488 nm</i>
1	0.15	93	1.023±0.004	77.7±1.1	0.52
2	0.22	90	1.060±0.007	70.7±1.0	0.69
3	0.39	82	1.093±0.001	66.2±0.1	0.87

Typical pore properties of the synthesized aerogels characterized by using nitrogen physisorption are tabulated in Table 4.2. As the sample density increased, BET surface area, BJH desorption average pore radius and total pore volume of the sample decreased. The pore volume, the surface area, and the average pore radius of the low-density sample (0.15 g/cm^3) were $3.6 \text{ cm}^3/\text{g}$, $662 \text{ m}^2/\text{g}$, and 11.1 nm , respectively. The sample with the highest density (0.39 g/cm^3) had a significantly lower pore volume and pore radius of $0.35 \text{ cm}^3/\text{g}$ and 1.4 nm , respectively.

Table 4.2. Pore characteristics of HMDS-treated aerogel samples of various density

<i>Sample</i>	<i>BET Surface Area (m^2/g)</i>	<i>BJH Desorption Average Pore Radius (nm)</i>	<i>Total Pore Volume (cm^3/g)</i>
Silica aerogel ($\rho=0.15\text{ g/cm}^3$)	662	11.1	3.61
Silica aerogel ($\rho=0.22\text{ g/cm}^3$)	549	7.5	2.48
Silica aerogel ($\rho=0.39\text{ g/cm}^3$)	467	1.4	0.35

The measured refractive indices of the samples at 632.8 nm are given in Table 4.1 and Figure 4.7. The refractive index of each sample was sufficiently lower than that of the core liquid water ($n_{H_2O} = 1.33$) making each one of them suitable for waveguide cladding. In agreement with the expected behavior, the refractive indices of the aerogel samples increased linearly with their density, as the optical density characterized by the index of refraction is directly proportional to the material density following the functional form of Equation 4.2, where k is a proportionality constant:

$$n = 1 + k\rho \quad \text{Equation 4.2}$$

Even the densest synthesized samples studied in ³⁷ retained a relatively low value of the refractive index (below ~ 1.09). Some of the alternative empirical correlations between the density and refractive index of aerogels proposed in the literature are summarized in Table 2.1 in Chapter 2 ⁷⁸.

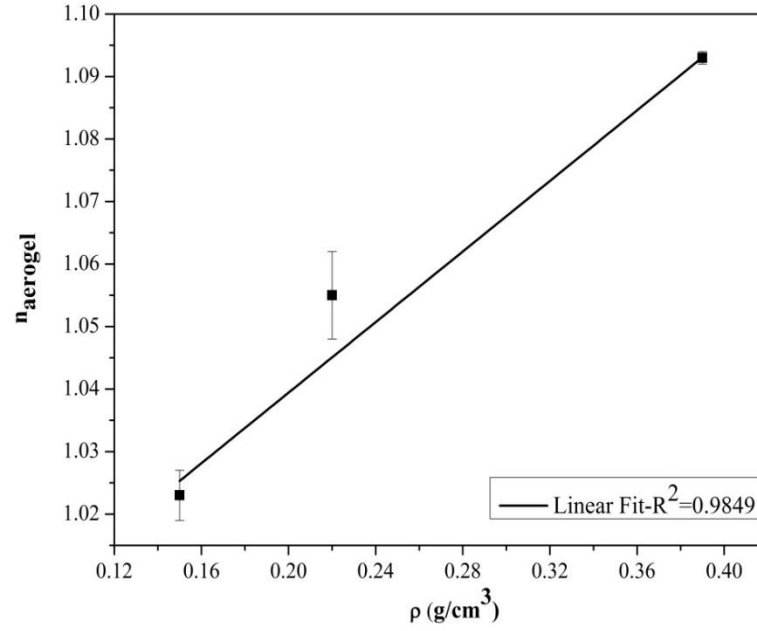


Figure 4.7. Refractive index of silica aerogels as a function of aerogel density. The proportionality constant between the refractive index and density is $k = (0.27 \pm 0.016) \text{ cm}^3/\text{g}$ ³⁷.

As a measure of their light-gathering ability, numerical apertures (NAs) of the optical waveguides in aerogels were determined using Equation 4.3 ³⁸:

$$NA = \sqrt{n_{\text{core}}^2 - n_{\text{cladding}}^2} \quad \text{Equation 4.3}$$

where n_{core} is the refractive index of the liquid in the microchannel and n_{cladding} is the refractive index of the cladding.

Water-filled multimode optofluidic waveguides in the synthesized aerogels yielded high numerical aperture values of 0.85, 0.81, and 0.76, ranking from the lowest to the highest aerogel density. In comparison, numerical aperture of doped silica fibers is typically around 0.37 and around 0.66 in Teflon-coated optical fibers ¹⁶⁰. Aerogel-based optofluidic waveguides with high numerical aperture collect light very efficiently when the light is coupled into the liquid core from a wide input angle and distribute light into a broad angle at the output.

Besides, absorption coefficients of the samples (α) were determined from the sample thickness (t) and absorbance (A) at the working wavelength (488 nm) using Equation 4.4 ¹⁶¹:

$$a = 2.303 \times A/t$$

Equation 4.4

Using the measured absorbance values at 488 nm from Figure 4.8 and thicknesses of individual samples 1-3 ($t_1 = 1.2$ cm, $t_2 = 1.2$ cm, $t_3 = 1.7$ cm), the values of the absorption coefficients were calculated as $\alpha_1 = 0.52$ cm⁻¹, $\alpha_2 = 0.69$ cm⁻¹ and $\alpha_3 = 0.87$ cm⁻¹, respectively. These values are still relatively low compared to the common cladding materials such as polytetrafluoroethylene (PTFE) ¹⁶²⁻¹⁶³. For instance, transmission spectrum of a PTFE film with a thickness of 0.1 mm and a refractive index of 1.4 indicates that transmission of Teflon is lower than 10 % at 488 nm which results in the absorbance around 1 and the absorption coefficient of the film about 230 cm⁻¹ ¹⁶³. Thus, even the highest density aerogel samples have a lower absorption coefficient than PTFE. Furthermore, it was found that the diffuse transmittance and the total transmittance at 488 nm increased with decreasing density of the samples as shown in Figure 4.9.

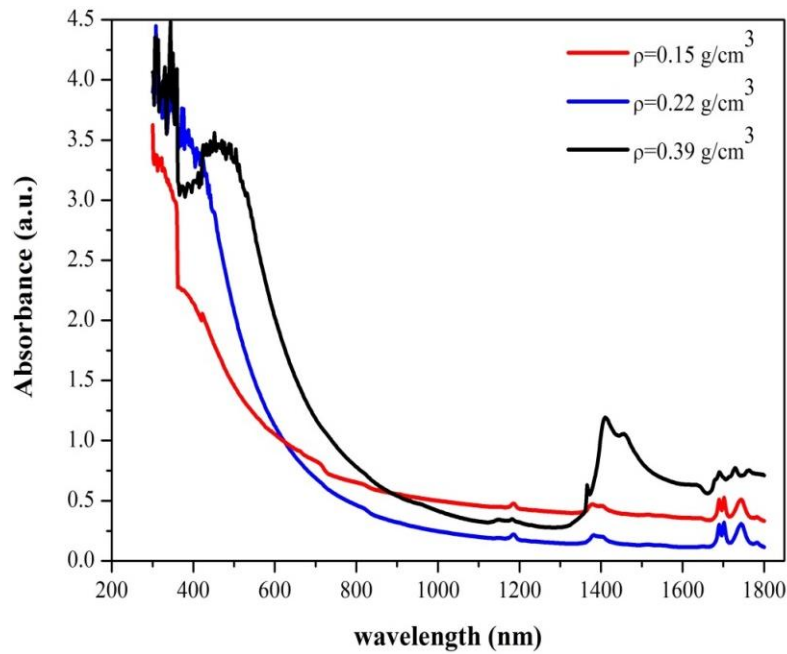


Figure 4.8. Absorption spectra of synthesized aerogel samples of various densities.

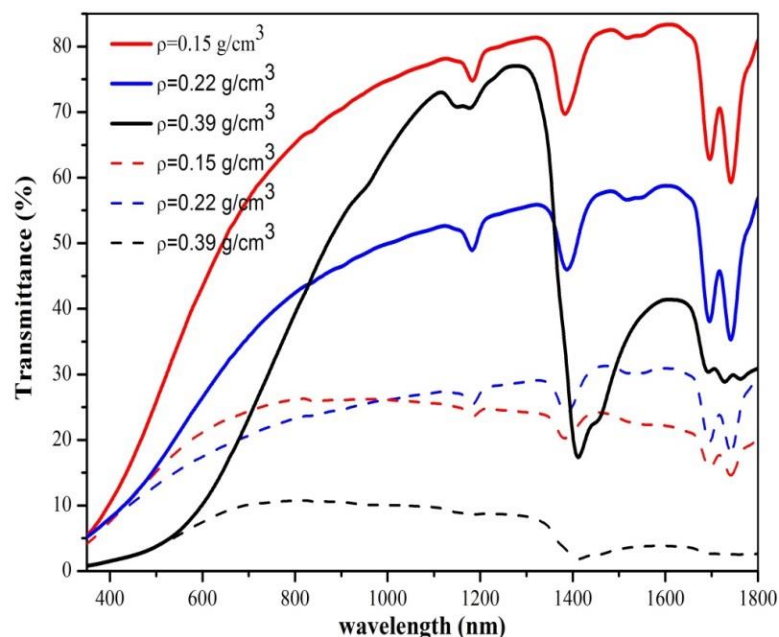


Figure 4.9. Total transmittance spectrum (solid lines) and diffuse transmittance spectrum (dashed lines) of synthesized aerogel samples of various densities in the spectral range between 350 nm-1800 nm.

The Haze of the samples which was quantified by using Equation 2.3 is provided in Figure 4.10. The results point out that the haze of aerogels increased with increasing density aerogels. The sample with the lowest density of 0.15 g/cm³ suggest that a large fraction of the transmitted light is scattered (diffused) in the UV region of the spectra, lowering the transmission and causing the sample to be translucent milky and, it started to decrease beyond this region in the visible region from 400 nm up to NIR, 1200 nm. The sample with the density of 0.22 g/cm³ demonstrated the similar trend. The haze of the sample is the highest in UV region up to around 400 nm and it decreases beyond this region up to 1200 nm. In the sample with the highest density, almost all of the transmitted light is found to be scattered up to around 500 nm of the spectra in the samples with the highest density, resulting in the sample to be opaque and beyond this region up to 1200 nm it starts to decrease and demonstrating the lowest haze among the samples.

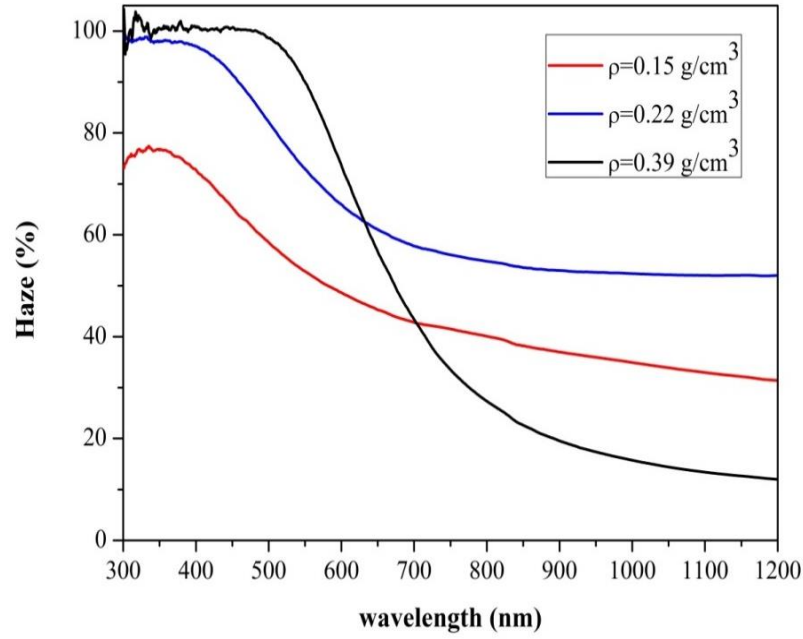
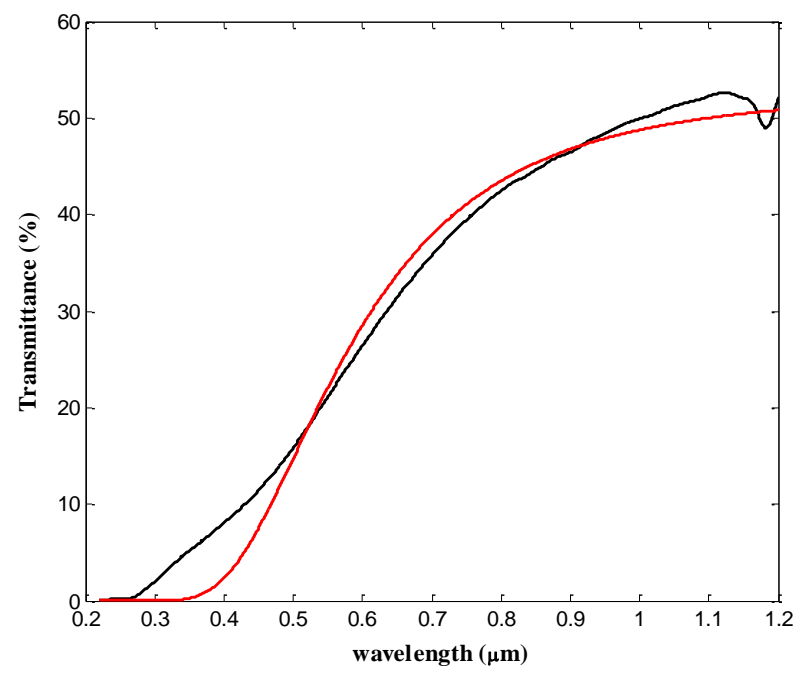
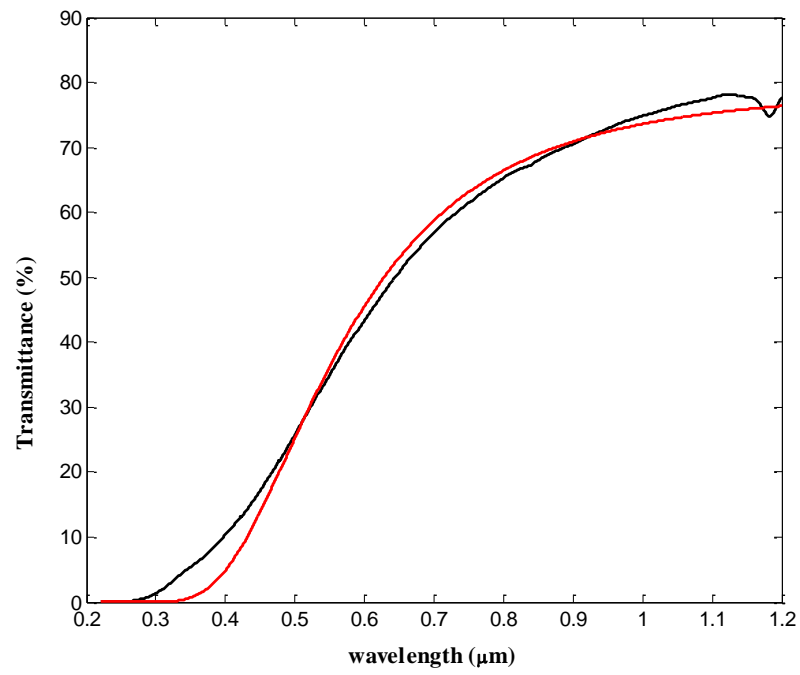


Figure 4.10. Haze (%) measurement of aerogel samples

Exponential regression model based on Hunt formula in Equation 2.2 applied to the measured transmittance spectra of aerogels for the range from 220 nm to 1200 nm, which are given in Figure 4.11 provided A and C values for the samples. The similar behavior of the haze of aerogels was obtained in the clarity coefficient. As shown in Table 4.3, the clarity coefficient increased with increasing density of aerogels. The aerogel with the highest density showed the highest value of C and the aerogel with the lowest density demonstrated the lowest value. However, A was obtained to be the lowest in the sample with the density of 0.22 g/cm^3 , and the highest with the sample with the density of 0.39 g/cm^3 for the range from 220 nm to 1200 nm.



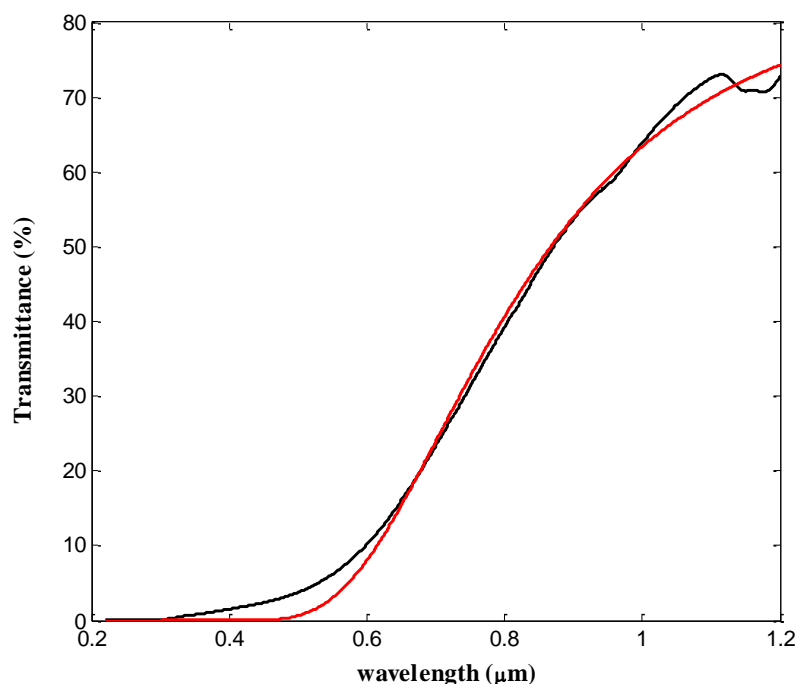


Figure 4.11. Transmittance spectra of silica aerogels in the spectral range between 220 nm-1220 nm. (a) Transmittance spectra of the silica aerogel with a density of 0.15 g/cm³. (b) Transmittance spectra of the silica aerogel with a density of 0.22 g/cm³. (c) Transmittance spectra of the silica aerogel with a density of 0.39 g/cm³.

Table 4.3. Hunt parameters for the silica aerogels.

<i>Sample</i>	<i>A</i>	<i>C</i> ($\mu\text{m}^4/\text{cm}$)
Silica aerogel ($\rho=0.15 \text{ g/cm}^3$)	0.79	0.059
Silica aerogel ($\rho=0.22 \text{ g/cm}^3$)	0.53	0.066
Silica aerogel ($\rho=0.39 \text{ g/cm}^3$)	0.86	0.18

4.3.2 Channel Formation in Aerogel Blocks

Images of channels created in hydrophobic aerogel blocks by manual drilling are shown in Figure 4.12a-d. Relatively long channels (~7.5 cm) could be created with varying geometries such as straight and L-shaped inclined channels, while maintaining the nanoporous and monolithic structure of the aerogels blocks.

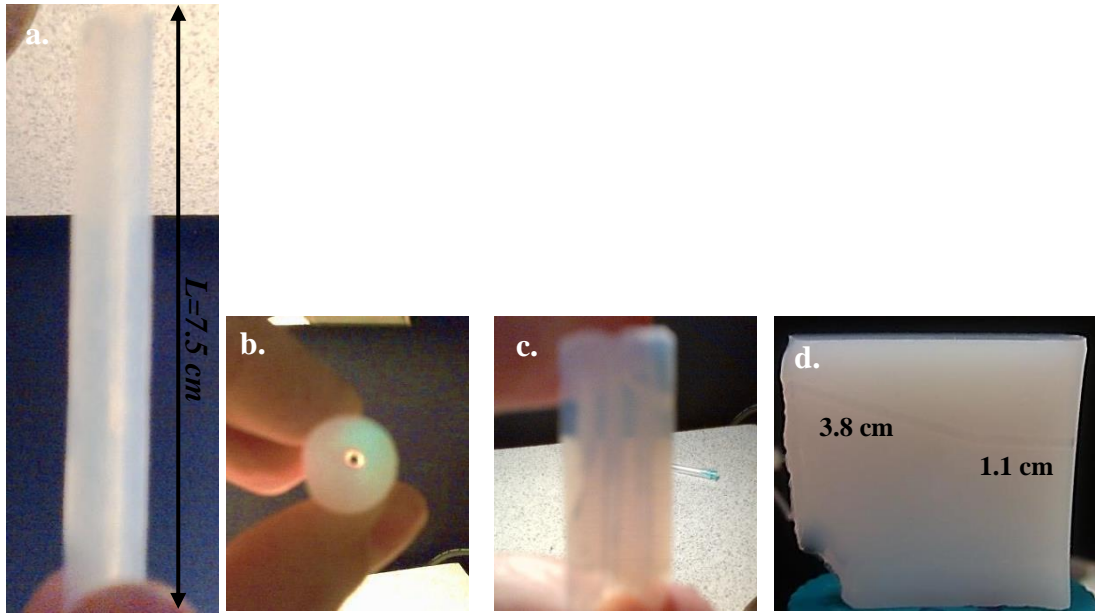


Figure 4.12 **a.** Side view of a hydrophobic silica aerogel rod with a channel parallel to the rod axis (channel length $L = 7.5$ cm, channel diameter $D = 2.1$ mm) **b.** Top-view of the aerogel rod shown in (a) with a channel parallel to the rod axis **c.** Silica aerogel sample with multiple channels **d.** Side view of a L-shaped channel with one horizontal and one inclined channel (channel lengths $L_1 = 1.2$ cm and $L_2 = 3.8$ cm, respectively; channel diameters $D_1 = D_2 = 2.1$ mm).

4.3.3 Light-guiding in liquid-core optofluidic waveguides in aerogels

Following the successful microchannel formation inside the aerogel blocks, multimode optofluidic waveguides were generated by filling the channels with water as the core liquid. The channel was filled with water by using a syringe as described in Section 4.5. Water could be confined within the channels with hydrophobic walls without penetrating the porous network of the aerogel.

Laser light with the wavelength of 488 nm was coupled into the optical waveguide in the aerogel ($\rho = 0.15$ g/cm³) with the aid of the optical fiber, as shown schematically in Figure 4.5. As the light propagates inside the channel, some of the propagating light rays which strike the boundary between water and the aerogel at an angle greater than the critical angle are reflected back to the opposite wall of the channel (Figure 4.13 and Figure 4.14b). As illustrated in the photograph of the channel with coupled light shown in Figure 4.13, the light was totally internally reflected in the channel several times after emerging from the input fiber, before leaving the waveguide.

Consecutive reflections appear more faintly as the light intensity decreases during the propagation through light scattering and absorbance by the aerogel.

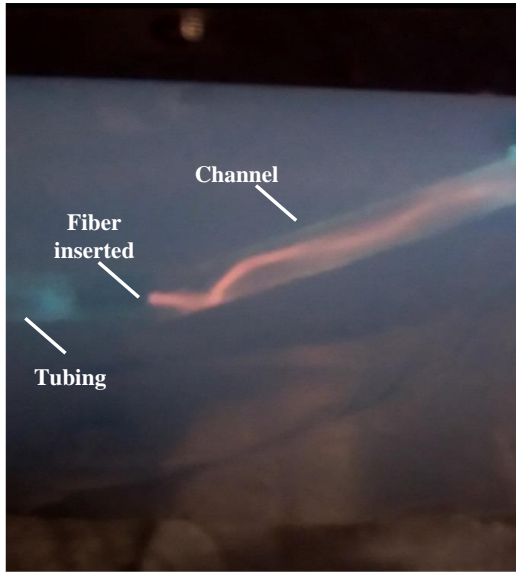


Figure 4.13. Total internal reflection in the water-filled channel in a monolithic aerogel ($\rho = 0.15 \text{ g/cm}^3$)

The expected number and spacing of subsequent reflections of a ray from the channel walls during the light propagation was also estimated using Snell's Law with the output half-angle α of the optical fiber immersed in water calculated from the numerical aperture of the fiber. Figure 4.14a illustrates light transmission through an optical fiber inserted into water. Because the numerical aperture of the fiber is preserved regardless of the medium outside the fiber, angle α can be determined from $NA = n_{\text{water}} \sin \alpha$ where NA is the numerical aperture of the fiber ($NA = 0.22$)¹⁶⁴ and $n_{\text{water}} = 1.33$. Inserting these values then gives $\alpha = 9.5^\circ$. From Figure 4.14b, the angle β at which the light is reflected from the microchannel wall back into water can be calculated as $\beta = 90^\circ - \alpha = 80.5^\circ$. From the geometry of the configuration (channel diameter $D = 2.1 \text{ mm}$, fiber core diameter $d = 0.3 \text{ mm}$), the light exiting the fiber propagates over a lateral distance $\Delta = (D - d)/2 = 0.9 \text{ mm}$ before the first incidence on the channel wall. This corresponds to the distance x between the fiber tip and the point where the wave first strikes the channel wall equal to $x = \Delta \tan \beta = 5.4 \text{ mm}$. The distance in the axial direction over which the light propagates between successive reflections is then $2x = 10.8 \text{ mm}$. For a channel with the length of 27 mm , it was found that a ray of light can do about three total internal reflections at most, neglecting intensity loss. As demonstrated in Figure 4.13, this is in agreement with experimental observation.

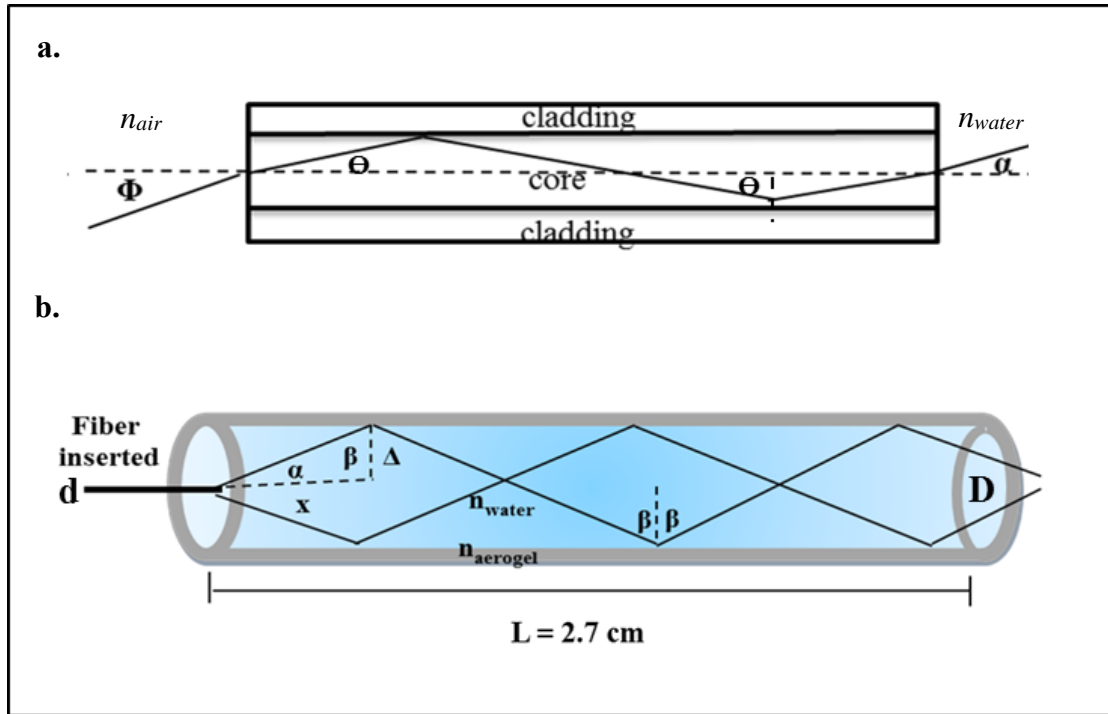


Figure 4.14. (a). Light propagation through an optical fiber inserted into a water-filled channel in aerogel. A ray with the maximum acceptance half-angle of the fiber in air (ϕ) is coupled into the fiber and subsequently propagates along the fiber and emerges with angle (α) into water. (b) Total internal reflection in the microchannel. d is the diameter of the fiber core (0.3 mm), D is the diameter of the microchannel (2.1 mm).

The same phenomena could also be observed with inclined L-shaped waveguides fabricated in denser aerogel samples (see Figure 4.12d). In the experiments, the laser light was coupled into the horizontal part of the channel and the transmitted light was collected from the open end of the inclined part of the channel. When the light was coupled into an empty channel, no guiding of light to the opposite end of the channel was observed; instead, the light was scattered strongly from the junction of the two sections of the channel (see Figure 4.15a). Upon filling the channel with water, situation changed dramatically and the waveguides became fully operational. As shown in Figure 4.15b, for water-filled channel, the light was guided along the channel and delivered to the opposite end of the channel (seen at the top of the aerogel block). A side-view image of water filled channel with light coupling in Figure 4.15b. demonstrates that the entire length of the channel is filled with light with a bright spot on the top which indicates that the light is transmitted along the liquid-core optofluidic waveguide. Because of the opacity of dense aerogels, straight path of the light through

the aerogel is not well visible; however, scattering of light beam at the edges of the channel can be clearly observed.

Overall losses of water-filled L-shaped waveguides were quantified by measuring the power of the transmitted light using a power meter. At the wavelength of 488 nm, output power of 2.1 mW was measured when the laser light was coupled with an incident power of 8.0 mW from the fiber output. The overall optical throughput of the optical waveguide could be quantified by Equation 2.9 and the propagation loss of the waveguide, η , could be calculated as -1.45 dB/cm by Equation 2.10. This value compares favorably to the previously measured propagation loss of -9.9 dB/cm for liquid-core optofluidic waveguide prepared using laser ablation in silica aerogels³⁸.

The loss in power is primarily due to the light scattering at the junction of the two channel sections since the vertical part of the channel is inclined with an angle of 62 ° and most of the rays possibly strike the channel surface with the incident angle smaller than the critical angle (71.4 °). They are therefore partially reflected or transmitted in many different directions, leaving a bright spot clearly visible at the channel junction (see Figure 4.15b). If the inclined channel is formed with a moderate angle around 20°, light-guiding efficiency can possibly be improved. Furthermore, light intensity also decreases during subsequent reflections at the channel walls due to the surface roughness. Absorption loss by water at 488 nm is low and it transmits within water with 0.05 % incident light attenuation for 1 cm length¹⁶⁵. Thus, the use of water as the core liquid does not represent the main limitation on the performance of our optofluidic waveguides.

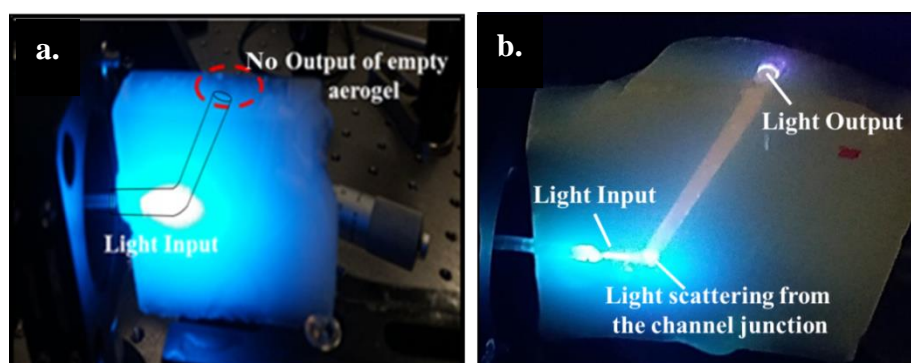


Figure 4.15. (a) Light coupling into an empty channel in the aerogel (b) Light propagation in liquid-filled channel within the aerogel monolith (side view).

4.4 Conclusions

Multimode liquid-core optofluidic waveguides based on total internal reflection of light in water-filled microchannels located within high-density hydrophobic silica aerogels were fabricated by direct mechanical drilling. The synthesized aerogel samples with high densities had still sufficiently low refractive indices and absorption coefficient values, exhibiting ideal optical cladding material properties for efficient guiding of light by total internal reflection over a wide range of wavelengths without the use of any additional optical coatings. Relatively long channels of various shapes (straight and inclined L-shape) were created preserving the nanoporous and monolithic structure of the aerogel. Water-filled multimode optofluidic waveguides in the synthesized aerogels provided high numerical aperture values making them ideal for applications involving aqueous liquid cores. Efficient wave-guiding upon light coupling (at 488 nm) into the water-filled channel and channel output could be demonstrated. The total internal reflection phenomena within the water-filled channel in the hydrophobic aerogel as a multimode core waveguide could also be visually revealed. Therefore, the demonstrated fabrication technique could enable the use of aerogel-based optofluidic waveguides for innovative applications including photochemical reactions as well as light-driven detection, identification, and quantification of particular chemical compounds and metabolic variables with the aid of improved light distribution through the reaction space represented by the waveguide core.

Chapter 5

A NEW TYPE OF MICROPHOTOREACTOR WITH INTEGRATED OPTOFLUIDIC WAVEGUIDE BASED ON SOLID-AIR NANOPOROUS AEROGELS

5.1 Introduction

In this study, we developed a new type of microphotoreactor based on an optofluidic waveguide with aqueous liquid core fabricated inside a nanoporous aerogel. This optofluidic microphotoreactor consists of a single liquid-filled channel fabricated inside a monolithic silica aerogel within which photochemical reactions are carried out. Due to the contrast of refractive indices between the aerogel and the liquid, optofluidic waveguides based on TIR are naturally formed to deliver the light to the liquid reaction medium inside the microchannel, as shown schematically in Figure 5.1. To this end, we synthesized a hydrophobic silica aerogel monolith with a density of 0.22 g/cm^3 and a low refractive index of 1.06 that – from the optical point of view - effectively behaves like solid air. Subsequently, we drilled an L-shaped channel within the monolith that efficiently confined both the aqueous core liquid and the guided light, the latter property arising due to total internal reflection of light from the liquid-aerogel interface. The efficiency of light guiding in a liquid-filled channel was characterized and – using the light delivered by waveguiding – photochemical reactions in a channel filled with aqueous solutions of methylene blue dye were carried out. It was demonstrated that this configuration provides an excellent overlap between guided light and fluids in the channel for efficient photochemical activation and methylene blue could be efficiently degraded in the optofluidic photoreactor, with conversion increasing with increasing power of the incident light.

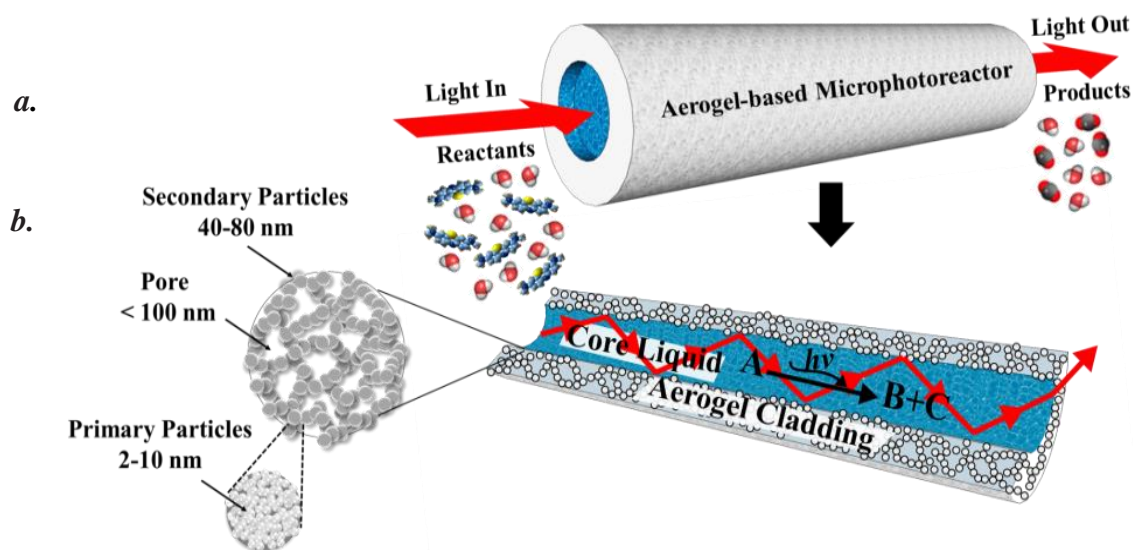


Figure 5.1. (a) Aerogel-based microphotoreactor with an integrated optofluidic waveguide (b) Cross-sectional view of the microphotoreactor/waveguide system illustrating light guiding in the liquid by TIR.

5.2 Materials and Methods

5.2.1 Materials

TEOS (98%), ethanol ($\geq 98\%$) and NH_4OH (2.0 M in ethanol) were purchased from Sigma Aldrich. HCl (37% purity) was obtained from Riedel-de Haen and HMDS ($\geq 98\%$) was purchased from Merck. Carbon dioxide (99.998 %) was purchased from Messer Aligaz. All chemicals were used as received.

5.2.2 Synthesis of Silica Aerogels

Silica aerogels were prepared by the way described in our recent study³⁷. TEOS was used as the silica precursor and it was initially hydrolyzed with water in the presence of ethanol as co-solvent and HCl as acid catalyst. After the addition of the acid catalyst, the solution was continuously stirred at room temperature for 1 h. Subsequently, NH_4OH was added to the solution as the base catalyst. The molar ratio of TEOS:ethanol:water:HCl: NH_4OH was 1:4:3:0.0023:0.009. Before gelation, the solution was transferred into rectangular polymethylmethacrylate (plexiglass) molds (height = 7 cm, length = 5 cm, width = 1.3 cm) tightly sealed to prevent evaporation of the solvent. After the gelation, the resulting alcogels were soaked in an aging solution (40 v/v %

TEOS, 10 v/v % water, 50 v/v % ethanol) in an oven at 50 °C for 24 h. The samples were further kept in the same aging solution at room temperature for 3 days. The alcogels were then placed in fresh ethanol for 3 days to remove any impurities and water remaining in their pores. As the last step, the alcogels were dried at 40 °C and 100 bar with supercritical CO₂ (scCO₂) in an Applied Separations Speed SFE unit for 6 h and monolithic and crack-free aerogels were obtained. The resulting silica aerogels were hydrophilic due to the presence of the polar hydroxyl groups within their porous framework which promote high capillary stress and water adsorption once they are in contact with water. Therefore, the aerogel samples were made hydrophobic by replacing the hydrophilic hydroxyl surface groups with hydrophobic methyl groups via HMDS vapor treatment. Monolithic and crack-free hydrophobic silica aerogel was obtained. The hydrophobicity of the samples was determined by measuring water contact angle of the aerogel surface³⁷.

5.2.3 Characterization of Silica Aerogels

Average pore size, pore size distribution and surface area of the samples were determined using nitrogen physisorption (Micromeritics ASAP 2020). Samples were initially degassed at 300 °C under vacuum for 1 day to remove remaining impurities from the surface. The pore analysis was performed using N₂ adsorption/desorption isotherms with a relative pressure (P/P_0) ranging from 10^{-7} to 0.999. The surface area of the samples was determined by Brunauer-Emmett-Teller (BET) method and the pore volume and pore size distributions were determined by Barrett-Joyner-Halenda (BJH) analysis using the N₂ adsorption-desorption isotherms. Total pore volume of the sample was determined by converting the adsorbed N₂ volume at STP to liquid N₂ volume at 77 K. Bulk density of monolithic aerogel samples was determined by dividing their mass by their final volume which was obtained by measuring their physical dimensions using a caliper. Hydrophobicity of HMDS-treated aerogels was quantified by contact angle measurements based on direct imaging of water droplets deposited on the surface of the sample. Static contact angle measurements were carried out on a Krüss G-10 goniometer, fitted with a high resolution digital camera (Spot Insight Color, by Diagnostic Instruments, Inc.) at room temperature (23 ± 1 °C). 10 µL of deionized, triple distilled water was used in the contact angle measurements. In addition, wetting

properties of the internal channel walls were characterized by cutting the aerogel sample along its channel and dropping a water droplet directly on the inner channel surface. Fourier transform infrared spectroscopy-attenuated total reflectance (FTIR-ATR) spectra of hydrophilic and hydrophobic aerogel samples were recorded on a Thermo Scientific Smart iTR spectrometer to investigate the chemical composition of the samples. Refractive index of the aerogel monoliths was determined by measuring the angle of refraction of a laser beam from the aerogel block placed on a goniometer stage as described in our recent study ⁴⁰.

5.2.4 Fabrication of Channels in Aerogel Monoliths

The technique demonstrated in our recent study was utilized for the channel fabrication ³⁷. Cylindrical channels were fabricated in hydrophobic aerogel monoliths by using a drill bit (diameter = 2.1 mm, length = 4 cm). An inclined L-shaped channel consisting of a horizontal channel intersecting with an inclined channel was formed by two successive steps. First, a straight channel with a length of 1.1 cm and a diameter of ~2.1 mm was opened from one of the two narrow side faces of the aerogel block. Next, another channel of ~2.1 mm diameter and 3.7 cm length was delicately drilled starting from the opposite side face of the block with an angle of about 30° with respect to the horizontal, up to the end of the initially created straight channel. The side view of the resulting inclined channel is provided in Figure 5.2.

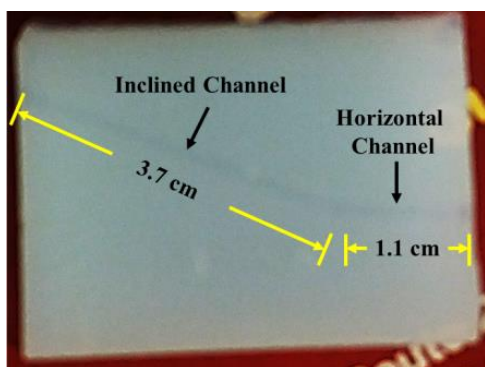


Figure 5.2. A side-view of an aerogel monolith with the fabricated inclined L-shaped channel

5.2.5 Experimental Setup for Carrying Out Photochemical Reactions

Figure 5.3 shows a schematic diagram of the experimental setup that was employed for studying model photochemical reaction - degradation of methylene blue in an aqueous solution contained inside the microchannel within a hydrophobic silica aerogel. Hydrophobic aerogel block with the inclined L-shaped channel was mounted on an adjustable metal holder. A small piece of plastic tubing was glued to one end of the channel by epoxy and the other end of the tubing was connected to a Union Tee adapter. Central port of the Union Tee was then connected to a syringe and the remaining end of the Union Tee was used to insert a solarization-resistant multimode optical fiber (Thorlabs; UM22-300, NA=0.22) into the aerogel channel. This fiber served for delivering photoactivation light to the reaction volume and its end was held at a fixed position at the channel entrance. The channel was filled with the aqueous MB solution using the syringe. The MB solution could be confined within the channel without penetrating into its porous network due to hydrophobic walls of the channel. In order to initiate light-induced degradation of MB, we used a laser beam from a femtosecond-pulsed, tunable laser light source (Coherent Chameleon Ti:Sapphire Laser) with a maximal output power of 4 W. The laser beam was coupled into the free end of the multimode optical fiber with the aid of an objective lens. The operating wavelength of the laser was tuned to 388 nm. The input power coupled into the optofluidic waveguide could be adjusted from the laser source. The incident power values were measured before coupling the light into the optical fiber. Due to losses introduced by the beam focusing optics and imperfect coupling of light into the fiber, about 20 % of the incident power actually reached the sample. The intensity of light transmitted through the waveguide was visually monitored and measured at the outlet of the channel by a laser power meter. In order to monitor the progress of photodegradation of MB, samples with a volume of 10 μ L were collected at various times from the end of the channel by a micropipette and subsequently analyzed by Nanodrop ND-1000 Spectrophotometer for absorbance-based quantification of MB concentration which was converted to the concentration using a calibration curve provided in Figure 5.4.

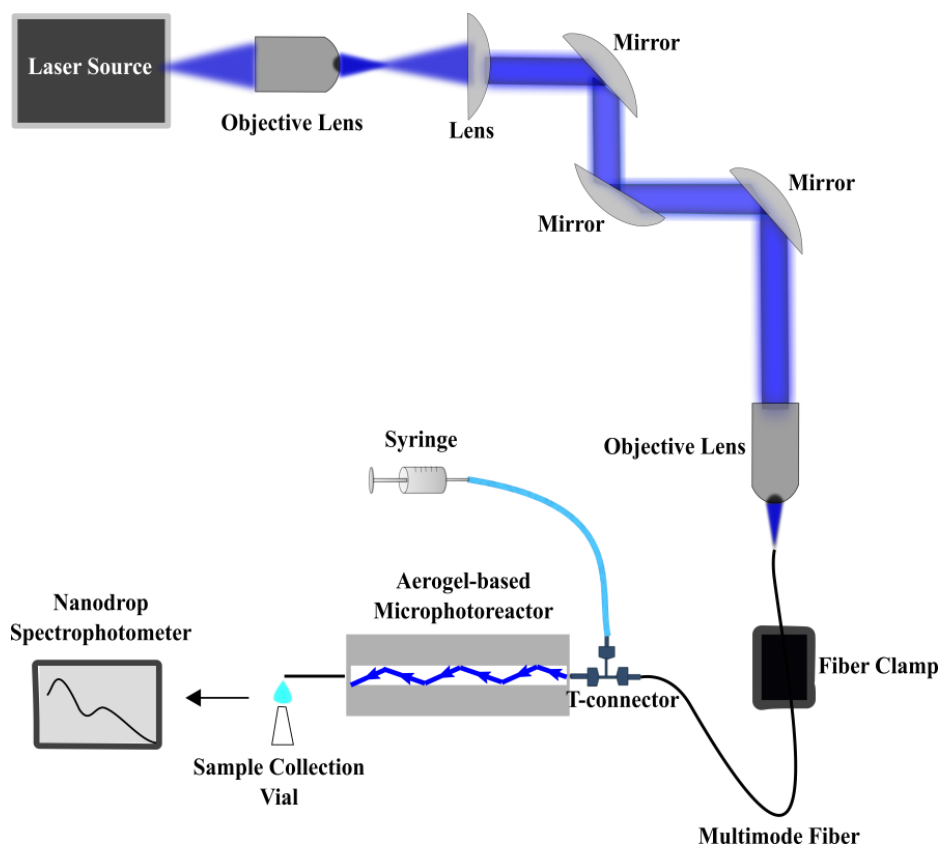


Figure 5.3. Schematics of experimental set-up used in the characterization of light guiding and photochemical reactions in aerogel-based optofluidic microphotoreactors.

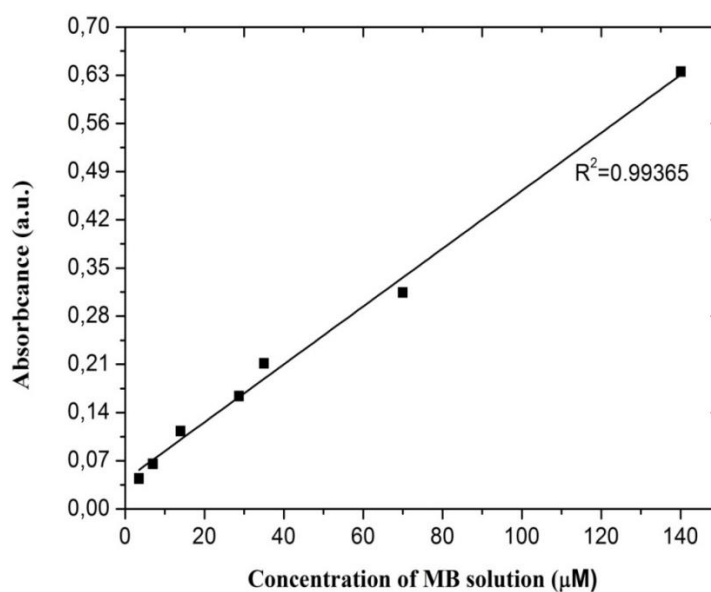


Figure 5.4. Calibration curve of aqueous MB solutions used for quantification of sample concentration in 2-140 μM range.

5.3 Results and Discussion

5.3.1 Properties of Synthesized Aerogel Samples

Synthesis of aerogel monoliths with high mechanical strength and sufficiently low refractive index is a critical step for fabricating our photoreactors^{36, 40}. This was accomplished by aging of intermediate alcogels in a solution containing the silica precursor (see “Materials and Methods” for additional details on the procedure). Reactions between partially hydrolyzed tetraethylorthosilicate (TEOS) in the aging solution and silanol groups on the silica surface resulted in the formation of additional siloxane bonds and increased the solid content of the porous aerogel. These additional condensation reactions enhanced the mechanical strength and stiffness of the aerogel, most likely by increasing the size of the connecting silica necks within the solid network. After aging, the resulting sample had a density of 0.22 g/cm³. The critical angle of incidence for a laser beam incident upon the aerogel – air interface from the aerogel side was measured to be 71 ° which translated into the aerogel refractive index of 1.06 at 632.8 nm, much lower than the refractive index of an aqueous solution. Therefore, the silica aerogel sample with a density higher than the silica aerogel prepared using the conventional two-step sol-gel method without any additional aging is still suitable for TIR-based optofluidic waveguides without the use of any additional optical coatings.

The reaction of surface silanol groups with HMDS vapor resulted in monoliths impermeable for aqueous reaction solutions. As shown in Figure 5.4, average contact angles were found to be greater than 150°, showing that the samples are, in fact, superhydrophobic. Furthermore, their superhydrophobic nature was preserved during the experiments over several weeks, as water did not penetrate into the aerogel pores and did not crack the aerogel blocks in the course of the experiments. In addition to the contact angle measurements, both treated and untreated samples were studied by infrared spectroscopy to investigate their chemical composition. FTIR-ATR measurement of aerogel monoliths was carried out for the samples that we crushed into powder. For the spectrum of the channel surface fabricated in an aerogel monolith, the channel was broken along its axial direction and the surface of the channel walls were gently ground by the aid of a spatula tip. Then, FTIR-ATR measurement was performed

for the collected powder. Figure 5.6 presents the FTIR-ATR spectra of originally synthesized hydrophilic aerogels and HMDS-treated aerogels. The absorption bands observed in the spectra were interpreted based on the data available in the literature^{149, 166}. In particular, in the spectrum of hydrophilic silica aerogel (Figure 5.6), broad bands centered around 960 cm^{-1} and 3400 cm^{-1} represent stretching of surface silanol (Si-OH) groups. A strong and broad band at around 1090 cm^{-1} and a shoulder at around 1200 cm^{-1} correspond to Si-O-Si asymmetric stretching vibrations. Intense peak in that spectral region indicates the presence of a dense silica network. A peak at around 800 cm^{-1} is due to symmetric stretching vibrations of Si-O-Si. The comparison of the spectra of untreated (Figure 5.6a) and treated (Figure 5.6b) samples clearly indicates that the aerogels have been modified since the intensities of the broad Si-OH band around 3400 cm^{-1} and the other Si-OH peak around 960 cm^{-1} were reduced upon treatment. In addition, the presence of a sharp Si-CH₃ peak around 2900 cm^{-1} and a peak at 837 cm^{-1} corresponding to Si-C stretching vibrations indicates that HMDS reacted with silanol groups on the backbone of the treated samples.

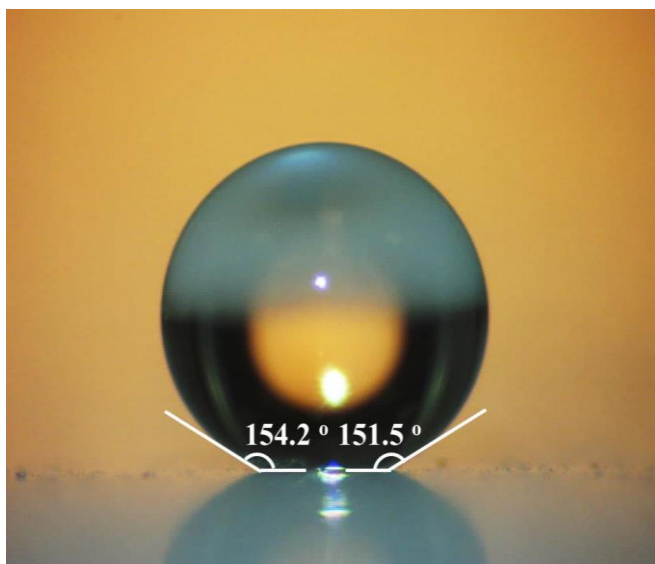


Figure 5.5. Water droplet resting on the surface of HMDS-treated silica aerogel monolith.

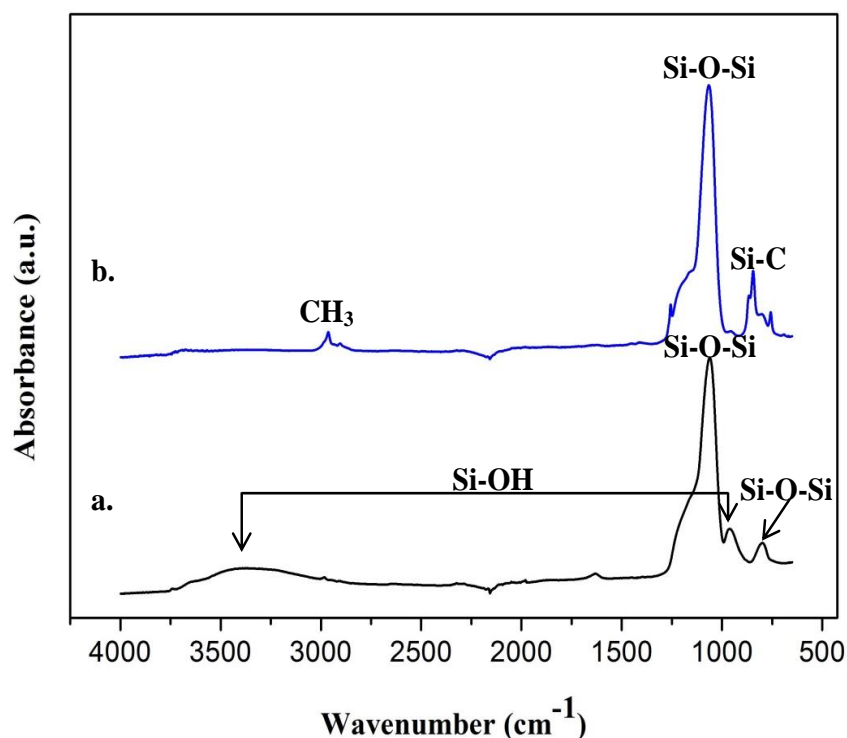


Figure 5.6. FTIR-ATR spectra of (a) an untreated hydrophilic silica aerogel, (b) the surface of the channel fabricated in a HMDS-treated hydrophobic silica aerogel.

The pore properties of the resulting HMDS-treated aerogels were determined by using nitrogen physisorption. The specific pore volume, specific surface area and average pore size of the sample were measured as 2.5 cm³/g, 549 m²/g and 17 nm, respectively. Samples prepared using the standard solvent exchange process without additional ageing have commonly reported specific pore volume of 4.0 cm³/g, specific surface area of 1000 m²/g and an average pore size of 20 nm¹⁶⁷. The slightly lower specific surface area, specific pore volume and pore size of modified aerogels with higher mechanical strength can be most likely attributed to the ageing process in TEOS solution that probably blocks or closes some of the pores.

5.3.2 Light-guiding in Aerogel-based Microphotoreactors

Light-guiding experiments in aerogel-based optofluidic microphotoreactors were performed using the experimental set-up shown in Figure 5.3. The horizontal part of the channel fabricated within the aerogel monolith (see Figure 5.2 for illustration of channel geometry) was illuminated by the tunable laser (Coherent Chameleon Ti:Sapphire

Laser) at 488 nm coupled into the channel through the optical fiber (Thorlabs; UM22-300, NA=0.22). When the light was coupled into an empty channel, the beam exiting from the fiber was transmitted straight along the x-axis (the direction of the horizontal channel part), without any light guiding into the inclined part of the channel, and only scattering could be observed from the junction of the two parts of the channel. Subsequently, a multimode optofluidic waveguide was formed by filling the channel with an aqueous MB solution which has a higher refractive index than the aerogel. Owing to the prior hydrophobic treatment of the aerogel, the solution could be confined within the channel fabricated in the aerogel without penetrating into the porous network of the aerogel. When the light was coupled into the channel filled with the aqueous MB solution, the solution served both as the waveguide core liquid and the reaction medium and the light was guided along the full length of the channel including its inclined section and finally exited from the opposite end of the channel (seen at the top of the lateral face of the aerogel block shown in Figure 5.7). When the light rays propagating in the channel strike the channel wall at an angle greater than the critical angle, they are reflected back to the solution. The rays then strike the opposite wall of the channel and are again reflected back to the solution. The rays propagate in this manner until they exit from the channel. Since the aerogels are highly porous and, therefore, effectively behave like solid air, the propagation losses are significantly lower than 3 dB/cm^{36-37, 39}. As illustrated in the photographs of the solution-filled channel with coupled light shown in Figure 5.7a and Figure 5.7b, the light was totally internally reflected in the channel several times after emerging from the fiber, before leaving the waveguide. Consecutive reflections appear more faintly under ambient light; however, it is clearly visible in the dark that the entire length of the channel is filled with guided light which indicates that the light is indeed confined along the liquid-core optofluidic waveguide.

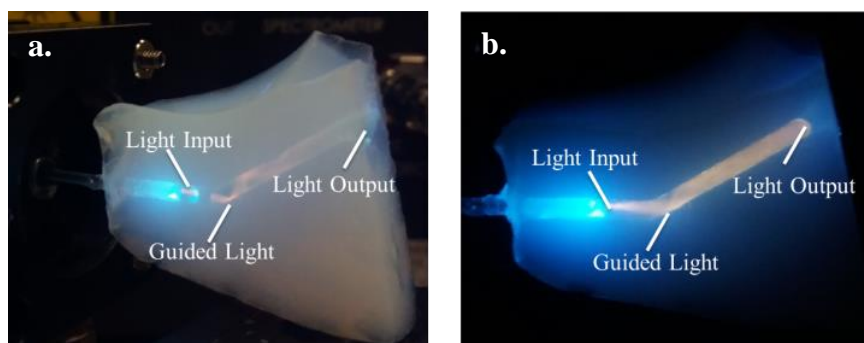


Figure 5.7. (a) Light propagation in a channel fabricated in an aerogel monolith and filled with aqueous MB solution under ambient light illumination (side view). (b) Light propagation in the same channel as shown in part a without ambient light illumination (side view). The guided light fills the whole volume of the channel.

5.3.3 Photodegradation of Organic Compounds

MB was chosen as a model organic compound to evaluate the performance of our aerogel-based photoreactor with integrated optofluidic waveguide in photochemical reactions. An aqueous solution of MB with a concentration of $37.2\ \mu\text{M}$ was loaded into an L-shaped aerogel channel. An L-shaped microchannel was chosen instead of a straight microchannel in order to make sure that the sample of the MB solution taken from the exit port of the reactor was exposed only to the light guided along the channel by TIR and not to the light emitted directly from the input optical fiber. Consequently, light-induced degradation of MB at the exit port occurred only due to waveguiding in the microchannel.

Since MB might be gradually adsorbed on the surface of the aerogel channel, the concentration of MB solution collected from the channel at various times after starting the experiment might be lower than the initial concentration of the solution due to adsorption rather than photolytic degradation. In order to find out if there is a decrease in MB concentration due to adsorption, aerogel channel filled with MB solution was first kept in the dark for a certain period of time. The samples were periodically collected from the end of the channel and the concentration of MB in these samples was measured using a Nanodrop Spectrophotometer. Figure 5.8 shows that the concentration of MB solution kept in the dark remained almost constant for 120 min with a very little variation, thus indicating that MB was not adsorbed at the channel surface. FTIR-ATR

spectra acquired from the internal surface of the channel, which are provided in Figure 5.9, then reveal that the chemical composition of the channel walls remained unchanged before and after MB photolysis took place in the channel and, thereby, they also confirm that MB was not adsorbed at the walls. Low affinity of MB for the aerogel surface may be attributed to the surface hydrophobicity, in combination with the fact that a very small amount of solid constitutes the actual liquid-aerogel interface.

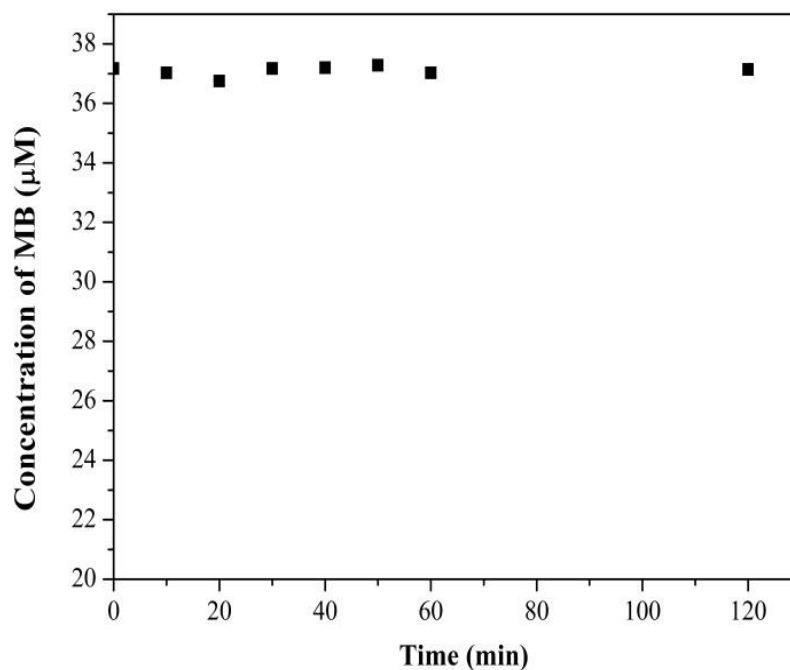


Figure 5.8. Time variation of the concentration of aqueous MB solution contained in an aerogel channel kept in the dark. The initial concentration of MB was 37.2 μM .

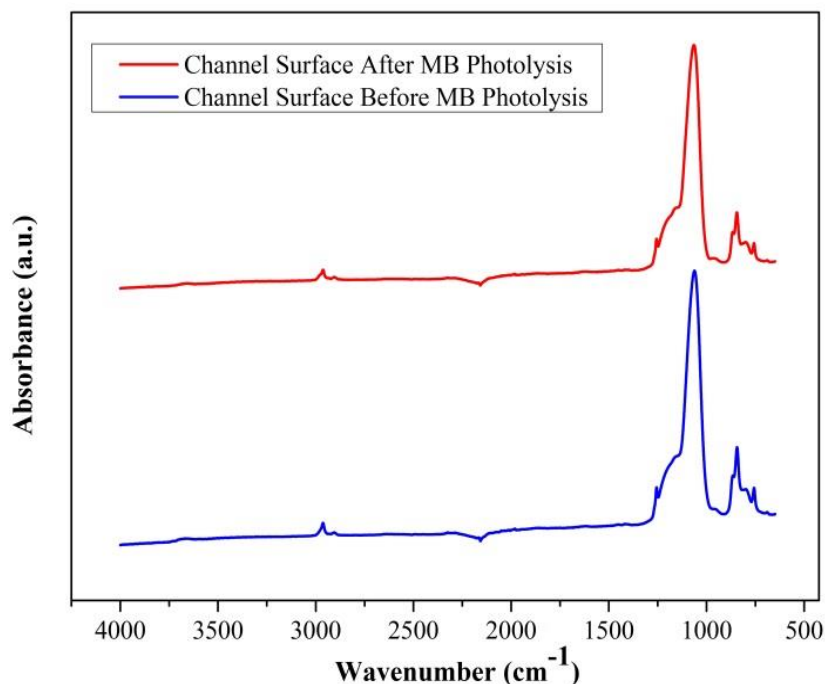


Figure 5.9. FTIR-ATR spectra of internal surfaces of channels fabricated in silica aerogel monoliths acquired before and after MB photolysis took place in the channel.

Subsequently, laser light with the wavelength of 388 nm was coupled into the aerogel channel filled with MB solution with initial concentration of 36 μM and propagated to the end of the channel by TIR-assisted waveguiding. Under these experimental conditions, MB could be gradually degraded along the full length of the channel by the guided light. The degree of photodegradation then depended on the light exposure time and the incident light power. Figure 5.10 demonstrates that the concentration of MB samples collected from the channel end decreased with time under illumination with a constant power of the incident light. In particular, within 60 minutes, the concentration of MB decreased to 6.4 μM under the exposure with the highest incident light power of 250 mW while it reduced to 15.3 μM with the incident light power of 125 mW and to 18.8 μM under the exposure with the incident light power of 64 mW. The percent conversion of the MB dye compound was calculated from Equation 3.7.

Here, C_0 is the initial concentration of the dye and C_t is the dye concentration at time t . As shown in Figure 5.11, the conversion of MB dye at various times increased with the increasing power of the incident light within the studied power range. In our

system, since the light is coupled to the open end of the channel (see Figure 5.7) and the light intensity is highest at the entrance and decreases through the channel towards the other end of the channel, Therefore, degradation rate is highest at the entrance and decreases towards the end of the channel; resulting in a concentration gradient of MB through the channel. As a result, MB diffuses from highly concentrated region, near the end of the channel, to the region with a lower concentration of MB. The change of concentration of MB in the channel as a function of time is given by the solution of Equation 5.1.

$$\frac{\partial C}{\partial t} = D \frac{\partial}{\partial z} \left(\frac{\partial C}{\partial z} \right) - \phi * I_a \quad \text{Equation 5.1}$$

$$I_a = I_o \left(1 - e^{-\int_0^z 2.303 * \epsilon * C(z) * dz} \right) \quad \text{Equation 5.2}$$

where D is diffusion coefficient of MB in water ($\text{cm}^2 \text{s}^{-1}$), C is concentration of MB (M), I_o is incident light intensity ($\mu\text{E L}^{-1} \text{cm}^{-1}$), ϕ is quantum yield of MB, which is defined as the number of moles of MB decomposed per mole of light photons absorbed by MB, ϵ is molar absorption coefficient of MB in aqueous solution ($\text{M}^{-1} \text{cm}^{-1}$) and z is pathlength of the light (cm). Numerical solution of Equation 5.1 and Equation 5.2 for our system indicates that the concentration of MB increases as a function of the incident light power in a complex manner.

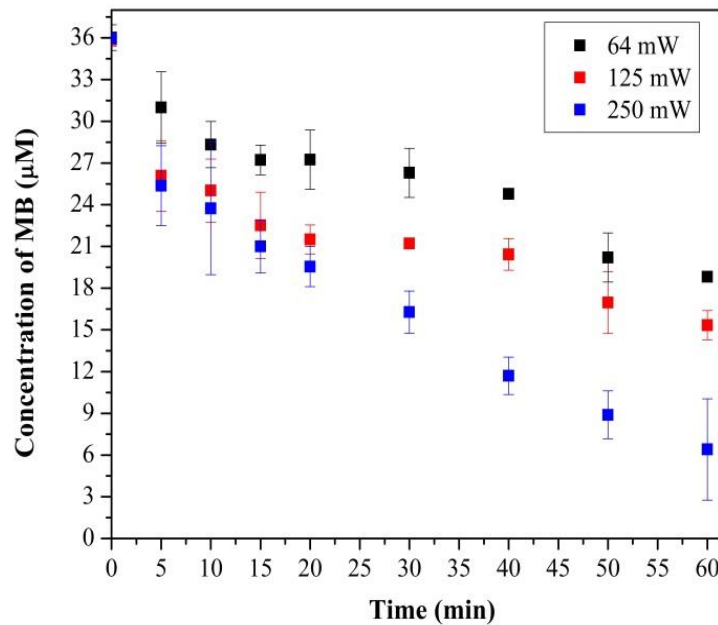


Figure 5.10. Time variation of the concentration of aqueous MB solution contained in an aerogel channel under illumination at 388 nm with varying power of the incident light. The initial concentration of MB was 36 μM . The incident power values were measured before coupling the light into the input optical fiber.

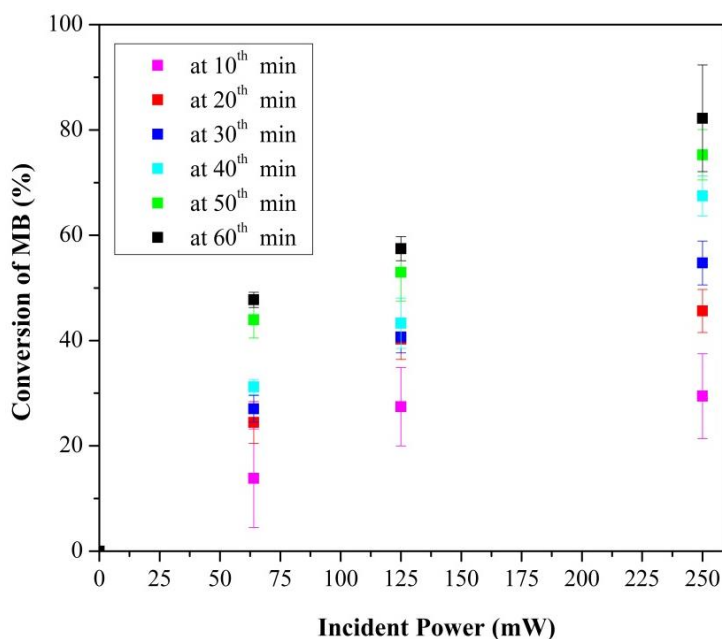


Figure 5.11. Variation of photoconversion of aqueous MB solution illuminated by incident light at 388 nm with increasing power. The initial MB concentration was 36 μM .

In order to demonstrate the vital importance of light guiding for the functionality of our photoreactor system, we carried out control experiments, in which the aerogel block with liquid-filled channel was replaced by a piece of conventional plastic tubing. In particular, the used tubing had an outer diameter of 4 mm and an inner diameter of 2 mm and its L-shaped geometry and dimensions were almost identical to those of the channel fabricated in the aerogel monolith. In order to maintain constant shape during the course of an experiment, the tubing was mounted on a metal plate using clamps (see Figure 5.13 for illustration). Subsequently, the tubing was connected to the Union Tee adapter in the same way as in the experiments conducted with the aerogel (see Section 5.2.5). Prior to the actual photodegradation experiments, light propagation in the tubing filled with MB solution was investigated. The light at 488 nm was coupled into the tubing by the optical fiber, using the same optical set-up as used previously in the

aerogel experiments (see Section 5.3.2). A photograph of the tubing filled with MB solution and 488 nm laser light coupled into it is shown in Figure 5.12. As expected, the laser light delivered by the fiber cannot propagate in the liquid-filled tubing by TIR, since the refractive index of the tubing is higher than the refractive index of water. Thus, a large fraction of the incident light coupled into the horizontal section of the tubing is scattered at the tubing elbow. Only a small fraction of the incident light can reach the end of the tubing, exploiting TIR at the interface between the tubing and ambient air. Subsequently, the tubing filled with fresh MB solution was kept in the dark and samples were collected from the end of the tubing at various times up to 60 min. Figure 5.13 illustrates that in this experiment, MB concentration remained almost constant, with a slight variation that might be possibly attributed to interaction between MB and the surface of the inner walls of the tubing. After completing the control experiment under dark conditions, photolysis of MB contained in the tubing was carried out under illumination at 388 nm with an incident light power of 64 mW, measured before coupling the light into the input optical fiber. The power at the tubing output end was measured to be lower than $\sim 8 \mu\text{W}$. shows that in the photolysis experiment carried out in the tubing, the conversion of MB increased only slightly with time, eventually fluctuating around the maximum of $\sim 10\%$ after 60 min exposure (red squares). In contrast, the conversion of MB carried out in the aerogel-based waveguide (black squares) reached the maximum of 48 % under the same experimental conditions (incident light power and exposure time). The comparison of the results obtained with aerogel-based and tubing-based photoreactors clearly shows that the light-guiding effect enabled by the contrast of refractive index between the aerogel and the aqueous reaction solution is essential for the high performance of the microphotoreactor.

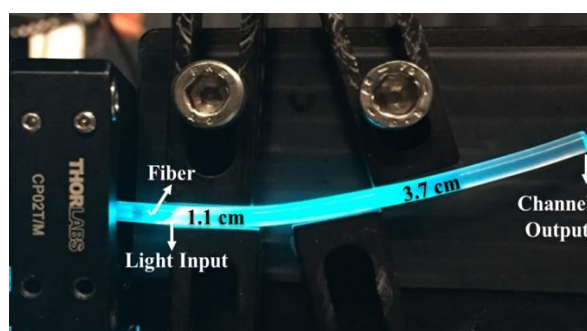


Figure 5.12. Light propagation in the plastic tubing filled with aqueous MB solution under ambient light illumination (side view).

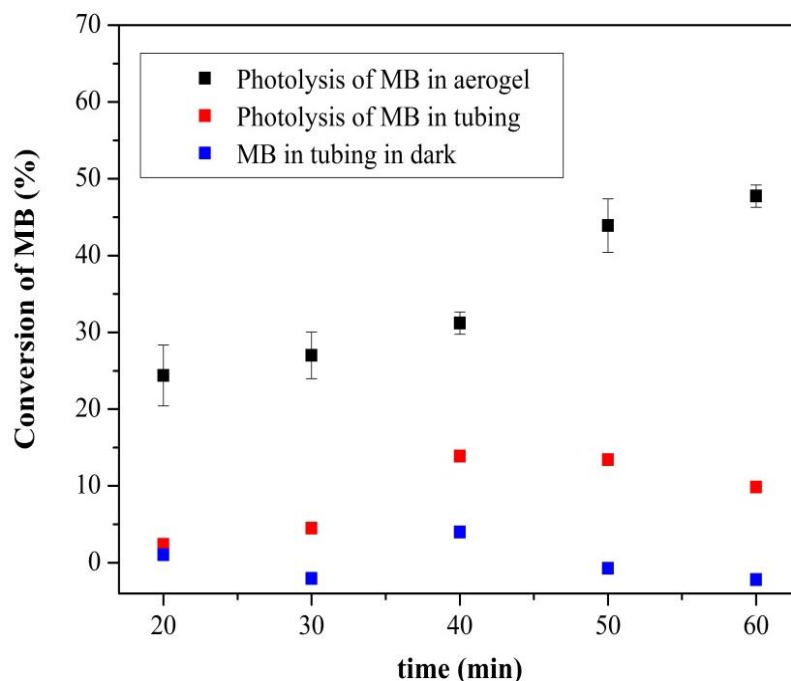


Figure 5.13. Time variation of the percentage conversion of aqueous MB solution contained in the tubing and its photoconversion at an incident light of 70 mW. The initial concentration of MB was 30 μ M.

The above results demonstrate that aerogel-based optofluidic waveguides can serve to build efficient optofluidic photoreactor systems for a wide variety of potential applications. Thanks to the integrated light waveguide, these photoreactors may enable a large effective penetration depth of the incident light and a more uniform light distribution in the radial direction within the reaction volume, in comparison to the conventional bulk photoreactors. As the light is delivered to the reacting species in the liquid core by optical waveguiding, the reactor itself can be operated under dark ambient conditions. Furthermore, thanks to the interconnected open-pore architecture of the aerogel network forming the waveguide cladding, the platform is also interesting for implementing membrane-like microreactors with selective molecular transport. In particular, while the core liquid is confined within the channel and cannot penetrate the porous aerogel cladding, the pores still allow for efficient two-way diffusive transport of gases between the core liquid and the reactor surroundings. Thus, oxygen required for

the photolysis of organic compounds such as methylene blue can be delivered from the outside whereas the gaseous products of the photolysis such as CO₂ can be readily removed through the porous framework of the aerogel. Moreover, the selectivity of transport through the porous aerogel network can be tuned for specific applications by adjusting the parameters of sol-gel synthesis and post-synthesis treatment of the aerogels. Permeability of aerogels to gases also allows for the removal of air bubbles formed in the liquid channel, leaving behind a continuous, bubble-free light path. Air bubbles are detrimental for the performance of optofluidic waveguides since they hinder the light propagation through the channel and lead to high optical losses due to light scattering, eventually resulting in the failure of the waveguide. However, such bubbles cannot be removed from conventional microfluidic channels with gas-impermeable walls³⁹.

Finally, aerogel-based optofluidic microphotoreactors hold a great promise for carrying out photocatalytic reactions. The high porosity and high surface area of aerogels with interconnected open pore structure, combined with a fully tunable three-dimensional architecture, make aerogels very well suited for the deposition of a photocatalyst. Walls of channels fabricated in an aerogel monolith are porous and, thus, photocatalyst particles can be immobilized within these pores with a good adhesion to the solid network. With photocatalyst particles present in the aerogel channel wall, the guided light can be partially absorbed in the near-surface region of the wall. Subsequently, the reactants can be converted into desired products on the catalyst surface.

It should be also possible to operate our optofluidic photoreactors in a continuous manner by delivering the reactant solution using a suitable pump. In order to increase the overall throughput of the photochemical/photocatalytic reaction, the aerogel-based photoreactors can be fabricated with multiple channels operating in parallel. Moreover, using processes such as preform removal or femtosecond laser ablation, uniform and extended microchannels with much smaller diameters can be created^{36, 39, 108}, expanding further the potential for large-scale parallelization which is needed for industrial applications of the presented platform.

5.4 Conclusions

We have demonstrated a novel type of microphotoreactor with integrated optofluidic waveguide which is formed by a liquid-filled channel fabricated in a monolithic aerogel block. The unique optical properties of aerogels - particularly, their low refractive index - allow them to be used as the cladding material of TIR-based optofluidic waveguides with aqueous liquid cores that do not require any additional coatings. Post-synthesis modification of the prepared aerogel monoliths rendered the aerogel surface hydrophobic. Thus, aqueous solutions of methylene blue serving both as the waveguide core liquid and the reaction medium could be confined inside a channel embedded in the aerogel, without being adsorbed on the channel walls or without compromising the monolithic structure of the aerogel. We have directly visualized TIR-assisted light propagation along liquid-filled channels fabricated in aerogel blocks and verified that light could be efficiently guided even along paths with a curved geometry. Subsequently, we have successfully shown light-driven photolysis of methylene blue by the light guided along the full length of the photoreactor channel. For the studied range of the incident light powers, quantitative analysis of the dependence of the conversion of the dye on the incident power indicated a linear trend. Aerogel-based liquid-core optofluidic waveguides represent a straightforward way for guiding and controlled routing of light which is also fully compatible with carrying out photochemical and photocatalytic reactions in aqueous media. Thanks to the flexibility of the procedures used for aerogel synthesis and post-synthesis modifications, aerogel-based photoreactors hold the potential for practical applications in photochemical and photocatalytic synthesis or degradation of various organic and inorganic compounds.

Chapter 6

PHOTOCATALYTIC TRANSFORMATION IN SILICA-TITANIA COMPOSITE AEROGEL-BASED OPTOFLUIDIC MICROREACTORS

6.1 Introduction

In this part of the study, a new type of microphotoreactor for photocatalytic reactions formed by a liquid-core optofluidic waveguide fabricated inside hydrophobic monolithic aerogel is demonstrated. The field of optofluidics and highly porous, membrane-like properties of aerogels combined with fully tunable three-dimensional structures are both exploited to construct microphotoreactors for controlled distribution of light through the reaction medium maintaining good interaction of light, fluid and the solid photocatalyst particles. Anatase TiO_2 nanoparticles were used as photocatalysts and it was successfully introduced into the mesoporous network of silica aerogels during sol-gel step of aerogel synthesis obtaining monolithic composite aerogels with varying titania content from 1 wt % to 50 wt %. The presence of TiO_2 and its desired crystalline structure in aerogel matrix was confirmed by XRD patterns and FE-SEM

images. The silica-titania composite aerogels retained their interconnected mesoporous network with high porosity and pore volume as well as high surface area. Surface modification by HMDS was devised to alter the wetting conditions of the reactor walls for construction of liquid-core optofluidic waveguides in the channel. Cylindrical straight channels were then fabricated in the synthesized monolithic composites. Light was confined in the liquid in the channel and is guided in a controlled manner by total internal reflection from the channel walls. Low and favorable propagation losses ranged from 2.6 dB/cm to 3.9 dB/cm with increasing amount of the TiO_2 in the structure from 1 wt % to 50 % wt. The band gap of the SiO_2 - TiO_2 composites was estimated from Tauc plot calculated by Kubelka-Munk function from diffuse reflectance spectra of samples obtained using UV-visible reflectance spectroscopy. Using this technique, the anatase TiO_2 band gap was observed near expected value of ≈ 3.2 eV. The photocatalytic degradation of phenol over the immobilized photocatalysts in the channel walls by the light delivered through the constructed waveguide was used as model reaction to test the reactor and demonstrating very promising performance. We further demonstrated the effect of incident light power, flow rate of the reactant and mass fraction of the photocatalyst in aerogel composites and additional oxygen supply on the performance of the reactor. Along with experimental studies, a simple model for immobilized photocatalytic microphotoreactors with integrated waveguide following a first order reaction rate with light dependency was developed and compared with experimental data for various conditions investigated. The reaction rate parameters were estimated from an exponential regression model. The model and experimental were found to be in good agreement.

Construction of a microphotoreactor with channels made out of an interconnected open porous network which acts as a membrane for separation of the air bubbles from the liquid and concurrently manipulates the path of light in the channel might be a possible key to overcome the problems in conventional microphotoreactors. The channels thus behave as an optical waveguide which simultaneously confines and overlap light and reactants. It was recently demonstrated that aerogels are promising candidates to be efficiently used for optical waveguiding in liquids³⁵⁻³⁸. Optofluidic waveguides can be constructed by opening channels inside monolithic aerogel blocks. These channels are surrounded by a wall made up of interconnected particles that are

around 40 to 80 nm in size, with pockets of air in between them that constitute pores with sizes less than 100 nm. The air in the aerogel pockets is responsible for guiding light by TIR in a liquid-filled channel. Following appropriate chemical treatment that makes the channel surface compatible either with polar or with non-polar liquids, the channels can be filled with a suitable reactant solution that also serves as the waveguide core liquid. In such an approach, the channel fabricated within the aerogel simultaneously confines the reaction medium and also serve as the waveguide cladding whereas the reaction volume resides within the liquid core of the waveguide ^{36, 39}. In addition, the surface of aerogels can be chemically modified; therefore, there is no restriction on the type of liquid or aerogel that can be used, as long as the liquid can be confined inside the aerogel block without penetrating its porous network ^{36, 40}.

The above statements indicate that both optofluidics and highly porous, membrane-like properties of aerogels combined with a fully tunable three-dimensional structure show their respective advantages to promote development of photocatalytic microphotoreactors. In this study, we successfully integrated the concept of optofluidics into the monolithic aerogel to newly propose an aerogel-based microphotoreactor for photocatalytic reactions called as “aerogel-based microphotoreactor with an integrated optofluidic waveguide”. The reactor consists of a cylindrical channel in a monolithic aerogel. Since the channel walls in the aerogel block are still porous, photocatalysts can be immobilized within the porous network with a good adhesion to the solid network. Silica aerogel was chosen as the template for its appealing attributes of interconnected nanoporous framework with high surface area-to-volume ratio to immobilize high amount of photocatalyst and its desirable properties that complement photocatalytic processes acting as charge transfer catalyst. Unlike conventional microphotoreactors, light was directly implemented into the channel within the same path of the reactant stream, which resulted in low and favorable propagation losses of light. Desired and stable crystalline structure of titania along with effective pore characteristics of the photomicroreactors were obtained. We demonstrated that our microphotoreactor is well suited for photocatalytic degradation of a model organic compound – phenol– and we investigated the effects of incident light power, flow rate of the reactant and mass fraction of the photocatalyst in aerogel composites on photocatalytic decomposition of

phenol and the effect of oxygen supply to the reactant solution on the performance of the reactor.

6.1.1 Design of Aerogel-based Microphotoreactor

Figure 6.1. Schematic of the $\text{SiO}_2\text{-TiO}_2$ composite aerogel-based microphotoreactor. illustrates the schematic of the aerogel-based microphotoreactor. In this design of the microphotoreactor, the porous solid network of silica-titania aerogel surrounding the channel forms the aerogel-cladding. The liquid reactant stream and light is simultaneously passed through the hydrophobic channel sharing the same path. The liquid reactant therefore constitutes the core-liquid of the optofluidic waveguide. Light is confined in the reactant in the liquid solution in the channel and is guided in a controlled manner by the aid of liquid core optical waveguides based on TIR from the channel walls. The reactant flow through in and out by inlet and outlet of the channel while it is irradiated. The light with energy equal or greater than the band gap of catalyst and delivered through the waveguide by TIR along the channel is absorbed by the immobilized catalyst in the walls which results in excitation of electrons (e^-) to the conduction band, leaving holes (h^+) in the valence band. The e^- and h^+ pair either recombines or diffuses to the catalyst surface to lead to oxidation-reduction reactions with reactants adsorbed on the surface. These photoinduced charge carriers at the photocatalyst surface employ oxidation-reduction reactions of phenol by the aid of oxygen available in the solution and in the pores by totally decomposing to CO_2 .

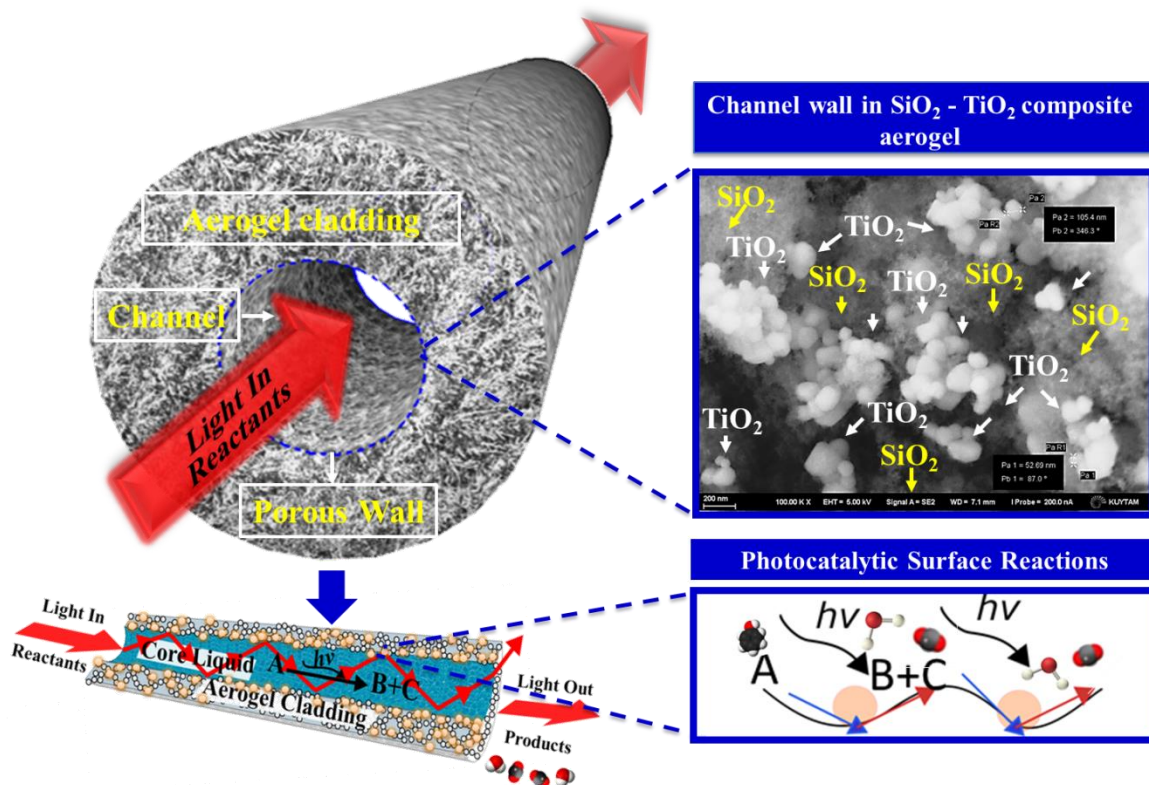


Figure 6.1. Schematic of the SiO₂-TiO₂ composite aerogel-based microphotoreactor.

6.2 Materials and Methods

6.2.1 Materials

TEOS (98%), ethanol ($\geq 98\%$) and NH₄OH (2.0 M in ethanol) were purchased from Sigma Aldrich. HCl (37% purity) was obtained from Riedel-de Haen and HMDS ($\geq 98\%$) was purchased from Merck. Anatase titanium dioxide particles in powder form was purchased from Jiangsu Hongyuan Pharmaceutical Co. Ltd.. Carbon dioxide (99.998 %) was purchased from Messer Aligaz. All chemicals were used as received.

6.2.2 Synthesis of SiO₂-TiO₂ Composite Aerogels

SiO₂-TiO₂ composite aerogels were synthesized by a two-step sol-gel process followed by supercritical drying, as shown in Figure 6.2. TEOS, used as the silica precursor, was initially hydrolyzed with water in the presence of ethanol as co-solvent and HCl (0.06 M in ethanol) as acid catalyst. The mole ratio of TEOS/ethanol/water/HCl used in the synthesis was 1:4:3:0.0023. The amount of SiO₂ produced as a result of the reaction was calculated on a mole basis that 1 mole of TEOS forms 1 mole of SiO₂. The titania particles were then added to the solution to obtain a weight percent of titania to silica in a range from 1 wt % to 50 wt% and it was

continuously stirred at room temperature for 2 h. The sol containing dispersed titania particles was sonicated for 40 min for the homogenous particle dispersion. 1 M of NH_4OH in ethanol was added as the base catalyst such that the condensation reactions were accelerated which eventually led to the gelation of the solution within 5 min. The mole ratio of NH_4OH to TEOS was 1:13.4. Before gelation, the solution was transferred into polyethylene molds tightly sealed to prevent evaporation of the solvent. After the gelation, the sol-called alcogels were aged in 50:50 (v%) mixture of water and ethanol at 323.2 K for 24 h. The alcogels were then placed in fresh ethanol for 3 days to remove any impurities and water remaining in their pores. Following the aging step, the alcogels were subsequently dried with supercritical CO_2 (scCO_2) at 40 °C and 100 bar in an Applied Separations Speed SFE unit for 6 h and monolithic and crack-free SiO_2 - TiO_2 aerogels were obtained. The monolithic shape of the synthesized composite aerogel is demonstrated in a photograph given in Figure 6.3.

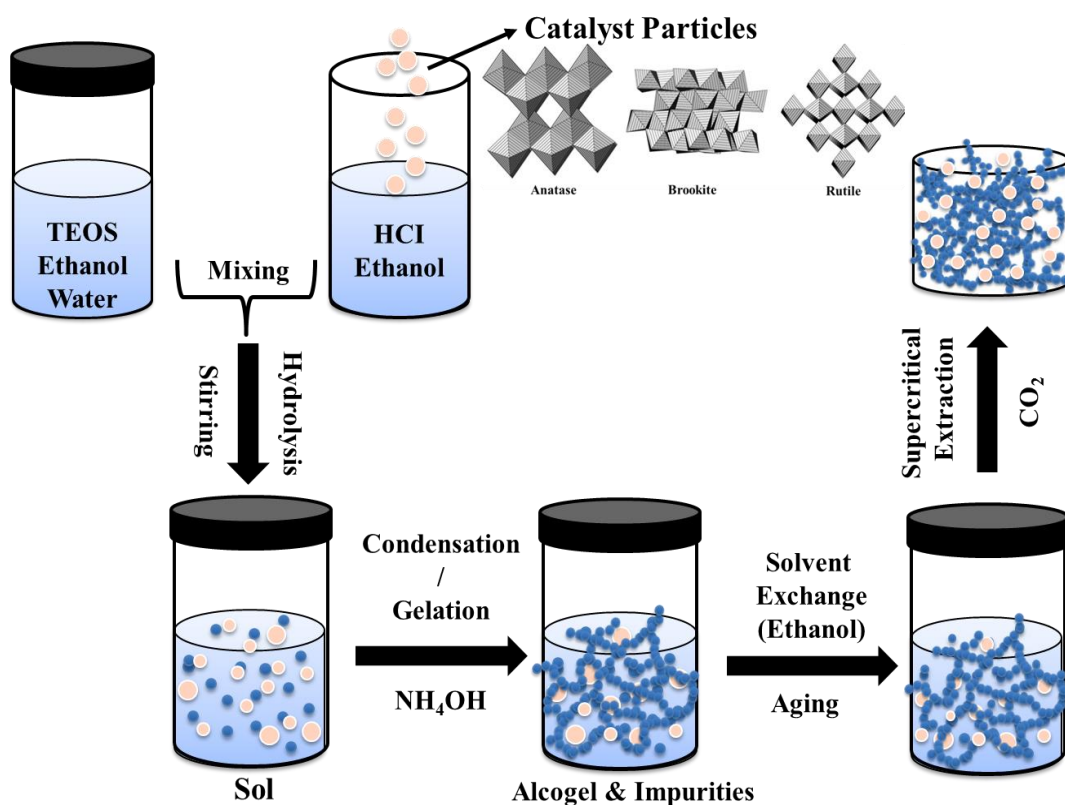


Figure 6.2. Schematics of silica-titania composite aerogel synthesis through sol-gel method.



Figure 6.3. A photograph of the synthesized monolithic silica-titania aerogel composite with 50 wt% of titania.

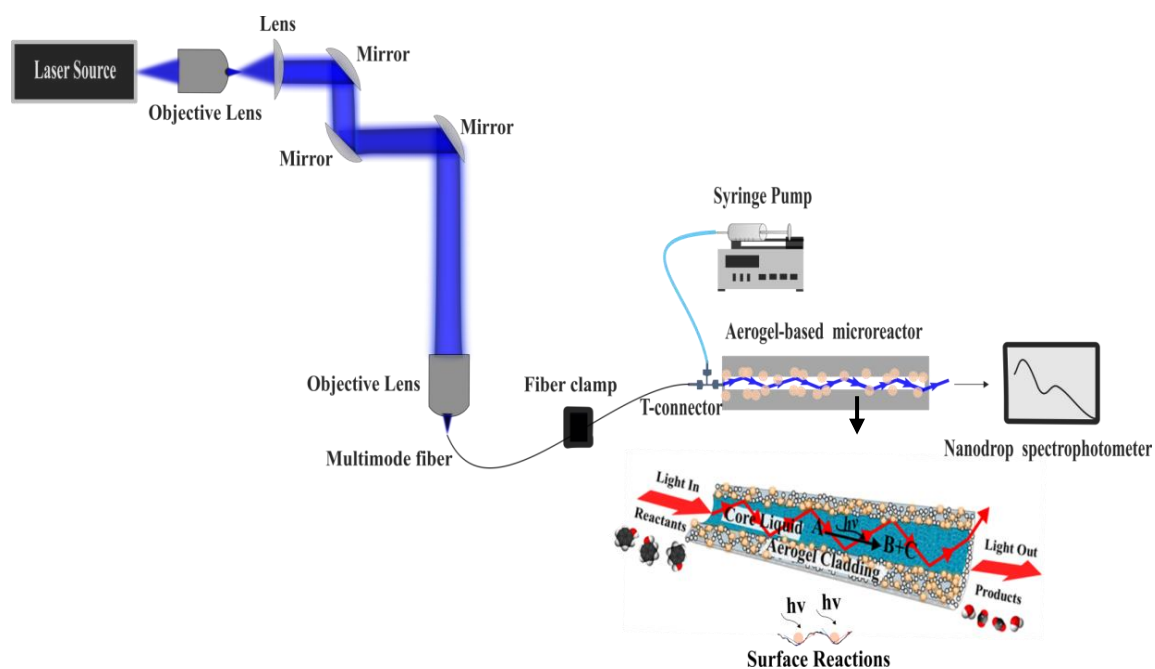
6.2.3 Surface Modification with HMDS

The resulting composite aerogels were hydrophilic due to the presence of the polar hydroxyl groups within porous silicon dioxide network which promote high capillary stress and water adsorption once they are in contact with water. HMDS was used to render the aerogel surface hydrophobic by replacing the hydrophilic hydroxyl surface groups of the aerogel with hydrophobic methyl groups. 4 ml of liquid HMDS were first added to the beaker and a stainless steel screen was placed in the middle of the beaker, above the liquid level. A block of hydrophilic aerogel was placed on top of the screen. The beaker was then tightly sealed and heated to 110 °C in an oven. The aerogel block was exposed to HMDS vapor for about 2 h. The sample was then removed from the beaker and placed in the oven at 120 °C for 1 h to remove the unreacted HMDS inside the pores and the reaction products of HMDS with surface hydroxyl groups by evaporation. Monolithic and crack-free hydrophobic SiO₂-TiO₂ aerogel was eventually obtained. Wetting properties of the aerogels were characterized by placing a water droplet on the aerogel surface. The water droplet behavior was visualized so that the droplet sat with a spherical shape without penetrating the porous network of the aerogels maintaining their intact structures. Then the samples were cut and the cross-sections were examined through the same method.

6.2.4 Experimental Set-up for Photocatalytic Chemical Reactions

Prior to the photocatalytic reactions, cylindrical and straight channels which would confine reactants and would serve as a cladding for the light propagation were fabricated in hydrophobic $\text{SiO}_2\text{-TiO}_2$ aerogel monoliths by manual drilling as described in our previous study for the channel fabrication in silica aerogels⁴⁰. The hand-driven drill bit was positioned perpendicularly to the aerogel surface and – while rotating continuously – moved slowly into the sample to prevent stress buildup. This way, a single straight channel with two open ends was opened. One open end of the channel was glued to a piece of plastic tubing by epoxy to connect the channel to a syringe pump for continuous flow of the reactant without any leakage during the reaction. Figure 6.4 shows a schematic diagram of the experimental setup that was employed for studying model photocatalytic reaction - degradation of phenol in an aqueous solution contained inside the channel. The $\text{SiO}_2\text{-TiO}_2$ aerogel monolith with an embedded channel inside was mounted on an inclined adjustable holder in Figure 6.4. The tubing was connected to a Union Tee adapter and central port of the Union Tee was connected to a syringe and the remaining end of the Union tee was used to insert a solarisation-resistant multimode optical fiber (Thorlabs; UM22-300, NA=0.22) into the aerogel channel. This optical fiber served for delivering the photoactivation light to the reaction volume and its end was kept at a fixed position at the channel entrance. Fluidic connections were made by 1/8 in. PEEK tubing and flangeless fittings (Upchurch Scientific). After building channels in composite aerogel monoliths and connecting to the light and fluid path, liquid-core optofluidic waveguides could be constructed by filling the channels with the aqueous solution of phenol which was utilized as the reactant and the core liquid for the optofluidic waveguide. The flow of phenol solution was driven by a syringe pump and it was confined within the channel without penetrating into its porous network. After filling the channel with the reactant and while maintaining the continuous feeding of the phenol solution at the constant flow rate, the light was delivered to the multimode optical fiber was delivered from a femtosecond-pulsed, tunable laser light source (Coherent Chameleon Ti:Sapphire Laser) with a maximal output power of 4 W. The laser beam was coupled into the free end of the multimode optical fiber with the aid of an objective lens. The operating wavelength of the laser was tuned to 366 nm. The input power coupled into the optofluidic waveguide

could be adjusted from the laser source. The incident power values were measured by a laser power meter before coupling the light into the liquid-core optofluidic waveguide in the channel. The light coupled from the fiber into the reactant-filled channel was confined and was guided in a controlled manner by the aid of liquid core optofluidics waveguides based on TIR from the porous channel walls. The propagated light by TIR and hitting the channel walls was absorbed by the embedded photocatalyst in the walls, resulting in e^- and h^+ pairs formation which is used to decompose the phenol through redox reactions. The progress of the photocatalytic degradation of phenol over the titania was subsequently monitored through absorbance-based quantification of phenol concentration using Nanodrop ND-2000C Spectrophotometer. Samples with a volume of 5 μ L were collected at various times from the end of the channel by a micropipette and subsequently analyzed by Nanodrop ND-1000 Spectrophotometer for the concentration. The phenol conversion was calculated by Equation 3.7.



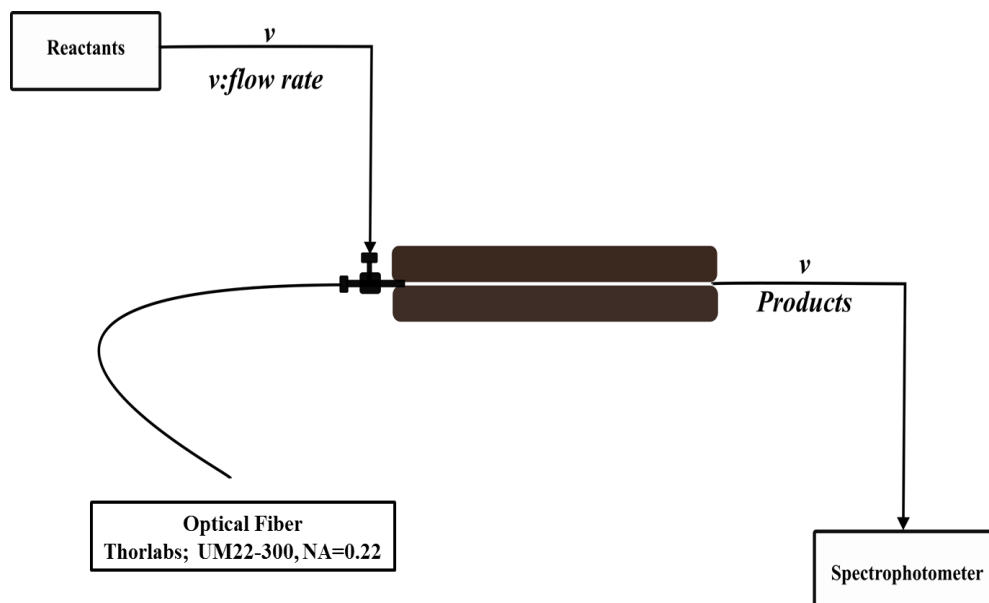


Figure 6.4. (a) Schematics of experimental set-up used in the characterization of light guiding and photocatalytic reactions in aerogel-based optofluidic microphotoreactors. (b) Schematics of the reactor system.

6.3 Results and Discussion

6.3.1 Properties of SiO₂-TiO₂ Aerogel-based Microphotoreactor

XRF measurement results provided in Table 6.1 verified that monolithic silica-titania aerogels could be synthesized with the expected content of the titania, initially dispersed in the sol. This also points out that the titania nanoparticles could be uniformly distributed in the composite samples during the sol-gel process. The effect of incorporation of titania nanoparticles into the silicon dioxide network on the pore characteristics of the samples such as surface area, pore volume and pore size distribution and density of the composites were investigated by analyzing the N₂ adsorption-desorption isotherms. The analysis results were summarized in Table 6.2 together with densities. With increasing titania content, densities of the samples increased as expected, whereas surface areas and total pore volumes decreased. However, the synthesized aerogel monoliths retained their high porosity and pore volume as well as high surface area. BET surface area of the native silica aerogel decreased from 962 m²/g to 289 m²/g by the addition of titania to obtain 50 wt% and the total pore volume of the native silica aerogel decreased from 4.32 cm³/g to 1.1 cm³/g.

However, average pore radius of the samples did not demonstrate a significant change and a trend with the increasing titania content. The BJH desorption average pore diameter of native silica decreased increased from 19.6 nm to 23.7 nm in the sample with 50 wt % of titania. Furthermore, pore size distribution of the composite samples and the native silica aerogel for comparison obtained from the desorption branch of the isotherm by employing BJH method was provided in Figure 6.5. The pore size distributions of the samples were compared with the native silica aerogel in Figure 6.5 which shows that the average pore diameter of the composites changed very slightly upon titania addition to the silica aerogel matrix.

Table 6.1. Titania fraction measured by XRF

<i>wt % of titania expected</i>	<i>% wt of titania measured</i>
1	2.9
14	12.3
24	26.7
32	32.4
48	46.2

Table 6.2. Densities and pore characteristics of synthesized silica-titania composite aerogels.

<i>wt % of titania</i>	<i>Density (g/cm³)</i>	<i>BET Surface Area (m²/g)</i>	<i>Total Pore Volume (cm³/g)</i>	<i>BJH Desorption Average Pore Radius (nm)</i>
------------------------	---------------------------------------	---	---	--

Native Silica Aerogel	0.15	962	4.3	19.6
1	0.17	706	3.4	27.8
14	0.175	594	2.4	25.5
24	0.183	556	3.2	21.3
32	0.195	409	2.0	25.4
48	0.196	289	1.1	23.7

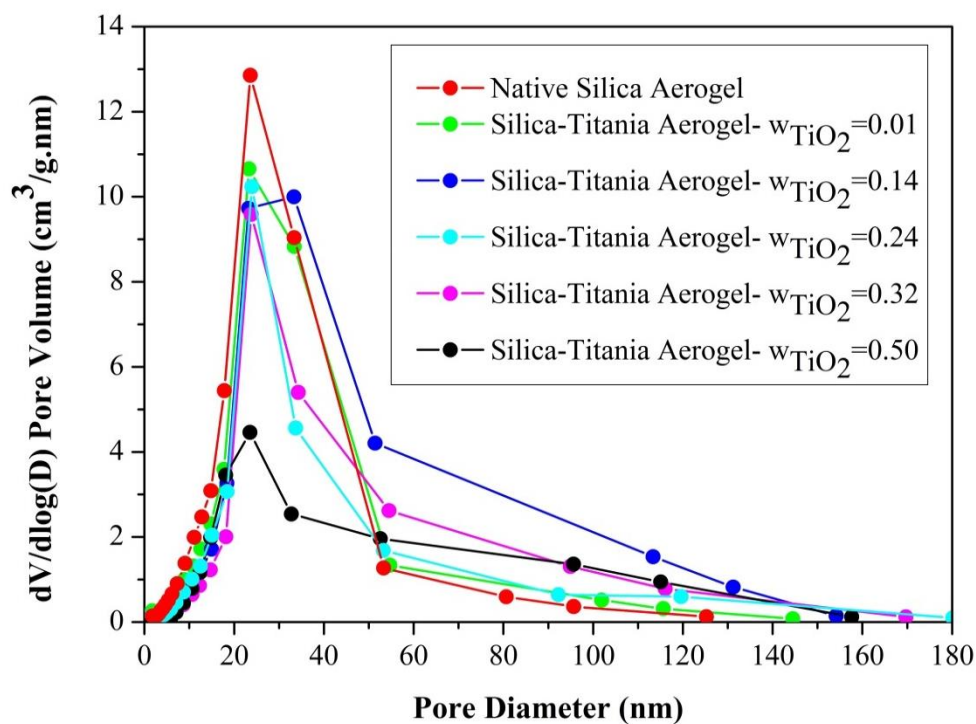


Figure 6.5. Pore size distribution and N₂ adsorption–desorption isotherms of the silica aerogel and silica–titania composite aerogels.

The N₂ adsorption–desorption isotherms of the native silica aerogel and composite aerogels with a titania content in the range from 1 to 50 wt % were additionally given in Figure 6.6. It is clearly observed that the native aerogel and SiO₂-TiO₂ composite aerogels show type-IV isotherms with a H1 type hysteresis loop with desorption branch reflecting equilibrium capillary condensation. The type-IV isotherm in the composite samples evidenced by the hysteresis is characteristic of the mesoporous structure of aerogels. The synthesized composite aerogels thus retain the

mesoporous structure of the native silica aerogel with the three dimensional network. Furthermore, H1 hysteresis loops are characteristic of materials with cylindrical pore geometry and high degree of pore-size uniformity; therefore, this confirms that the silica-titania composite aerogels have a pore size uniformity and facile pore connectivity. The isotherm also indicates that the pores are not completely filled and the aerogels have some larger pores except from the mesoporosity since there is no obvious platform at high relative pressure which implies that the all pores are in the mesoporous range.

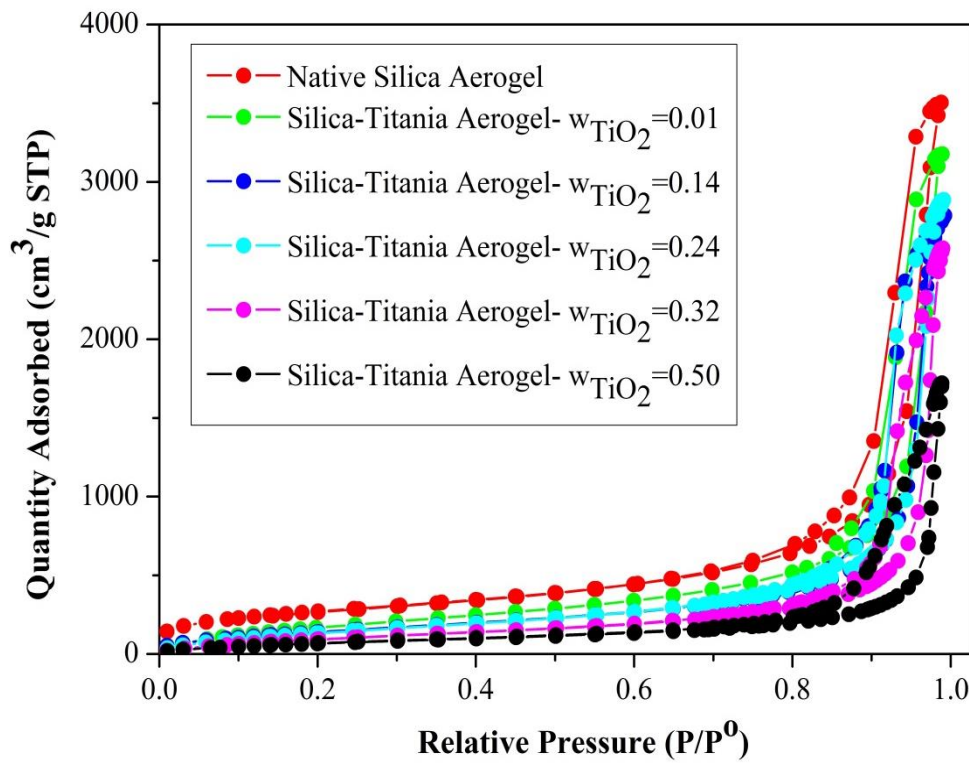
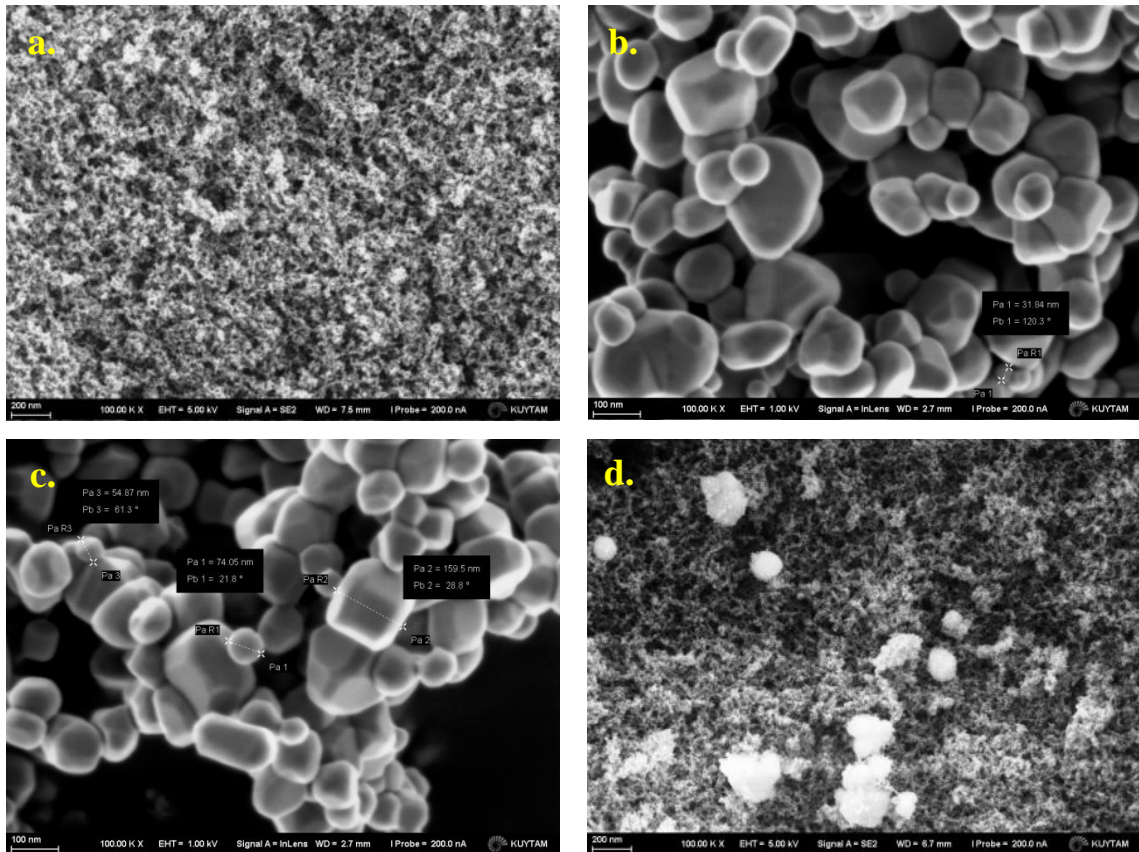
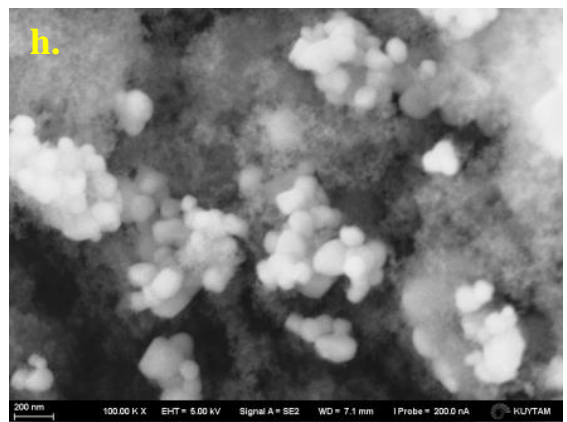
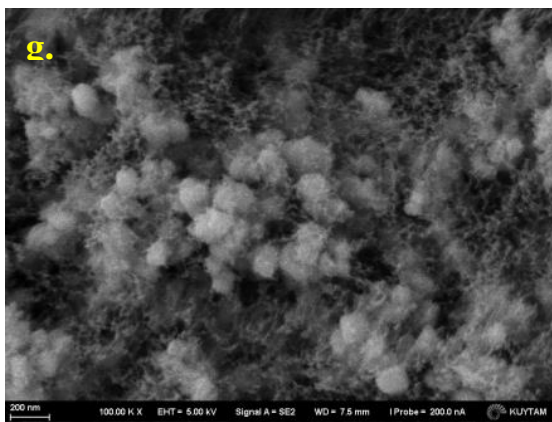
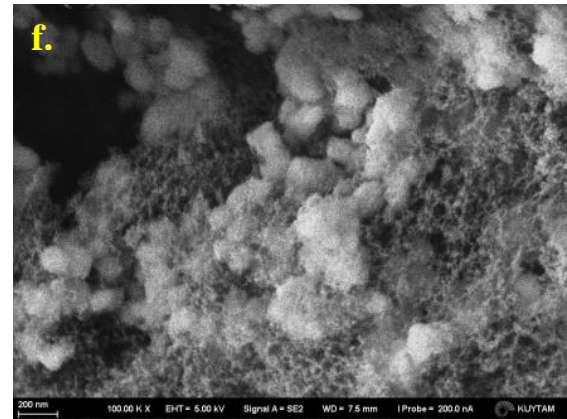
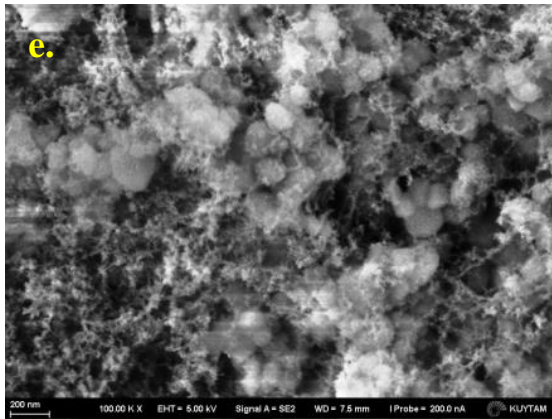


Figure 6.6. N₂ adsorption/desorption isotherms for the silica aerogel and silica–titania composite aerogels.

For comparison of surface morphologies of samples after titania incorporation to the silicon dioxide network, FE-SEM images of the native silica aerogel and the silica-titania composites are provided in Figure 6.7a and Figure 6.7d-j, respectively. FE-SEM images show that anatase titania particles appearing with sizes typically in range from 32 nm to 160 nm (see Figure 6.7b and Figure 6.7c) were successfully introduced into the interconnected mesoporous structure of the silica aerogel during the sol-gel step of the aerogel synthesis. Furthermore, it is obvious and noteworthy to mention that there is

no significant change observed in the mesoporous structure of the silica-titania aerogels with the increase of the titania content and the composite aerogels' network structure is highly porous and the porous morphology is clearly visible from the images. The titania particles in each sample were embedded into the silicon dioxide network as agglomerated spherical clusters. The clusters in the network appearing in white color in the images was also confirmed to be titania by the EDX measurement obtaining a typical spectrum in Figure 6.7k. The FE-SEM images of the samples with 24 and 50 wt % of titania at a larger scale bar of 1 μm , which are given in Figure 6.7g and Figure 6.7h also demonstrate that the clusters of nanoparticles are obviously distributed in a high homogeneity.





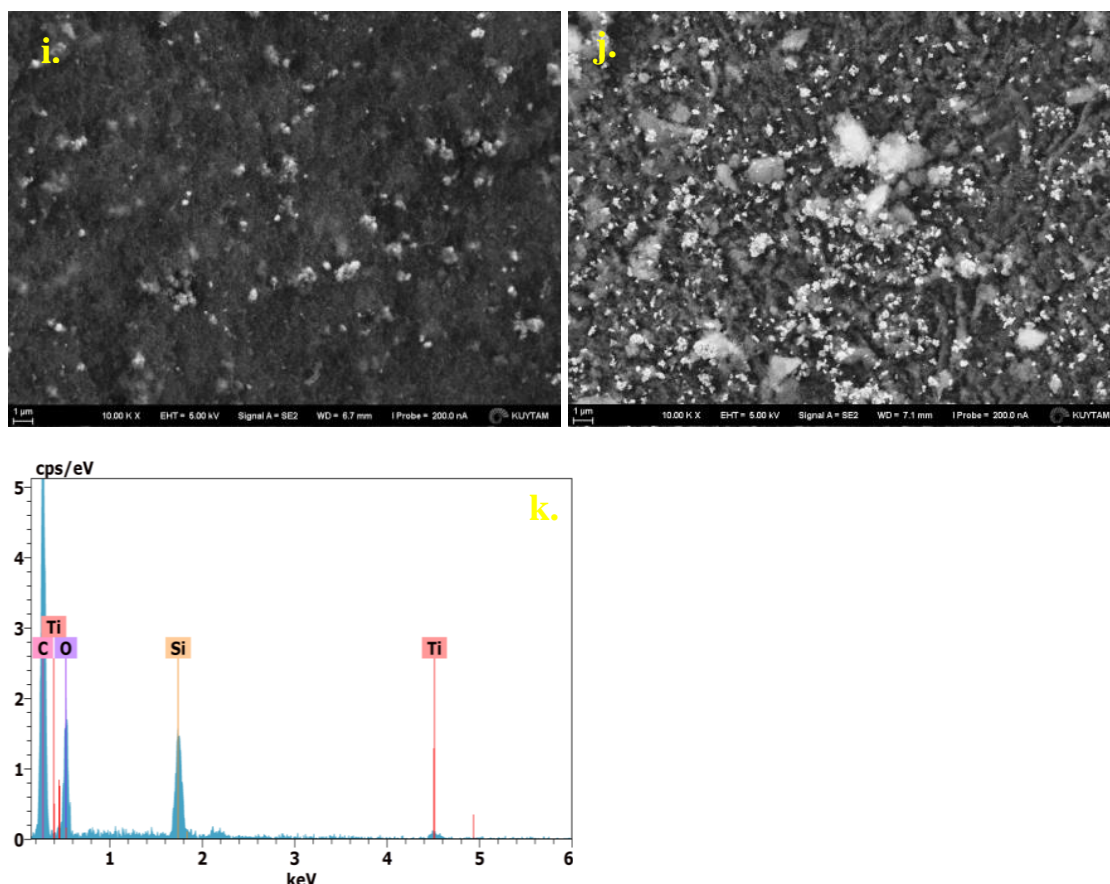


Figure 6.7. FESEM images of native silica aerogel and silica-titania aerogel composites. (a) FESEM images of the native silica aerogel (scale bar=200 nm). (b-c) FESEM images of anatase titania particles (scale bar=200 nm). (d-h) FESEM images of the silica-titania aerogel composites with increasing wt% of titania (scale bar=200 nm): 1, 14, 24, 32, 50 wt%, respectively. (i-j) FESEM images of silica-titania aerogel composites 24 and 50 wt % of titania, respectively (scale bar=1 μ m). (k) A typical EDX spectrum of the synthesized silica-titania composite.

One of the critical parameters, from the point of view of photocatalytic activity of the silica-titania composites, is the presence of anatase crystalline phase of the titania in the porous network of the composites. Figure 6.8 provides the X-ray diffraction patterns for the SiO_2 - TiO_2 composite aerogels with varying titania content and a native silica aerogel for comparison. XRD pattern of the native silica aerogel displays a hump in the range from 20° to 30° without any diffraction peaks due to amorphous structure of the silica aerogels. The silica-titania composite aerogels have thus both crystalline and amorphous phases. The intensity of the hump decreases, while the intensity of the

diffraction peaks increases with increasing amount of the titania in the structure. All the four studied aerogels with a titania content in the range from 12.5 wt % to 50 wt % exhibit sharp diffraction peaks at 25 °, 38 °, 48 °, 54 °, 55 °, 63 °, 69 °, 70 °, 75 ° and 83 ° due to the scattering from (101), (103), (004), (200), (105), (211), (213), (116), (220), (215) and (224) planes of anatase titania nanoparticles¹⁶⁸. However, the composite with 1 wt % of titania content demonstrates the weakening diffraction peaks corresponding to (101), (103), (004), (200), (105), (211) planes with a distinctive hump due to substantial fraction of the silica by weight. All peaks in the patterns of the composites were in good agreement with the XRD pattern of the anatase titania powder and standard spectrum (PDF 00-064-0863 TiO₂ anatase, nano - Titanium oxide). The patterns therefore suggest that anatase crystalline structure of the titania particles in the silicon dioxide network were stable during the sol-gel process and supercritical drying followed by HMDS-treatment at 112 ° C.

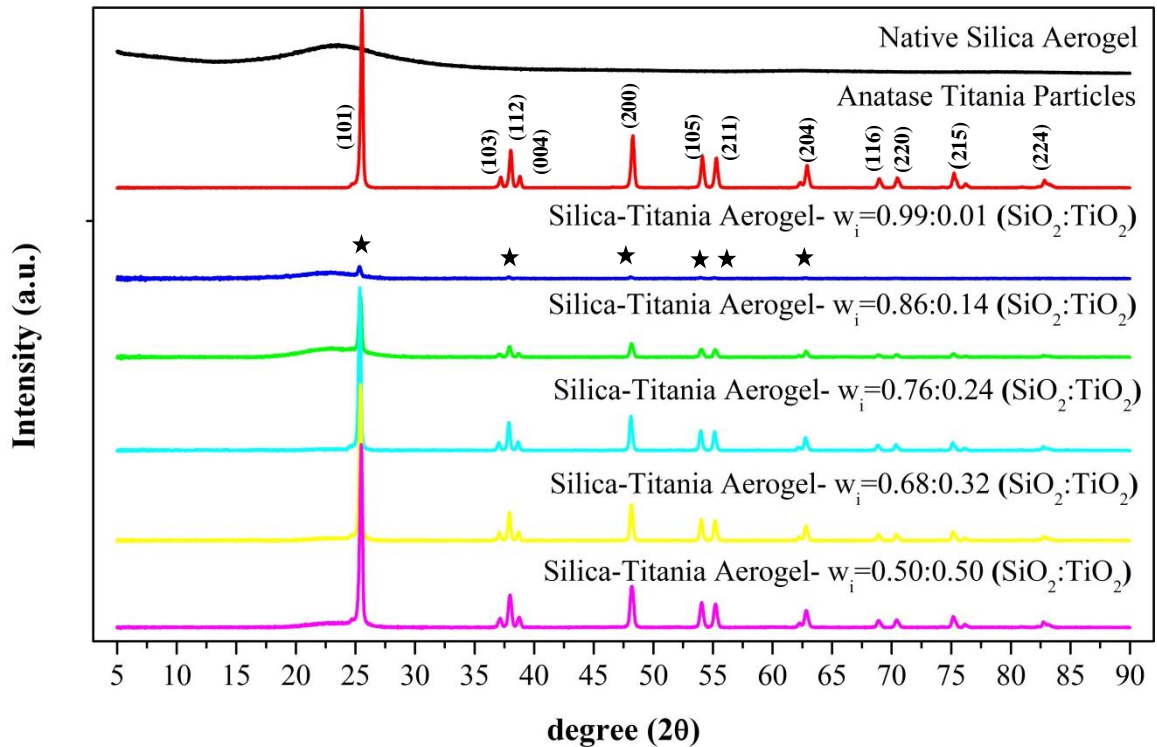


Figure 6.8. XRD patterns of native silica aerogel, silica-titania composites with increasing titania content from 1 to 50 wt % and anatase titania powder.

The crystallite size (D) could be determined by the Scherrer's formula ($D = K\lambda/(\beta \cos \theta)$) where λ is the wavelength of X-ray radiation ($\text{CuK}\alpha = 0.15406 \text{ nm}$),

K is a constant taken as 0.89, β is the line width at half maximum height (FWHM) of the peak, and θ is the diffracting angle. The (101) plane was chosen to calculate the crystalline size (either plane can be used for this purpose). The average crystallite size for the samples with increasing titania content are approximately 1.5 nm, 26 nm, 35 nm, 33 nm and 30 nm respectively. The average crystallite size for the anatase titania particle was calculated as 34 nm.

6.3.2 Optical Properties of SiO₂-TiO₂ Aerogel-based Microphotoreactor

One another significant parameter, from the point of view of photocatalytic activity, is the light-absorption properties of the SiO₂-TiO₂ composite aerogels. The Diffuse reflectance UV-Vis spectra (DRS) recorded for the silica-titania aerogel samples with the increasing titania content including the reflectance spectra of the native silica aerogel in the inset are shown in Figure 6.9a. The native silica aerogel show a reflection minimum in the UV region of the spectra which indicates an absorption maximum and a broadened reflection peak at around 300 nm and 400 nm which decreases along the visible region of the spectra. The reflection occurs from the pores and solid network of the silica with a size which is close to the wavelength of the incident light in this region. As to the composites, all samples demonstrated the same behaviour, yet different from the native silica aerogel. The samples exhibit a hump and reflection maxima at around 390 nm and the reflection decreases towards to the UV region making a minima at around 350 nm. This reflectance decrease could be attributed to the absorption due to the band-to-band transition of the titania.

Assuming the indirect allowed optical transition of TiO₂, the band gap energy of SiO₂-TiO₂ aerogel composites could be estimated from the Tauc plot calculated by Kubelka-Munk function from the DRS of the samples given in Figure 6.9a. The resulting plots given in Figure 6.9b have a distinct linear regime which represents the onset of the absorption of light. The extrapolation of this linear part to the axis yielded the energy of the optical band gap of the samples as shown in the inset in Figure 6.10b for the clarity. Using this technique, the anatase TiO₂ band gap was observed near expected value of ≈ 3.22 eV in agreement with the band gap of anatase titania reported in the literature for each sample with a slight difference. This band gap energy corresponds to the wavelength of 385 nm, which suggests that the photocatalyst can be

excited to generate e^-h^+ pairs by exposure of the light irradiation at the wavelength of 385 nm or below.

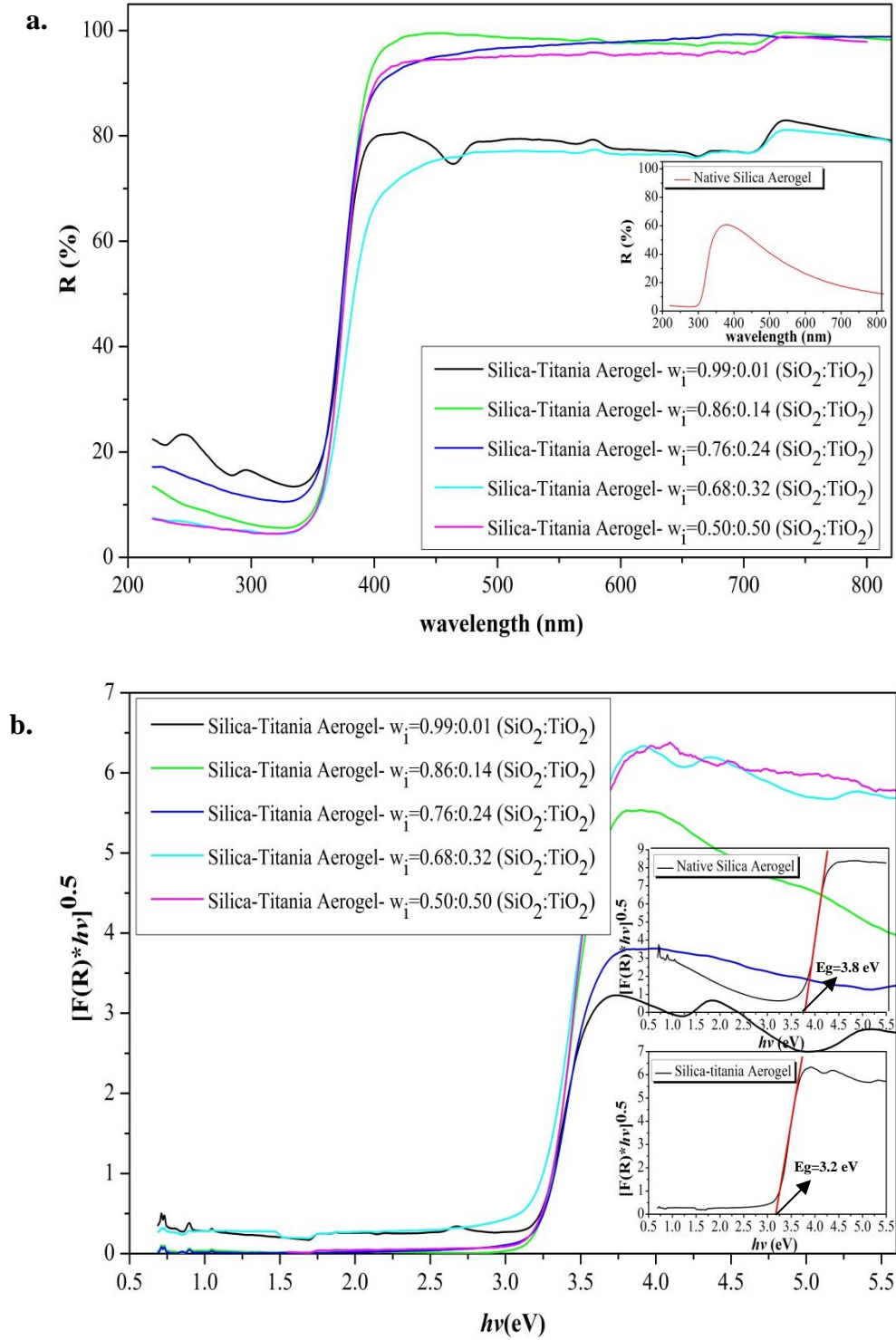


Figure 6.9. (a) DRS of the SiO₂-TiO₂ aerogel composites. The inset represents the diffuse reflectance spectra of the native silica aerogel. (b) Tauc plot of transformed

Kubelka Munk function versus the energy of the light absorbed for the SiO₂-TiO₂ aerogel composites. The inset (top) represents Kubelka Munk function vs. the energy of light absorbed of the native silica aerogel and the inset (bottom) is Kubelka Munk function vs. the energy of light absorbed for the SiO₂-TiO₂ aerogel composite with 32 wt% of titania.

The band gap of the sample with 32 wt% of titania slightly shifted to around 3.15 eV. The decrease in the band gap could be due to the presence of localized defect states in the band gap of titania. During transition of an electron from the top of the valence band into the bottom of the conduction band across the energy band gap, the electrons encounter disorder which causes to produce an absorption tail which extends deep into the forbidden gap. This tail of the absorption is called as Urbach tail and the associated energy as Urbach energy. The Urbach energy given in Equation 6.1 represents the quantitative characteristic and degree of static disorder on the structure and reflects the band tail extent of the density of electron states ¹⁶⁹⁻¹⁷¹.

$$\alpha = \alpha_0 e^{\left(\frac{E}{E_u}\right)} \quad \text{Equation 6.1}$$

where α is the absorption coefficient, E is energy of the photon ($h\nu$) and E_u is the Urbach energy.

Since the absorption coefficient is proportional to the absorbance (or F(R) in DRS mode), $\ln F(R)$ vs $h\nu$ (eV) could be plotted for the calculation of Urbach energy and provided in Figure 6.10 ¹⁶⁹. The reciprocal of the slope of the linear part below the optical band gap gave the Urbach energy for each sample. The energies were calculated as 62 meV, 51 meV, 54 meV, 84 meV and 51 meV, respectively for the silica-titania aerogel composites with the increasing titania content from 1 wt% to 50 wt%. The slight difference in Urbach energy was obtained as expected except from the sample with 32 wt% with the highest energy value which might suggest the formation of more defect pairs during probably the sol-gel process and the surface modification by HMDS. The defects might then lead to an increase in the disorder of the states in the sample.

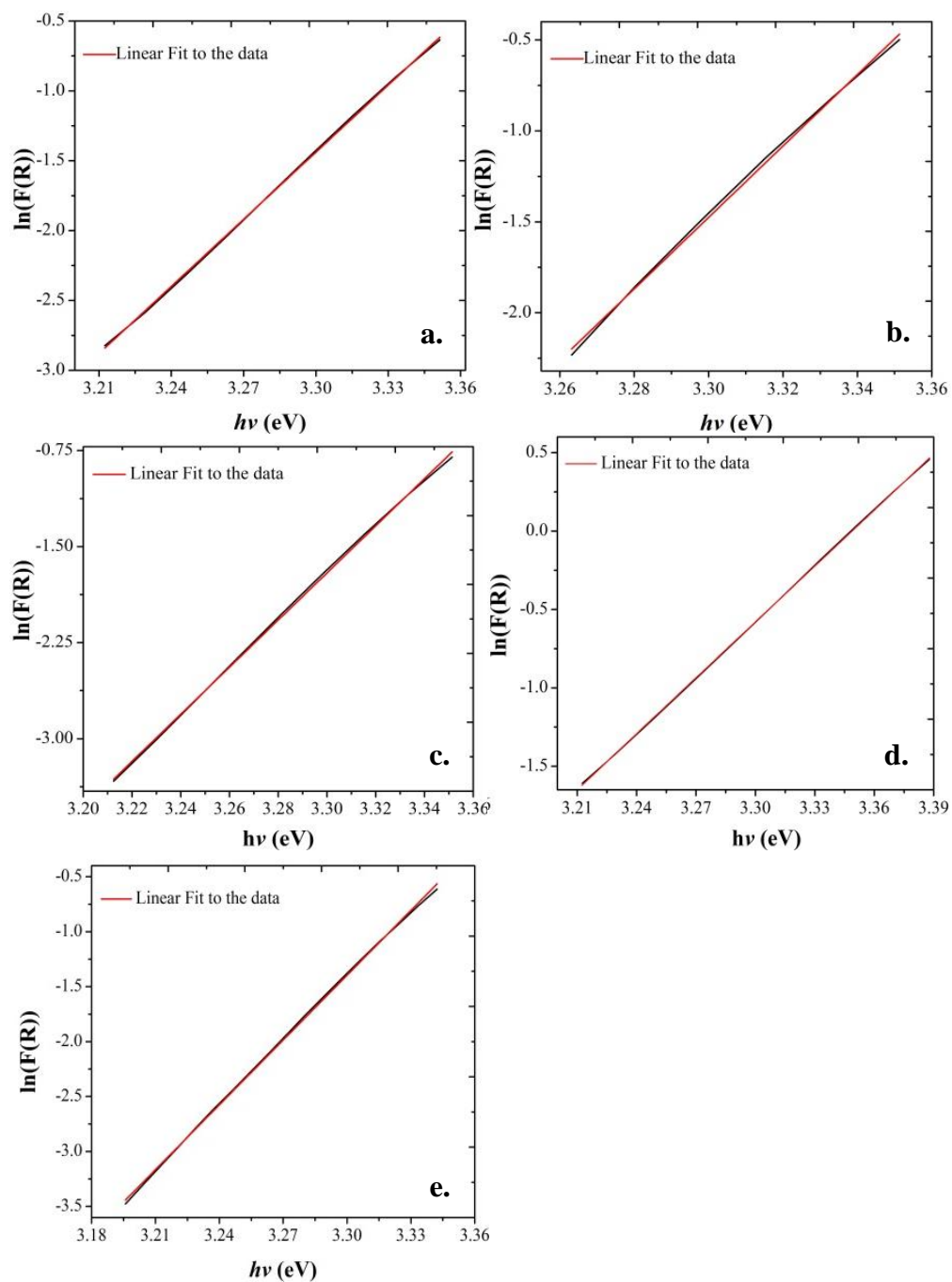


Figure 6.10. (a-e) Urbach energy plots for the silica-titania aerogel composites with increasing titania content from 1 to 50 wt%, respectively.

Finally, light propagation losses of the liquid-core optical waveguide constructed in the fabricated channels were quantified for the optical properties of the silica-titania aerogel to be used as an optical waveguide to efficiently confine and guide the light in the channels for the light-driven photocatalytic reactions. Since reactions will be carried out at 366 nm, the wavelength of the incident light was tuned to 366 nm

for the light propagation characterization in the channels and the channels were filled with water as aqueous phenol solution will be used as the reactant. The power of the optical fiber inserted into the bubble-free water-filled channel in the silica-titania aerogel composites was measured and the light emerging from the fiber guided through the channel and the power at the output of the water-filled channel exiting as a circular beam was then measured. The overall optical throughput of optical waveguides could be quantified by Equation 2.9 in terms of the input optical power, P_o , and the output power, $P(z)$, observed after the light has propagated a distance, z , along the waveguide axis. Therefore, the propagation loss of the waveguide, η , in the units of dB/cm could be calculated from Equation 2.10.

The calculated attenuation values in the samples with the titania content from 1 wt % to 50 wt % are given in Figure 6.11. The attenuation of light increased as the amount of titania embedded in the channel walls increases due to the absorption of the light by the titania. However, the propagation loss remained low and reasonable with increasing amount of titania and the silica-titania aerogel composites demonstrated to be promising to be used as optical waveguide. It increased from around 2.6 dB/cm for the sample with 1 wt % of titania to around 4 dB/cm for the sample with 50 wt % of titania.

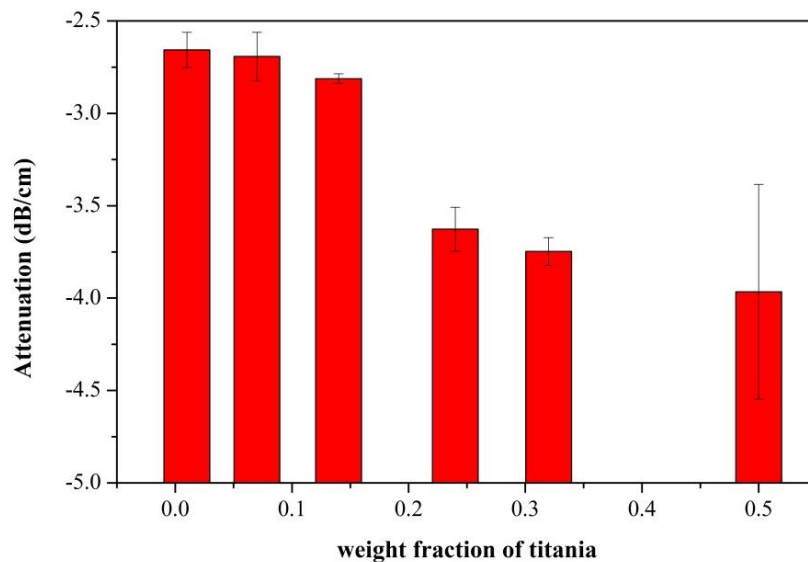
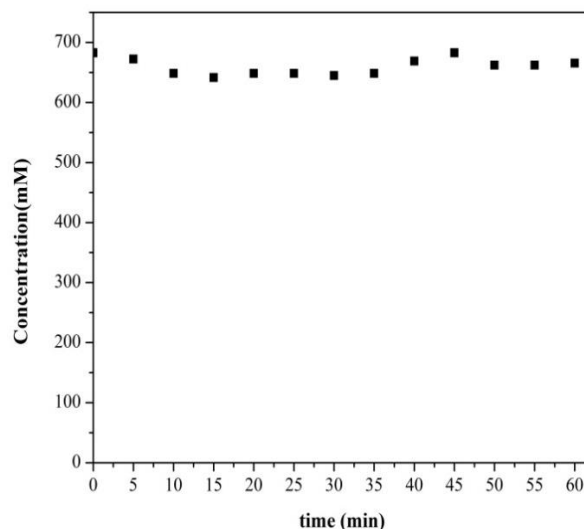


Figure 6.11. Light propagation loss in the water-filled channel in the silica-titania aerogel composites with titania content varying in the range from 1 wt% to 50 wt%.

6.3.3 Photocatalytic Reactions in Silica-Titania Aerogel-based Microphotoreactor

Photocatalytic performance of the fabricated $\text{SiO}_2\text{-TiO}_2$ aerogel-based microphotoreactors with integrated optofluidic waveguide was evaluated using phenol as a model organic compound and; therefore, photocatalytic degradation of the phenol was used as a model to test the reactor. The effects of reactant flow rate, amount of titania, incident light intensity and initial concentration of phenol on the photocatalytic degradation of the phenol were investigated in microphotoreactor with 50 wt% of titania. In the experiments, the samples were periodically collected from the exit stream of the reactor and the concentration of phenol in these samples was measured using a Nanodrop Spectrophotometer. Since phenol might be gradually adsorbed on the surface of the silica-titania aerogel channel, the concentration of phenol solution collected from the exit stream of the photomicroreactor at various times after starting the experiment might be lower than the initial concentration of the solution due to the adsorption rather than photocatalytic degradation. Therefore, prior to the photocatalytic reaction of phenol under illumination, the cylindrical channel fabricated 1.1 mm in diameter and 4.1 cm in length in the silica-titania aerogel composite was continuously fed with aqueous phenol solution with a concentration of 680 μM at 12.4 μLmin^{-1} in the dark for 60 min in order to find out if there is a decrease in phenol concentration due to adsorption. Figure 6.12a shows that the concentration of phenol solution flew in the dark remained almost constant for 60 min with a very little decrease, thus indicating that phenol was not adsorbed at the channel surface. Low affinity of phenol for the silica-titania aerogel surface may be attributed to the surface hydrophobicity, in combination with the fact that a very small amount of solid constitutes the actual liquid-aerogel interface. In addition to the adsorption, phenol concentration can be lower than the initial concentration of phenol since it can degrade by the absorption of the UV-light through the photolysis. To evaluate the occurrence of the phenol photolysis under illumination, the phenol solution (680 μM) were fed into the channel fabricated within the native silica aerogel (1.1 mm X 4.1 cm) without presence of the photocatalyst at 12.4 μLmin^{-1} under illumination at 366 nm and the power of 41 mW. It was found that phenol concentration remained almost constant during the UV-light exposure with a slight decrease, as shown in Figure 6.12b. The figure in Figure 6.12b reveals that phenol hardly degrades by the UV-light absorption.

a.



b.

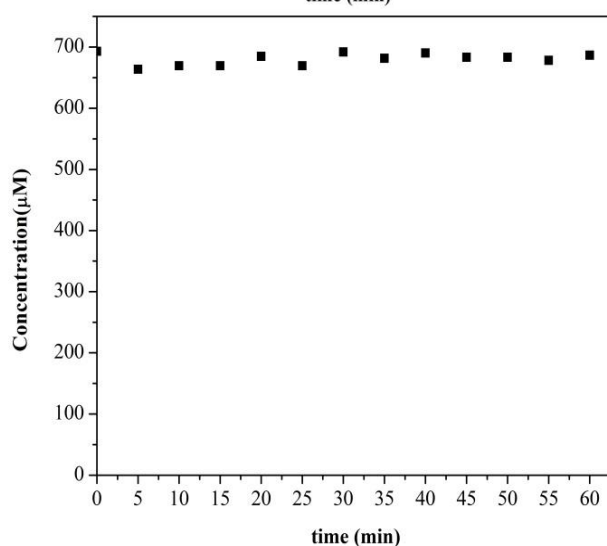


Figure 6.12. (a) Concentration of phenol in the exit stream of the silica-titania aerogel-based microphotoreactor (50 wt% titania) as a function of time in dark. (b) Concentration of phenol in the exit stream in the silica aerogel-based microphotoreactor as a function of time under illumination at 366 nm.

Subsequent to the investigation of phenol adsorption over the porous silica network with embedded anatase titania particles in the walls of the channel and photolysis of the phenol under UV-light illumination without photocatalyst, the performance of the microphotoreactor was tested using the phenol solution in water which was saturated with pure oxygen by continuous bubbling prior to the experiment. The phenol saturated with the oxygen with a concentration of 340 μM in water was continuously fed into the microphotoreactor with a flow rate of 14.3 μLmin^{-1} in dark in

the initial stage of the experiment. Figure 6.13a demonstrates that concentration of the phenol at the exit stream slightly decreased due to the adsorption of phenol by silica and titania in the channel walls and the system almost reached equilibrium after 60 min. At the end of the 60th min of the experiment in dark, the reactor was illuminated at 366 nm with the incident power of 65 mW for 60 min duration. Figure 6.13b demonstrated that phenol concentration at the exit stream decreased significantly due to the photocatalytic reaction of phenol over the titania surface and reached to the steady state in 30 min and acted as a typical plug-flow reactor. The decrease in the concentration indicated a phenol degradation of ~ 93%. When the laser was shut-down and while the reactant was constantly fed into the channel, the phenol concentration at the exit stream increased and reached to the initial stage of the experiment as shown in Figure 6.13c.

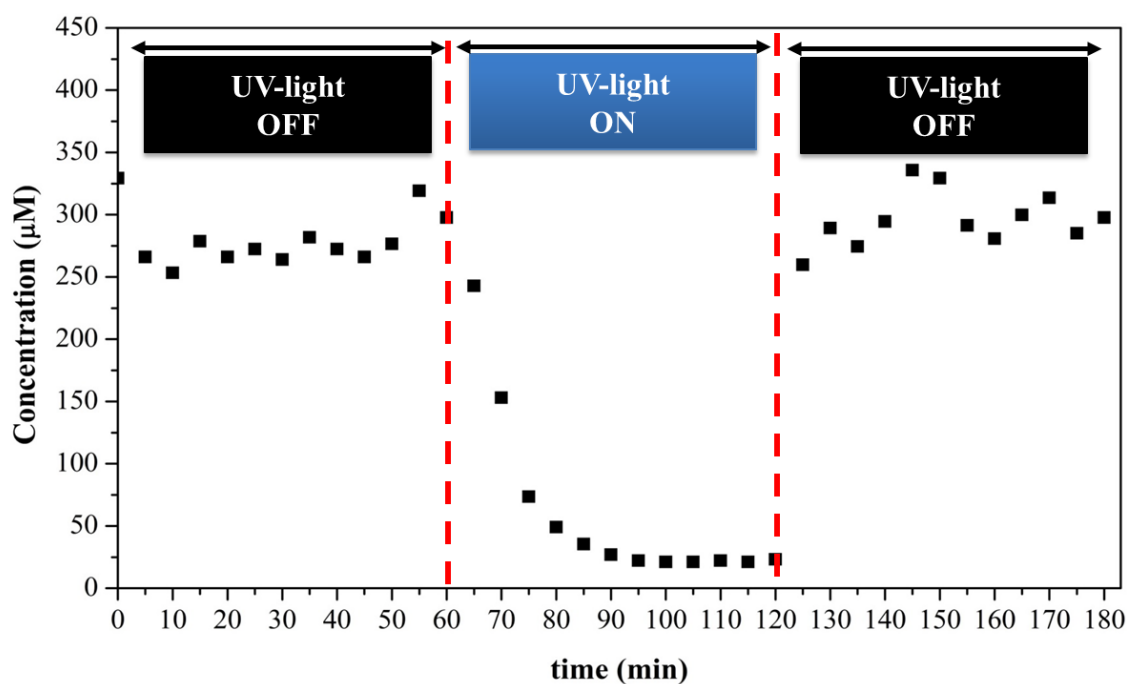
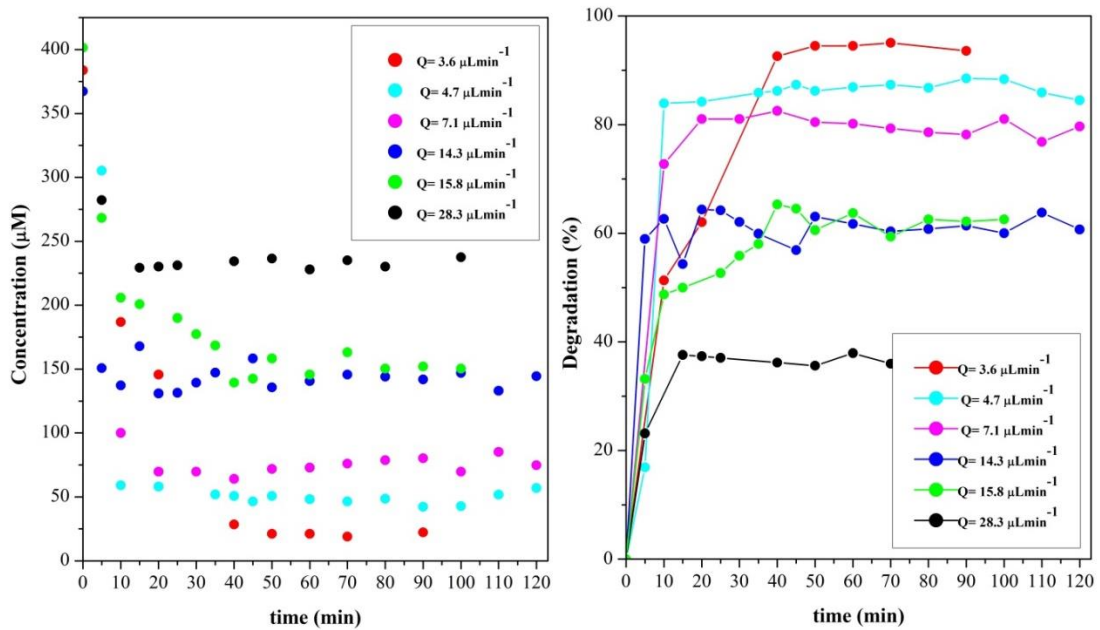


Figure 6.13. (a) Concentration of phenol in the exit stream of the silica-titania aerogel-based microphotoreactor (50 wt% titania) in dark. (b) Concentration of phenol in the exit stream in the silica aerogel-based microphotoreactor under illumination at 366 nm. (c) Concentration of phenol in the exit stream in the silica aerogel-based microphotoreactor in the dark after illumination.

6.3.4 Effect of Flow Rate on Photocatalytic Degradation of Phenol

The effect of reactant flow rate on the photocatalytic degradation of phenol was investigated by performing experiments with varying flow rates while keeping incident light power constant. The experiments were carried out using flow rates in the range from $3.6 \mu\text{Lmin}^{-1}$ to $28.3 \mu\text{Lmin}^{-1}$. The residence times of the flow rates changed from 16.9 min to 2.2 min, respectively. As shown in Figure 6.14a, the phenol concentration of the exit stream decreased and reached steady state within varying times depending on the varying flow rates; however, the degradation of phenol decreased with increasing flow rate as expected and given in Figure 6.14b due to the decreasing residence time. The reaction occurred with the flow rate of $3.6 \mu\text{Lmin}^{-1}$ provided the highest photocatalytic degradation, while the flow rate of $28.3 \mu\text{Lmin}^{-1}$ resulted in the lowest photocatalytic conversion of the phenol. The flow rates in between provided the degradation efficiencies between these values with the inverse relation.



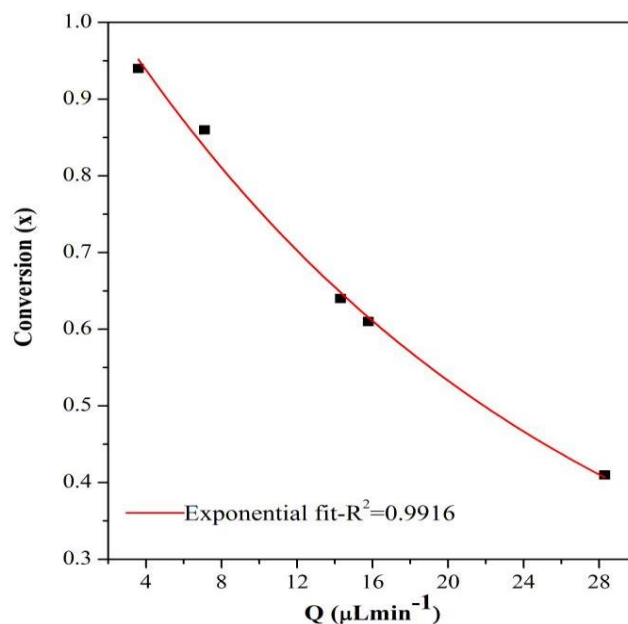


Figure 6.14. (a) Time variation of the concentration of phenol in the exit stream in the silica aerogel-based microphotoreactor with varying reactant flow rate under illumination at 366 nm and incident power of 41 mW. (b) The corresponding percent degradation of phenol with varying flow rates. (c) The variation of phenol conversion with varying reactant flow rates.

6.3.5 Effect of photocatalyst amount on photocatalytic degradation of phenol

The amount of the photocatalyst in the walls of the channels in the microphotoreactors is another important factor in the photocatalytic degradation of phenol. The fabricated microphotoreactors prepared by titania with 1 wt%, 14 wt% and 50 wt% were employed to evaluate their performance by pumping the phenol solution in water (368 μM) with a flow rate of 14.3 μLmin⁻¹ at the incident light power of 41 mW at 366 nm. As demonstrated in Figure 6.15a and Figure 6.15b, higher catalyst loading yielded an increase in the photocatalytic degradation efficiency with higher decrease in the phenol concentration within a certain period time. The concentration of phenol decreased noticeably in channel in the reactor prepared by 50 wt% as compared to the two other reactors; and therefore, the conversion of phenol is the highest with ~ 60%. The sample with 1 wt% and 14 wt% of titania resulted in the conversion of ~ 15% and ~ 60%, respectively. This can be justified by the increase of the number of photon absorbed and resulting in the increase of number of e⁻-h⁺ pairs.

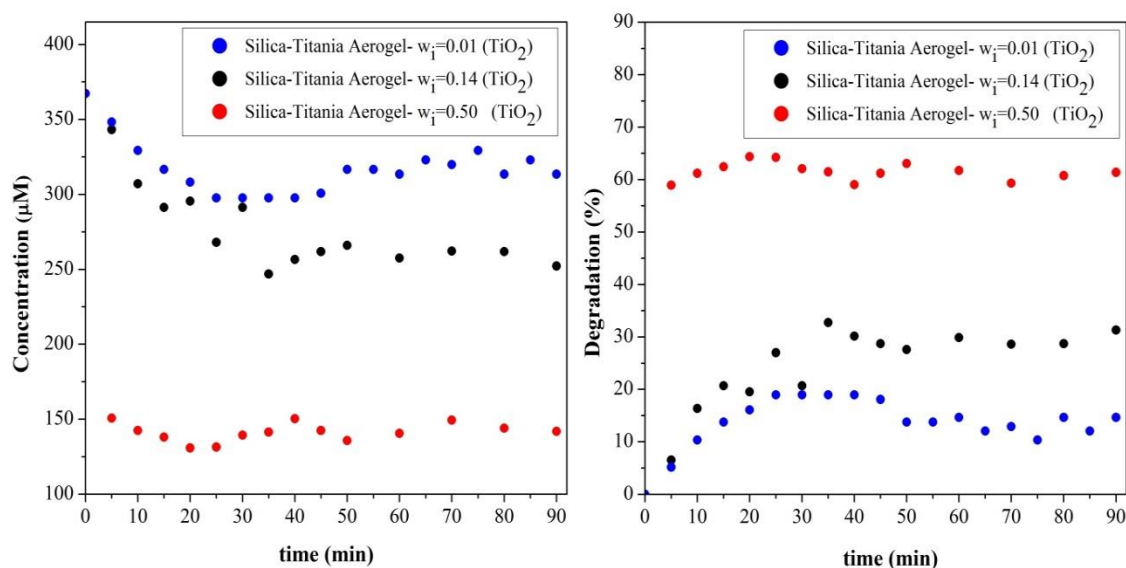


Figure 6.15. (a) Time variation of the concentration of phenol in the exit stream in the silica aerogel-based microphotoreactor with varying reactant flow rate under illumination at 366 nm and incident power of 41 mW. (b) The corresponding percent degradation of phenol in varying amount of titania.

6.3.6 Effect Of Dissolved Oxygen on Photocatalytic Degradation of Phenol

Oxygen is an indispensable reactant in the photocatalytic degradation to generate highly reactive oxygen radicals which play the key role in the photocatalytic degradation of organic molecules; therefore, the effect of oxygen on the photocatalytic degradation of phenol was investigated. The reactant solutions with concentration of 400 μM were prepared by either saturating oxygen in the solution by bubbling or using distillate water containing only dissolved oxygen in water without bubbling. The reactant was pumped to the microphotoreactor with a flow rate $14.3 \mu\text{Lmin}^{-1}$ and the incident light power of 61 mW at 366 nm in the experiments. Figure 6.16a and Figure 6.16b show that the concentration of phenol gradually decreased and reached to the steady state within about 30 min and the corresponding percent degradation was obtained as 89%. However, the additional supply of oxygen into the solution did not significantly affect the degradation efficiency. The concentration decrease with time demonstrated very similar trend which is given in Figure 6.16a in the presence of the saturated oxygen and the degradation of phenol increased to 92% with only slight enhancement of 3% as shown in Figure 6.16b. This indicates that dissolved oxygen in

water might provide sufficient electron scavengers to accelerate the photocatalytic degradation under irradiation at 366 nm and with a power of 65 mW. This may be related to the fact that the low initial concentration of phenol might require only a low amount of oxygen. According to the results, it can be pointed out that rate of reaction is zeroth order with respect to the oxygen concentration.

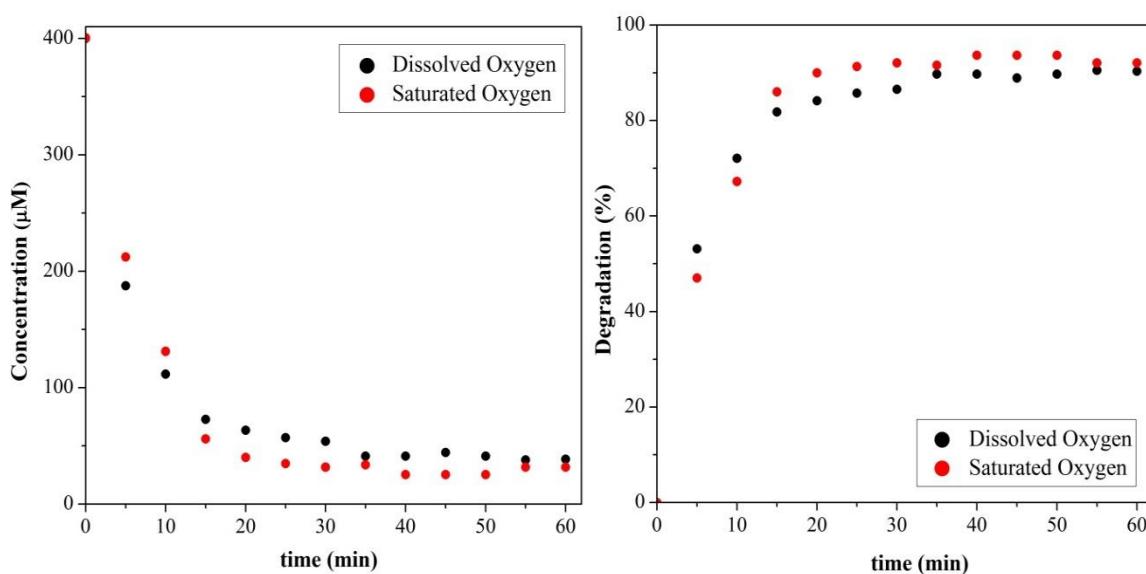


Figure 6.16. (a) Time variation of the phenol concentration with varying oxygen concentration. (b) The corresponding percent degradation of phenol in varying oxygen concentration.

6.3.7 Effect of light power on photocatalytic degradation of phenol

Effect of incident light power on the photocatalytic degradation of phenol was studied by tuning the light emerging from the optical fiber at 366 nm with the power in the range from 9.4 mW to 67 mW at the constant flow rate of $14.3 \mu\text{Lmin}^{-1}$. Figure 6.17a shows the phenol concentration as a function of irradiation time as the incident light power increased and photocatalytic degradation of phenol increased with increasing incident light power and correspondingly, the phenol conversion increased exponentially with increasing incident power; as shown in Figure 6.17b and Figure 6.17c. The highest incident light power of 67 mW yielded the highest conversion of phenol as 94%; however, the lowest light power yielded the lowest photodegradation of phenol as ~20% as expected. Since the light power increases, number of photons

absorbed by the titania increases, which results in increase in e^-h^+ pair formation in the photocatalyst surface; and therefore, the number of highly active radicals increases.

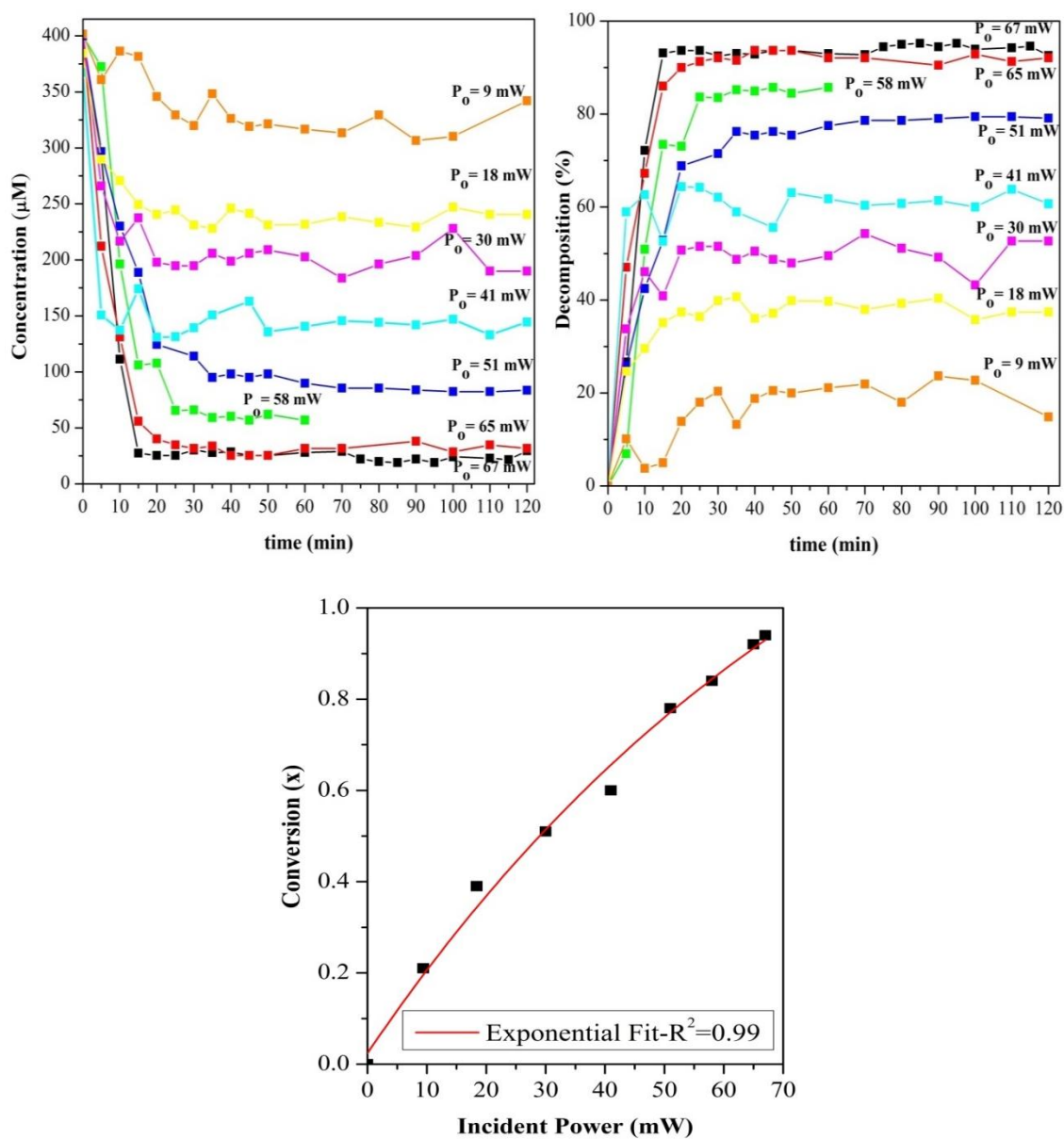


Figure 6.17. (a) Time variation of the phenol concentration with varying incident light power. (b) Corresponding percent degradation of phenol with varying incident light power with time variation. (c) Corresponding conversion of phenol with varying incident light power.

6.3.8 Photocatalytic Transformation of Phenol In Carbon Nanotube Silica and Titania Composite Aerogel-Based Optofluidic Microphotoreactors

Carbon nanotubes (CNTs) were embedded into the silica-titania composite aerogels to investigate the efficacy with which anatase nanocrystalline titania and silica composites to reduce the charge recombination and hence enhance the efficiency of the photocatalysis. The composite aerogels were prepared by the sol-gel method in the way given in Figure 6.2. (-OH) functionalized single-walled CNTs ($D_{\text{avg}}=1$ nm, Length= 0.5-2 μm) and (-COOH) functionalized multi-walled CNTs (OD=8-18 nm and ID=5-10 nm, Length= 0.5-2 μm) were used to prepare composites with a equal weight fraction of $\text{SiO}_2\text{:TiO}_2$ and varying the CNT fraction in the range from 0.01 to 0.05 in the network. CNTs and anatase titania particles were dispersed in the solvents with varying mass of CNTs and dried by the supercritical drying. The resulting monolithic composite aerogels were treated by HMDS to convert the skeleton surface to hydrophobic in the same way used in the silica aerogels and silica-titania composite aerogel treatment. A straight channel was fabricated using the drilling technique used in the silica aerogels and silica-titania composite aerogels. Figure 6.18 shows the monolithic silica-titania composite with embedded SWCNTs with 1 wt% (Length= 6.1 cm Diameter= 1.41 μm) which is connected to the fluidic connection for reactant flow and optical fiber coupling. The channel fabricated in the monolith is in the length of 6.1 cm and the diameter of ~ 1.1 mm.

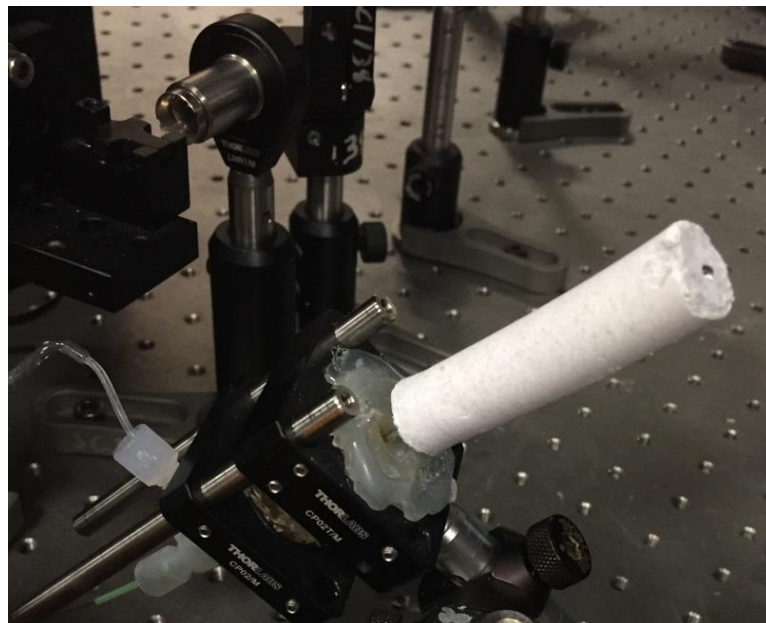


Figure 6.18. A photograph of a monolithic silica-titania composite aerogel with embedded SWCNTs in 1 wt%.

The effect of incorporation of CNTs into the network on the pore characteristics of the samples such as surface area, pore volume and pore size distribution and density of the composites were investigated by analyzing the N₂ adsorption–desorption isotherms. The analysis results were summarized in

Table 6.3 together with densities. With increasing titania content, densities of the samples increased as expected, whereas total pore volumes decreased. However, the synthesized aerogel monoliths retained their pore volume as well as high surface area. BET surface area showed an increase with increasing amount of CNT from 339 to 432 m²/g in the sample with 1 wt % of CNT to 5 wt %. The average pore radius of the samples remained almost constant with the increasing CNT content. Furthermore, the N₂ adsorption–desorption isotherms of composite aerogels with varying CNT content in the range from 1 to 5 wt % in Figure 6.19 reveal that the resulting composites showed type-IV isotherms with the H1 type hysteresis loop and thus retained the mesoporous structure of the silica aerogels.

Table 6.3. Densities and pore characteristics of synthesized silica-titania composite aerogels.

<i>wt % CNT</i>	<i>Density (g/cm³)</i>	<i>BET Surface</i>	<i>Total Pore</i>	<i>BJH Desorption</i>
		<i>Area (m²/g)</i>	<i>Volume (cm³/g)</i>	<i>Average Pore Radius (nm)</i>
1 (SWCNT)	0.22	339	1.67	25.4
3 (SWCNT)	0.24	423	1.59	27.3
5 (MWCNT)	0.26	432	1.4	24.2

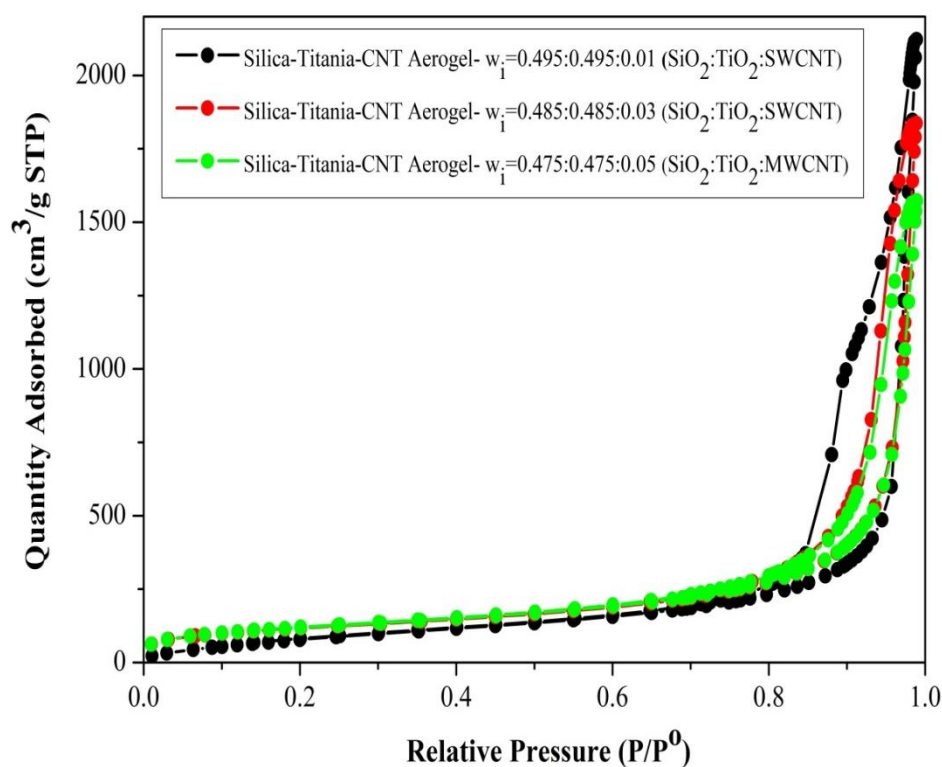


Figure 6.19. N₂ adsorption/desorption isotherms for the silica aerogel and silica–titania composite aerogels.

The presence of CNTs in the TiO₂/CNT composites and the surface morphology of the composites were characterized by FE-SEM. Figure 6.20 demonstrates the FE-

SEM images of the composites with CNTs comprising from 1 wt% to 5 wt%. The images show that CNTs were successfully introduced into the interconnected mesoporous structure of the silica aerogel during the sol-gel step of the aerogel synthesis. Furthermore, there is no significant change observed in the mesoporous structure of the silica-titania aerogels with the increase of the CNT content and the composite aerogels' network structure is highly porous and the porous morphology is clearly visible from the images. The images show that composites were made up of a random mixture of titania nanoparticles and CNTs. The CNTs were embedded into the network as randomly distributed bundles. The images of the samples with 1 wt% of SWCNTs demonstrate that some of the anatase titania particles grew over the bundles with silica network as the agglomerated spherical clusters and in contact with the bundles. The clusters were also identified by EDX measurement obtaining a typical spectrum in Figure 6.20d. The images indicate that SWCNT assembly can provide better dispersion and support for the anatase titania as compared to the MWCNTs. The silicon dioxide network appear to grow over the bundles in the aerogel with 5 wt% of MWCNTs without titania particles.

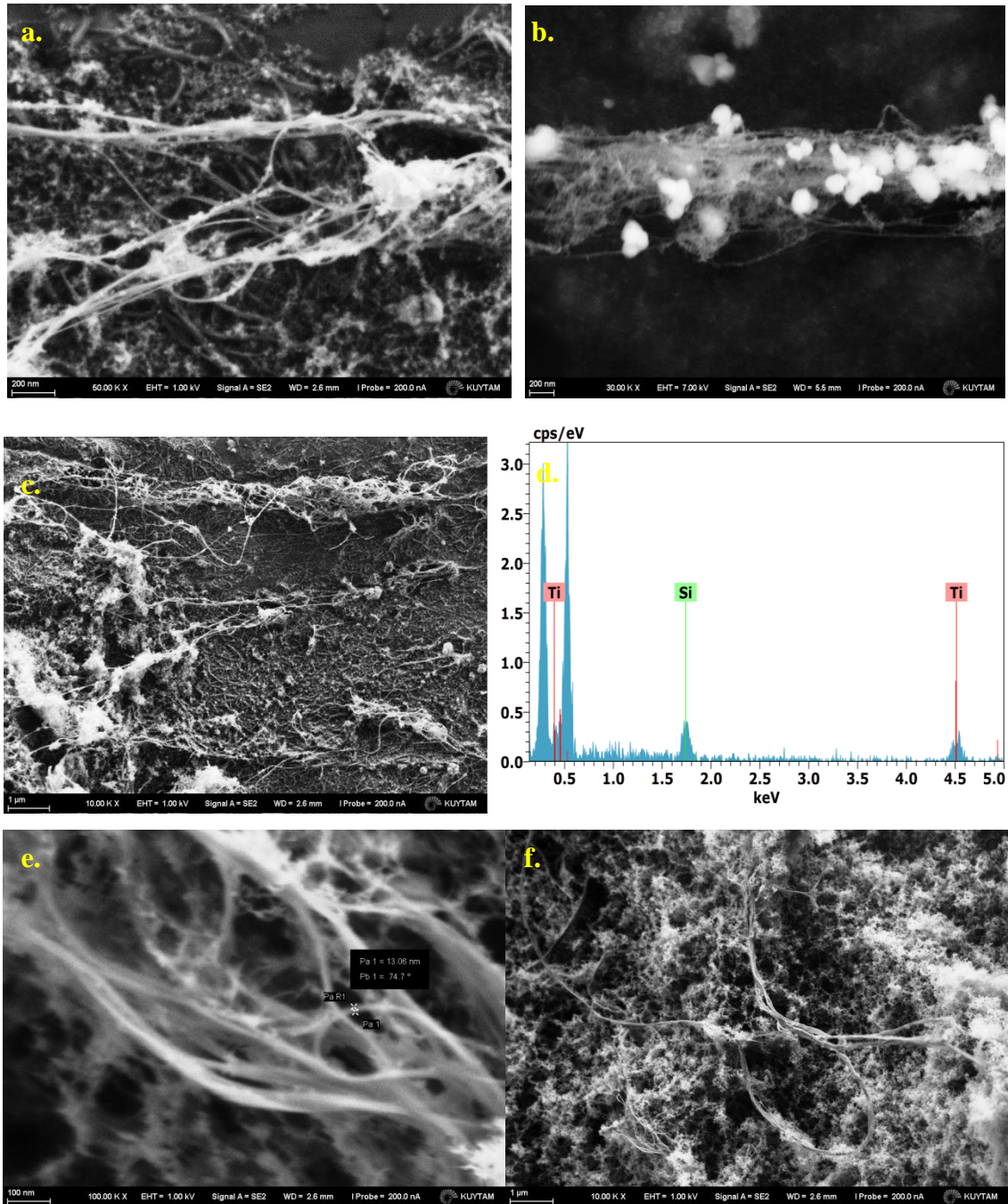


Figure 6.20. FESEM images of silica-titania aerogel composites with embedded CNTs with increasing weight percent. **(a-b)** FESEM images of the aerogel composites with 1 wt% of SWCNTs (scale bar=200 nm) **(c)** FESEM images of the silica-titania aerogel composites with 1 wt% of SWCNTs (scale bar=1 μ m). **(d)** EDX spectrum of silica-titania composite with 1 wt% of SWCNTs. **(e-f)** FESEM images of silica-titania aerogel composites 5 wt% of MWCNTs (scale bars=100nm and 1 μ m, respectively).

Figure 6.21 provides the X-ray diffraction patterns for the $\text{SiO}_2\text{-TiO}_2$ composite aerogels with varying CNT content. All the studied aerogels exhibited sharp diffraction peaks as the silica-titania composite demonstrated at 25° , 38° , 48° , 54° , 55° , 63° , 69° , 70° , 75° and 83° due to the scattering from (101), (103), (004), (200), (105), (211), (213), (116), (220), (215) and (224) planes of anatase titania nanoparticles without showing the characteristic peaks of CNTs.

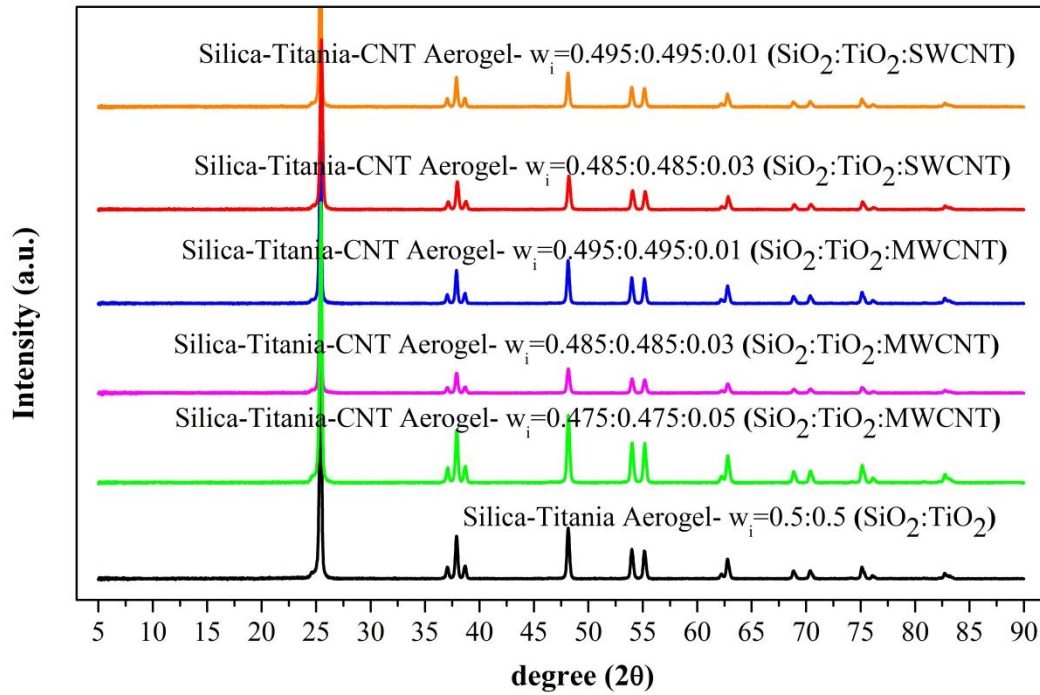


Figure 6.21. XRD patterns of native silica aerogel, silica-titania composites with increasing CNT content from 1 to 5 wt %.

The band gap energy of $\text{SiO}_2\text{-TiO}_2$ aerogel composites could be estimated from the Tauc plot in Figure 6.22 calculated by Kubelka-Munk function from the DRS of the samples. Using this technique, the band gap was observed near value of ≈ 3.22 eV.

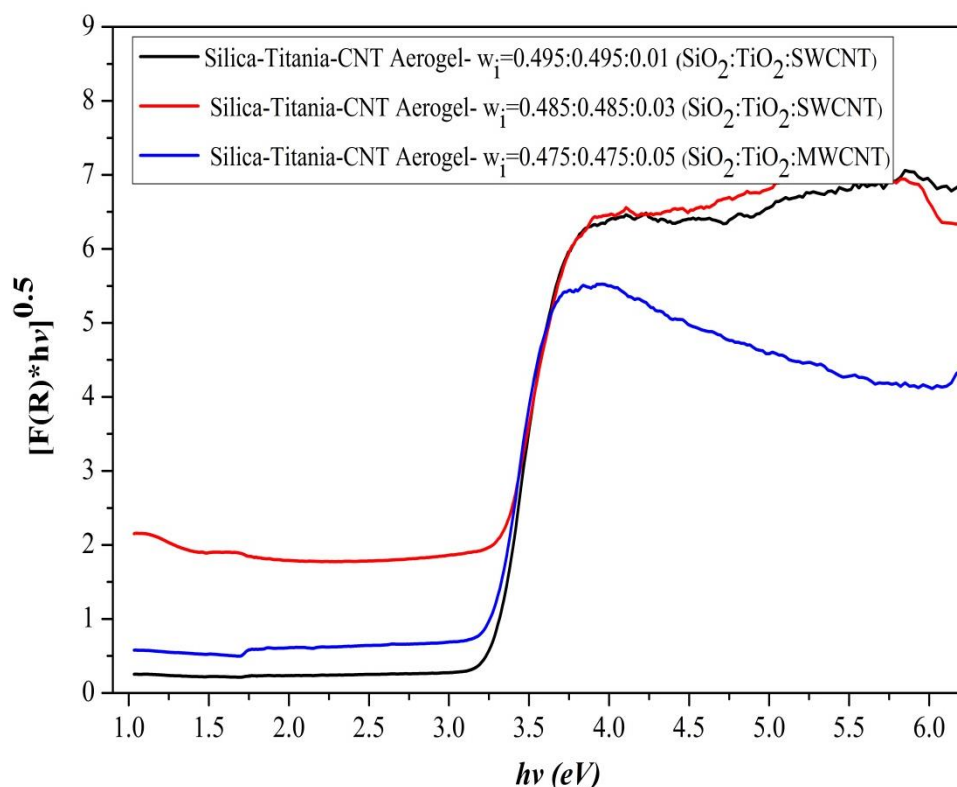


Figure 6.22. Tauc plot of transformed Kubelka Munk function versus the energy of the light absorbed for the SiO₂-TiO₂-CNTs aerogel composites.

Finally, the function of CNTs on the photocatalytic degradation was tested by phenol degradation in the fabricated channels in the samples with 1 wt% of SWCNTs and MWCNTs. The phenol solution in water saturated with the oxygen with a concentration of 340 μM was continuously fed into the microphotoreactor with a flow rate of 14.3 μLmin^{-1} with an incident power of 41 mW at 366 nm. However, a positive photocatalytic effect from simply mixing CNTs with TiO₂ presumably was not obtained. Figure 6.23 demonstrates that silica-titania composites exhibit better photocatalytic efficiency than the composites with CNTs. This may be attributed to decrease the CNTs interphase contact at the titania surface, which hinders its reactive surface. One another possible reason may be light attenuation by the CNTs. The results also reveal that a large fraction of the concentration of the phenol is reduced in dark and the change in concentration is lower in the illumination. This may be due to the adsorption of phenol on the CNTs. The sample with SWCNTs showed slightly higher degradation of phenol and adsorption capacity as compared to the sample with MWCNTs, while the phenol adsorption in the composite of silica and titania is far

lower. On the other hand, this part of the study needs to be extended to elucidate this behavior of the composites and try to improve their synthesis to obtain the $\text{SiO}_2/\text{TiO}_2/\text{CNTs}$ arrangement that optimizes their interaction to increase active surface area of titania and hindered charge recombination.

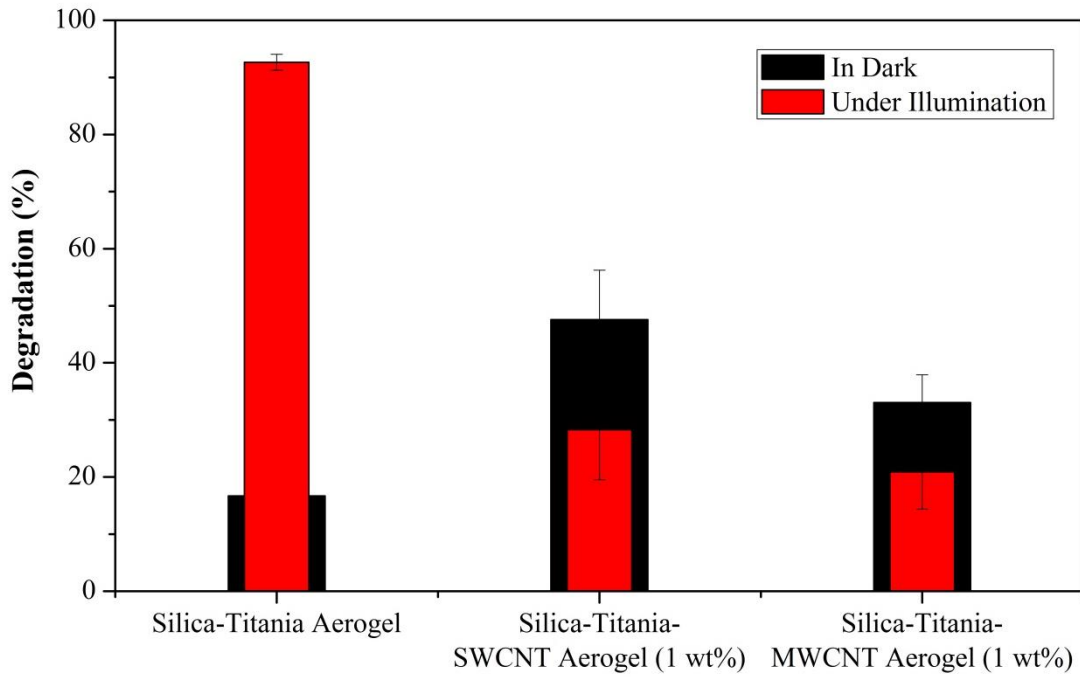


Figure 6.23. Phenol degradation in silica-titania composite aerogel ($w_i=0.5:0.5$ $\text{SiO}_2:\text{TiO}_2$) and silica-titania-CNTs composite aerogel ($w_i=0.495:0.495:0.01$ $\text{SiO}_2:\text{TiO}_2:\text{CNTs}$)

6.3.9 Model Study In Fabricated Microphotoreactors

Figure 6.24 demonstrates the schematic representation of the model in the aerogel-based microphotoreactor. The reactor with the single channel was divided into two domains: the fluid phase and the immobilized photocatalyst layer.

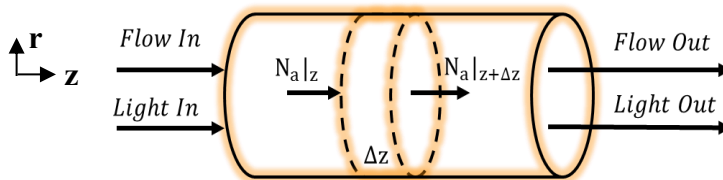


Figure 6.24. Schematic representation of 1D model in the aerogel-based microphotoreactor with photocatalyst deposited channel.

Conversion of phenol was derived from a mass balance over a differential volume in the cylindrical channel at steady state. The mass balance includes the transportation of phenol by convective mass transfer from the fluid phase to the immobilized photocatalyst surface (at the interface between fluid phase and solid phase) and the reaction on the photocatalyst surface. The material balance which is given in Equation 6.2. The governing equation on the catalyst comprises reaction including light intensity dependency. The material balance for the phenol at the photocatalyst surface results in Equation 6.3 where the mass transfer flux through convection across the boundary layer is equal to rate of reaction at the surface.

$$-v_z \frac{dC_i}{dz} = k_c \frac{4}{D} (C_i - C_{i,s}) \quad \text{Equation 6.2}$$

$$-r_i'' = k_c (C_i - C_{i,s}) \quad \text{Equation 6.3}$$

where C_i is concentration of phenol in the fluidic phase, (μM), $C_{i,s}$ concentration of phenol at the titania surface, (μM), v_z is average velocity of fluid in the channel, (cm/min), k_c is external mass transfer coefficient, (cm/min), D is channel diameter, (cm).

The rate of reaction is expressed by Equation 6.4¹⁷²⁻¹⁷³. The reaction rate is assumed to be the first order with respect to the phenol concentration and dependency of the absorbed light intensity on the reaction rate is expressed to be n which will be regressed from the experimental data. The concentration of phenol at the titania surface is then written by Equation 6.5:

$$-r_i'' = k(\lambda)_{app} I_a^n C_{i,s} \quad \text{Equation 6.4}$$

where absorbed light intensity by the photocatalyst, I_a , is defined by $I_a = I * \varepsilon$ in which I is propagated light intensity and ε is absorption coefficient of anatase titania (cm^{-1}), $k(\lambda)_{app}$ is apparent rate constant (cm^3/mWmin).

$$C_{i,s} = \frac{k_c}{k_c + k(\lambda)_{app} I_a^n} * C_i \quad \text{Equation 6.5}$$

Equation 6.2 is eventually written as Equation 6.6 which represents conversion of phenol at the channel output ($z=L$).

$$x = 1 - \exp\left(\frac{-4Lk_c}{Dv_z}\left(1 - \frac{k_c}{(I\varepsilon)^n k(\lambda)_{app} + k_c}\right)\right) \quad \text{Equation 6.6}$$

External mass transfer coefficients in the monolith reactors are usually described by using dimensionless parameter called Sherwood number, Sh . This parameter is used to define the ratio between convective and molecular (diffusion) transport properties over the entire reactor length. An empirical correlation given in Equation 6.7 developed by Giani *et al.*¹⁷⁴⁻¹⁷⁵ for catalyst-wash coated open-celled metal foams with three dimensional interconnected structure used in gas-solid catalytic processes with high porosities was used to calculate mass transfer coefficient.

$$Sh = 1.16 (Re)^{0.43} (Sc)^{1/3} \quad \text{Equation 6.7}$$

$$Re = \frac{Dv_z\rho}{\mu} \quad \text{Equation 6.8}$$

$$Sc = \frac{\mu\rho}{D_{phenol-water}} \quad \text{Equation 6.9}$$

$$Sh = \frac{Dk_c}{D_{phenol-water}} \quad \text{Equation 6.10}$$

where Re represents Reynolds number, Sc indicates Schmidt number, ρ and μ are fluid density, (g/cm^3), and viscosity, ($g/cm/min$), respectively and $D_{phenol-water}$ is binary diffusion coefficient of phenol in water, (cm^2/min).

ε , $k(\lambda)_{app}$ and n were determined by exponential regression model using Equation 6.6. The parameters were extracted from the exponential fit to the experimental conversion data at $z=L$ at steady state with varying light intensities. The propagated light intensity, I , in Equation 6.6 was described in Equation 6.11 by measured propagation losses given in Figure 6.11. and using Equation 2.9 and Equation 2.10.

$$I = P_o \frac{4}{\pi D^2} e^{\left(\frac{2.303}{10}\eta L\right)} \quad \text{Equation 6.11}$$

The exponential regression, shown in Figure 6.25 demonstrated that model and experimental data is in a good agreement; particularly until the absorbed light intensity of $\sim 0.375 \text{ mW/cm}^2$ and the model yielded $k(\lambda)_{app}$, ε and n as 0.098, 0.0029 and 1.5, respectively. A more relevant and comparable empirical correlation to our system for estimation of external mass transfer coefficient might improve the results.

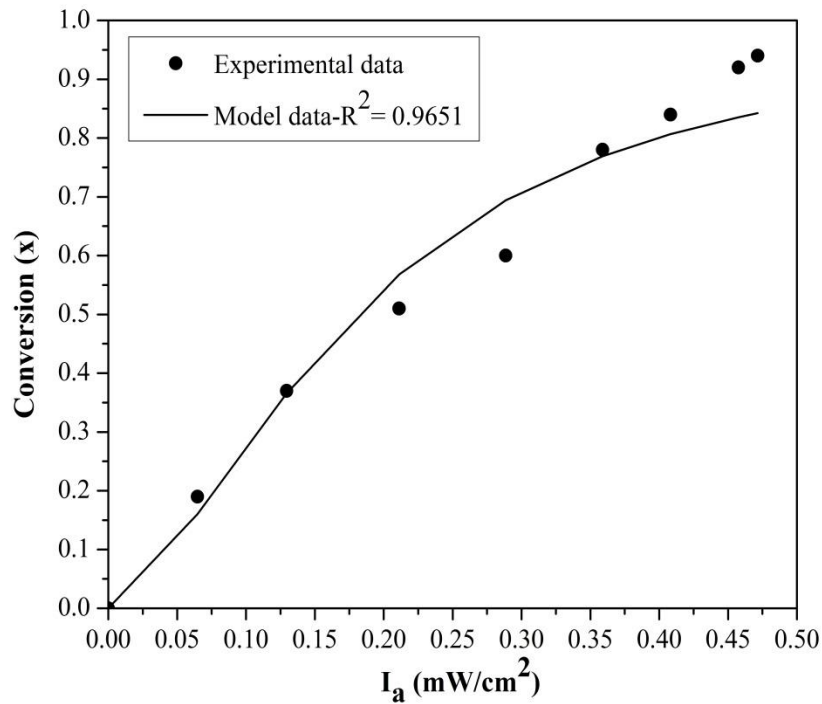


Figure 6.25. The comparison of model and experimental data of phenol conversion at varying absorbed light intensity by titania.

The differential equation in Equation 6.2 which represents the phenol concentration in the fluid phase and at the catalyst surface at steady state along the channel length was numerically solved using regressed parameters, for the reaction with the phenol flow rate of $14.3 \mu\text{Lmin}^{-1}$ and at 41 mW of incident power in the silica-titania aerogel with 50 wt% of titania. The model revealed that the model equation should consist of a parameter accounting for surface properties of channel including titania and silica. This parameter was included in the model equation as a multiplier of the term, $(I_a)^n$, Figure 6. 26. shows that surface concentration of phenol increases along the channel while the concentration of phenol gradually decreases along the length of the channel and therefore, the conversion of phenol along the channel which is shown in Figure 6. 27 steadily increased and the conversion at $z=L$ yielded 0.6 with a good match with the experimental data.

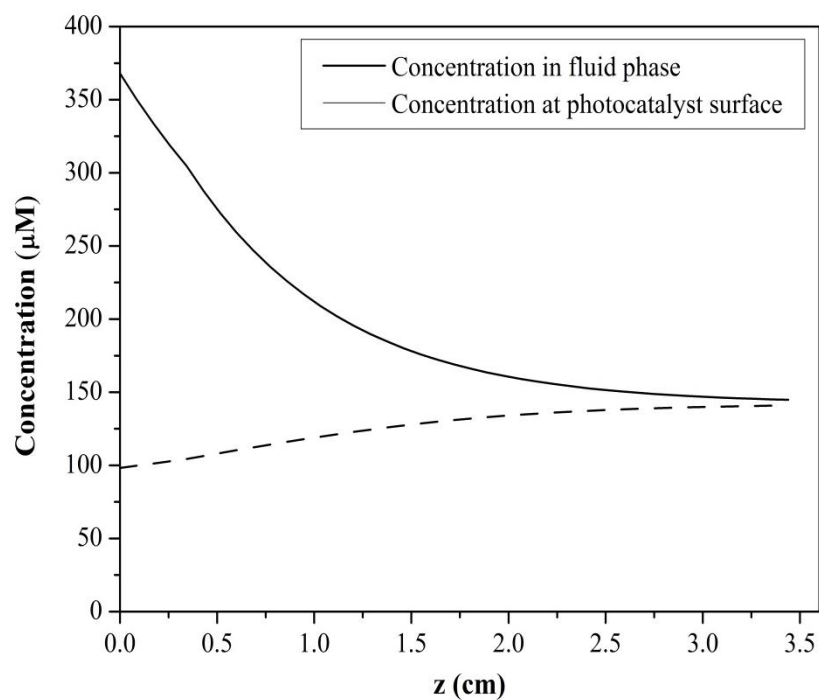


Figure 6. 26. The variation of phenol concentration along the length of the channel in the microphotoreactor. ($C_o=368 \mu\text{M}$, $Q = 14.3 \mu\text{Lmin}^{-1}$ and $P_o= 41 \text{ mW}$)

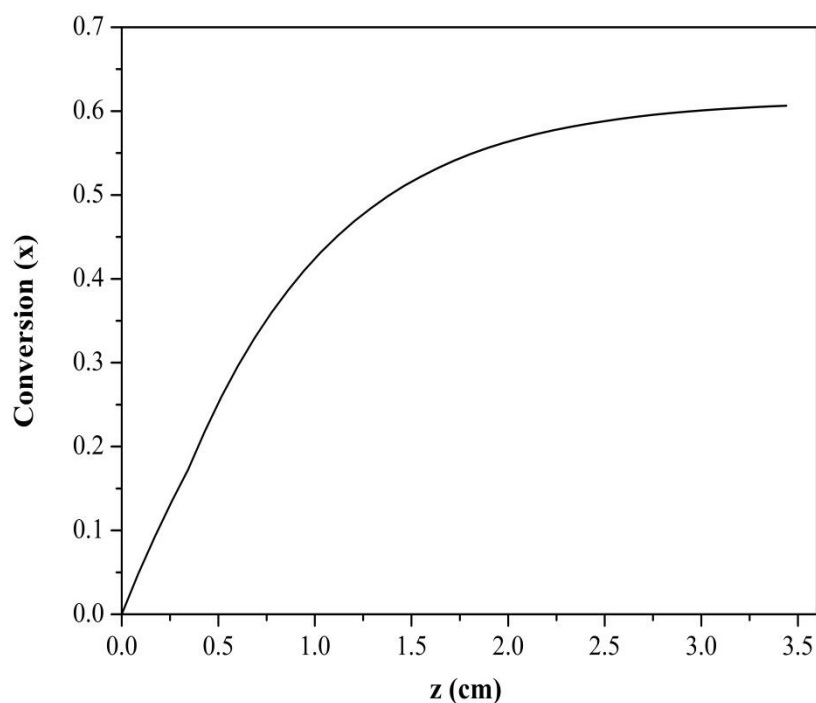


Figure 6. 27. The variation of phenol conversion along the length of the channel in the microphotoreactor. ($C_o=368 \mu\text{M}$, $Q = 14.3 \mu\text{Lmin}^{-1}$ and $P_o= 41 \text{ mW}$)

6.4 Conclusions

A new type of microphotoreactor for photocatalytic systems which integrates optofluidic concept into the nanostructured aerogels was introduced in this study. In contrast to the existing conventional microphotoreactors illuminated by a mounted external light source, light was directly implemented into the reaction volume sharing the same path with the reactant. The channels were fabricated in silica-titania aerogel composites, surrounded by a wall made up of interconnected mesoporous silicon dioxide network with embedded anatase titania particles with pockets of air in between them. The air in the aerogel pockets enabled the guiding of light by TIR in the liquid-filled channel in surface-treated aerogel composites. The unique nanoporous features of aerogels with high pore volume and surface area with open pore network combined with a fully three-dimensional structure made them effective for stable photocatalyst deposition in high amount as well as gas transfer to the surroundings leaving a bubble-free core liquid. The synthesized composite aerogels retained their interconnected mesoporous network with high porosity and pore volume as well as high surface area. The reactor operated at steady-state exhibiting plug flow characteristics. The photocatalytic degradation of phenol over the immobilized photocatalysts in the channel walls by the light delivered through the constructed waveguide was demonstrated with an efficient performance of the microphotoreactor. The effects of incident light power, flow rate of the reactant and mass fraction of the photocatalyst in aerogel composites and additional oxygen supply on the performance of the reactor were demonstrated. Furthermore, CNTs were successfully incorporated into the silica-titania matrix resulting in monolithic composites and their function on the photocatalytic degradation was investigated. The results revealed that silica-titania composite aerogels presumably exhibit higher photocatalytic efficiency than the simply mixing CNTs with TiO_2 . Finally, the experimental studies were supported by a simple model for immobilized photocatalytic microphotoreactors with integrated waveguide following a first order reaction rate with light dependency. The reaction rate parameters were estimated from the exponential regression model. The model and experimental were found to be in good agreement. In parallel with all results in this study, it is highlighted that the highly porous nanostructure of aerogels are versatile tools for integration of high fraction of photocatalyst in a stable form and simultaneously acting as optofluidic waveguide

cladding to propagate the light by TIR. Light could be confined in the reaction volume allowing for a direct interaction of light and photocatalysts and reactant in the channel, which results in high photocatalytic efficiency.

Chapter 7

CONCLUSION

A new, straightforward technique that uses direct manual drilling to manufacture TIR-based liquid-core optofluidic waveguides in aerogel monoliths was first developed. This method was shown to be capable of producing channels with lengths significantly larger than those reported previously in the literature and it also provides relative flexibility in the channel shaping. The synthesized aerogel samples with high densities had still sufficiently low refractive indices and absorption coefficient values, exhibiting ideal optical cladding material properties for efficient guiding of light by total internal reflection over a wide range of wavelengths without the use of any additional optical coatings. Relatively long channels of various shapes (straight and inclined L-shape) were created preserving the nanoporous and monolithic structure of the aerogel. The total internal reflection phenomena within channel in the hydrophobic aerogel as a multimode core waveguide could also be visually revealed and verified that light could be efficiently guided even along paths with a curved geometry.

As a result, the demonstrated fabrication technique could enable the use of aerogel-based optofluidic waveguides for innovative applications including photochemical and photocatalytic reactions with the aid of improved light distribution through the reaction space represented by the waveguide core. A new type microphotoreactor formed by a liquid-core optofluidic waveguide fabricated inside aerogel monoliths for photochemical and photocatalytic reactions was introduced in this study. The reactor consists of cylindrical channel in a monolithic aerogel block and the porous solid network of the aerogel surrounding the channel forms the aerogel-cladding. Unlike the existing conventional microphotoreactors illuminated by a mounted external light source, light was directly implemented into the reaction volume sharing the same path with the reactant. Light is confined in the liquid in the channels and is guided in a controlled manner by the aid of liquid core optofluidics waveguides based on TIR from the channel walls. Aqueous solutions of a model organic compound – methylene blue (MB) dye serving both as the waveguide core liquid and the reaction medium could be confined inside the channel embedded in the aerogel, without being adsorbed on the channel walls or without compromising the monolithic structure of the aerogel.

Subsequently, the light-driven photolysis of MB by the light guided along the full length of the microphotoreactor channel was successfully shown.

Furthermore, anatase TiO_2 nanoparticles were used as photocatalysts and they were successfully introduced into the mesoporous network of silica aerogels during sol-gel step of aerogel synthesis obtaining monolithic composite aerogels with varying titania content from 1 wt % to 50 wt %. The channel walls are thus made out of aerogel which contain photocatalysts which absorb the light delivered through the constructed waveguide resulting in photoinduced charge carriers at the photocatalyst surface which employ oxidation-reduction reactions of phenol. The effect of incident light power, flow rate of the reactant and mass fraction of the photocatalyst in aerogel composites and additional oxygen supply on the performance of the reactor were demonstrated. Along with experimental studies, a simple model for immobilized photocatalytic microphotoreactors with integrated waveguide following a first order reaction rate with light dependency was developed and compared with experimental data for various conditions investigated. The reaction rate parameters were estimated from an exponential regression model. The model and experimental were found to be in good agreement. Finally, CNTs were incorporated into the silica-titania matrix resulting in monolithic composites and their function on the photocatalytic degradation was investigated. It was obtained that silica-titania composite aerogels presumably exhibit higher photocatalytic efficiency than the simply mixing CNTs with TiO_2 .

Finally, this study have served to extend the optical applications of aerogels and opened up a new perspective for optofluidic microphotoreactors. This study can be further extended with use of other types of aerogels with superior mechanical properties such as tensile strength or flexibility or with interesting optical properties can be adopted to enlarge the spectrum of possible applications. Polymeric and hybrid aerogels which exhibit high flexibility and mechanical robustness can be fully integrated with the fabrication techniques to construct channels in complex geometries¹⁷⁶⁻¹⁷⁸. In addition, increasing market availability of various aerogels makes these materials attractive for development of optofluidics-related applications on a commercial scale in the near future. The number of optical and photonic applications is expected to increase in the coming years, as the relationship between the nanostructure of aerogels and their optical properties is better understood. Improvements in current techniques described in this

study or development of new techniques for fabrication will lead to development of aerogel based optical devices including lenses, waveguides, optical fibers, filters and dye lasers. In the near future, one can expect many more new, hybrid optical components to join the family of already existing successful optical solutions based on aerogels.

BIBLIOGRAPHY

1. Ozcelik, D.; Parks, J.; Wall, T.; Stott, M.; Cai, H.; W Parks, J.; Hawkins, A.; Schmidt, H., *Optofluidic wavelength division multiplexing for single-virus detection*. 2015; Vol. 112.
2. Fan, X.; White, I. M., Optofluidic microsystems for chemical and biological analysis. *Nature Photonics* **2011**, *5*, 591.
3. Zhao, Y.; Stratton, Z. S.; Guo, F.; Lapsley, M. I.; Chan, C. Y.; Lin, S. S.-C.; Huang, T. J., Optofluidic imaging: now and beyond. *Lab on a chip* **2013**, *13* (1), 17-24.
4. Pang, L.; Chen, H. M.; Freeman, L. M.; Fainman, Y., Optofluidic devices and applications in photonics, sensing and imaging. *Lab on a chip* **2012**, *12* (19), 3543-51.
5. Powless, A. J.; Majid, A. A.; Boice, J. W.; Prieto, S. P.; Pierce, M. C.; Balachandran, K.; Sharma, S.; Muldoon, T. J. In *A Fluorescence Imaging Optofluidics Device for Cytologic Morphology Assessment*, Biomedical Optics 2014, Miami, Florida, 2014/04/26; Optical Society of America: Miami, Florida, 2014; p BT3A.17.
6. Yin, D.; Deamer, D. W.; Schmidt, H.; Barber, J. P.; Hawkins, A. R., Single-molecule detection sensitivity using planar integrated optics on a chip. *Opt. Lett.* **2006**, *31* (14), 2136-2138.
7. Ozcelik, D.; Parks, J. W.; Wall, T. A.; Stott, M. A.; Cai, H.; Parks, J. W.; Hawkins, A. R.; Schmidt, H., Optofluidic wavelength division multiplexing for single-virus detection. *Proceedings of the National Academy of Sciences* **2015**, *112* (42), 12933-12937.
8. Ozcelik, D.; Phillips, B. S.; Parks, J. W.; Measor, P.; Gulbransen, D.; Hawkins, A. R.; Schmidt, H., Dual-core optofluidic chip for independent particle detection and tunable spectral filtering. *Lab on a Chip* **2012**, *12* (19), 3728-3733.
9. Brennan, D.; Lambkin, P.; Moore, E. J.; Galvin, P., An Integrated Optofluidic Platform for DNA Hybridization and Detection. *IEEE Sensors Journal* **2008**, *8* (5), 536-542.
10. Monat, C.; Domachuk, P.; Eggleton, B. J., Integrated optofluidics: A new river of light. *Nat Photon* **2007**, *1* (2), 106-114.
11. Psaltis, D.; Quake, S. R.; Yang, C., Developing optofluidic technology through the fusion of microfluidics and optics. *Nature* **2006**, *442* (7101), 381-386.
12. Erickson, D.; Sinton, D.; Psaltis, D., Optofluidics for energy applications. *Nat Photon* **2011**, *5* (10), 583-590.
13. Wang, N.; Zhang, X.; Wang, Y.; Yu, W.; Chan, H. L. W., Microfluidic reactors for photocatalytic water purification. *Lab on a Chip* **2014**, *14* (6), 1074-1082.
14. Wang, N.; Zhang, X.; Chen, B.; Song, W.; Chan, N. Y.; Chan, H. L. W., Microfluidic photoelectrocatalytic reactors for water purification with an integrated visible-light source. *Lab on a Chip* **2012**, *12* (20), 3983-3990.
15. Lei, L.; Wang, N.; Zhang, X. M.; Tai, Q.; Tsai, D. P.; Chan, H. L., Optofluidic planar reactors for photocatalytic water treatment using solar energy. *Biomicrofluidics* **2010**, *4* (4), 43004.
16. Matthias, S.; M., C. A.; Nicola, T.; G., E. T.; Till, C.; Florian, M.; Hans-Peter, S.; J., R. P. S.; Peter, W.; M., E. B. J., Chemical and (Photo)-Catalytical Transformations in Photonic Crystal Fibers. *ChemCatChem* **2013**, *5* (3), 641-650.
17. Paolo, M.; Roberto, O.; Cinzia, S.; Zhao, S.; Omenetto, F. G.; Kristinn, B. G.; Tommy, H.; Yibo, Z.; Aydogan, O.; Adam, W.; Frieder, M.; Holger, S.; Genni, T.;

- Romeo, B.; Jochen, G.; Carlo, L.; Kirstine, B.-S.; Jian, C.; Markus, P.; Sha, X.; Ai-Qun, L.; Chia-Chann, S.; Shih-Kang, F.; David, E.; David, S., Roadmap for optofluidics. *Journal of Optics* **2017**, *19* (9), 093003.
18. Cheng, X.; Chen, R.; Zhu, X.; Liao, Q.; An, L.; Ye, D.; He, X.; Li, S.; Li, L., An optofluidic planar microreactor for photocatalytic reduction of CO₂ in alkaline environment. *Energy* **2017**, *120*, 276-282.
 19. Das, S.; Srivastava, V. C., Microfluidic-based photocatalytic microreactor for environmental application: a review of fabrication substrates and techniques, and operating parameters. *Photochemical & Photobiological Sciences* **2016**, *15* (6), 714-730.
 20. Wang, N.; Tan, F.; Wan, L.; Wu, M.; Zhang, X., Microfluidic reactors for visible-light photocatalytic water purification assisted with thermolysis. *Biomicrofluidics* **2014**, *8* (5), 054122.
 21. Li, L.; Tang, D.; Song, Y.; Jiang, B., Dual-film optofluidic microreactor with enhanced light-harvesting for photocatalytic applications. *Chemical Engineering Journal* **2018**, *339*, 71-77.
 22. Meng, Z.; Zhang, X.; Qin, J., A high efficiency microfluidic-based photocatalytic microreactor using electrospun nanofibrous TiO₂ as a photocatalyst. *Nanoscale* **2013**, *5* (11), 4687-4690.
 23. Hartman, R. L.; Jensen, K. F., Microchemical systems for continuous-flow synthesis. *Lab on a chip* **2009**, *9* (17), 2495-507.
 24. Jähnisch, K.; Hessel, V.; Löwe, H.; Baerns, M., Chemistry in Microstructured Reactors. *Angewandte Chemie International Edition* **2004**, *43* (4), 406-446.
 25. Ehrfeld, W.; Hessel, V.; Löwe, H., Modern Microfabrication Techniques for Microreactors. In *Microreactors*, Wiley-VCH Verlag GmbH & Co. KGaA: 2004; pp 15-39.
 26. Fuse, S.; Tanabe, N.; Yoshida, M.; Yoshida, H.; Doi, T.; Takahashi, T., Continuous-flow synthesis of vitamin D₃. *Chemical Communications* **2010**, *46* (46), 8722-8724.
 27. Lu, H.; Schmidt, M. A.; Jensen, K. F., Photochemical reactions and on-line UV detection in microfabricated reactors. *Lab on a Chip* **2001**, *1* (1), 22-28.
 28. Sakeda, K.; Wakabayashi, K.; Matsushita, Y.; Ichimura, T.; Suzuki, T.; Wada, T.; Inoue, Y., Asymmetric photosensitized addition of methanol to (R)-(+)-(Z)-limonene in a microreactor. *Journal of Photochemistry and Photobiology A: Chemistry* **2007**, *192* (2-3), 166-171.
 29. Hofstadler, K.; Bauer, R.; Novalic, S.; Heisler, G., New Reactor Design for Photocatalytic Wastewater Treatment with TiO₂ Immobilized on Fused-Silica Glass Fibers: Photomineralization of 4-Chlorophenol. *Environmental Science & Technology* **1994**, *28* (4), 670-674.
 30. Peill, N. J.; Hoffmann, M. R., Development and Optimization of a TiO₂-Coated Fiber-Optic Cable Reactor: Photocatalytic Degradation of 4-Chlorophenol. *Environmental Science & Technology* **1995**, *29* (12), 2974-2981.
 31. Peill, N. J.; Hoffmann, M. R., Chemical and Physical Characterization of a TiO₂-Coated Fiber Optic Cable Reactor. *Environmental Science & Technology* **1996**, *30* (9), 2806-2812.
 32. Wu, J. C. S.; Lin, H.-M.; Lai, C.-L., Photo reduction of CO₂ to methanol using optical-fiber photoreactor. *Applied Catalysis A: General* **2005**, *296* (2), 194-200.

33. Nguyen, T.-V.; Wu, J. C. S., Photoreduction of CO₂ in an optical-fiber photoreactor: Effects of metals addition and catalyst carrier. *Applied Catalysis A: General* **2008**, *335* (1), 112-120.
34. Cubillas, A. M.; Unterkofler, S.; Euser, T. G.; Etzold, B. J. M.; Jones, A. C.; Sadler, P. J.; Wasserscheid, P.; Russell, P. S. J., Photonic crystal fibres for chemical sensing and photochemistry. *Chemical Society Reviews* **2013**, *42* (22), 8629-8648.
35. Cerkauskaite, A.; Drevinskas, R.; Rybaltovskii, A. O.; Kazansky, P. G., Ultrafast laser-induced birefringence in various porosity silica glasses: from fused silica to aerogel. *Optics Express* **2017**, *25* (7), 8011-8021.
36. Özbakır, Y.; Jonas, A.; Kiraz, A.; Erkey, C., Aerogels for optofluidic waveguides. *Micromachines* **2017**, *8* (4), 98.
37. Özbakır, Y.; Jonáš, A.; Kiraz, A.; Erkey, C., Total internal reflection-based optofluidic waveguides fabricated in aerogels. *Journal of Sol-Gel Science and Technology* **2017**, *84* (3), 522-534.
38. Yalizay, B.; Morova, Y.; Dincer, K.; Ozbakir, Y.; Jonas, A.; Erkey, C.; Kiraz, A.; Akturk, S., Versatile liquid-core optofluidic waveguides fabricated in hydrophobic silica aerogels by femtosecond-laser ablation. *Optical Materials* **2015**, *47*, 478-483.
39. Xiao, L.; Birks, T. A., Optofluidic microchannels in aerogel. *Opt. Lett.* **2011**, *36* (16), 3275-3277.
40. Özbakır, Y.; Jonáš, A.; Kiraz, A.; Erkey, C., Total internal reflection-based optofluidic waveguides fabricated in aerogels. *Journal of Sol-Gel Science and Technology* **2017**, 1-13.
41. Ahsan, S. S.; Gumus, A.; Erickson, D., Redox mediated photocatalytic water-splitting in optofluidic microreactors. *Lab on a Chip* **2013**, *13* (3), 409-414.
42. Bartholomäus, P.; Menny, S.; Markus, A.; H., S. P.; Kerry, G., Continuous Heterogeneous Photocatalysis in Serial Micro-Batch Reactors. *Angewandte Chemie International Edition* **0** (0).
43. Bruno, R.; Atieh Parisi, C.; Shinichi, O.; Antonio Carlos Silva Costa, T., *Single-Phase Flow in a Micro-Structured Packed Bed Photo-Reactor: Effect of Packing Size on Flow Regime and on the Reactor Performance for Homogeneous Photocatalysis*. 2018.
44. Li, X.; Wang, H.; Inoue, K.; Uehara, M.; Nakamura, H.; Miyazaki, M.; Abe, E.; Maeda, H., Modified micro-space using self-organized nanoparticles for reduction of methylene blue. *Chemical Communications* **2003**, (8), 964-965.
45. Matsushita, Y.; Ohba, N.; Kumada, S.; Sakeda, K.; Suzuki, T.; Ichimura, T., Photocatalytic reactions in microreactors. *Chemical Engineering Journal* **2008**, *135*, S303-S308.
46. Takei, G.; Kitamori, T.; Kim, H.-B., Photocatalytic redox-combined synthesis of l-pipecolinic acid with a titania-modified microchannel chip. *Catalysis Communications* **2005**, *6* (5), 357-360.
47. Fan, X.; White, I. M., Optofluidic microsystems for chemical and biological analysis. *Nat Photon* **2011**, *5* (10), 591-597.
48. Schmidt, H.; Hawkins, A. R., Optofluidic waveguides: I. Concepts and implementations. *Microfluidics and Nanofluidics* **2008**, *4* (1), 3-16.
49. Rowland, K. J.; Afshar, V. S.; Stolyarov, A.; Fink, Y.; Monroe, T. M., Bragg waveguides with low-index liquid cores. *Opt. Express* **2012**, *20* (1), 48-62.

50. Pone, E.; Dubois, C.; Guo, N.; Gao, Y.; Dupuis, A.; Boismenu, F.; Lacroix, S.; Skorobogatiy, M., Drawing of the hollow all-polymer Bragg fibers. *Opt. Express* **2006**, *14* (13), 5838-5852.
51. Bernini, R.; Campopiano, S.; Zeni, L.; Sarro, P. M., ARROW optical waveguides based sensors. *Sensors and Actuators B: Chemical* **2004**, *100* (1–2), 143-146.
52. Testa, G.; Persichetti, G.; Bernini, R., Liquid Core ARROW Waveguides: A Promising Photonic Structure for Integrated Optofluidic Microsensors. *Micromachines* **2016**, *7* (3), 47.
53. Risk, W. P.; Kim, H. C.; Miller, R. D.; Temkin, H.; Gangopadhyay, S., Optical waveguides with an aqueous core and a low-index nanoporous cladding. *Opt. Express* **2004**, *12* (26), 6446-6455.
54. Hawkins, A. R.; Schmidt, H., Optofluidic waveguides: II. Fabrication and structures. *Microfluidics and Nanofluidics* **2008**, *4* (1), 17-32.
55. Uranus, H. P. Guiding light by and beyond the total internal reflection mechanism. University of Twente, 2005.
56. Freeberg, B. Liquid Fiber Optics. Available online: <http://www.aapt.org/Programs/contests/winnersfull.cfm?id=2687&theyear=2011> (accessed on 25 February 2017).
57. Schelle, B.; Dress, P.; Franke, H.; Klein, K. F.; Slupek, J., Physical characterization of lightguide capillary cells. *Journal of Physics D-Applied Physics* **1999**, *32* (24), 3157-3163.
58. Dress, P.; Franke, H., *An optical fiber with a liquid H₂O core*. Spie - Int Soc Optical Engineering: Bellingham, 1996; Vol. 2686, p 157-163.
59. Cai, H.; Parks, J. W.; Wall, T. A.; Stott, M. A.; Stambaugh, A.; Alfson, K.; Griffiths, A.; Mathies, R. A.; Carrion, R.; Patterson, J. L.; Hawkins, A. R.; Schmidt, H., Optofluidic analysis system for amplification-free, direct detection of Ebola infection. *Scientific Reports* **2015**, *5*, 14494.
60. Jung, J. H.; Lee, K. S.; Im, S.; Destgeer, G.; Ha, B. H.; Park, J.; Sung, H. J., Photosynthesis of cyanobacteria in a miniaturized optofluidic waveguide platform. *RSC Advances* **2016**, *6* (14), 11081-11087.
61. Cho, S. H.; Godin, J.; Lo, Y. H., Optofluidic Waveguides in Teflon AF-Coated PDMS Microfluidic Channels. *Ieee Photonics Technology Letters* **2009**, *21* (15), 1057-1059.
62. Datta, A.; Eom, I. Y.; Dhar, A.; Kuban, P.; Manor, R.; Ahmad, I.; Gangopadhyay, S.; Dallas, T.; Holtz, M.; Temkin, F.; Dasgupta, P. K., Microfabrication and characterization of Teflon AF-coated liquid core waveguide channels in silicon. *Ieee Sensors Journal* **2003**, *3* (6), 788-795.
63. Wu, C. W.; Gong, G. C., Fabrication of PDMS-based nitrite sensors using Teflon AF coating microchannels. *Ieee Sensors Journal* **2008**, *8* (5-6), 465-469.
64. Fricke, J., Aerogels — highly tenuous solids with fascinating properties. *Journal of Non-Crystalline Solids* **1988**, *100* (1), 169-173.
65. Handbook, A., MA Aegerter, N. Leventis and MM Koebel. Springer, New York: 2011.
66. Ulker, Z.; Erkey, C., An emerging platform for drug delivery: Aerogel based systems. *Journal of Controlled Release* **2014**, *177*, 51-63.
67. Pierre, A. C.; Pajonk, G. M., Chemistry of Aerogels and Their Applications. *Chemical Reviews* **2002**, *102* (11), 4243-4266.

68. Zuo, L.; Zhang, Y.; Zhang, L.; Miao, Y.-E.; Fan, W.; Liu, T., Polymer/Carbon-Based Hybrid Aerogels: Preparation, Properties and Applications. *Materials* **2015**, *8* (10), 5343.
69. Du, A.; Zhou, B.; Zhang, Z.; Shen, J., A Special Material or a New State of Matter: A Review and Reconsideration of the Aerogel. *Materials* **2013**, *6* (3), 941.
70. Zhang, X. X.; Su, W. M.; Lin, M. Y.; Miao, X.; Ye, L. Q.; Yang, W. B.; Jiang, B., Non-supercritical drying sol-gel preparation of superhydrophobic aerogel ORMOSIL thin films with controlled refractive index. *Journal of Sol-Gel Science and Technology* **2015**, *74* (3), 594-602.
71. Hrubesh, L. W., Aerogel applications. *Journal of Non-Crystalline Solids* **1998**, *225*, 335-342.
72. Soleimani Dorcheh, A.; Abbasi, M. H., Silica aerogel; synthesis, properties and characterization. *Journal of Materials Processing Technology* **2008**, *199* (1-3), 10-26.
73. Randall, J. P.; Meador, M. A. B.; Jana, S. C., Tailoring Mechanical Properties of Aerogels for Aerospace Applications. *ACS Applied Materials & Interfaces* **2011**, *3* (3), 613-626.
74. Bellunato, T.; Calvi, M.; Matteuzzi, C.; Musy, M.; Perego, D. L.; Storaci, B., Refractive index of silica aerogel: Uniformity and dispersion law. *Nuclear Instruments and Methods in Physics Research Section A: Accelerators, Spectrometers, Detectors and Associated Equipment* **2008**, *595* (1), 183-186.
75. Tabata, M.; Adachi, I.; Kawai, H.; Kubo, M.; Sato, T., Recent Progress in Silica Aerogel Cherenkov Radiator. *Physics Procedia* **2012**, *37*, 642-649.
76. Adachi, I.; Sumiyoshi, T.; Hayashi, K.; Iida, N.; Enomoto, R.; Tsukada, K.; Suda, R.; Matsumoto, S.; Natori, K.; Yokoyama, M.; Yokogawa, H., STUDY OF A THRESHOLD CHERENKOV COUNTER BASED ON SILICA AEROGELS WITH LOW REFRACTIVE-INDEXES. *Nucl. Instrum. Methods Phys. Res. Sect. A-Accel. Spectrom. Dect. Assoc. Equip.* **1995**, *355* (2-3), 390-398.
77. Nappi, E., Aerogel and its applications to RICH detectors. *Nucl. Phys. B* **1998**, *270*-276.
78. Cantin, M.; Casse, M.; Koch, L.; Jouan, R.; Mestreau, P.; Roussel, D.; Bonnin, F.; Moutel, J.; Teichner, S. J., Silica aerogels used as Cherenkov radiators. *Nuclear Instruments and Methods* **1974**, *118* (1), 177-182.
79. Pajonk, G. M., Some applications of silica aerogels. *Colloid and Polymer Science* **2003**, *281* (7), 637-651.
80. Chen, Q.; Long, D.; Chen, L.; Liu, X.; Liang, X.; Qiao, W.; Ling, L., Synthesis of ultrahigh-pore-volume carbon aerogels through a “reinforced-concrete” modified sol-gel process. *Journal of Non-Crystalline Solids* **2011**, *357* (1), 232-235.
81. Al-Muhtaseb, S. A.; Ritter, J. A., Preparation and Properties of Resorcinol-Formaldehyde Organic and Carbon Gels. *Advanced Materials* **2003**, *15* (2), 101-114.
82. Zhao, S.; Malfait, W. J.; Demilecamps, A.; Zhang, Y.; Brunner, S.; Huber, L.; Tingaut, P.; Rigacci, A.; Budtova, T.; Koebel, M. M., Strong, Thermally Superinsulating Biopolymer-Silica Aerogel Hybrids by Cogelation of Silicic Acid with Pectin. *Angewandte Chemie International Edition* **2015**, *54* (48), 14282-14286.
83. Mekonnen, B. T.; Ragothaman, M.; Kalirajan, C.; Palanisamy, T., Conducting collagen-polypyrrole hybrid aerogels made from animal skin waste. *RSC Advances* **2016**, *6* (67), 63071-63077.

84. Dong, W.; Rhine, W.; White, S., Polyimide-Silica Hybrid Aerogels with High Mechanical Strength for Thermal Insulation Applications. *MRS Proceedings* **2011**, 1306.
85. Yang, Q.; Tan, X.; Wang, S.; Zhang, J.; Chen, L.; Zhang, J.-P.; Su, C.-Y., Porous organic–inorganic hybrid aerogels based on bridging acetylacetonate. *Microporous and Mesoporous Materials* **2014**, 187, 108-113.
86. Yim, T.-J.; Kim, S. Y.; Yoo, K.-P., Fabrication and thermophysical characterization of nano-porous silica-polyurethane hybrid aerogel by sol-gel processing and supercritical solvent drying technique. *Korean Journal of Chemical Engineering* **2002**, 19 (1), 159-166.
87. Thapliyal, P. C.; Singh, K., Aerogels as Promising Thermal Insulating Materials: An Overview. *Journal of Materials* **2014**, 2014, 10.
88. Ülker, Z.; Sanli, D.; Erkey, C., Applications of Aerogels and Their Composites in Energy-Related Technologies-Chapter 8.
89. Jelle, B. P., Traditional, state-of-the-art and future thermal building insulation materials and solutions – Properties, requirements and possibilities. *Energy and Buildings* **2011**, 43 (10), 2549-2563.
90. Hotaling, S. P., Ultra-low density aerogel optical applications. *Journal of Materials Research* **2011**, 8 (2), 352-355.
91. Hrubesh, L. W.; Poco, J. F., Thin aerogel films for optical, thermal, acoustic and electronic applications. *Journal of Non-Crystalline Solids* **1995**, 188 (1), 46-53.
92. Tong, L.; Lou, J.; Gattass, R. R.; He, S.; Chen, X.; Liu; Mazur, E., Assembly of Silica Nanowires on Silica Aerogels for Microphotonic Devices. *Nano Letters* **2005**, 5 (2), 259-262.
93. Wang, H. Q.; Du, A.; Zhang, Z. H.; Zhou, B.; Shen, J., An optical dustbin made by the subwavelength-induced super-black carbon aerogels. *Journal of Materials Research* **2017**, 32 (18), 3524-3531.
94. Nicola, H.; Ulrich, S., Aerogels—Airy Materials: Chemistry, Structure, and Properties. *Angewandte Chemie International Edition* **1998**, 37 (1-2), 22-45.
95. Xiao, L.; Grogan, M. D.; Leon-Saval, S. G.; Williams, R.; England, R.; Wadsworth, W. J.; Birks, T. A., Tapered fibers embedded in silica aerogel. *Opt. Lett.* **2009**, 34 (18), 2724-2726.
96. Yalizay, B.; Morova, Y.; Ozbakir, Y.; Jonas, A.; Erkey, C.; Kiraz, A.; Akturk, S. In *Optofluidic waveguides written in hydrophobic silica aerogels with a femtosecond laser*, SPIE OPTO, SPIE: 2015; p 9.
97. Hüsing, N.; Schubert, U., Aerogels—Airy Materials: Chemistry, Structure, and Properties. *Angewandte Chemie International Edition* **1998**, 37 (1-2), 22-45.
98. Kharzheev, Y. N., Use of silica aerogels in Cherenkov counters. *Physics of Particles and Nuclei* **2008**, 39 (1), 107-135.
99. Akimov, Y. K., Fields of Application of Aerogels (Review). *Instruments and Experimental Techniques* **2003**, 46 (3), 287-299.
100. Tabata, M.; Adachi, I.; Hatakeyama, Y.; Kawai, H.; Morita, T.; Sumiyoshi, T., Large-area silica aerogel for use as Cherenkov radiators with high refractive index, developed by supercritical carbon dioxide drying. *The Journal of Supercritical Fluids* **2016**, 110, 183-192.
101. Sprehn, G. A.; Hrubesh, L. W.; Poco, J. F.; Sandler, P. H., Aerogel-clad optical fiber. Google Patents: 1997.

102. Xiao, L.; Grogan, M.; England, R.; Wadsworth, W.; Birks, T. In *Gas Sensing with a Sub-Micron Tapered Fibre Embedded in Hydrophobic Aerogel*, Conference on Lasers and Electro-Optics 2010, San Jose, California, 2010/05/16; Optical Society of America: San Jose, California, 2010; p JThB6.
103. Birks, T. A.; Wadsworth, W. J.; Russell, P. S. J., Supercontinuum generation in tapered fibers. *Optics Letters* **2000**, 25 (19), 1415-1417.
104. Braidotti, M. C.; Gentilini, S.; Fleming, A.; Samuels, M. C.; Falco, A. D.; Conti, C., Optothermal nonlinearity of silica aerogel. *Applied Physics Letters* **2016**, 109 (4), 041104.
105. Gentilini, S.; Ghajeri, F.; Ghofraniha, N.; Di Falco, A.; Conti, C., Optical shock waves in silica aerogel. *Opt. Express* **2014**, 22 (2), 1667-1672.
106. Hongbing, Z.; Wenzhe, C.; Minquan, W.; Zhengchan; Chunlin, Z., Optical limiting effects of multi-walled carbon nanotubes suspension and silica xerogel composite. *Chemical Physics Letters* **2003**, 382 (3), 313-317.
107. Eris, G.; Sanli, D.; Ulker, Z.; Bozbag, S. E.; Jonás, A.; Kiraz, A.; Erkey, C., Three-dimensional optofluidic waveguides in hydrophobic silica aerogels via supercritical fluid processing. *The Journal of Supercritical Fluids* **2013**, 73, 28-33.
108. Yalizay, B.; Morova, Y.; Ozbakir, Y.; Jonas, A.; Erkey, C.; Kiraz, A.; Akturk, S., Optofluidic waveguides written in hydrophobic silica aerogels with a femtosecond laser. In *Integrated Optics: Devices, Materials, and Technologies Xix*, Broquin, J. E.; Conti, G. N., Eds. 2015; Vol. 9365.
109. Seo, J. T.; Yang, Q.; Creekmore, S.; Tabibi, B.; Temple, D.; Kim, S. Y.; Yoo, K.; Mott, A.; Namkung, M.; Jung, S. S., Large pure refractive nonlinearity of nanostructure silica aerogel. *Applied Physics Letters* **2003**, 82 (25), 4444-4446.
110. Seo, J. T.; Yang, Q.; Creekmore, S.; Temple, D. In *Large pure refractive nonlinearity of nanostructure silica aerogel at near infrared wavelength*, Proceedings of the 2nd IEEE Conference on Nanotechnology, 2002; 2002; pp 495-497.
111. Seo, J.; Ma, S.; Yang, Q.; Creekmore, L.; Brown, H.; Battle, R.; Lee, K.; Jackson, A.; Skyles, T.; Tabibi, B., Large optical nonlinearity of highly porous silica nanoaerogels in the nanosecond time domain. *JOURNAL-KOREAN PHYSICAL SOCIETY* **2006**, 48 (6), 1395.
112. Birks, T. A.; Grogan, M. D. W.; Xiao, L. M.; Rollings, M. D.; England, R.; Wadsworth, W. J. In *Silica aerogel in optical fibre devices*, 2010 12th International Conference on Transparent Optical Networks, June 27 2010-July 1 2010; 2010; pp 1-4.
113. Gunay, A. A.; Kim, H.; Nagarajan, N.; Lopez, M.; Kantharaj, R.; Alsaati, A.; Marconnet, A.; Lenert, A.; Miljkovic, N., Optically Transparent Thermally Insulating Silica Aerogels for Solar Thermal Insulation. *Acs Applied Materials & Interfaces* **2018**, 10 (15), 12603-12611.
114. Moretti, E.; Zinzi, M.; Merli, F.; Buratti, C., Optical, thermal, and energy performance of advanced polycarbonate systems with granular aerogel. *Energy and Buildings* **2018**, 166, 407-417.
115. Svendsen, S., Solar collector with monolithic silica aerogel. *Journal of Non-Crystalline Solids* **1992**, 145, 240-243.
116. Zhao, L.; Yang, S.; Bhatia, B.; Strobach, E.; Wang, E. N., Modeling silica aerogel optical performance by determining its radiative properties. *AIP Advances* **2016**, 6 (2), 025123.
117. Beck, A.; Caps, R.; Fricke, J., Scattering of visible light from silica aerogels. *Journal of Physics D: Applied Physics* **1989**, 22 (6), 730.

118. Fu, T.; Tang, J.; Chen, K.; Zhang, F., Visible, near-infrared and infrared optical properties of silica aerogels. *Infrared Physics & Technology* **2015**, 71, 121-126.
119. Hüsing, N.; Schubert, U., Aerogels—Airy Materials: Chemistry, Structure, and Properties. *Angewandte Chemie International Edition* **1998**, 37 (1-2), 22-45.
120. Pajonk, G. M., Transparent silica aerogels. *Journal of Non-Crystalline Solids* **1998**, 225, 307-314.
121. Wang, P.; Beck, A.; Korner, W.; Scheller, H.; Fricke, J., Density and refractive index of silica aerogels after low- and high-temperature supercritical drying and thermal treatment. *Journal of Physics D: Applied Physics* **1994**, 27 (2), 414.
122. Tamon, H.; Kitamura, T.; Okazaki, M., Preparation of Silica Aerogel from TEOS. *Journal of Colloid and Interface Science* **1998**, 197 (2), 353-359.
123. M., A. J.; Abdul, M. M.; A., W. J.; Z., X. W.; Wei, W.; A., C. P., Silica aerogel–poly(ethylene-co-vinyl acetate) composite for transparent heat retention films. *Journal of Polymer Science Part B: Polymer Physics* **2014**, 52 (14), 927-935.
124. Xu, X.; Zhou, J.; Jiang, L.; Lubineau, G.; Ng, T.; Ooi, B. S.; Liao, H.-Y.; Shen, C.; Chen, L.; Zhu, J. Y., Highly transparent, low-haze, hybrid cellulose nanopaper as electrodes for flexible electronics. *Nanoscale* **2016**, 8 (24), 12294-12306.
125. Carter, P., The aerogel radiator of the HERMES RICH: on behalf of the HERMES collaboration. *Nuclear Instruments and Methods in Physics Research Section A: Accelerators, Spectrometers, Detectors and Associated Equipment* **1999**, 433 (1), 392-395.
126. Buzykaev, A. R.; Danilyuk, A. F.; Ganzhur, S. F.; Kravchenko, E. A.; Onuchin, A. P., Measurement of optical parameters of aerogel. *Nuclear Instruments and Methods in Physics Research Section A: Accelerators, Spectrometers, Detectors and Associated Equipment* **1999**, 433 (1), 396-400.
127. Richter, D.; Lipka, D., Measurement of the refractive index of silica aerogel in vacuum. *Nuclear Instruments and Methods in Physics Research Section A: Accelerators, Spectrometers, Detectors and Associated Equipment* **2003**, 513 (3), 635-638.
128. Henning, S.; Svensson, L., Production of Silica Aerogel. *Physica Scripta* **1981**, 23 (4B), 697.
129. Buzykaev, A.; Danilyuk, A.; Ganzhur, S.; Gorodetskaya, T.; Kravchenko, E.; Onuchin, A.; Vorobiov, A., Aerogels with high optical parameters for Cherenkov counters. *Nuclear Instruments and Methods in Physics Research Section A: Accelerators, Spectrometers, Detectors and Associated Equipment* **1996**, 379 (3), 465-467.
130. Danilyuk, A. F.; Kirillov, V. L.; Savelieva, M. D.; Bobrovnikov, V. S.; Buzykaev, A. R.; Kravchenko, E. A.; Lavrov, A. V.; Onuchin, A. P., Recent results on aerogel development for use in Cherenkov counters. *Nuclear Instruments and Methods in Physics Research Section A: Accelerators, Spectrometers, Detectors and Associated Equipment* **2002**, 494 (1), 491-494.
131. Poelz, G.; Riethmüller, R., Preparation of silica aerogel for Cherenkov counters. *Nuclear Instruments and Methods in Physics Research* **1982**, 195 (3), 491-503.
132. Zuo, Y.; Zhu, X.; Shi, Y.; Liang, L.; Yang, Y., Light Manipulation in Inhomogeneous Liquid Flow and Its Application in Biochemical Sensing. *Micromachines* **2018**, 9 (4), 163.

133. Raymond, C.; Ronca, S., Chapter 6 - Relation of Structure to Electrical and Optical Properties. In *Brydson's Plastics Materials (Eighth Edition)*, Gilbert, M., Ed. Butterworth-Heinemann: 2017; pp 103-125.
134. Cai, Z.; Qiu, W.; Shao, G.; Wang, W., A new fabrication method for all-PDMS waveguides. *Sensors and Actuators A: Physical* **2013**, *204*, 44-47.
135. Mathur, B. K., *Introduction to Geometrical and Physical Optics*. Gopal Printing: 1967.
136. Bajpai, A. K.; Bajpai, J.; Saini, R. K.; Agrawal, P.; Tiwari, A., *Smart Biomaterial Devices: Polymers in Biomedical Sciences*. CRC Press: 2016.
137. Sirleto, L.; Coppola, G.; Iodice, M.; Casalino, M.; Giofrè, M.; Rendina, I., 3 - Thermo-optical switches. In *Optical Switches*, Li, B.; Chua, S. J., Eds. Woodhead Publishing: 2010; pp 61-96.
138. French, R. H.; Rodriguez-Parada, J.; Yang, M.; Derryberry, R.; Lemon, M.; Brown, M.; Haeger, C.; Samuels, S.; Romano, E.; Richardson, R. In *Optical properties of materials for concentrator photovoltaic systems*, Photovoltaic Specialists Conference (PVSC), 2009 34th IEEE, IEEE: 2009; pp 000394-000399.
139. Testa, G.; Persichetti, G.; Zeni, L.; Sarro, P. M.; Bernini, R. In *Optofluidics: a new tool for sensing*, Fifth European Workshop on Optical Fibre Sensors, SPIE: 2013; p 6.
140. Özbakır, Y.; Erkey, C., Experimental and theoretical investigation of supercritical drying of silica alcogels. *The Journal of Supercritical Fluids* **2015**, *98*, 153-166.
141. Özbakır, Y.; Ulker, Z.; Erkey, C., Monolithic composites of silica aerogel with poly (methyl vinyl ether) and the effect of polymer on supercritical drying. *The Journal of Supercritical Fluids* **2015**, *105*, 108-118.
142. Cheng, H.; Xue, H.; Hong, C.; Zhang, X., Characterization, thermal and mechanical properties and hydrophobicity of resorcinol-furfural/silicone hybrid aerogels synthesized by ambient-pressure drying. *RSC Advances* **2016**, *6* (79), 75793-75804.
143. Alnaief, M.; Smirnova, I., Effect of surface functionalization of silica aerogel on their adsorptive and release properties. *Journal of Non-Crystalline Solids* **2010**, *356* (33-34), 1644-1649.
144. Jiang, F.; Hsieh, Y.-L., Amphiphilic superabsorbent cellulose nanofibril aerogels. *Journal of Materials Chemistry A* **2014**, *2* (18), 6337-6342.
145. Wang, S.; Peng, X.; Zhong, L.; Tan, J.; Jing, S.; Cao, X.; Chen, W.; Liu, C.; Sun, R., An ultralight, elastic, cost-effective, and highly recyclable superabsorbent from microfibrillated cellulose fibers for oil spillage cleanup. *Journal of Materials Chemistry A* **2015**, *3* (16), 8772-8781.
146. Zhou, S.; Liu, P.; Wang, M.; Zhao, H.; Yang, J.; Xu, F., Sustainable, Reusable, and Superhydrophobic Aerogels from Microfibrillated Cellulose for Highly Effective Oil/Water Separation. *ACS Sustainable Chemistry & Engineering* **2016**, *4* (12), 6409-6416.
147. Venkateswara Rao, A.; Kulkarni, M. M.; Amalnerkar, D. P.; Seth, T., Superhydrophobic silica aerogels based on methyltrimethoxysilane precursor. *Journal of Non-Crystalline Solids* **2003**, *330* (1-3), 187-195.
148. Lee, K.-H.; Kim, S.-Y.; Yoo, K.-P., Low-density, hydrophobic aerogels. *Journal of Non-Crystalline Solids* **1995**, *186*, 18-22.

149. Kartal, A. M.; Erkey, C., Surface modification of silica aerogels by hexamethyldisilazane–carbon dioxide mixtures and their phase behavior. *The Journal of Supercritical Fluids* **2010**, *53* (1–3), 115-120.
150. Smirnova, I.; Mamic, J.; Arlt, W., Adsorption of Drugs on Silica Aerogels. *Langmuir* **2003**, *19* (20), 8521-8525.
151. Sun, J.; Longtin, J. P.; Norris, P. M., Ultrafast laser micromachining of silica aerogels. *Journal of Non-Crystalline Solids* **2001**, *281* (1–3), 39-47.
152. Bian, Q. M.; Chen, S. Y.; Kim, B. T.; Leventis, N.; Lu, H. B.; Chang, Z. H.; Lei, S. T., Micromachining of polyurea aerogel using femtosecond laser pulses. *Journal of Non-Crystalline Solids* **2011**, *357* (1), 186-193.
153. Leventis, N.; Elder, I. A.; Rolison, D. R.; Anderson, M. L.; Merzbacher, C. I., Durable Modification of Silica Aerogel Monoliths with Fluorescent 2,7-Diazapyrenium Moieties. Sensing Oxygen near the Speed of Open-Air Diffusion. *Chemistry of Materials* **1999**, *11* (10), 2837-2845.
154. Leventis, N.; Rawashdeh, A.-M. M.; Elder, I. A.; Yang, J.; Dass, A.; Sotiriou-Leventis, C., Synthesis and Characterization of Ru(II) Tris(1,10-phenanthroline)-Electron Acceptor Dyads Incorporating the 4-Benzoyl-N-methylpyridinium Cation or N-Benzyl-N'-methyl Viologen. Improving the Dynamic Range, Sensitivity, and Response Time of Sol–Gel-Based Optical Oxygen Sensors. *Chemistry of Materials* **2004**, *16* (8), 1493-1506.
155. Applegate, M. B.; Perotto, G.; Kaplan, D. L.; Omenetto, F. G., Biocompatible silk step-index optical waveguides. *Biomed. Opt. Express* **2015**, *6* (11), 4221-4227.
156. Chen, B. J.; Shen, L. F.; Pun, E. Y. B.; Lin, H., Sm³⁺-doped germanate glass channel waveguide as light source for minimally invasive photodynamic therapy surgery. *Opt. Express* **2012**, *20* (2), 879-889.
157. Kim, Y.; Hwang, H. M.; Wang, L.; Kim, I.; Yoon, Y.; Lee, H., Solar-light photocatalytic disinfection using crystalline/amorphous low energy bandgap reduced TiO₂. *Scientific Reports* **2016**, *6*, 25212.
158. Liu, H.; Raza, A.; Aili, A.; Lu, J.; AlGhaferi, A.; Zhang, T., Sunlight-Sensitive Anti-Fouling Nanostructured TiO₂ coated Cu Meshes for Ultrafast Oily Water Treatment. *Scientific Reports* **2016**, *6*, 25414.
159. Barbarić-Mikočević, V. D.-M. Ž.; Itrić, K., Kubelka-Munk theory in describing optical properties of paper (I). *Technical Gazette* **2011**, *18* (1), 117-124.
160. Issa, N. A., High numerical aperture in multimode microstructured optical fibers. *Applied optics* **2004**, *43* (33), 6191-7.
161. Djouadi, D.; Meddouri, M.; Chelouche, A., Structural and optical characterizations of ZnO aerogel nanopowder synthesized from zinc acetate ethanolic solution. *Optical Materials* **2014**, *37*, 567-571.
162. Optical Substrates. (accessed 16 November).
163. Riedel, D.; Castex, M. C., Effective absorption coefficient measurements in PMMA and PTFE by clean ablation process with a coherent VUV source at 125 nm. *Applied Physics A* **1999**, *69* (4), 375-380.
164. Multimode Fiber Optic Patch Cables. (accessed 16 November).
165. Pope, R. M.; Fry, E. S., Absorption spectrum (380–700 nm) of pure water. II. Integrating cavity measurements. *Applied optics* **1997**, *36* (33), 8710-8723.
166. Al-Oweini, R.; El-Rassy, H., Synthesis and characterization by FTIR spectroscopy of silica aerogels prepared using several Si (OR)₄ and R'' Si (OR')₃ precursors. *Journal of Molecular Structure* **2009**, *919* (1), 140-145.

167. Soleimani Dorcheh, A.; Abbasi, M. H., Silica aerogel; synthesis, properties and characterization. *Journal of Materials Processing Technology* **2008**, 199 (1), 10-26.
168. Bagheri, S.; Shameli, K.; Abd Hamid, S. B., Synthesis and Characterization of Anatase Titanium Dioxide Nanoparticles Using Egg White Solution via Sol-Gel Method. *Journal of Chemistry* **2013**, 2013, 5.
169. Biswajit, C.; Bikash, B.; Amarjyoti, C., Extending Photocatalytic Activity of TiO₂ Nanoparticles to Visible Region of Illumination by Doping of Cerium. *Photochemistry and Photobiology* **2012**, 88 (2), 257-264.
170. Choudhury, B.; Choudhury, A., Oxygen defect dependent variation of band gap, Urbach energy and luminescence property of anatase, anatase–rutile mixed phase and of rutile phases of TiO₂ nanoparticles. *Physica E: Low-dimensional Systems and Nanostructures* **2014**, 56, 364-371.
171. Sharma, N.; Sharma, S.; Prabakar, K.; Amirthapandian, S.; Ilango, S.; Dash, S.; Tyagi, A., Optical band gap and associated band-tails in nanocrystalline AlN thin films grown by reactive IBSD at different substrate temperatures. *arXiv preprint arXiv:1507.04867* **2015**.
172. Behnajady, M. A.; Modirshahla, N., Nonlinear regression analysis of kinetics of the photocatalytic decolorization of an azo dye in aqueous TiO₂ slurry. *Photochemical & Photobiological Sciences* **2006**, 5 (11), 1078-1081.
173. Mehrotra, K.; Yablonsky, G. S.; Ray, A. K., Kinetic Studies of Photocatalytic Degradation in a TiO₂ Slurry System: Distinguishing Working Regimes and Determining Rate Dependences. *Industrial & Engineering Chemistry Research* **2003**, 42 (11), 2273-2281.
174. Giani, L.; Groppi, G.; Tronconi, E., Mass-Transfer Characterization of Metallic Foams as Supports for Structured Catalysts. *Industrial & Engineering Chemistry Research* **2005**, 44 (14), 4993-5002.
175. Groppi, G.; Giani, L.; Tronconi, E., Generalized Correlation for Gas/Solid Mass-Transfer Coefficients in Metallic and Ceramic Foams. *Industrial & Engineering Chemistry Research* **2007**, 46 (12), 3955-3958.
176. Hasegawa, G.; Shimizu, T.; Kanamori, K.; Maeno, A.; Kaji, H.; Nakanishi, K., Highly Flexible Hybrid Polymer Aerogels and Xerogels Based on Resorcinol-Formaldehyde with Enhanced Elastic Stiffness and Recoverability: Insights into the Origin of Their Mechanical Properties. *Chemistry of Materials* **2017**, 29 (5), 2122-2134.
177. Mahadik, D. B.; Jung, H.-N.-R.; Han, W.; Cho, H. H.; Park, H.-H., Flexible, elastic, and superhydrophobic silica-polymer composite aerogels by high internal phase emulsion process. *Composites Science and Technology* **2017**, 147, 45-51.
178. Zuo, L.; Zhang, Y.; Zhang, L.; Miao, Y.-E.; Fan, W.; Liu, T., Polymer/Carbon-Based Hybrid Aerogels: Preparation, Properties and Applications. *Materials* **2015**, 8 (10), 6806-6848.

APPENDIX

APPENDIX A. Calibration Curve of Phenol Solution

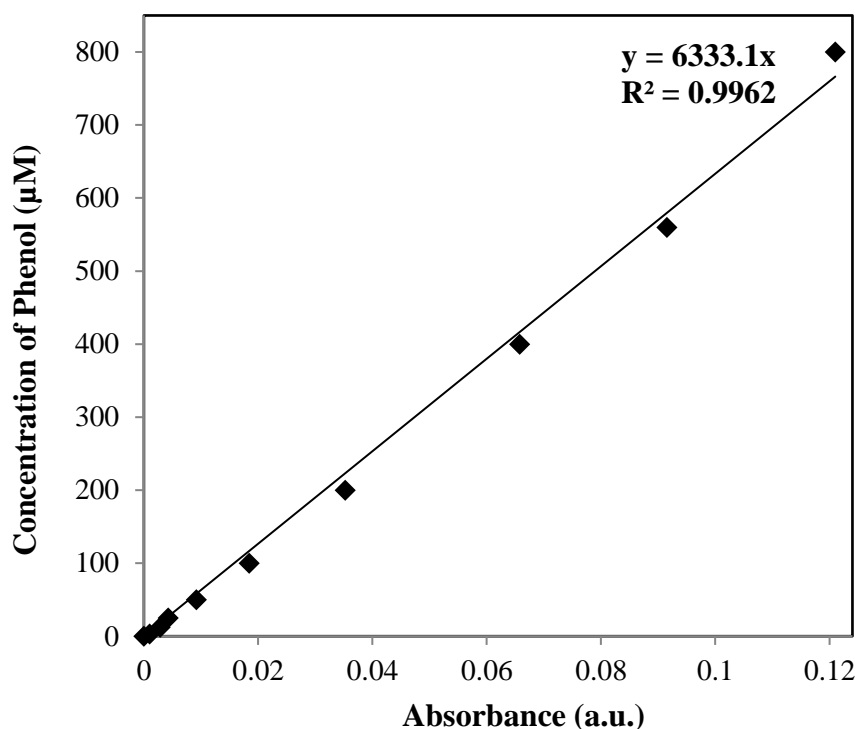


Figure A.1. Calibration curve for aqueous phenol solution in 0-800 μM range

APPENDIX B. Matlab code for determination of rate expression constants

```
clear all, clc
```

```
a=[67;65;58;51;41;30;18.4;9.2;0]; %% Incident power at the fiber output in the experiments, mW.
```

```
t=[0.94;0.92;0.84;0.78;0.6;0.51;0.37;0.19;0]; %% corresponding conversion of phenol at light powers in the experiments.
```

```
L=3.45; %% Length of the microphotoreactor, cm.
```

```
D1=0.15; %% Diameter of the fabricated channel in the aerogel composite, cm.
```

```
area=3.14*(D1/2)^2; %% Cross sectional area of the channel end, cm^2.
```

```
x=a';
```

```
y=t';
```

```
P=(a'/(area))*exp(-3.97*L*2.303/10) %% Power of light at the channel end calculated by attenuation of light, mW.
```

```
ro=1.001; %% density of the phenol solution, g/cm^3.
```

```
mu=0.0089; %% viscosity of the phenol solution, g/cm/min.
```

```
D=60*1.012*(10^(-5)) %% Diffusion coefficient of phenol in water, cm^2/min.
```

```
Q=0.0143; %% volumetric flow rate of the reactant, cm^3/min.
```

```
Io=41; %% Incident power in the experiment, mW.
```

```
V=L*3.14*(D1/2)^2; %% Volume of the channel, cm^3.
```

```
T=V/Q; %% residence time, min.
```

```

vz=Q/(3.14*(D1/2)^2) %% Velocity of reactant.
Re=(vz*D1*ro/mu) %% Reynolds Number.
Sc=(mu/(ro*D)) %% Schmidt number
Sh=1.16*((Re)^(0.43))*(Sc^(1/3)) %% Sherwood Number.
km=Sh.*D/D1 %% external mass transfer coefficient.
b(1)=0.098 %% constant in the rate expression, k_app.
b(2)=0.0029 %% constant in the rate expression, absorption coefficient, epsilon.
b(3)=1.5 %% constant in the rate expression, dependency of the absorbed light intensity
on the reaction rate.
f = (1-exp((-km*4*L./(D1*vz))*(1-(km./(((b(1).*(P*(b(2))).^(b(3))))+km))))); % %
Objective Function
q=P*b(2)
figure(1)
plot(q, y, '*g')
hold on
plot(q, f, '-r')
hold off
grid
xlabel('P')
ylabel('X')

SStot=sum(((y(1)-mean(y))^2)+((y(2)-mean(y))^2)+((y(3)-mean(y))^2)+((y(4)-
mean(y))^2)+((y(5)-mean(y))^2)+((y(6)-mean(y))^2)+((y(7)-mean(y))^2)+((y(8)-
mean(y))^2)+((y(9)-mean(y))^2))
SSreg=sum(((y(1)-f(1))^2)+((y(2)-f(2))^2)+((y(3)-f(3))^2)+((y(4)-f(4))^2)+((y(5)-
f(5))^2)+((y(6)-f(6))^2)+((y(7)-f(7))^2)+((y(8)-f(8))^2)+((y(9)-f(9))^2))
R=1-SSreg/SStot %% R^2, least square calculation.

```

APPENDIX C. Matlab Code for numerical solution of concentration profile in the channel along z

```

function f = photo(z,y)
ro=1.001; %% density of the phenol solution,g/cm^3 .
mu=0.0089; %% viscosity of the phenol solution, g/cm/min.
D=60*1.012*(10^(-5)) %% Diffusion coefficient of phenol in water, cm^2/min.
Q=0.0143; %% volumetric flow rate of the reactant, cm^3/min.
Po=41; %% Incident power in the experiment, mW.
D1=0.15; %% Diameter of the fabricated channel in the aerogel composite, cm.
L=3.44; %% Length of the microphotoreactor, cm.
V=L*3.14*(D1/2)^2; %% Volume of the channel, cm^3.
T=V/Q; %% residence time, min.

```

```

vz=Q/(3.14*(D1/2)^2) %% Velocity of reactant.
Re=(vz*D1*ro/mu) %% Reynolds Number.
Sc=(mu/(ro*D)) %% Schmidt number.
Sh=1.1*((Re)^(0.43))*(Sc^(1/3))
Kx=Sh.*D/D1 %% Sherwood Number.
b(1)=0.098 %% constant in the rate expression, kappa.
b(2)=0.0029 %% constant in the rate expression, absorption coefficient, epsilon.
b(3)=1.5 %% constant in the rate expression, dependency of the absorbed light intensity
on the reaction rate.
area=3.14*(D1/2)^2; %% Cross sectional area of the channel end, cm^2.
nu=3.97; %% attenuation of light in the channel.

```

```

f=[Kx*(-4*y/(D1*vz))*((1-(Kx./((((b(1))*(((0.125*Po*exp(-
nu*2.303*z/10))/area)*(b(2))).^(b(3))))+Kx)))));

```

On command window:

```

b(1)=0.098
b(2)=0.0029
b(3)=1.5
Po=41;
D1=0.15
area=3.14*(D1/2)^2;
Co=368;
L=3.44;
nu=3.97;
z=[0 L];
[z, C] = ode45(@photo2,[0,L],Co)
figure (1)
plot(z,C,'b')
Kx=0.0275
m=C.*(Kx./((((b(1))*(((0.125*Po*exp(-nu*2.303*z/10))/area)*(b(2))).^(b(3))))+Kx)))
hold on
plot(z,m,'k')
figure (2)
plot(z, (1-C/Co))
x=100*(C(1)-C(41))/(C(1))

```